# PhD Thesis

Dissertation

# Synthesis and Characterization of Novel Photoresists for Extreme UV Lithography

ausgeführt zum Zwecke der Erlangung des akademischen Grades
eines Doktors der technischen Wissenschaften

unter der Leitung von

**Univ.Prof. Dipl.-Ing. Dr.mont. Jürgen Stampfl**

Institut für Werkstoffwissenschaft und Werkstofftechnologie

eingereicht an der Technischen Universität Wien Fakultät für
Maschinenwesen und Betriebswissenschaften

von

**Ching-Chung Huang, MSc**

11742803

No.120 Wendong St., East Dist., Tainan City 701, Taiwan (R.O.C.)

“Have no fear of perfection; you’ll never reach it.”

Maria Skłodowska-Curie

# Danksagung

My scientific journey would not have been possible without the guidance from my supervisor Prof. Jürgen Stampfl. The utmost gratitude of mine goes to him for helping me to become matured as a professional researcher through discussions and instructions. I am very grateful to Prof. Robert Liska and Dr. Christian Gorsche for offering me this PhD opportunity to join their successful group at TU Wien and fulfilling my work. Special thanks go to European Union's Horizon 2020 research for funding and facilitating ELENA project.

I need to thank the supervisory and advisory committee of ELENA project for continuous support on scientific and personal skill training. My gratitude goes to Prof. Oddur Ingólfsson and Ms. Brynja Dís Guðmundsdóttir for maintaining and organising the project and all the training activities. I thank my fellow ESRs Ali, Reza, René, Maria, Elif, Cristiano, Linh, Aya, Jakub, Najmeh, Ashish, Dominik, Abid and Po, who have devoted themselves to the conferences, meetings and training schools within ELENA community. You guys are amazing!

I am extremely grateful to the scientific and technical support during my secondment abroad from Prof. Fred Brouwer, Dr. Sonia Castellanos, Lianjia, Neha, Olivier, Jarich at ARCNL; Prof. Janina Kopyra and Paulina at Siedlce University of Natural Sciences and Humanities; Dr. Danilo De Simone, Dr. Ivan Pollentier, Dr. Hyo Seon Suh at IMEC.

For an important part, my gratitude goes to all my colleagues that welcomed me the first day with open arms at DVSPM. Special thanks to Moritz and György for constantly supporting me and joining me on the trip back to my home country Taiwan. We should plan for another trip soon! I thank my fellow PhD students in room H45 Pazi, Sebi, Roli, Kathi, Sandra, Alex, Paul and Nico. I enoyed not only the fruitful discussions and scientific input, but the laughs and special smells that we have been through together. I also appreciate the tims and beer with Elise, Markus L., Yazgan, Philip, Raffi, Schnölli, Gernot, Hansi, Raffael, Babsi, AD, Hofi, David, Lisa, Markus K., Betti, Olga, Stefan, Sarah, Daniel and Davide. I would also like to thank Dagmar, Helena and Walter for administrative work.

Last but not least, I am very thankful to my parents, sister and cousins for all the support in every possible way. Your encouragements have always been touching to me. Thank you Sharon for marrying me during my PhD and moving all the way from Taiwan to Vienna. Your company has been and will always be significant for me. I am also grateful to my lovely friends from Taiwan, Hsu-Yi Tseng, Ya-Chun Tang, Ming-Lun Wu, Ping-Wei Lu, Guan-Yu Chen, Cheng-Hsien Yeh and Chun-Kai Chen.

This thesis would not have been completed without your support.

Thank you!

Danke!

謝謝!

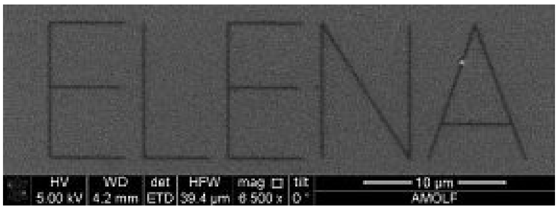

# Abstract

Considered as the most promising integrated circuit (IC) fabrication technology for the next generation, extreme ultraviolet lithography (EUVL) plays a significant role for miniaturisation in semiconductor industry. As this technique has been introduced for high volume manufacturing (HVM) since three years ago, present photoresist system still requires major optimisations before being utilised in ultrahigh-resolution patterning. High EUV-dose remains necessary for printing dense structures with acceptable roughness using current chemically amplified photoresists, which slows down manufacturing throughput. Non-chemically amplified resist system has attracted much attentions recently from academy and industry owing to its potentials in improving resolution, sensitivity and line edge roughness of printing quality. Instead of using photoacid generator (PAG), high EUV-absorbance metals are incorporated into resist system with organic moieties to solve roughness and resolution issue resulted from acid diffusion. They are also believed to have preferable mechanical properties to prevent pattern collapse during development process.

In this work, two main categories of metal oxo clusters based on titanium, zirconium and hafnium and their process conditions for lithographic patterning have been developed. Mono-metallic Zr clusters built on identical crystal structures contain crosslinkable (methacrylate, vinylacetate and dimethacrylate) and/or non-crosslinkable pivalate ligands for performance comparison. It was discovered that crosslinking density plays a crucial role with respect to increasing resist sensitivity towards both electron beam and EUV photons by providing more unsaturated allyl groups for polymerisation. Yet steric hindrance caused by different positions of allyl group did not significantly affect material sensitivity and resolution. Moreover, multi-metallic oxo clusters revealed a superior patterning performance with assistance from additional Ti and Hf. Having higher EUV linear absorption, these multi-metallic compounds could be patterned with lower doses than those for Zr clusters. Resolution has also been meliorated in the same dose range.

To understand photochemical interaction of the clusters with EUV photons, dissociative electron attachment spectroscopy, outgassing analysis and thin-film FTIR were conducted for study of solubility switch mechanism. The results have indicated both crosslinking and condensation pathways are feasible yet it is difficult to distinguish which one dominates. Therefore, a time-resolved spectroscopy will be beneficial and facilitate further research on detailed physical chemistry of photoresist upon EUV exposure.

# Kurzfassung

Die Lithographie im extremen UV (EUVL) gilt als die vielversprechendste Technologie zur Herstellung integrierter Schaltkreise für die nächste Halbleitergeneration und spielt eine wichtige Rolle für die Miniaturisierung in der Elektronikindustrie. Da diese Technik vor drei Jahren für die Massenfertigung eingeführt wurde, erfordert das derzeitige Fotolacksystem noch erhebliche Optimierungen, bevor es für die ultrahochauflösende Strukturierung verwendet wird. Eine hohe EUV-Dosis bleibt erforderlich, um dichte Strukturen mit akzeptabler Rauheit unter Verwendung aktueller chemisch verstärkter Fotolacke zu drucken, was den Herstellungsdurchsatz verlangsamt. Das chemisch nicht verbesserte Fotolacksystem hat in jüngster Zeit aufgrund seiner Möglichkeiten zur Verbesserung der Auflösung, Empfindlichkeit und Kantenrauheit der Druckqualität in der Forschung und Industrie große Aufmerksamkeit erregt. Anstelle der Verwendung eines Photosäuregenerators werden Metalle mit hoher EUV-Absorption in ein Fotolacksystem mit organischen Resten eingebaut, um das durch die Säurediffusion verursachte Problem der Rauheit und Auflösung zu lösen. Es wird auch angenommen, dass sie ausreichende mechanische Eigenschaften haben, um ein Zusammenfallen der Struktur während des Entwicklungsprozesses zu verhindern.

In dieser Arbeit wurden zwei Hauptkategorien von Metalloxoclustern auf der Basis von Titan, Zirkonium und Hafnium sowie deren Prozessbedingungen für die lithographische Strukturierung entwickelt. Monometallische Zr-Cluster, die auf identischen Kristallstrukturen aufgebaut sind, enthalten zum Leistungsvergleich vernetzbare (Methacrylat, Vinylacetat und Dimethacrylat) und / oder nicht vernetzbare Pivalatliganden. Es wurde entdeckt, dass die Vernetzungsdichte eine entscheidende Rolle bei der Erhöhung der Fotolackempfindlichkeit sowohl gegenüber Elektronenstrahl- als auch gegenüber EUV-Photonen spielt, indem mehr ungesättigte Allylgruppen für die Polymerisation bereitgestellt werden. Die durch verschiedene Positionen der Allylgruppe verursachte sterische Hinderung hatte jedoch keinen signifikanten Einfluss auf die Materialempfindlichkeit und -auflösung. Darüber hinaus zeigten multimetallische Oxo-Cluster mit Hilfe von zusätzlichem Ti und Hf eine überlegene Leistung während der Strukturierung. Mit einer höheren linearen EUV-Absorption könnten diese multimetallischen Verbindungen mit niedrigeren Dosen als die für Zr-Cluster strukturiert werden. Die Auflösung wurde im gleichen Dosisbereich ebenfalls verbessert.

Um die photochemische Wechselwirkung der Cluster mit EUV-Photonen zu verstehen, wurden dissoziative Elektronenanlagerungsspektroskopie, Ausgasungsanalyse und Dünnschicht-FTIR zur Untersuchung des Löslichkeitsschaltmechanismus durchgeführt. Die Ergebnisse haben

gezeigt, dass sowohl Vernetzungs- als auch Kondensationsmöglichkeiten gegeben sind, es ist jedoch schwierig zu unterscheiden, welcher dominiert. Daher ist eine zeitaufgelöste Spektroskopie von Vorteil und erleichtert die weitere Erforschung der detaillierten physikalischen Chemie von Fotolacke bei EUV-Belichtung.

# Table of Contents

# 1 Introduction

Integrated circuits (IC) and microelectronic devices are existing throughout the entire modern society. From biochips in human body to supercomputers employed in NASA international Space Station, the ubiquity of this technology has to be attributed to downscaling of transistor size that leads to the exponential growth of computing power. They have completely changed the way people communicate, work and travel. Gordon Moore, the co-founder and chairman emeritus of Intel Corporation, published a paper in 1965 stating an observation of the number of transistors in an integrated circuit, in which he concluded that the density of transistors would double every 24 months [1]. This observation was named as Moore's Law (see Figure 1-1). However, this growing trend has been slowed down since 2005 when the feature size of IC approached single-digit nanometre range [2, 3].

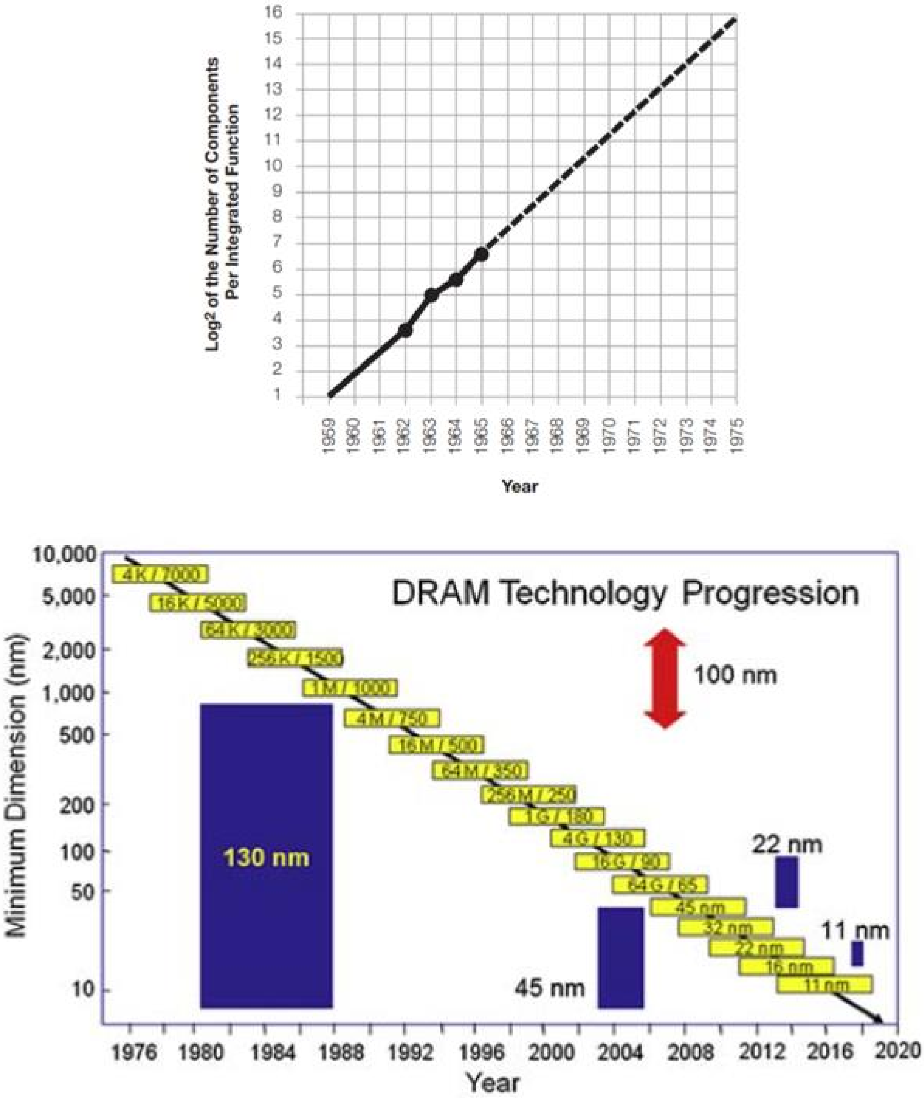

*Figure 1-1: Moore´s Law prediction and microprocessor transistor counts from 1971-2018 [1, 4].*

## 1.1 Lithography

The advancement of lithography has made a significant impact on downsizing of transistors. Lithography is a process of IC fabrication that prints circuit features on silicon wafers (Figure 1-2). By applying a layer of photosensitive or radiation-sensitive material, namely photoresist, the desired patterns are able to be transferred from photomask onto silicon wafer surfaces through the property change of the resist material and developing procedure. Nevertheless, the critical dimension (size limitation of feature printed) is closely dependent upon the light source, numerical aperture, as well as photoresist properties.

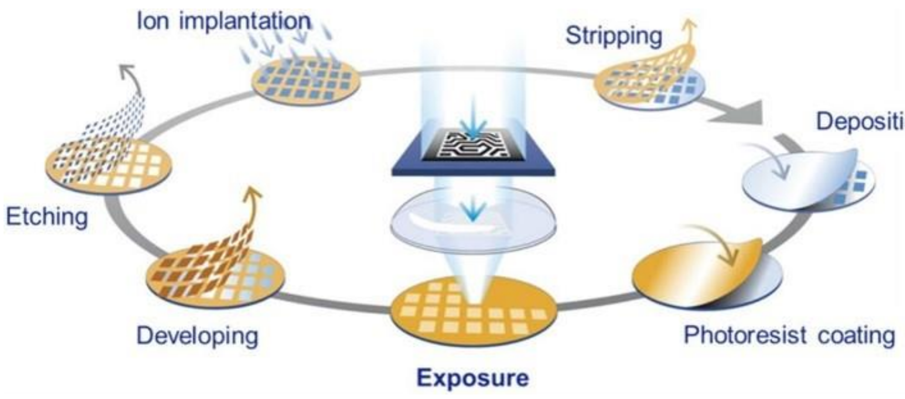

*Figure 1-2: Scheme of repetitive production of semiconductor devices* [5].

In 1867, Ernst Abbe developed and proposed two expressions regarding the most crucial characteristics of an optical imaging system. He discovered the critical dimension CD (or minimum width of the printed circuit, F) is determined by:

$$F = CD = k_1 \cdot \frac{\lambda}{NA} = k_1 \cdot \frac{\lambda}{n\, sin\alpha}$$

where $\lambda$ is the wavelength of the light used, NA is the numerical aperture of the system´s lens, $k_1$ is the resolution factor, which is a function of the photoresist, photomask, illumination and resolution enhancement technique (RET), n is the refraction index of the medium between the lens and wafer and $\alpha$ is the collection half angle [6]. In order to reach smaller critical dimension or even down to atomic width scale, vast research sources have been devoted to minimising the wavelength of light source, increase numerical aperture of device setup, and developing novel photoresist materials.

Deep Ultraviolet (DUV) has been utilised as the light source of exposure tools since 1990 for commercial ICs manufacturing and remains the most widely-used light source nowadays [7]. From the initial KrF excimer laser producing 248 nm wavelength to the current ArF excimer laser generating 193 nm wavelength, the limit of a single optical patterning at 45 nm half-pitch is still considered relatively immense despite of the much-improved numerical aperture. Multiple patterning technique was introduced to lithography process after Gurtej Sandhu of Micron Technology invented it during the 2000s. This method enables not only printing smaller feature size to become possible with multi-step exposure process, but prolonged the life of DUV tools due to the fact that it could be theoretically implemented into the existing machines (Figure 1-3) [8, 9]. However, on the other hand, the complexity of the process becomes a major issue when it comes to complicated patterns, e.g. multi-layers, 3D architecture, etc. The procedure is also very time-consuming for complex structure manufacturing, leading to considerable high cost of products. These drawbacks urged the development of a novel photolithography tool for semiconductor industry.

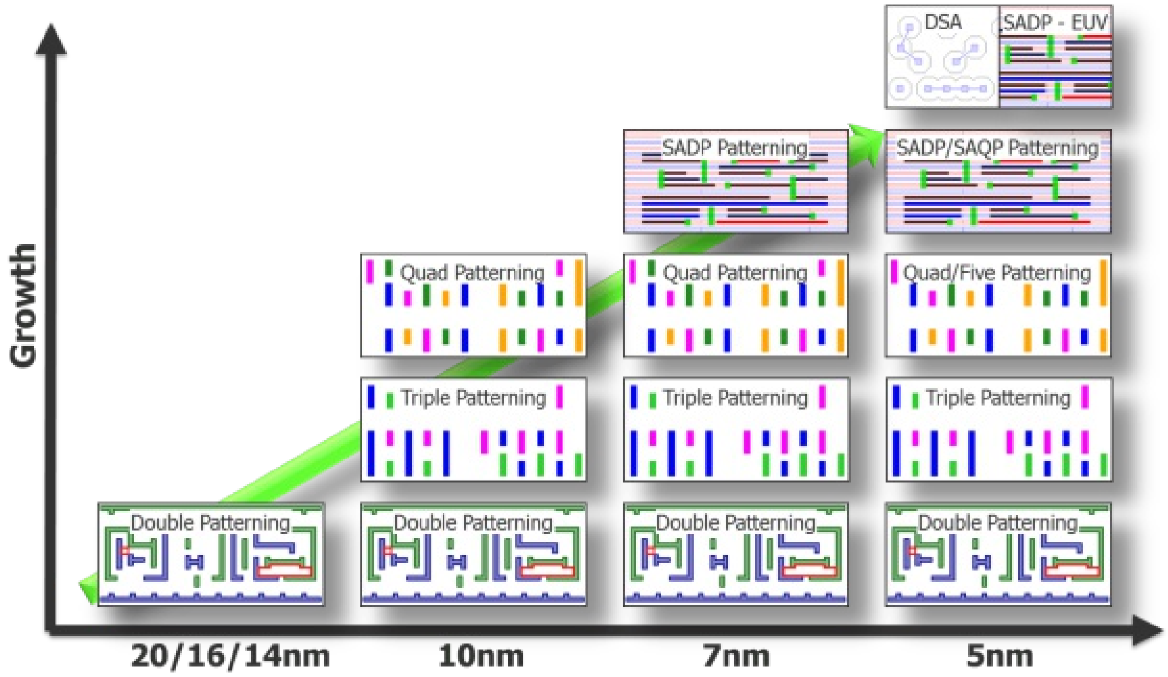

*Figure 1-3: Evolution of multiple patterning technique [10].*

Over the last decade, Extreme Ultraviolet (EUV) has risen from the horizon and been considered as one of the most promising candidates for future nanofabrication manufacturing [11, 12]. Despite the wavelength of EUV ranges from 10 to 120 nm, the most interesting region for lithography applications lies in between 10 and 14 nm. It is at least ten degrees lower than DUV wavelength, meaning the critical dimension of a single optical EUV patterning should be significantly smaller in theory. This cutting-edge technology has provided various potentials for semiconductor and microelectronic industry. However, the physics in EUV region are relatively different, resulting in a massive modification of tool design and component materials.

Unlike the DUV setup, the system of EUV lithography requires to be kept under high vacuum for operation since all materials absorb at EUV range. Quartz optics can no longer be installed as those in DUV tool. Instead, a new reflective unit consisting of multiple alternating layers of molybdenum and silicon is implemented to provide up to 70 % reflection at 13.5 nm. 6 to 12 sets of special, high transmissive mirrors are needed in order to form an accurate projection before reaching the photomask. Considering the reflectivity each reflective mirror has, only 1-5% of EUV photon produced initially can be captured and utilised for lithography at silicon wafer surfaces [4, 13, 14]. The photomask, on the other hand, also has to be re-designed. The thickness of EUV mask absorber and the off-axis illumination required from the reflective multilayer contained within mask make major impact on the shadowing effect, causing a degrade on patterning quality (Figure 1-4) [15].

The energy or the number of EUV photons has a substantial loss traveling from light source to silicon wafers due to transmission issue. This can be compensated primarily from two different aspects. The first solution is by improving the power of EUV source. Research of EUV power sources has been listed as one of the top priorities for EUV lithography technology in recent years [16-18]. In 2016, only 80 W of power could be generated on an actual demonstration field, while 200 W was detected in the laboratory environment. Nevertheless, the estimations indicated 250 W of power is required for a stable and long-term high volume manufacturing (HVM) [18].

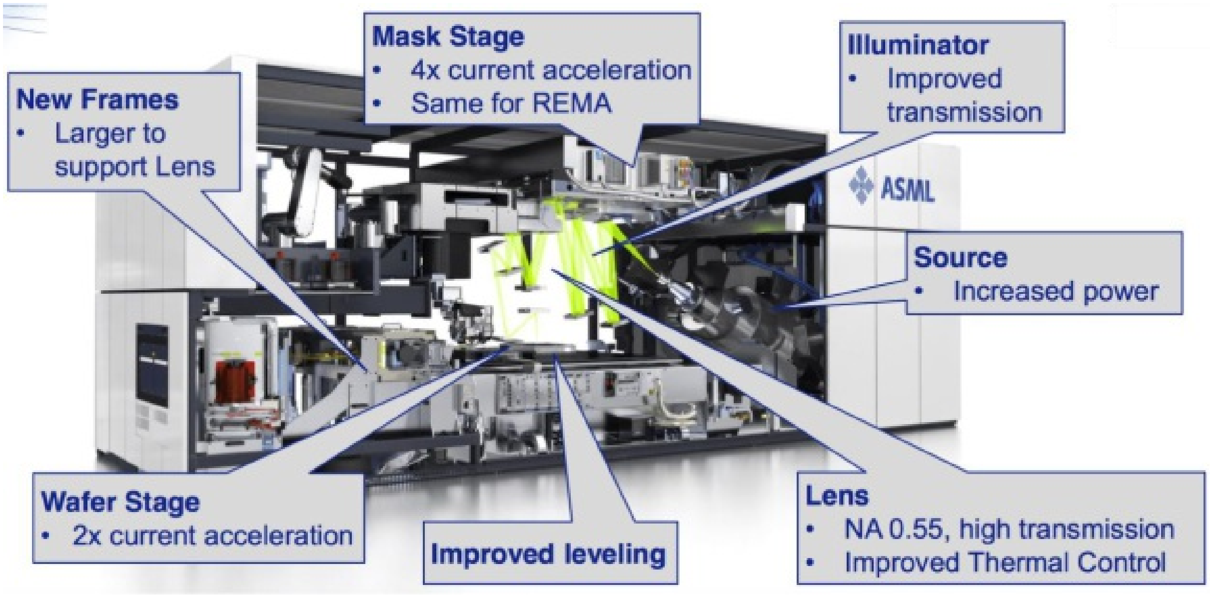

*Figure 1-4: The latest EUVL tool from ASML, NXE:3400C* [19, 20].

Until 2018, the new EUVL model, NXE:3400B, manufactured by ASML performed outstanding stability of maintaining EUV power at approximately 250 W up to a month. In addition, more than 85% of power availability at actual production plants of ASML customers could still be obtained over 13 weeks without any repairs or upgrades (Figure 1-5) [21]. The research revealed that current EUV power technology are becoming mature and able to sustain long-term HVM with sufficiently high output.

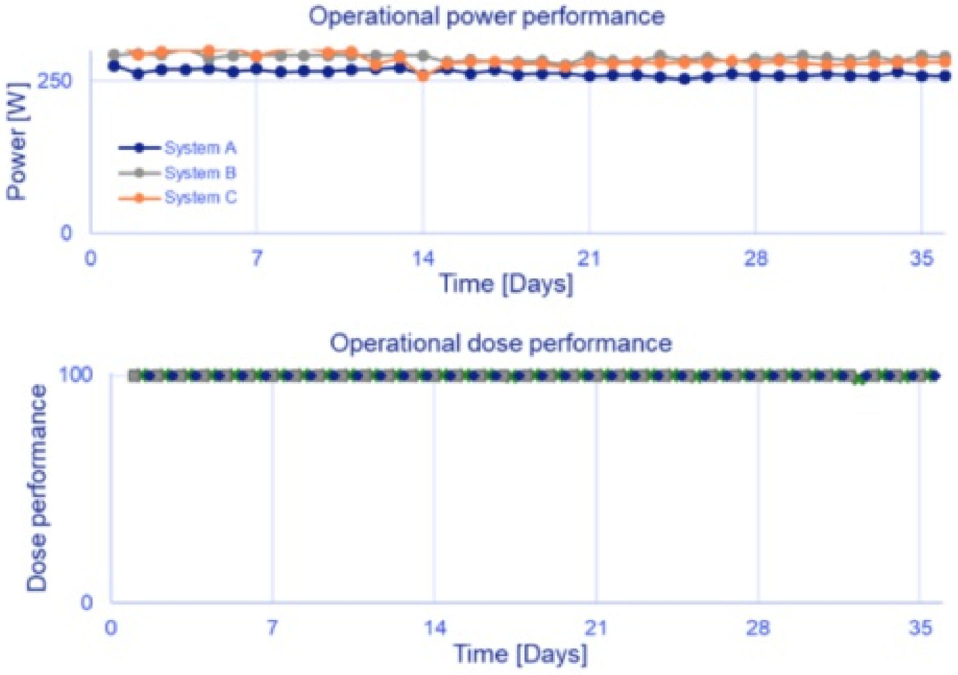

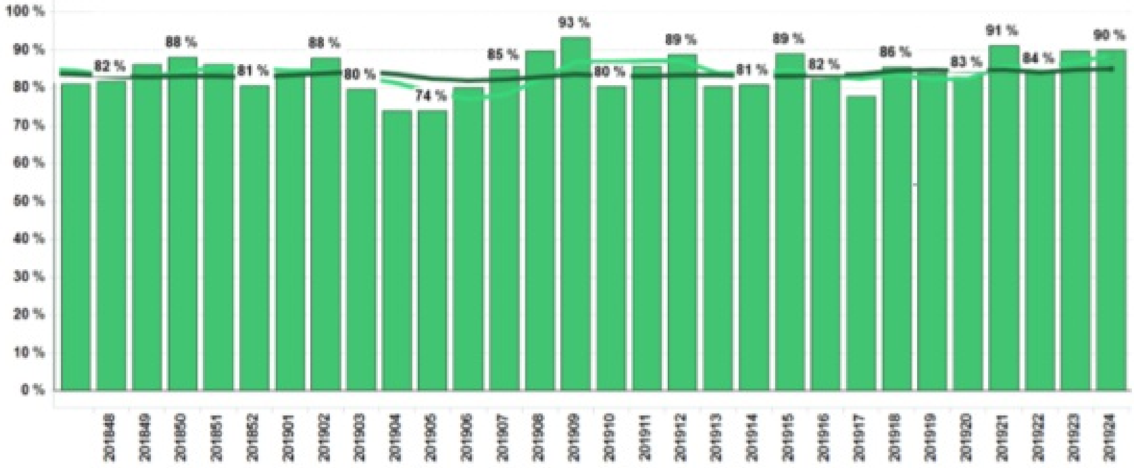

*Figure 1-5: Durability test of ASML NXE:3400B showed the EUV power could maintain at 250 W over 35 days and > 85% power availability at customer sites after 13 weeks without repairs and upgrades [21].*

## 1.2 Development of EUV Resist Materials

On the other hand, resist material is required for a substantial improvement, as it has also been considered as one of the major challenges for EUV technology. Since the physical interactions of EUV photon with photoresist are relatively different, modifications on chemical structures, formulations, and lithography processing have to be tailored to meet the demands of EUVL and moreover, to compensate the energy loss resulted from the tool. There are three crucial performances concerning lithographic patterning that are needed to be optimised: resolution (R), sensitivity (S), and line edge roughness (LER) or line width roughness (LWR). Resolution represents the smallest feature that is able to be printed with acceptable quality and control [22]. It is dependent on material properties, lithographic process (including casting, baking, developing conditions), as well as tool. Sensitivity of resist is the energy needed to generate the desired patterns, usually expressed as dose, i.e. amount of energy per unit area. Sensitivity is commonly quantified as dose-to-clear ($E_0$) or dose-to-size ($E_{size}$) [4]. Dose-to-clear is defined by dose required to enable a large exposed area to have a complete solubility switch of resist material, making it either soluble or insoluble in developer. Contrast curve analysis is a classic measure to determine the dose-to-clear for a resist material of interests. Dose-to-size is utilised to describe the dose needed to print a pattern at a specific feature size with acceptable quality.

Roughness of printed feature is usually described by LER and LWR (Figure 1-6). LER is the root-mean-squared deviation of the actual feature edge from an ideal line edge (viewed from top down). It is normally quantified as 3σ, where σ is the standard deviation. LWR is described as the root-mean-squared of the printed feature linewidth from the average critical dimension, quantified as 3σ. Research has indicated the values LER and LWR are related in most photoresist materials, showing LWR is equal to square root of two times LER [22, 23]. LER and LWR are crucial metrics to define IC performance, such as leakage of the circuit. The values strongly correlate with the analysis measures, parameters and tools. Therefore, it is important to consider the measuring conditions while comparing LER and LWR values. More efforts have also been devoted to the simulation and modelling study nowadays, aiming to develop a solution that is closer to reality [24-28].

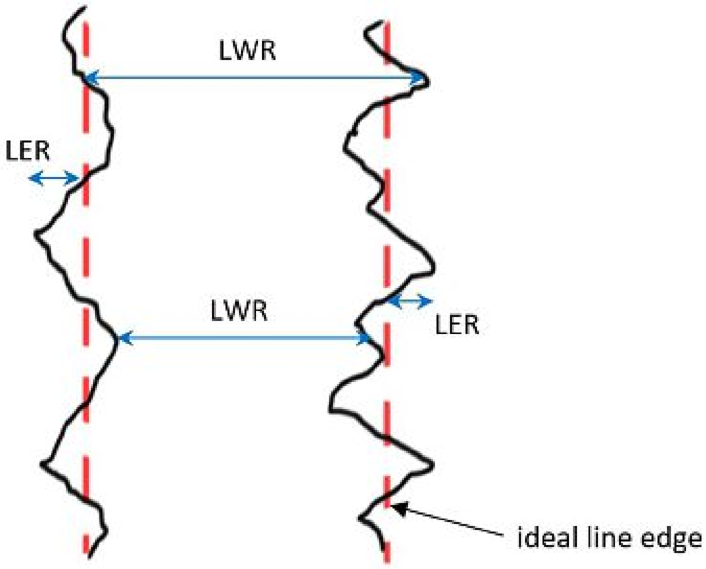

*Figure 1-6: Scheme of line edge roughness and line width roughness.*

Photoresist is a key ingredient for an efficient lithography process capable of transferring three dimensional patterns from the photomask to target substrates theoretically with no defect. It is essentially a type of photosensitive or radiation-sensitive material which microstructure rearranges upon light exposure, resulting in a substantial change in solubility, namely solubility switch. There are three major mechanisms that procures solubility switch:

- De-polymerisation: Matrices of this type of resist are mainly composed of polymers that produce hydrophilic products after light exposure. Decomposition then follows to make the exposed area turn into soluble in developers. They are categorised as positive tone resist.
- Photopolymerisation: The resists undergoing photopolymerisation pathway mostly consist of ally monomers, e.g. methacrylates and acrylates. Free radicals can be generated when they are exposed to light, initiating polymerisation within the matrix and making it become insoluble in developer. Consequently, they are mostly negative tone resists.

- Crosslinking: The resist contains crosslinkable moieties that can be crosslinked by the free radicals generated after the exposure of light source. They are conventionally used as negative tone resist.

Resist classified as positive or negative tone depends on its behaviour after development. Positive tone resist is able to keep the unexposed area remaining on the substrate, while solubility switch takes place within the exposed area, making it soluble and be etched away by the developer. On the contrary, negative tone resist is prone to leave the exposed part on the substrate owing to the solubility switch, whereas the unexposed part is removed by developer, as shown in Figure 1-7.

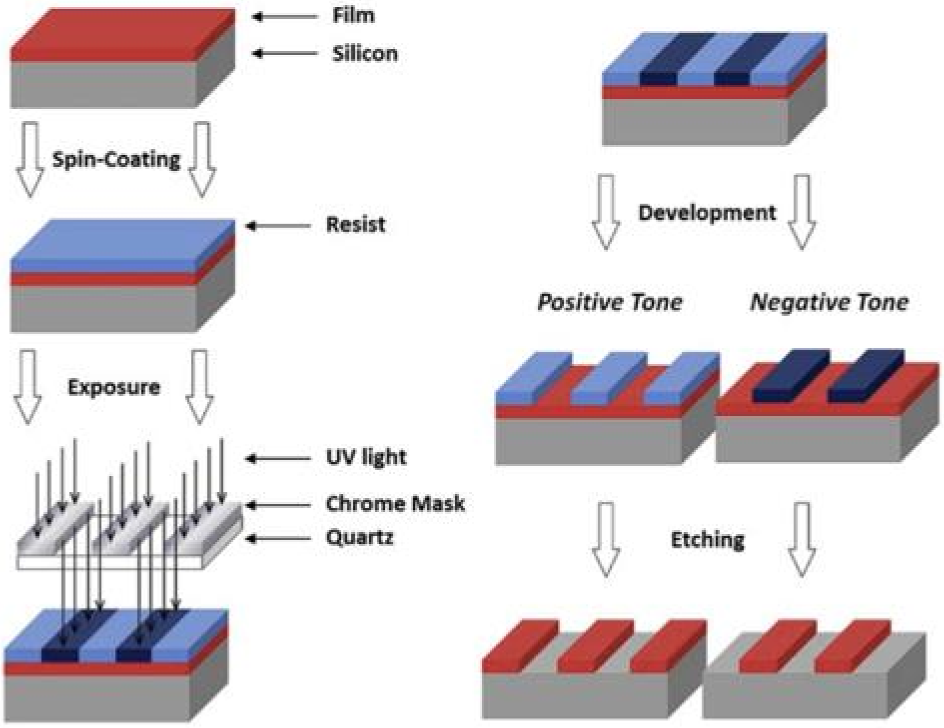

*Figure 1-7: Schematic diagram of developing process and two resist categories* [4].

Nevertheless, there is another classification that puts more emphasis on the formulation and chemical reaction upon exposure, where resist materials are categorised into chemically-amplified resist (CAR) and non-chemically-amplified (non-CA) resist. It is crucial especially for EUV photoresist since the mechanism of resist material makes a significant impact on patterning performance in terms of resolution, sensitivity, and line width roughness. Many of the oldest resist systems, such as hydrogen silsesquioxane (HSQ), DNQ-Novolac (a mixture of diazonaphthoquinone and a phenol formaldehyde resin) are non-CA resist. A single reaction occurring within non-CA resist requires to be triggered by one or more photons, leading to a quantum yield less or equal to one. In addition, the first chemically-amplified resist used in semiconductor lithography was invented by Prof. Hiroshi Ito et al. in 1982 [29]. A photo acid generator (PAG) is primarily embedded in a CAR system (2-10% wt.) to act as a catalyst. It dissociates to form an acid upon light exposure which reacts with circumjacent resist matrix and initiates the solubility switch (Figure 1-8) [30]. A single photon is capable of triggering multiple reactions and therefore the sensitivity of a CAR system is usually higher than that of a conventional non-CA resist formation.

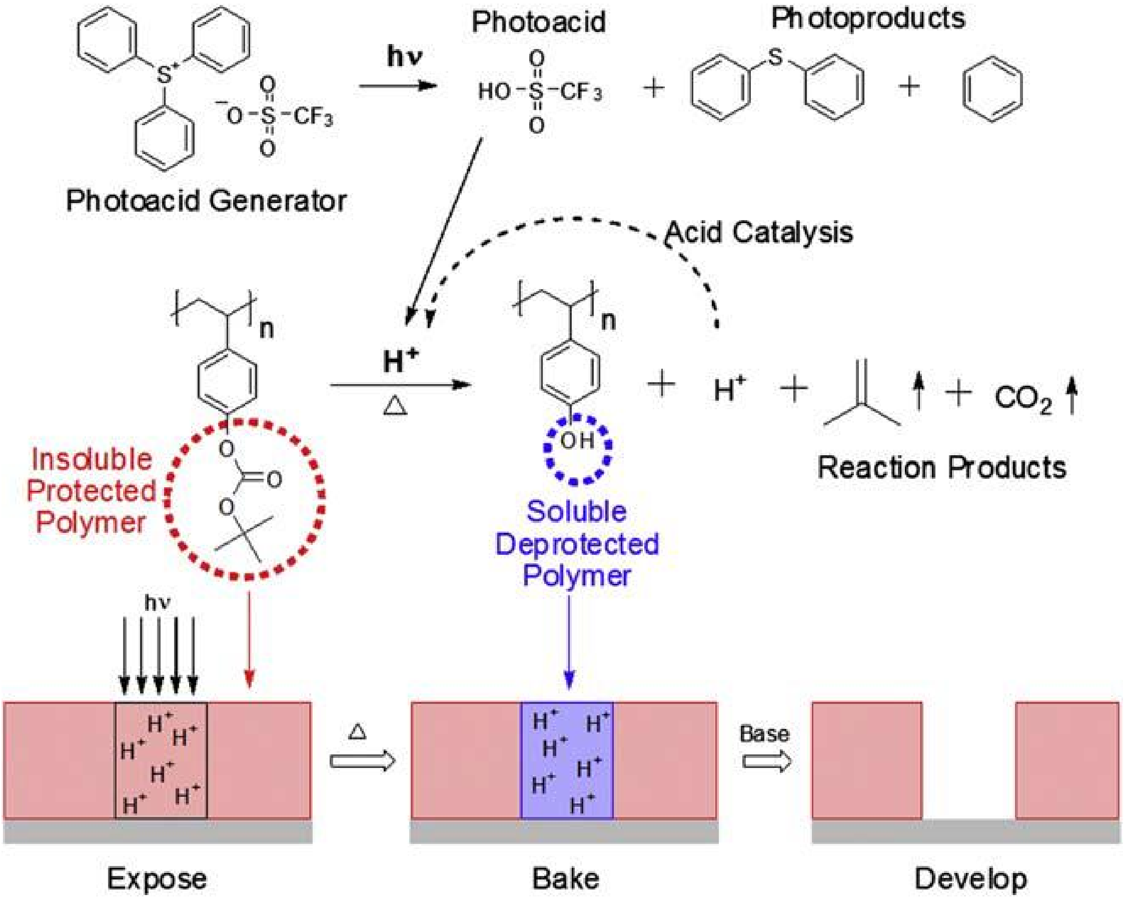

*Figure 1-8: General diagram showing the process of a typical CAR system using triphenylsulfonium triflate as PAG and tert-butyloxycarbonylprotected poly(4-hydroxystyrene) as resist matrix* [31].

The general working procedure for CAR in EUV lithographic processing is similar to that of DUV. It is spin-coated by organic solvent onto silicon wafers to form a thin film, followed by a post applied bake (PAB). After the exposure of EUV, the PAGs are decomposed into acids and react with protecting groups during a post exposure bake (PEB) process, generating more acids and rendering the continuation of amplification. Polymers of the exposed area become hydrophilic and therefore soluble in aqueous developer, performing as positive tone resist for transferring the desired pattern [32]. With the aim of feature size by EUVL manufacturing keeps decreasing towards atomic width territory, the issues of patterning with CAR have been gradually emerging.

Pattern collapse is one of the issues resulted from confinement effects that small feature patterning is suffering from (Figure 1-9). The development of pattern in semiconductor manufacturing usually involves immersion or spraying of liquid developing solvent. When feature size shrinks lower, the aspect ratio of printed line becomes significantly important. During the developing process, capillary pressure starts to apply towards printed lines while developer being dried by either nitrogen purging or spinning wafers. The force is able to mechanically deform the pattern at the top due to lack of support on either side but the bottom part remains attached to the substrate, causing the line to collapse and form a defect [33].

CAR is prone to have more severe pattern collapse owing to the elastoplastic property of polymers. The polymeric line performs elastically change at low strain but plastically above yield point. The deformation becomes irreversible afterwards and eventually it crushes into the adjacent line. One of the approaches that has been commonly used in the industry is by lower down the thickness of resist layer, optimising the line geometry to a reasonable aspect ratio in order to reduce the possibility of pattern collapse. Nevertheless, sensitivity is inevitably sacrificed in this case since thinner layer would absorb less photons to trigger solubility switch.

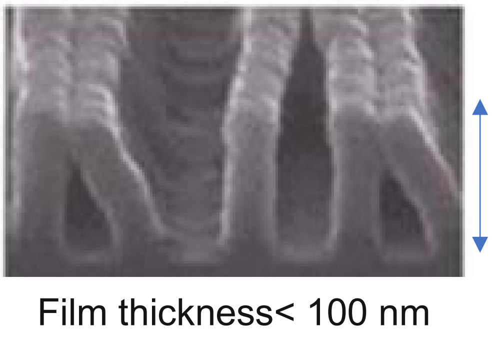

*Figure 1-9: SEM image of pattern collapse by capillary effect, with a film thickness less than 100 nm* [34].

Bad adhesion of resist materials to the substrate also leads to serious pattern collapse by detaching from the surface [35]. A common solution employed in semiconductor industry is applying specific type of primer such as bis(trimethylsilyl)amine (HMDS) before resist casting to improve the adhesion between photoresist layer and silicon wafer surface [36]. Another type of pattern collapse is resulted from resist material absorbing developer. Unlike the previous ones, it is not strictly related to capillary effect during drying of developer. Instead, the material tends to take in developing solvent, causing the swelling of the printed lines [37].

Besides pattern collapse, acid diffusion is another factor that mainly limits CAR applications in terms of small feature size patterning as well as EUVL. Physical chemistry within EUVL is significantly different from DUV lithography. Instead of reacting directly with PAG, most EUV photons containing comparatively high energy (about 92 eV at 13.5 nm) are prone to ionise resist material and produce a slightly less energetic photoelectron (approximately 80 eV). This photoelectron will then give rise to various types of secondary electrons via impact ionisation such as thermalisation and inelastic collision, as shown in Figure 1-10. PAG will eventually be triggered by secondary electrons (about 20 eV) and the amplification of the resist can propagate [38-40]. However, the length of acid diffusion should be substantially lower than critical dimension of the printed pattern. Shot noise, a discrete property caused by the particle nature of light, also deteriorates the quality of printed patterns by randomly generating acids within resist materials, leading to a degrade in resolution and line roughness. With the decreasing of feature size to single-digit nanometre range, the influence of acid diffusion in terms of LER/LWR and resolution has become critical upon EUVL manufacturing and applications. A solution to compromise the effect of acid diffusion was developed in the early 2000s involving introduction of base quencher in order to improve chemical contrast [41]. Advantage of embedding base quencher in a CAR system has two folds. This base quencher can not only suppress the function of unexpectedly generated acid in unexposed area, but have a relatively good control of acid distribution at the exposed area. One major drawback is base quencher also reduces the concentration of acid molecule in the exposed area. Amplification can no longer be as prominent as expected and therefore sensitivity becomes lower.

a)

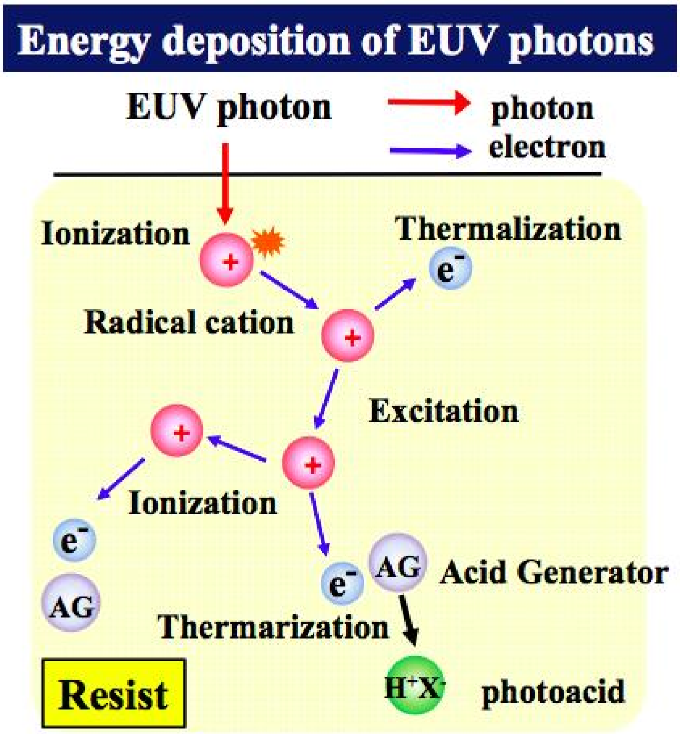

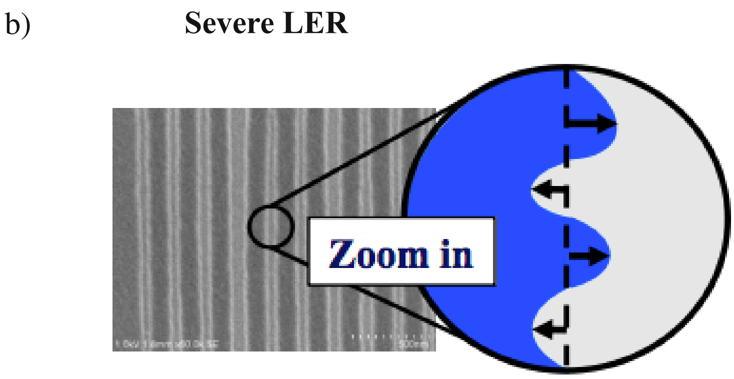

*Figure 1-10: a) Scheme of EUV photon interaction with CAR and b) Severe LER of printed lines due to long acid diffusion pathway* [34].

When it comes to the case of acid diffusion for optimising printing performance, there is an obvious trade-off relationship between resolution and sensitivity. Further research and simulation results have revealed that this trade-off relationship also involves line edge roughness, meaning two of the three metrics can be improved while the other being sacrificed. This trade-off between resolution, line edge roughness (or line width roughness) and sensitivity is known as RLS trade-off or tri-lateral challenge [42] and it exists within both chemically amplified and non-chemically amplified resists. A formula was developed by Wallow et al. in 2008 [43] to described mathematically the relationship between these three metrics as:

$$\text{Resolution}^3 \text{ x } \text{LER}^2 \text{ x Sensitivity} \approx Z$$

Z is often known as resist material constant for a specific CAR system and should be as smaller as possible. However, the physic nature of lithography remains a confinement for RLS trade-off, even though Z value can be improved via approaches such as base quencher or amplification effect. And the power of one parameter in the equation also makes an impact on the other two, i.e. two parameters might be altered substantially depending on the power of the third varied parameter. The development of CAR and non-CAR materials has reached a plateau where the lithographic performance cannot be pushed a big step forward. The availability of exposure tools and related experimental instruments became an obstacle for photoresist research since only few places in the world (Lawrence Berkeley National Lab and Paul Scherrer Institute) have appropriate device for public testing. Concerning the requirements from modern technology in terms of downsizing, more efforts and sources should be devoted to developing novel resist materials, aiming for a potential overcome of RLS trade-off.

Employing a different mechanism for solubility switch is a revolutionary aspect that is driving photoresist research to a whole new territory. The blur effect causing inferior resolution and line edge roughness undoubtedly needs to be solved while maintaining sufficient EUV absorption for superior sensitivity. Long acid diffusion path is the main reason why resolution deteriorates with the decreasing in critical dimension. In order to minimising blur effect, a novel solubility switch mechanism has to be initiated in relatively short distance from the ionisation point and a short mean free path of secondary electrons, meaning chemical amplification approach can no longer be involved. Ober's group of Cornell University published a negative tone resist system in 2008 based on molecular glass, which has outstanding performance in the sub-50 nm regime [44]. Palmer's group of University of Birmingham developed a novel type of fullerene-based material that can be used as negative tone resist [45]. Both systems are non-CA resists and contain no PAGs for amplification purpose. Their solubility switch is resulted from the crosslinking of epoxy triggered by EUV exposure and therefore they are negative tone resists. Another type of design for positive tone resist is via destroying polymer chains or densely crosslinked structure to acquire solubility switch. PMMA is a common substance used for de-polymerisation pathway [46]. EUV exposure should lead to cleavage of covalent bond of PMMA polymer chains and these small fragments can be dissolved away by organic solvents. The unexposed area has better mechanical properties and adhesion compared with conventional organic resist materials due to its three-dimensional structure, significantly reducing possibility of pattern collapse [47].

Until recent years, metal-containing resist (MCR) starts to attract a great deal of interests among EUV resist researchers. Embedding metal moiety into photoresist systems can provide several crucial advantages. Metals are known for having high atomic absorption cross section at 92 eV (13.5 nm) compared with organic elements like carbon, hydrogen, and oxygen (Figure 1-11) [48]. Resist formulation containing metal elements can efficiently increase sensitivity by capturing more EUV photons as well as making use of more secondary electrons, if the metal is properly selected. Moreover, high etch resistance of MCR enables not only the hard mask layer (a protecting layer for photoresist) to be no longer necessary, reducing the manufacturing cost and time, but also resist layer thickness to be thinner for preventing pattern collapse issue.

As the pioneer in high resolution MCR, American manufacturer Inpria is specifically focusing on metal oxide substance for EUV photoresist application. The materials they have developed are essentially metal oxo clusters with metal and organic moiety. The metal element is mainly responsible for rendering a productive interaction between EUV photon and metal oxide molecule, while the organic element is in charge of solubility switch. The Sn-based metal oxide resist, tin oxo cage, has produced remarkable results, showing a good resolution at 8 nm half pitch with good etch resistance [49]. Despite of using a high dose (200 mJ), it continued to gain considerable attentions from the EUV society, especially when CARs were struggling to reach sub-16 nm regime.

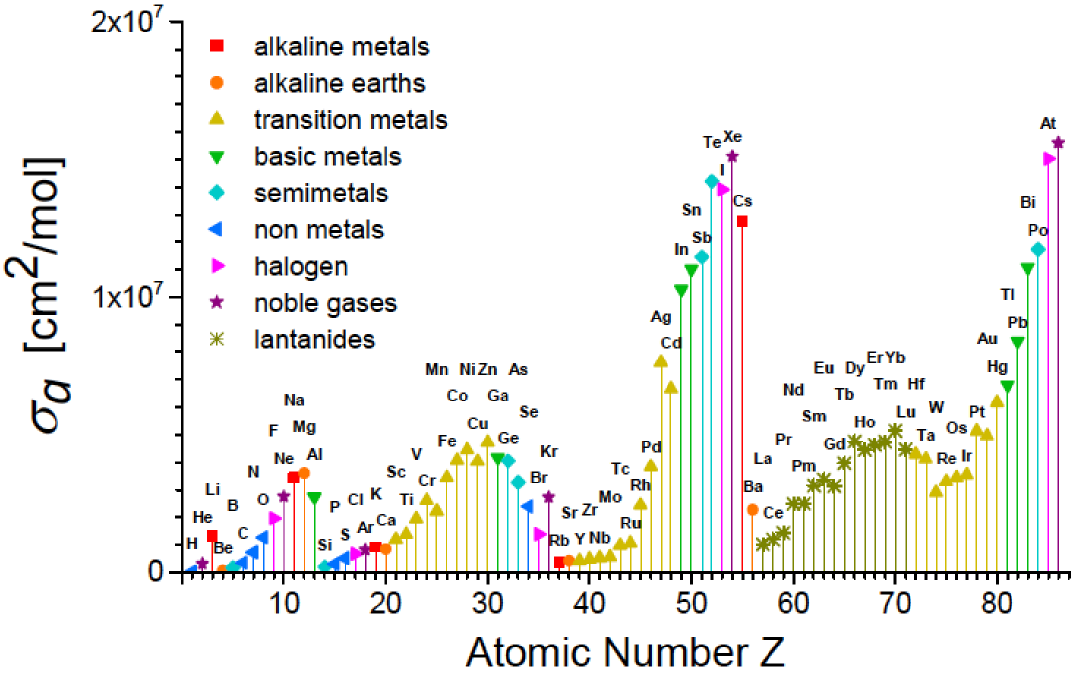

*Figure 1-11: Atomic absorption cross section of elements at 92 eV with atomic number from 1 to 86* [48,50].

Inpria also developed an optimised formulation that achieved 16 nm half pitch with 49 mJ via a commercial ASML NXE tool in 2015 [51]. Being an alternative to conventional organic resist without using a diffusional amplified mechanism, MCR has proven the feasibility of reaching high resolution at relatively low dose. However, RLS trade-off stays intact and cannot be overcome. LER is still far from the acceptable criteria. Cross-contamination becomes problematic for MCRs upon high volume manufacturing due to metals being intentionally utilised in the resist system, which, as a result, potentially causes a partial conflict against silicon. All these issues remain challenges for future research and EUV community are looking forwards to a revolutionary resist material that is capable of meeting the requirements from current situation.

# 2 Objectives

The goal of this work is focusing on development of a novel type of resist material for EUVL application leading to an improvement on the three most important metrics, resolution, line edge roughness (line width roughness) and sensitivity. These new materials are primarily based on metal ox clusters incorporated with organic crosslinkable ligands to render solubility switch. Titanium (Ti), zirconium (Zr) and hafnium (Hf) from group 4 of the periodic table are used as the major metallic composition since all metals show superior atomic absorption cross section at 92 eV and Zr as well as Hf metal oxide compounds were proven to have good patterning performance previously [52-54]. Methacrylate is employed in most metal oxo clusters to potentially form a crosslinking structure after light exposure. There are two possible mechanism proposed after light exposure (Figure 2-1). First, ligand cleavage takes place to generate an active site on the surface of metal oxo cluster. This active site will then promote crosslinking between adjacent clusters via condensation [55]. Secondly, the terminal methacrylate ligand will possibly undergo decarboxylation, leaving a free allyl radical that can either outgas or react further with methylene groups of other methacrylate ligands [54], as shown in Figure . The mechanism could be one or the combination of the two proposed pathways depending on the process conditions. These materials are expected to act as negative tone resists, meaning clusters at the exposed area should crosslink and become insoluble in organic solvents, whereas the unexposed clusters remain soluble and can be dissolved away.

There are four dimensions that are needed to be compared and verified:

- The influence of crosslinkable-ligand density in a single cluster on patterning performance.
- The influence of coordination numbers of the same metal in different clusters on patterning performance.
- The influence of metals from the same group with difference cross sections on patterning performance.
- The influence of two or more optical-sensitive metals in a single cluster on patterning performance.

To approach these, three different categories of metal oxo clusters were targeted within this work, which were Zr oxo clusters, multi-metallic oxo clusters, and Hf oxo clusters. As the first compound chosen to be synthesised, $Zr_4O_2(OMc)_{12}$ has 12 methacrylate ligands either bridging or chelating across zirconium atoms, as shown in Figure 2-2.

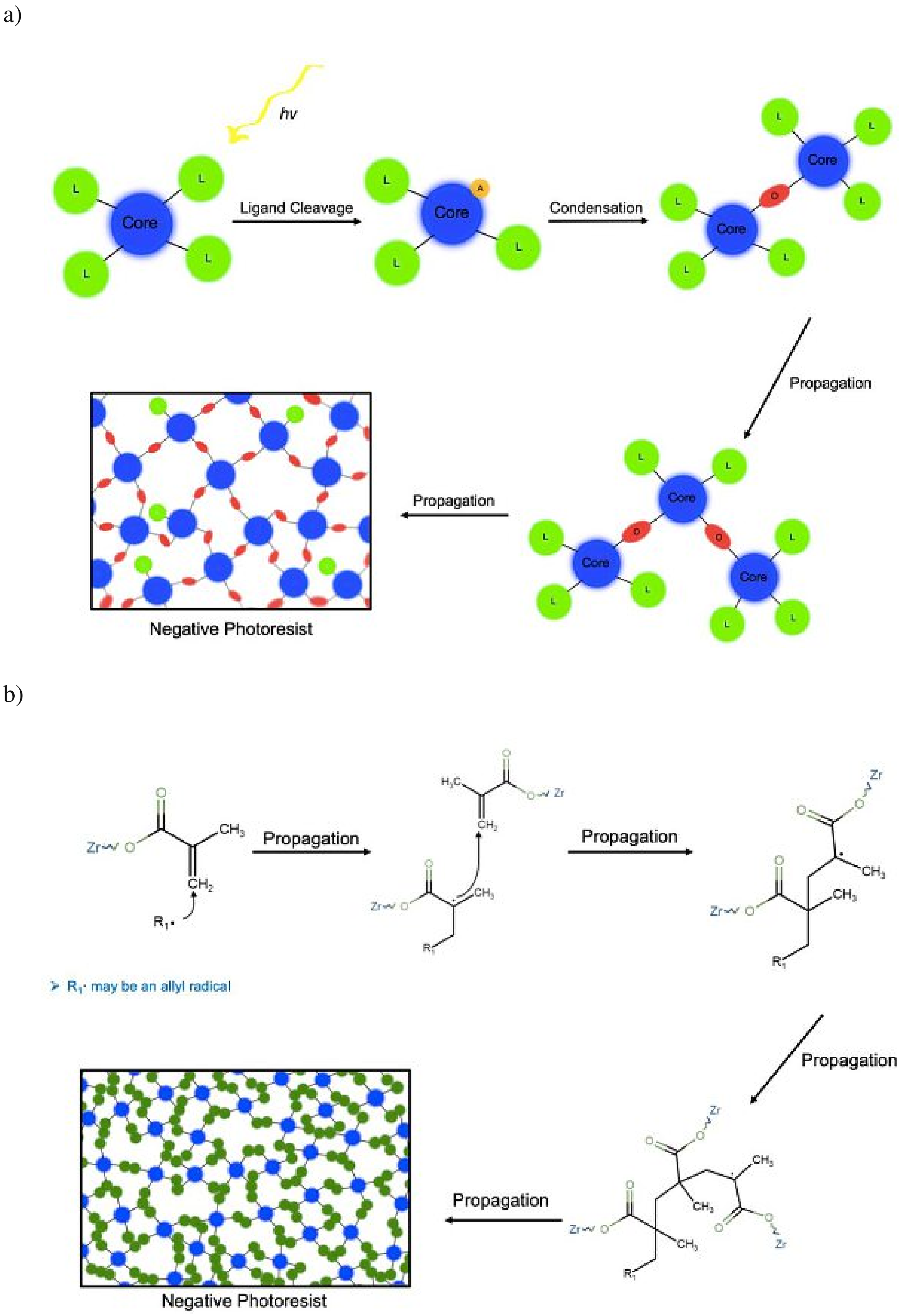

*Figure 2-1: Schematic diagram of two proposed mechanisms for the origin of Zr4O2(OMc)12 solubility switch: a) via ligand cleavage to form crosslinking between two metal oxo clusters* [56]*; b) decarboxylation after EUV exposure generates allyl free radical that induces polymerisation.*

Once $Zr_4O_2(OMc)_{12}$ is obtained, ligand exchange method can be applied afterwards to replace different amount of methacrylate ligands by non-crosslinkable pivalate, generating Zr oxo clusters with mixed ligands. In order to compare the different performance on LER and resolution resulted from the position of C=C bond relative to carboxylic group on the organic ligand, 3-butenoic acid and trans-2,3-dimethacrylic acid are also utilised for synthesising clusters with similar crystal structure from the scratch.

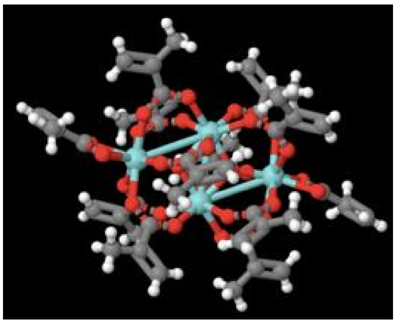

*Figure 2-2: Crystal structure of $Zr_4O_2(OMc)_{12}$.*

The multi-metallic oxo clusters consist of two or three kinds of metals in a single cluster. The amount of metals varies in each cluster (Figure 2-3), which should affect the sensitivity upon EUV exposure since absorption cross sections of Ti, Zr and Hf are different.

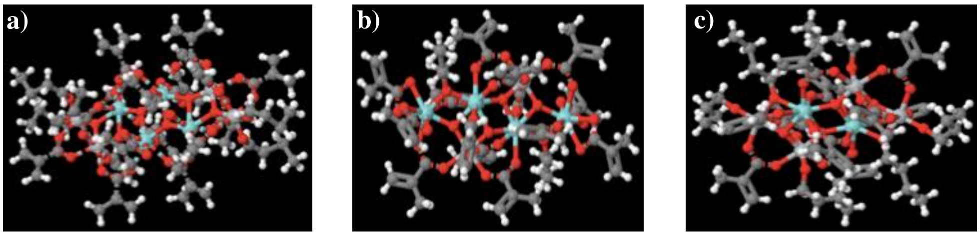

*Figure 2-3: Crystal structure of a) $Ti_4Zr_4O_6(OBu)_4(OMc)_{16}$, b) $Ti_2Zr_4O_4(OBu)_2(OMc)_{14}$, c) $Ti_4Zr_2O_4(OBu)_6(OMc)_{10}$ [57, 58].*

The chosen hafnium oxo cluster also has similar structure to $Zr_4O_2(OMc)_{12}$, with twelve methacrylate ligands attached to the hafnium core. Research carried out by Ober's group suggested Zr oxide resist has comparable sensitivity towards EUV photons with Hf oxide resist, despite the atomic absorption cross section of Hf is way higher than that of Zr [52, 53]. Therefore, it is intriguing to compare the patterning performance of the Zr- and Hf-oxo clusters with identical crystal structures.

In addition to chemical properties and structural characterisations, coatability and developability of the metal oxo clusters will be carried out with various organic solvents and determined via thin-film UV/Vis spectroscopy on quartz plates as well as thin-film IR spectroscopy on silicon wafers afterwards. Patternability will be done by DUV at 225 nm without photomask, followed by E-beam lithography for dose and line/space tests. Eventually, EUV exposure for contrast curve analysis and line/space patterning will be carried out with XIL-II beamline of Swiss Light Source (SLS) synchrotron at Paul Scherrer Institute (PSI) and ASML NXE3400B tool at IMEC.

# 3 State of the Art

As previously mentioned, metal oxide resist has potentials to improve patterning performance and RLS trade-off since no chemical amplification is involved. Instead, it makes use of high atomic absorption nature of metals to boost the sensitivity. Post-transition metals tend to have very high optical sensitivity (or atomic absorption) towards EUV (Figure 3-1). But the precursors are essentially toxic and/or expensive for mass production, leading to a high cost for IC manufacturing [59]. Copper and silver, on the other hand, are essentially not considered as composition for photoresist application since the residual can result in resistance-capacitance delay by interfering array and circuit lines. Influence of metal elements on integrated circuits, silicon wafers as well as other components inside EUV exposure tools is also a concern. Every alternative resist material contains elements other than C, H, O, N, S, F and I is required to be evaluated by ASML, the biggest manufacturer of EUV exposure tool, for the risk of contamination [60]. Instability under air is another issue. Although there are temperature and humidity control in most of the cleanrooms at semiconductor manufacturing plants, metal oxides are prone to hydrolyse or degrade encountered with moisture or oxygen. Several high EUV optical sensitive metals have been deeply researched such as Bi, Cr, Fe, Co and Sn [61-64]. Solution stability and variable water content of the film yet compromise reproducibility and printing performance.

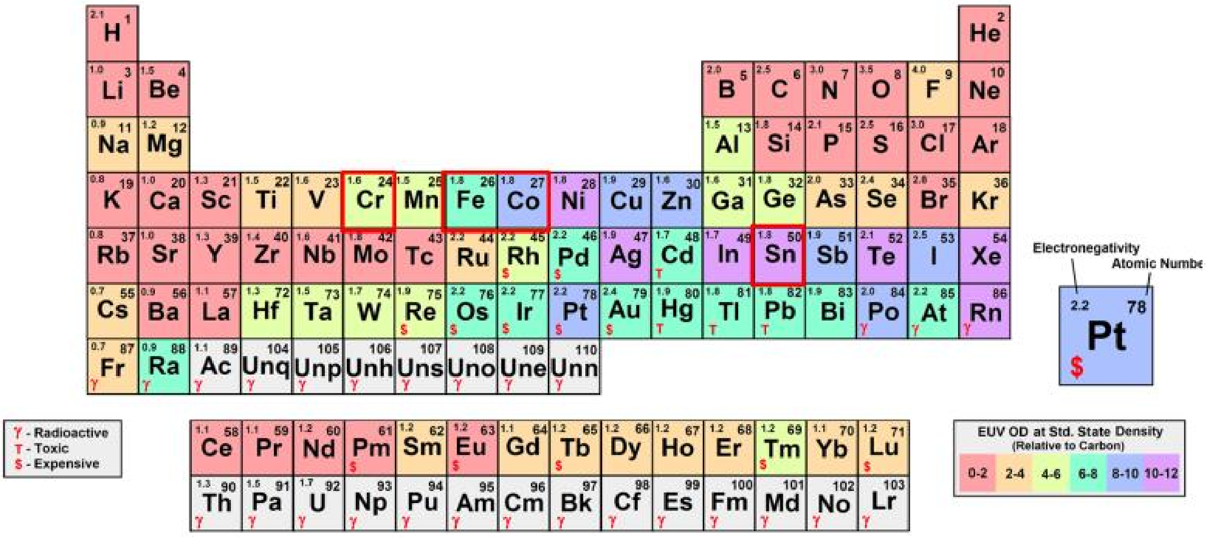

*Figure 3-1: Optical density of elements in the periodic table [59].*

Ti, Zr and Hf in group 4 do not have such high absorption coefficients as those in the post-transition region. The theoretical value of Zr is even close to the organic elements like C and O. Nonetheless, research has revealed that Zr oxo cluster showed a higher sensitivity matching that of Hf oxo cluster with identical structure [50, 55]. The reactants for Ti, Zr and Hf oxo cluster syntheses are far more cheaper and therefore the production cost can be substantially reduced. Zr and Hf oxo clusters also performed a good EUV patterning capability at extremely fast photospeeds [65]. Despite the LER was at acceptable level, Ti, Zr and Hf derivatives are still reckoned as promising candidates as EUVL photoresist application.

Previous researches on Ti, Zr and Hf oxo clusters are mostly focused on the influence of composition of metal core or employing different types of ligands to the printing performance. There are rare papers published by Castellanos' group of Advanced Research Centre for Nanolithography (ARCNL) that reported results of Zr and Ti oxo clusters with mixed organic shell [66], in which they replaced 33% and 40% of methacrylate ligands on $Zr_6O_4(OH)_4(OMc)_{12}$ and $Ti_8O_8(OMc)_{16}$ respectively with non-crosslinkable pivalate ligands (Figure 3-2). They discovered the EUV sensitivity of the clusters with mixed ligands decrease due to the loss of terminal methacrylate that can crosslink. Therefore, higher photon input required to compensate a relatively slower crosslinking kinetics. But no actual line/space patterning was conducted.

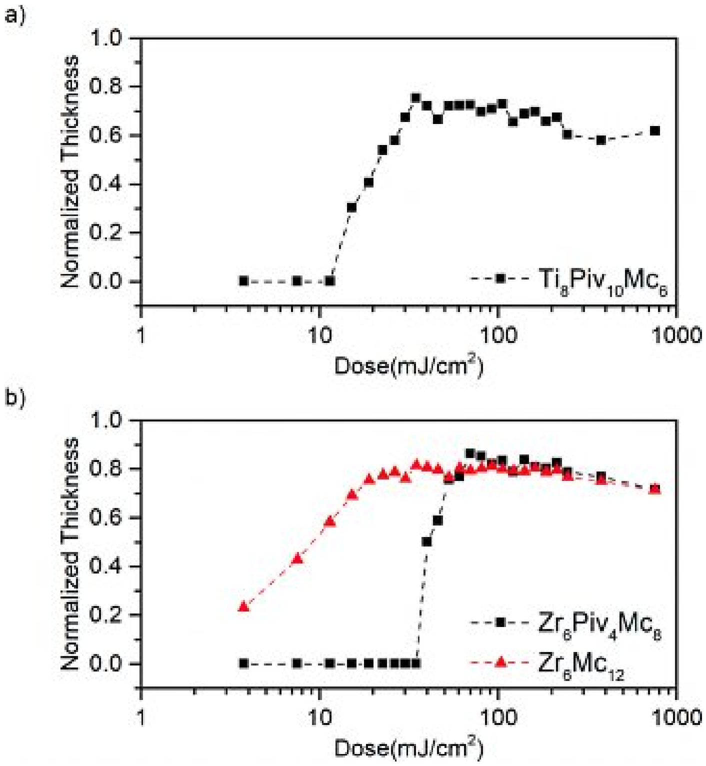

*Figure 3-2: Contrast curve of Ti and Zr ox clusters with hybrid organic shell [66].*

In this work, three clusters with mixed methacrylate and pivalate ligands based on $Zr_4O_2(OMc)_{12}$ will be synthesised via ligand exchange approach (detailed explanation in the following sections), which are $Zr_4O_2(OMc)_3(OPiv)_9$, $Zr_4O_2(OMc)_6(OPiv)_6$, and $Zr_4O_2(OMc)_9(OPiv)_3$ (Figure 3-3). Despite that incorporating non-crosslinkable pivalate ligands will reduce the resist sensitivity upon EUV exposure, bulkier pivalate ligand is potentially prone to cleave from the metal oxo cluster surface, forming an active site, and thus promote the crosslinking via condensation, as shown in Figure 12a. Furthermore, chance of pattern collapse and line roughness of the cluster with more bulky ligands might be also improved since metal oxo clusters can be densely-packed resulted from the lack of pivalate ligands and less ligands attached to the metal core. Contrast curve analysis and line/space patterning via EUVL are expected to be carried out.

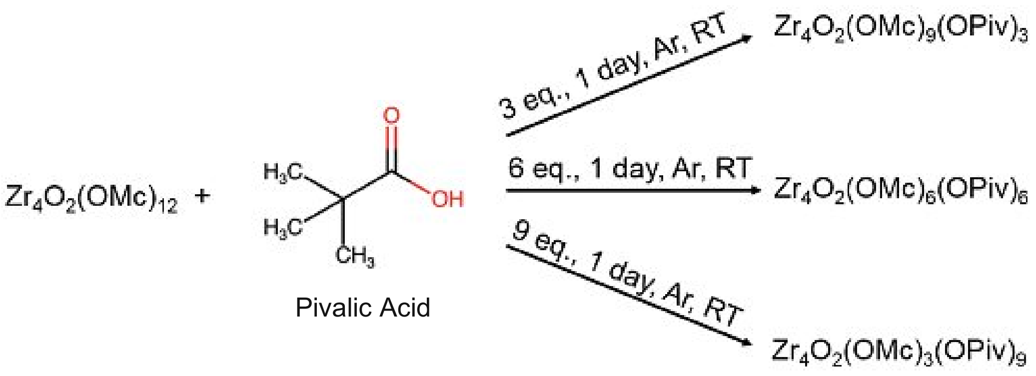

*Figure 3-3: Reaction conditions for synthesis of mixed ligands Zr4 clusters.*

On the other hand, metal composition of the cluster is another crucial aspect this work aims to investigate. In most of the photoresist researches reported, it is hardly to find one kind of material that consists of at least two different metals in a single molecule. Scientists tend to use one type of metal in an oxo cluster that has either good absorption coefficient or good coatability and developability. Some metal oxo clusters like Ti oxo clusters are notorious for low solubility in common organic solvents, leading to an insufficient thickness of coated film that cannot be used for commercial purposes. And instability of coated film after deposition also causes serious issue for processing owing to hydrolysis of air moisture or competing of chelating agent (Figure 3-4) [54]. Nevertheless, the high optical sensitivity of Ti cannot be ignored. In this work, Ti is incorporated into Zr to form a mixed metal core in order to make use of respective advantages. The EUV patterning capability of Zr oxo clusters has been proven in many studies and in the meantime, it also exhibits good coatability and developability. The combination of Ti and Zr can theoretically not only eliminate the relative instability of pure Ti oxo clusters, but also increase the sensitivity towards EUV exposure. Three different Ti-Zr oxo clusters will be synthesised, which are $Ti_4Zr_4O_6(OBu)_4(OMc)_{16}$, $Ti_2Zr_4O_4(OBu)_2(OMc)_{14}$ and $Ti_4Zr_2O_4(OBu)_6(OMc)_{10}$. The numbers of Ti and Zr are altered for comparison of patterning performance. Besides sensitivity, resolution and line edge roughness will be affected by the size of the molecule. This phenomenon gradually becomes more and more significant with the decrease of feature size.

Figure 3-4: An actual photo showed the bad coatability of $Ti_7O_4(OEt)_{20}$ spin-coated on a silicon wafer.

Incorporation of Hf into mixed metal core is beneficial for patterning performance. Hf has the highest absorption coefficient at 92 eV among these three elements. Its good printability was studied and reported previously. But never did a mixed-core Hf oxo cluster was researched in terms of photoresist applications. Having an identical single crystal structure as that of $Ti_4Zr_4O_6(OBu)_4(OMc)_{16}$, $Ti_4Hf_4O_6(OBu)_4(OMc)_{16}$ is planned to be synthesised by substituting a Hf-based precursor for the Zr-based one. It is expected to have higher sensitivity in comparison with $Ti_4Zr_4O_6(OBu)_4(OMc)_{16}$, whereas the line edge roughness might deteriorate due to larger size of hafnium. At last, three metals are merged into a single cluster with crosslinkable methacrylate ligand. $Ti_2Zr_5HfO_6(OMc)_{20}$ should in theory have the highest linear absorption coefficient among all the multi-metallic oxo clusters attributing to both the high optical sensitive metal moiety as well as the number of methacrylate ligands (Figure 3-5). However, the resolution and line edge roughness will turn out to be its biggest challenges.

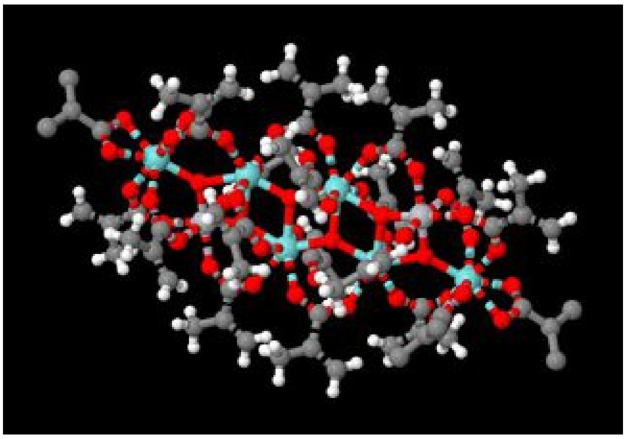

Figure 3-5: Crystal structure of $Ti_2Zr_5HfO_6(OMc)_{20}$ [67].

Last aspect required to be addressed is how the coordination number of metal moiety affects the patterning performance. For this reason, $Zr_4O_2(OMc)_{12}$ and $Zr_{12}O_8(OH)_8(OMc)_8(OAc)_{16}{\cdot}6HOAc$ are used to compared with the EUV patterning performance of $Zr_6O_4(OH)_4(OMc)_{12}$, which has been studied intensively by Castellanos et al. Even though the number of metals in a single oxo cluster does make an impact on the sensitivity upon EUV photon, the molecule structure should also influence the lithographic metrics. As far as it is known, the origin of solubility switch is likely via cleavage of organic ligand to create active sites for condensation crosslinking and crosslinking of methacrylate ligands. Consequently, the steric hindrance as well as bond angles become significantly important since they are related to the extent of promoting dissociation for organic ligands and methacrylate interactions.

Understanding the mechanisms of solubility switch remains problematic for EUV photoresist community. The complicated interactions between EUV photons and resist materials is required exquisite simulations as well as both direct and indirect characterisations to evaluate the actual reaction pathway. In this work, two measures will be utilised for studying the specific mechanism of these metal oxo clusters upon EUV exposure. Dissociative electron attachment (DEA) is a process where an incoming low-energy electron attaches to a molecule in gas phase and leads to a fragmentation, which is basically described as [68]:

$$AB + e^- \rightarrow AB^{(\#)-} \rightarrow A^{(\#)-} + B^{(\#)}$$

Substance of interest is usually introduced into the chamber by sublimation under high vacuum, followed by bombarding of electrons at low energy generated by a trochoidal electron monochromator. The influence of incident electron energy on fragmentation is then studied by means of mass spectroscopy. DEA spectroscopy is considered as a convincing approach to simulate resist material interactions with secondary electrons below 20 eV. The main precursors of clusters in this work will be analysed together with $Zr_4O_2(OMc)_{12}$ in order to elucidate more details regarding the origin of solubility switch.

The other approach is outgassing analysis. It is commonly used among EUV photoresist researches yet the accessibility to the device is rather limited. Outgassing is essentially carried out by exposing resist material that is spin-coated on a silicon wafer prior to the analysis to actual EUV source. The outgases are collected by residual gas analyser (RGA) and analysed by means of mass spectroscopy (Figure 3-6). This technique is originally utilised to prevent internal optics from being contaminated by certain outgassed species. Photoresist researchers have also discovered the application of outgassing tool on providing evidence that can be linked to the detailed mechanism within resist material encountering EUV photons. For instance, in the case of Zr oxo cluster resist ($Zr_6O_4(OH)_4(OMc)_{12}$), the crosslinking caused by cleavage of organic ligands results in a large quantity of free methacrylic acid. Its outgassing result has revealed an intense signal at 86 amu, which is in line with the proposed condensation crosslinking pathway (Figure 3-7). Similar outcome was also reported by Ober's group on another Zr oxo cluster [69].

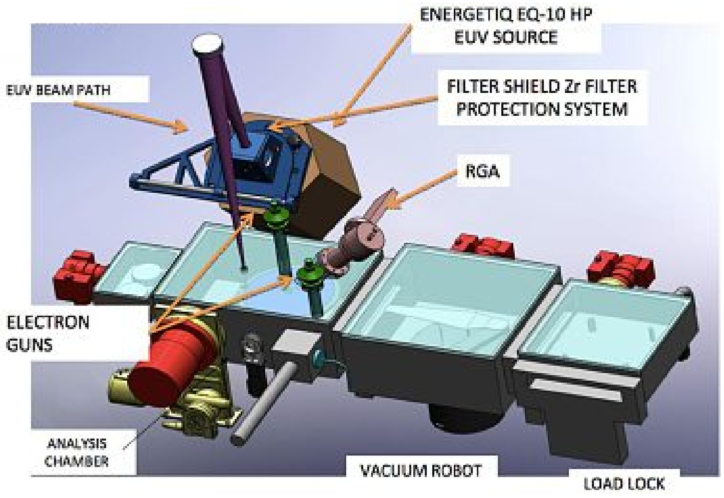

*Figure 3-6: Schematic illustration of EUV outgassing tool [70].*

Both DEA and outgassing will be conducted on precursors as well as metal ox clusters, while transmission thin-film FTIR and GATR-FTIR can provide the structural information before and after metal oxo clusters being exposed via EUV photons. The results combined should be more completed to clarify the actual scenario taking place after exposure of EUV. DEA experiments are expected to be carried out with Prof. Janina Kopyra of Siedlce University of Natural Sciences and Humanities in Poland, while outgassing tests and GATR-FTIR will be performed by a unique RGA setup provided by EUV Technology at IMEC, Belgium.

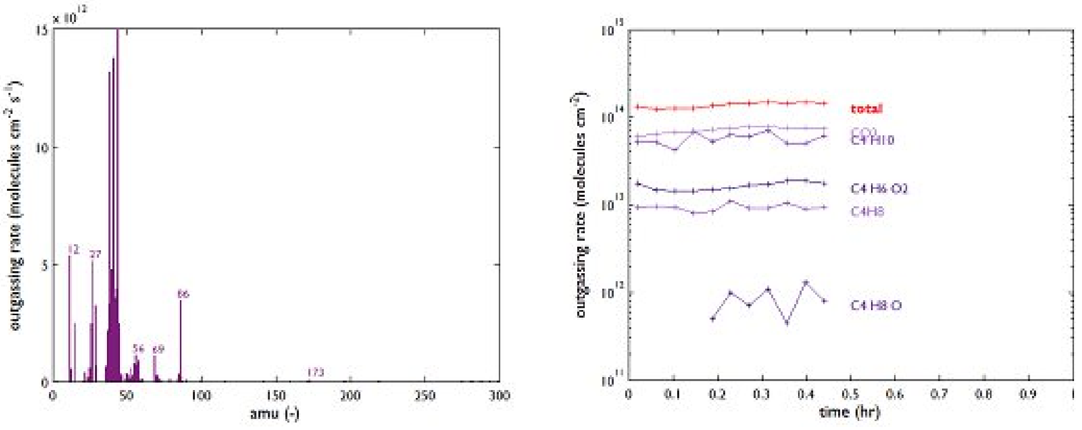

*Figure 3-7: Outgassing result of $Zr_6O_4(OH)_4(OMc)_{12}$ cluster.*

# 4 Zirconium Oxo Clusters

Photoresists combining metallic composition and organic entity have been widely studied with respect to EUV absorptivity and sensitivity that is essentially influenced by material photochemical reactivity. Investigations by Ober and Giannelis at Cornell University revealed similar sensitivity of Zr and Hf nanoparticle towards EUV exposure despite of Hf having a higher linear absorption coefficient. Castellanos's group at ARCNL has also been focusing on group 4 metal oxo clusters by comparing EUV patterning performance of three resembling Ti, Zr and Hf oxo clusters. Additionally, X-ray photoelectron spectroscopy (XPS) and Grazing incidence small angle x-ray scattering (GIXS) was conducted for understanding of solubility switch mechanism. Nevertheless, there are still many aspects that require further optimisations and explorations.

Zirconium oxo clusters of this research are essentially based on $Zr_4O_2(OMc)_{12}$. It was synthesised as a foundation for the mixed-ligand clusters, while the rest of Zr oxo clusters are built on similar structures but with different organic moieties. In addition to methacrylate, the mixed-ligand clusters also contain non-crosslinkable pivalate ligand in order to have a comparison with clusters possessing a single type of ligand. Three, six and nine methacrylates of $Zr_4O_2(OMc)_{12}$ were replaced by pivalates respectively to form three different Zr oxo clusters, as listed in Table 1. It is believed that the amount of crosslinkable ligand would make an impact on printing performance in terms of sensitivity and line edge roughness. Furthermore, the reactants needed for synthesising these compounds are relatively cheap and commercially available.

*Table 1: List of Zr oxo clusters for comparing the influence of non-crosslinkable pivalate ligand on patterning performance.*

| Cluster | Precursor | Carboxylic Acid | Remark | Reference |
|---|---|---|---|---|
| **$Zr_4O_2(OMc)_{12}$ (1)** | $Zr(OPr)_4$ | Methacrylic Acid (HOMc) | Molar Ratio: 1:4, propanol[a] | 71 |
| **$Zr_4O_2(OMc)_3(OPiv)_9$ (2)** | - | Methacrylic Acid (HOMc)<br>Pivalic Acid (HOPiv) | [b] | 72 |

| | | | | |
|---|---|---|---|---|
| **$Zr_4O_2(OMc)_6(OPiv)_6$ (3)** | - | Methacrylic Acid (HOMc)<br>Pivalic Acid (HOPiv) | [b] | 72 |
| **$Zr_4O_2(OMc)_9(OPiv)_3$ (4)** | - | Methacrylic Acid (HOMc)<br>Pivalic Acid (HOPiv) | [b] | 72 |
| **$Zr_4O_2(OPiv)_{12}$ (5)** | $Zr(OPr)_4$ | Pivalic Acid (HOPiv) | Molar Ratio: 1:4, propanol[a][b] | 71, 72 |

[a] prepared by carboxylic acid route, [b] prepared by ligand exchange route

Another group for comparison includes Zr oxo clusters using vinylacetic acid and trans-2,3-dimethacrylic acid as organic moieties (Table 2). Their crystal structures are similar with $Zr_4O_2(OMc)_{12}$. However, the steric difference of vinyl group of the ligands will affect final patterning capability especially on line edge roughness [52].

*Table 2: List of Zr oxo clusters for comparing the influence of sterically different organic ligands on patterning performance.*

| Cluster | Precursor | Carboxylic Acid | Remark | Reference |
|---|---|---|---|---|
| **$Zr_4O_2(OMc)_{12}$ (1)** | $Zr(OPr)_4$ | Methacrylic Acid (HOMc) | Molar Ratio: 1:4, propanol[a] | 71 |
| **$Zr_4O_2(OVinac)_{12}$ (6)** | $Zr(OPr)_4$ | Vinylacetic acid (HOVinac) | Molar Ratio: 1:4, propanol[a] | - |
| **$Zr_4O_2(ODiMc)_{12}$ (7)** | $Zr(OPr)_4$ | trans-2,3-dimethylacrylic acid (HODiMc) | Molar Ratio: 1:4, propanol[a] | - |

[a] prepared by carboxylic acid route

Last Zr oxo cluster selected for comparison is $Zr_{12}O_8(OH)_8(OMc)_8(OAc)_{16}\cdot 6HOAc$. In order to understand the effect caused by the coordination number of metals, the printing performance of $Zr_{12}O_8(OH)_8(OMc)_8(OAc)_{16}\cdot 6HOAc$ will be examined along with that of $Zr_4O_2(OMc)_{12}$ as a benchmark (Table 3). The synthesis for $Zr_{12}O_8(OH)_8(OMc)_8(OAc)_{16}\cdot 6HOAc$ is also via carboxylic acid route yet the precursor becomes zirconium n-butoxide ($Zr(OBu)_4$) instead of $Zr(OPr)_4$.

*Table 3: List of Zr oxo clusters for comparing the influence of metal coordination number on patterning performance.*

| **Cluster** | **Precursor** | **Carboxylic Acid** | **Remark** | **Reference** |
|---|---|---|---|---|
| **$Zr_4O_2(OMc)_{12}$ (1)** | $Zr(OPr)_4$ | Methacrylic Acid (HOMc) | Molar Ratio: 1:4, propanol[a] | 71 |
| **$Zr_{12}O_8(OH)_8(OMc)_8(OAc)_{16}\cdot 6HOAc$ (8)** | $Zr(OBu)_4$ | Methacrylic Acid (HOMc)<br>Acetic Acid (HOAc) | Molar Ratio: 1:1.5:3.5, butanol[a] | 73 |

[a] prepared by carboxylic acid route

## 4.1 Synthesis

For the synthesis of Zr oxo clusters, two possible pathways can be achieved. Although the detailed mechanism of organically modified metal oxide clusters remains unknown, the carboxylate-substituted metal oxo clusters are able to be explained by the following reaction sequences [74]:

$$\mathrm{M(OR)_x + nR'COOH \rightarrow M(OR)_{x-n}(OOCR')_n + nROH}$$

$$\mathrm{ROH + R'COOH \rightarrow R'COOR + H_2O}$$

$$\mathrm{(MOR)_{x-n}(OOCR')_n + H_2O \rightarrow M_aO_b(OR)_c(OOCR')_d + ROH}$$

The alcohol liberated from the substitution of carboxylate group(s) for alkoxide ligand(s) in the first reaction can undergo esterification, generating water that therefore hydrolyses the entire or part of the remaining alkoxide groups, which become the source of oxo or hydroxo groups in the final clusters.

Clusters containing both methacrylate and pivalate ligands can be synthesised via ligand exchange approach. Different mole equivalents of pivalic acid were added into an oxozirconium methacrylate ($Zr_4O_2(OMc)_{12}$) solution to replace some of the methacrylate ligands on the clusters. The mechanism for carboxylate ligand exchange is still unclear. Schubert and his team have proposed a possible mechanism derived from the structures of the two derivatives

$Zr_6O_4(OH)_4(OOCR)_{12}(HOX)$ (X=H, Bu) [75]. In general, after the addition of carboxylic acid, the metal oxo cluster will first experience the change of the coordination of the original carboxylato ligand ($OOCR_1$) from $\eta_2$ to $\eta_1$ (i). Then the H-$OOCR_2$ will preferably fill into the vacated coordination site (ii), followed by proton transfer between entering ($OOCR_2$) and leaving ($OOCR_1$) (iii). The H-$OOCR_1$ will eventually be eliminated (iv) and the coordination of $OOCR_2$ will switch again from $\eta_1$ to $\eta_2$ (v), as shown in Figure 4-1.

Both pathways involve moisture-sensitive substances and the products are prone to hydrolyse under air. Therefore, all reactions were required to be conducted using conventional Schlenk techniques to exclude the influence of water and oxygen. Prior to reactions, methacrylic acid and pivalic acid were distilled over phosphorus pentoxide ($P_2O_5$). Vinylacetic acid, trans-2,3-dimethacrylic as well as metallic precursors, $Zr(OPr)_4$ and $Zr(OBu)_4$, were opened and stored in the glovebox. Weighing process for reactants were carried out inside the glovebox and transferred into properly sealed glass containers. Dichloromethane (DCM) and n-hexane needed for product purification were dried over molecular sieves and Na/benzophenone respectively before being distilled. Their water contents were then measured via Karl Fischer titration and should be under 15 ppm.

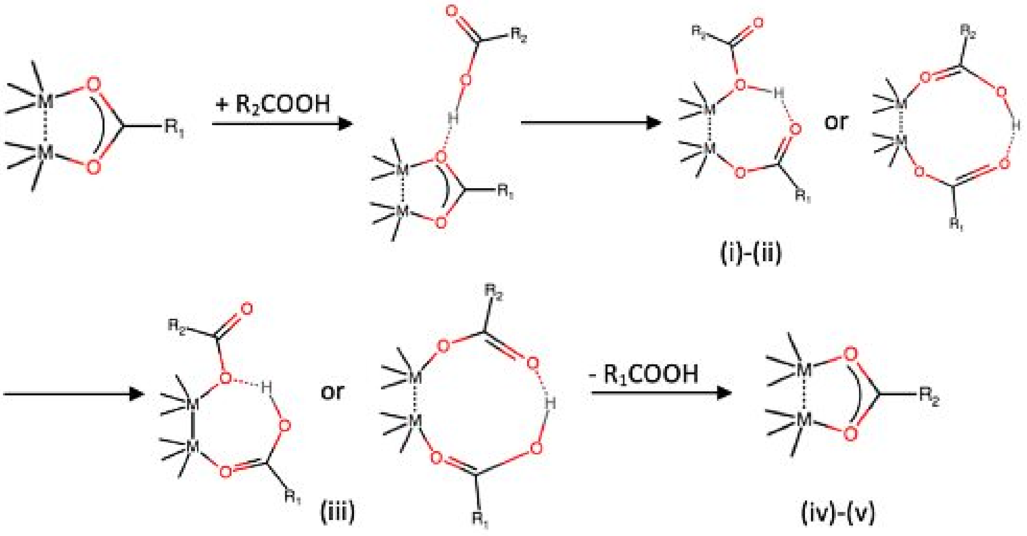

*Figure 4-1: Possible mechanism for carboxylate ligand exchange [76].*

### 4.1.1 Carboxylic Acid Route

#### 4.1.1.1 Synthesis of $Zr_4O_2(OMc)_{12}$ (1)

The synthesis of $Zr_4O_2(OMc)_{12}$ cluster was first reported by Kickelbick et al. [71] in 1996 and optimised by Trimmel later in 2001 (Figure 4-2) [77]. It was generated by reacting 70% zirconium n-propoxide solution in n-propanol with dry methacrylic acid to secure complete exclusion of oxygen and moisture.

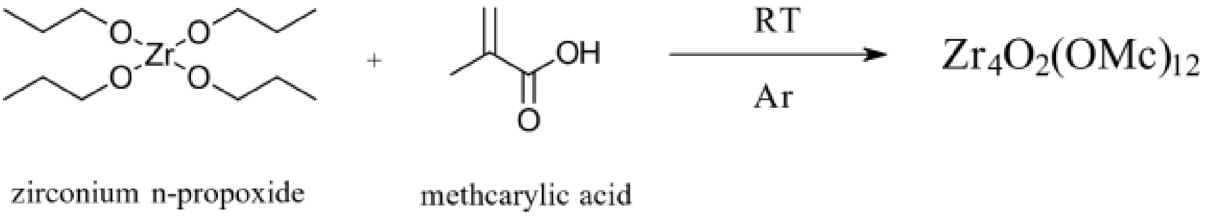

*Figure 4-2: Synthesis of $Zr_4O_2(OMc)_{12}$ oxo cluster via carboxylic acid route.*

For synthesising $Zr_4O_2(OMc)_{12}$ (1), a clean Schlenk flask was attached to the Schlenk tube and underwent a venting-pumping cycle with argon for three times to fully evacuate air. 1.00 eq. of zirconium n-propoxide and 4.07 eq. of methacrylic acid were weighed into separate glass vials that were sealed properly afterwards inside the glovebox. Methacrylic acid was transferred into the Schlenk flask under argon flow before addition of the zirconium reactant. Zirconium n-propoxide solution should be added dropwise into methacrylic acid under stirring and argon flow. The reaction was exothermic so an increase in temperature could be detected. After one hour of mixing, the stirring was interrupted and the clear mixture was kept still at room temperature under argon. The colourless and prismatic crystals could be generated after 2 days. For purification, the product was separated from its mother liquor before being rinsed with 10 mL of dry n-hexane. This rinsing was repeated for three times to ensure an exclusion of remaining reactants. The solids were eventually dried under high vacuum ($10^{-6}$ bar) for six hours for removing the solvents.

The initial three syntheses did not work out successfully. According to the purification procedure stated in the literature, the crystalline product was supposed to be recrystallized in dry n-hexane for three times to remove the reactants. During the first three syntheses, $Zr_4O_2(OMc)_{12}$ was dissolved in 2-3 mL of a pre-dried dichloromethane and added dropwise into 30 mL of n-hexane. The solution would gradually turn cloudy before the compound crystallizing. Dichloromethane and n-hexane mixture was then withdrawn via syringes. The whole purification process was repeated three times and eventually the crystals were dried under high vacuum. Nevertheless, the NMR of the product obtained indicated a trace of methacrylic acid existing. The intensity of methacrylic acid did decrease with increase in the number of recrystallization step. Yet it was still time-consuming and expensive to reach an acceptable level of purity concerning the amount of solvent used.

Multiple approaches have been conducted in order to solve the purity issue, one of which was via distillation using dry dichloromethane as solvent. The distillation was carried out under argon at 50 °C to prevent methacrylic acid from polymerise. To determine the source of the impurity and effect of distillation, a series of high-performance liquid chromatography (HPLC) analysis for $Zr_4O_2(OMc)_{12}$ with different distillation times as well as methacrylic acid were performed using 100% acetonitrile as solvent. The results in Figure 4-3 still showed significant peaks of methacrylic acid in all samples regardless the distillation time.

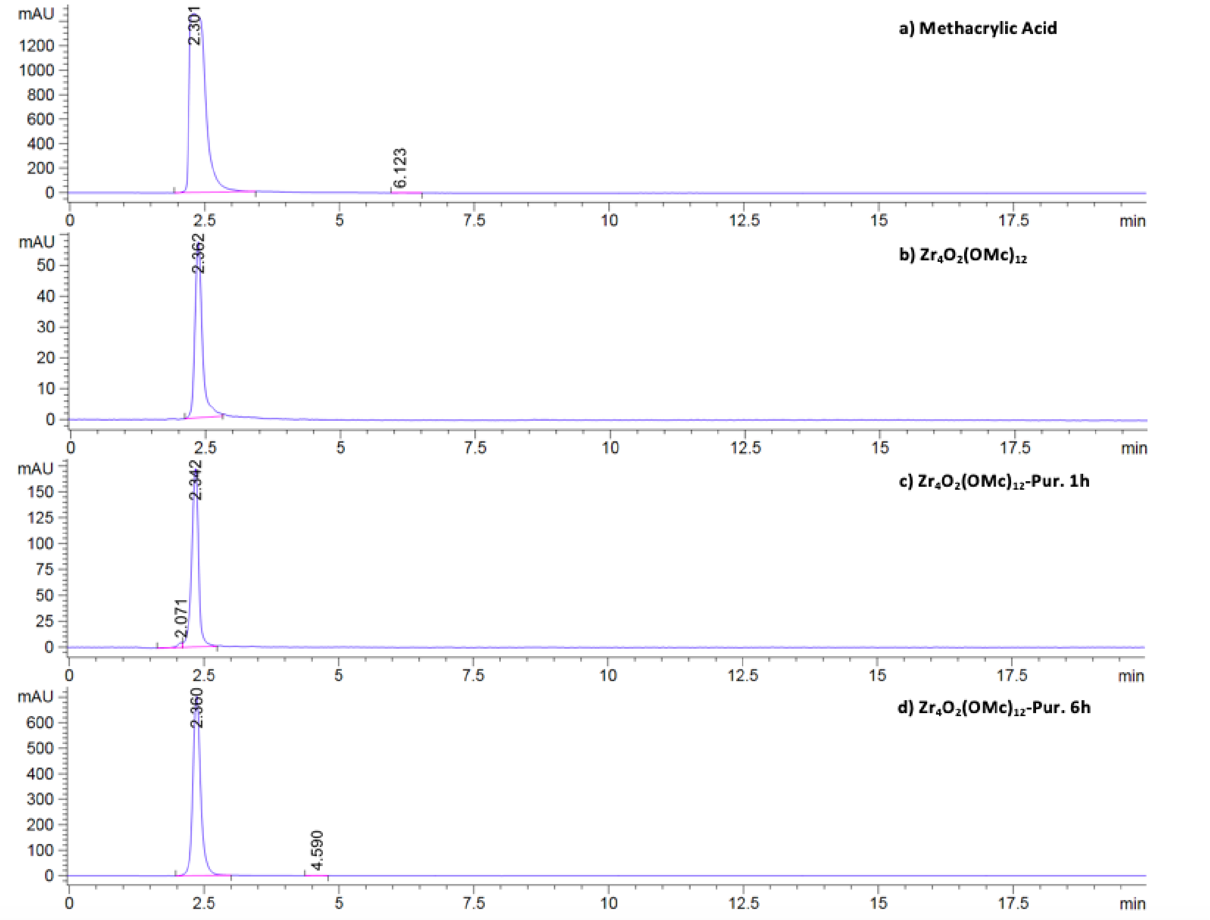

*Figure 4-3: HPLC results of methacrylic acid and $Zr_4O_2(OMc)_{12}$ clusters distilled for 0 hour, 1 hour and 6 hours, respectively.*

Another measure that has been tried was via Dean-Stark technique. Dean-Stark technique is a conventional synthetic chemistry method for collecting mainly water or occasionally other liquids. By constantly refluxing the solvent through a fractional condenser, the substance, which needs to be removed from the reactor, can be collected from the burette of Dean-Stark apparatus. 100 mL of toluene was used to dissolve 2 g of $Zr_4O_2(OMc)_{12}$ clusters for Dean-Stark process and the solution was refluxing at 110 °C. The distilled liquid was collected from the burette and analysed by $^1H$ NMR to monitor the amount of methacrylic acid residual. The cluster was eventually dried over high vacuum after 24 hours of Dean-Stark process. Dean-Stark technique proved to be feasible to remove remaining methacrylic acid from the cluster, as the TGA and $^1$H NMR indicated a purity up to 96%. However, the time and large quantity of expensive solvent required for this process revealed inadequateness of this process.

The last approach tried for $Zr_4O_2(OMc)_{12}$ purification was direct rinsing with dry n-hexane. Initially, the crystalline product was also separated from its mother liquor after the synthesis. 10 mL of dry n-hexane was introduced into the Schlenk flask to remove the remaining reactants. The solution was kept stirring for 5 minutes before n-hexane being withdrawn via syringes. The process was repeated 3 to 5 times depending on the amount of reactant residue. $Zr_4O_2(OMc)_{12}$ was eventually dried under high vacuum for 6 hours. $^1$H NMR showed a significant improvement on the purity with no trace of methacrylic acid signals were observed (Figure 4-4).

Moreover, scaling-up synthesis of $Zr_4O_2(OMc)_{12}$ is no longer an issue with this newly-developed process. The $^1$H NMR spectrum of a three-time scaling-up synthesis of $Zr_4O_2(OMc)_{12}$ revealed the feasibility of this purifying process, indicating this efficient and cheap process can not only be used for small scale but also potentially be applied in large-scale manufacturing. Therefore, the purifications of the other clusters have also adopted this approach with appropriate solvents.

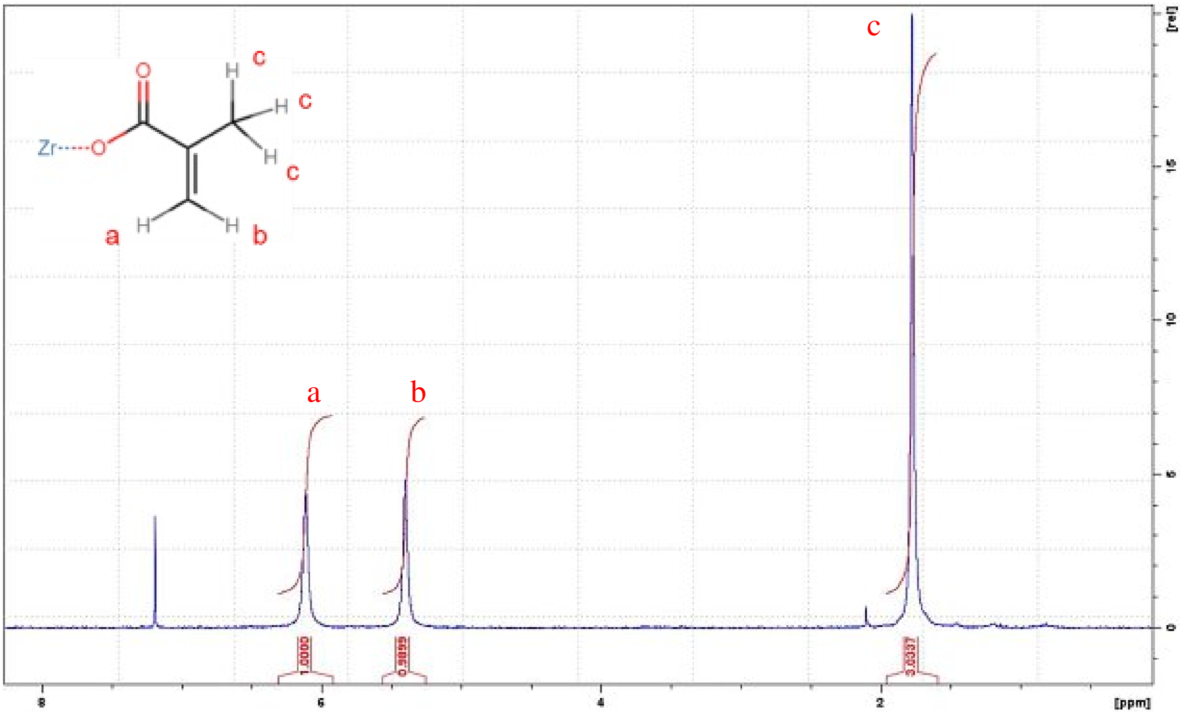

*Figure 4-4: $^1$H NMR spectrum of $Zr_4O_2(OMc)_{12}$ purified by direct rinsing of dry n-hexane.*

#### 4.1.1.2 Synthesis of $Zr_4O_2(OPiv)_{12}$ (5)

The synthesis of $Zr_4O_2(OPiv)_{12}$ was achieved by both ligand exchange route and carboxylic acid route (Figure 4-5). Ligand exchange for generating $Zr_4O_2(OPiv)_{12}$ was based on $Zr_4O_2(OMc)_{12}$ by reacting 12 eq. of dry pivalic acid with 1 eq. of $Zr_4O_2(OMc)_{12}$ [72]. $Zr_4O_2(OMc)_{12}$ was dissolved in dry dichloromethane in a Schlenk flask, followed by dropwise addition of pivalic acid to the solution under intensive stirring. After 1 hour, the solvent was removed directly by vacuum pump and cooling trap of Schlenk line. The solid product separated from the solvent was rinsed with 10 mL of dry n-hexane for three times before being dried under high vacuum.

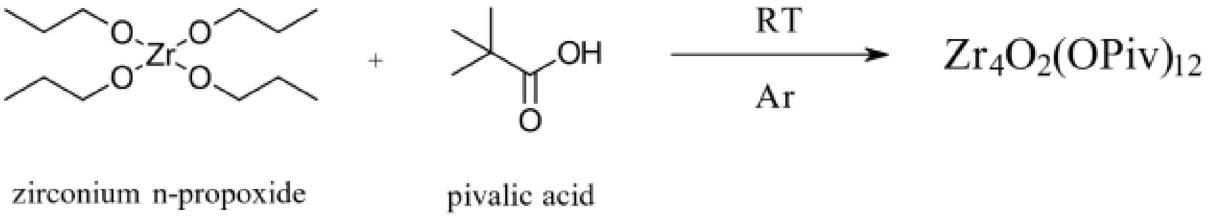

*Figure 4-5: Synthesis of $Zr_4O_2(OPiv)_{12}$ oxo cluster via carboxylic acid route.*

On the other hand, carboxylic acid route was conducted by a direct reaction of zirconium n-propoxide and pivalic acid. After being weighed inside the glovebox, 4.07 eq. of dry pivalic acid was transferred into a Schlenk flask via a syringe. 1.00 eq. of zirconium n-propoxide was then added dropwise into the Schlenk flask under stirring. The solution was kept mixing for one hour before being left still at room temperature for two days. For purification, 10 mL of n-hexane was utilised to dissolve the reactant residue for three times and the product was dried under high vacuum in the end.

The purity of $Zr_4O_2(OPiv)_{12}$ generated from two approaches both reached nearly 100%, leaving no trace of reactant in the products. Nonetheless, the yield for carboxylic acid route (94%) was relatively high compared with that for ligand exchange route (76%). It might be resulted from an incomplete ligand exchange reaction or product loss during the purification process. Despite of being slightly more time-consuming, carboxylic acid route was still used as the main measure for the following syntheses considering a potential application for mass production.

#### 4.1.1.3 Synthesis of $Zr_4O_2(OVinac)_{12}$ (6)

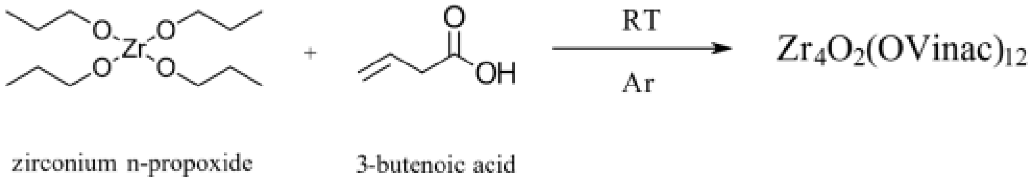

*Figure 4-6: Synthesis of $Zr_4O_2(OVinac)_{12}$ oxo cluster via carboxylic acid route.*

$Zr_4O_2(OVinac)_{12}$ has only been carried out via carboxylic acid route (Figure 4-6) since the reactant 3-butenoic acid has similar structure as that of methacrylic acid and as a result the reactivity should be quite close. 1.00 eq. of zirconium n-propoxide and 4.06 eq. of 3-butenoic acid were measured and packed in properly-sealed glass containers inside the glovebox. After 3-butenoic acid being transferred into a Schlenk flask, zirconium n-propoxide was added dropwise to the acid under stirring with argon flow. The mixing was interrupted after an hour and the solution was left still at room temperature for two days. For purification, 10 mL of n-hexane was used to rinsed the prismatic crystal for three times before undergoing drying at high vacuum for 6 hours. The products have to be stored inside the glovebox to prevent further degradation.

Despite the structural similarity of 3-butenoic and methacrylic acid, the amounts of products obtained are substantially different, giving just 8.7% yield for $Zr_4O_2(OVinac)_{12}$ compared with 84% for $Zr_4O_2(OMc)_{12}$. This phenomenon might be caused by the position of C=C bond on the reactant. C=C of methacrylic acid is relatively closer to carboxylic group, making the carboxylic hydrogen more prone to disintegrate and thus easier to form attachment to zirconium core. As for 3-butenoic acid, longer distance between C=C bond and carboxylic group slightly reduce the tendency of carboxylic hydrogen to be separated, which leads to a lower reactivity of forming the oxo cluster.

#### 4.1.1.4 Synthesis of $Zr_4O_2(ODiMc)_{12}$ (7)

$Zr_4O_2(ODiMc)_{12}$ was synthesised via both carboxylic acid and ligand exchange route (Figure 4-7). Ligand exchange approach was conducted by adding 12.00 eq. of dry trans-2,3-dimethacrylic acid into 1.00 eq. of $Zr_4O_2(OMc)_{12}$ that was previously dissolved in dry dichloromethane under stirring. The mixing was stopped after an hour and the solvent was evaporated directly by a Schlenk line and a cooling trap. However, the product turned into a sticky mixture after the evaporation of solvent, making the reactant unable to be separated from the product. Although recrystallization was performed subsequently, the $^1$H NMR spectrum still indicated a large quantity of trans-2,3-dimethacrylic acid existing within the product.

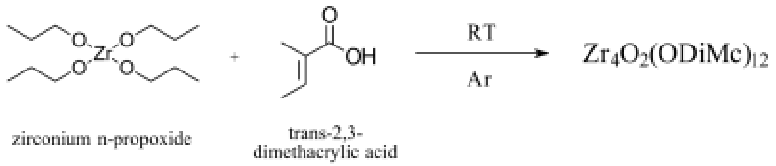

*Figure 4-7: Synthesis of $Zr_4O_2(ODiMc)_{12}$ oxo cluster via carboxylic acid route.*

After two failures through ligand exchange route, carboxylic acid measure was tried using the same molar ratio and parameters as those of $Zr_4O_2(OMc)_{12}$ synthesis. 1.00 eq. of zirconium n-propoxide was added to 4.06 eq. of trans-2,3-dimethacrylic acid under intensive stirring. The solution was left still after 1 hour of stirring and the Schlenk flask was kept at room temperature under argon atmosphere. The colourless crystal formed in 2 days. To purify the product, the solids were separated from its mother liquor before being rinsed with 10 mL of dry n-hexane for three times. The crystals were eventually dried under high for 6 hours and then stored inside glovebox.

Despite the $^1$H NMR still revealed a trace of trans-2,3-dimethacrylic acid within the product, its quantity has been significantly reduced compared to the ligand exchange product. The yield, on the other hand, was not as high as being expected. A possible explanation for it would be the steric hindrance of reactant. Two methyl groups on both side of C=C bond may not only create a rather high steric barrier but reduce the effect on carboxylic hydrogen disintegration, both of which lead to the decrease of reactivity. A longer crystallization time has been provided from 2 days up to one week, yet no obvious increase in the amount of product was observed.

#### 4.1.1.5 Synthesis of $Zr_{12}O_8(OH)_8(OMc)_8(OAc)_{16}\cdot 6HOAc$ (8)

The structure of $Zr_{12}O_8(OH)_8(OMc)_8(OAc)_{16}\cdot 6HOAc$ is comparatively different to the previous zirconium oxo clusters. It essentially consists of two $Zr_6O_4(OH)_4$ cores with four inter-bridging acetate ligands. Six methacrylate ligands are in chelating mode while the other four positions on the “cluster belt” were half occupied by methacrylates and the inversion related atoms as well as acetates [73].

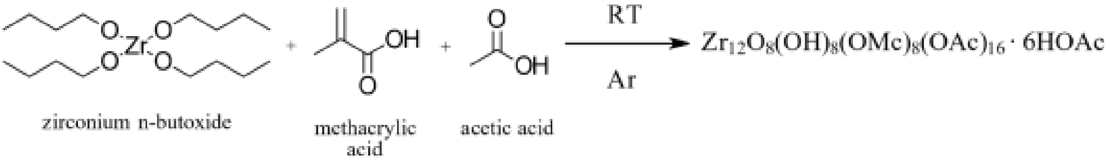

*Figure 4-8: Synthesis of $Zr_{12}O_8(OH)_8(OMc)_8(OAc)_{16}\cdot 6HOAc$ oxo cluster via carboxylic acid route.*

$Zr_{12}O_8(OH)_8(OMc)_8(OAc)_{16}\cdot 6HOAc$ was synthesised by carboxylic acid route (Figure 4-8). Instead of zirconium n-propoxide, zirconium n-butoxide was weighed in a Schlenk flask and sealed before the flask being transferred to the Schlenk line, while methacrylic acid and acetic acid were also weighed into two individual, properly-sealed glass vials inside the glovebox. The acids were added dropwise and sequentially to zirconium n-butoxide under stirring with argon flow. The mixing was stopped after an hour and the solution was allowed to stand at room temperature. Colourless needles formed after 12 hours. For purification, the solids were separated from its mother liquor before being rinsed with 10 mL of dry n-hexane for three times. The crystals were dried under high vacuum for 6 hours eventually.

### 4.1.2 Ligand Exchange Route

#### 4.1.2.1 Synthesis of $Zr_4O_2(OMc)_x(OPiv)_{12-x}$ (x=3, 6, 9)

The syntheses of $Zr_4O_2(OMc)_3(OPiv)_9$ (2), $Zr_4O_2(OMc)_6(OPiv)_6$ (3) and $Zr_4O_2(OMc)_9(OPiv)_3$ (4) can only be achieved via ligand-exchange route since only a partial of original ligands needed to be replaced (Figure 4-9). Non-crosslinkable pivalic acid was utilised as a substituent for reaction to generate these mixed-ligand clusters that have very resembling structures as $Zr_4O_2(OMc)_{12}$.

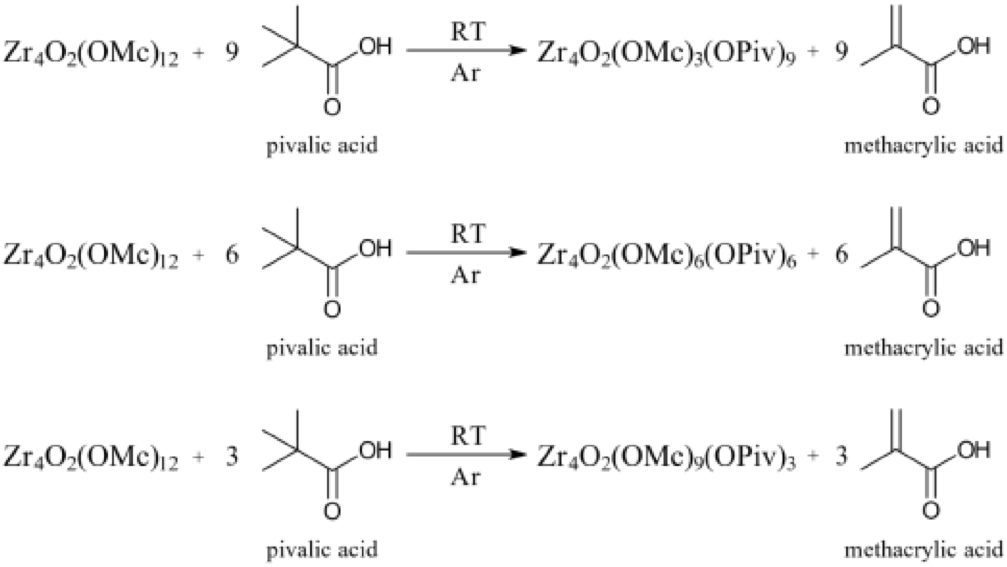

*Figure 4-9: Synthesis of $Zr_4O_2(OMc)_3(OPiv)_9$, $Zr_4O_2(OMc)_6(OPiv)_6$ and $Zr_4O_2(OMc)_9(OPiv)_3$ oxo cluster via ligand exchange route.*

9.00, 6.00 and 3.00 eq. of pivalic acid were added respectively to 1.00 eq. of $Zr_4O_2(OMc)_{12}$ dissolved in dry dichloromethane. To ensure a complete exchange process, the stirring of mixture was carried on for 24 hours at room temperature under argon atmosphere.

Dichloromethane was then removed by the Schlenk line and cooling trap. 10 mL of dry n-hexane was used to washed the product before being withdrawn via a syringe. The purification procedure was repeated for three times and the solid were eventually dried under high vacuum for 6 hours.

From the $^1$H NMR spectra of $Zr_4O_2(OMc)_6(OPiv)_6$ and $Zr_4O_2(OMc)_9(OPiv)_3$ clusters (Figure 4-10b and Figure 4-10c), the signals of protons on methacrylate and pivalate ligands were clearly indicated and identical to the corresponding peaks of $Zr_4O_2(OMc)_{12}$ and $Zr_4O_2(OPiv)_{12}$ NMR results. The integral ratio of peak a, b, c, d has also proven the number of methacrylate and pivalate ligands on the single clusters. The spectrum of $Zr_4O_2(OMc)_3(OPiv)_9$ (Figure 4-10a) yet revealed some trace of pivalic acid reactant remaining in the product. Nevertheless, it should be able to be removed by further rinsing with n-hexane.

a) $Zr_4O_2(OMc)_3(OPiv)_9$

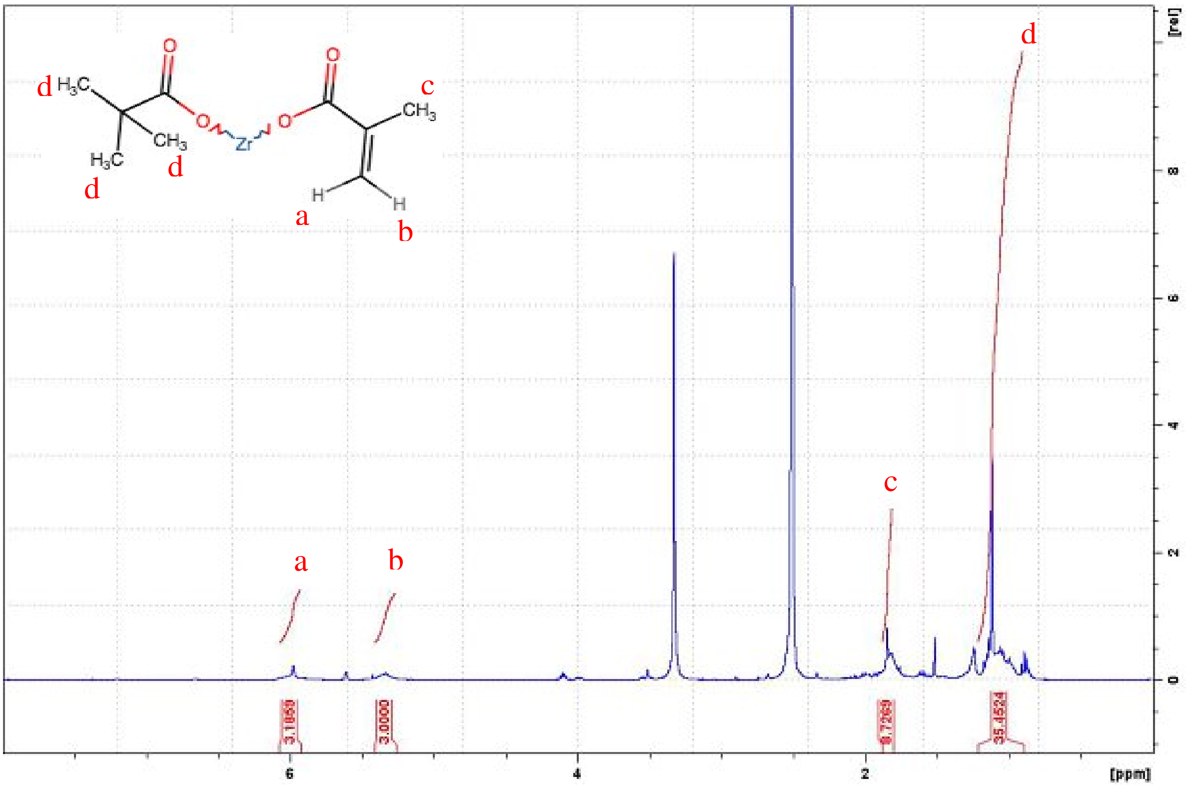

b) $Zr_4O_2(OMc)_6(OPiv)_6$

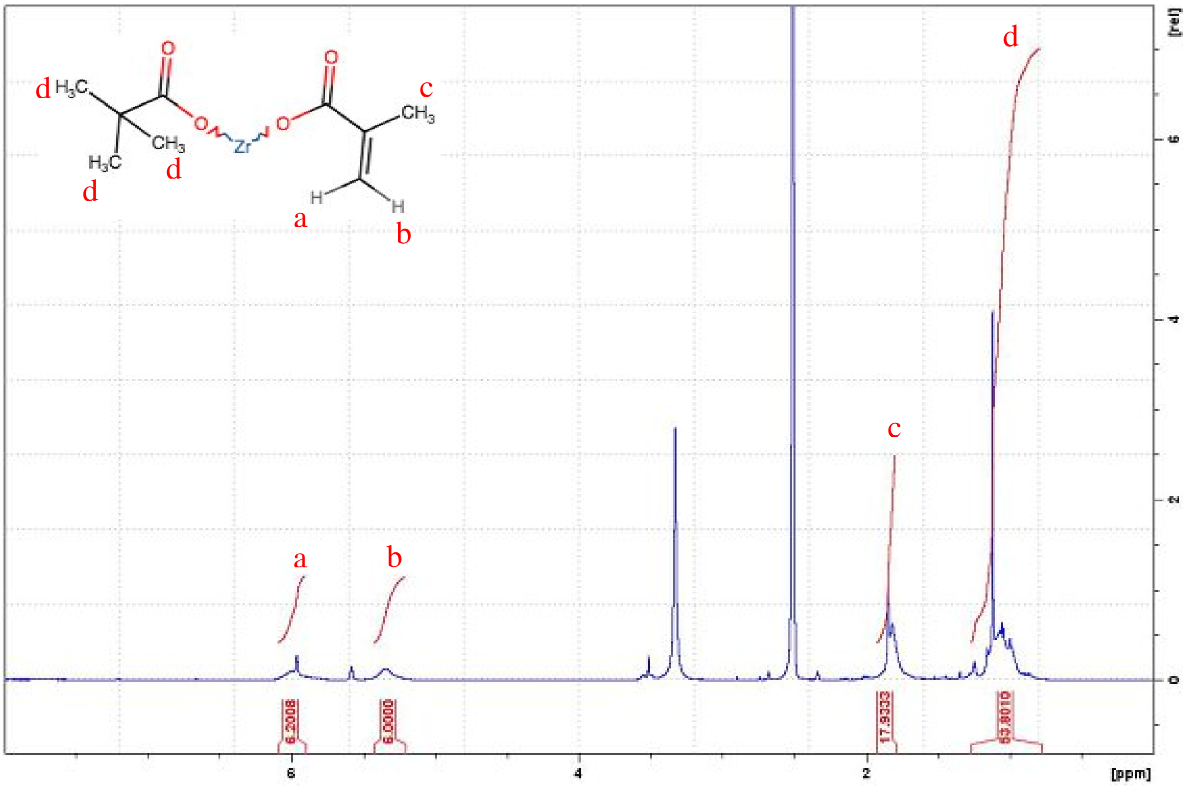

c) $Zr_4O_2(OMc)_9(OPiv)_3$

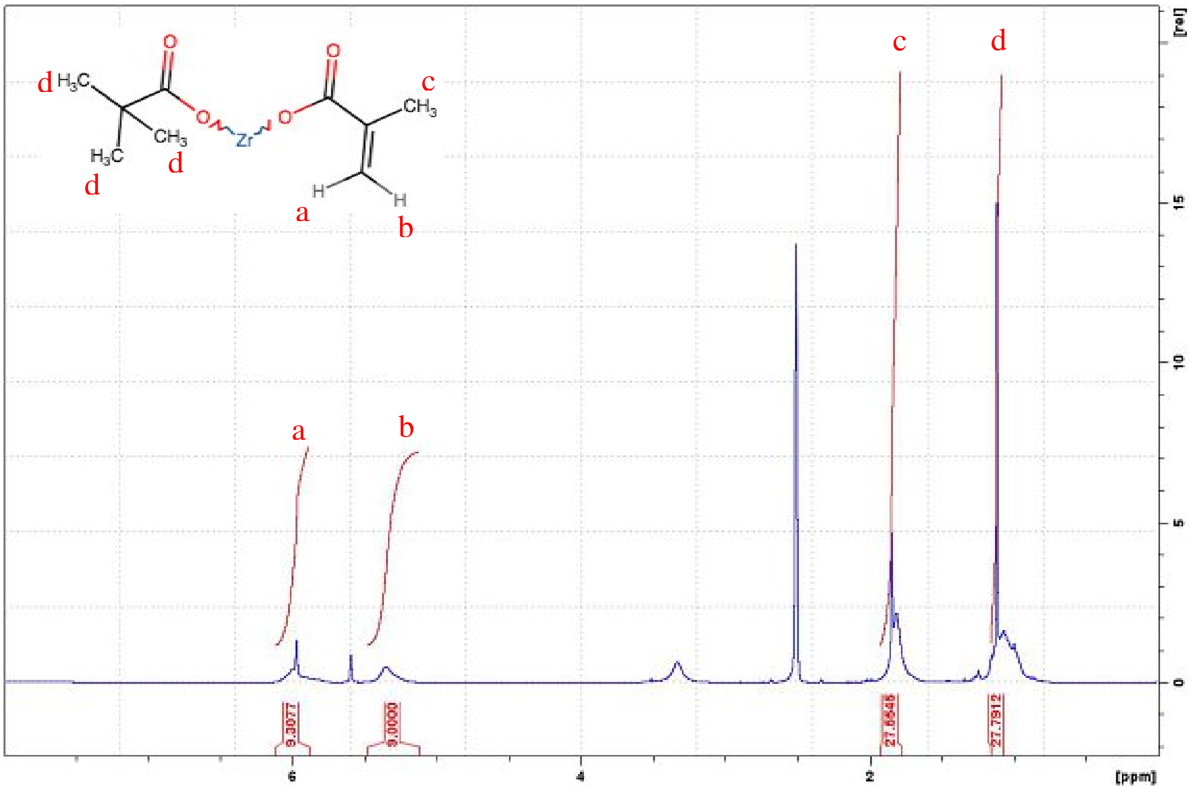

*Figure 4-10*: $^1$H NMR spectra of a) $Zr_4O_2(OMc)_3(OPiv)_9$, b) $Zr_4O_2(OMc)_6(OPiv)_6$ and c) $Zr_4O_2(OMc)_9(OPiv)_3$ in DMSO-d solvent.

## 4.2 Thermogravimetric Analysis (TGA)

Thermal stability of the resist material is extremely crucial. Several baking steps including post applied baking (PAB) and post exposure baking (PEB) are usually involved within the lithography process for achieving better patterning performance. The baking temperature is essentially dependent on the chemical nature of material used but mostly would reach 110 to 130 °C. In order to understand the thermal behaviour of the zirconium oxo clusters, thermogravimetric analysis was conducted. Another advantage of TGA is to reveal the purity of the products. The reactants and solvents employed for the synthesis have lower evaporation temperatures, and the operating temperature of the purification process is lower as well. By observing mass loss at the early stage of measurements, the purity of the product can therefore be defined.

The measurements were carried out under nitrogen atmosphere to exclude the influence from moisture and oxygen. Measurement temperatures started from room temperature (about 20 °C) to the maximum temperature of 500 °C, with a ramping rate limited at 10 K/min to ensure a detailed overview of mass variation. Approximately 10 mg of sample was weighed inside the glovebox and packed in an aluminium crucible which was covered with a lid. Each sample was loaded to the deck shortly before the end of the previous measurement in prevent hydrolysis.

### 4.2.1 $Zr_4O_2(OMc)_{12}$, $Zr_4O_2(OPiv)_{12}$ and Mixed-Ligand Zr Oxo Clusters

The TGA results of $Zr_4O_2(OMc)_{12}$, $Zr_4O_2(OPiv)_{12}$ and $Zr_4O_2(OMc)_x(OPiv)_{12-x}$ (x=3, 6, 9) clusters were depicted in Figure 4-11 for comparing the influence of incorporating non-crosslinkable pivalic ligand to the clusters. The mixed-ligand clusters started a minor degradation as the temperature went above 200 °C. The onset temperatures of the major mass loss were all above 330 °C, meaning the materials should be able to remain intact through the baking processes without degrading. This loss was contributed to the char formation and became more pronounced with the increase of crosslinking density in the mixed-ligand clusters [73], whereas the higher onset temperature $Zr_4O_2(OPiv)_{12}$ performed was caused by the agglomeration of more homogeneous structure [78]. $Zr_4O_2(OMc)_{12}$ showed the highest onset temperature of degradation since it owns the highest crosslinking density and homogeneity among these five zirconium oxo clusters.

Additionally, TGA results also provided the information regarding the purity of the clusters. $Zr_4O_2(OMc)_{12}$, $Zr_4O_2(OPiv)_{12}$ and $Zr_4O_2(OMc)_6(OPiv)_6$ all had zero mass loss before reaching 150 °C, while a mere 2.5 % mass loss in $Zr_4O_2(OMc)_3(OPiv)_9$ and $Zr_4O_2(OMc)_9(OPiv)_3$

respectively was observed attributed to the evaporation of unreacted reactants, which is in line with the results of NMR spectra and again proves the n-hexane rinsing purification process is feasible.

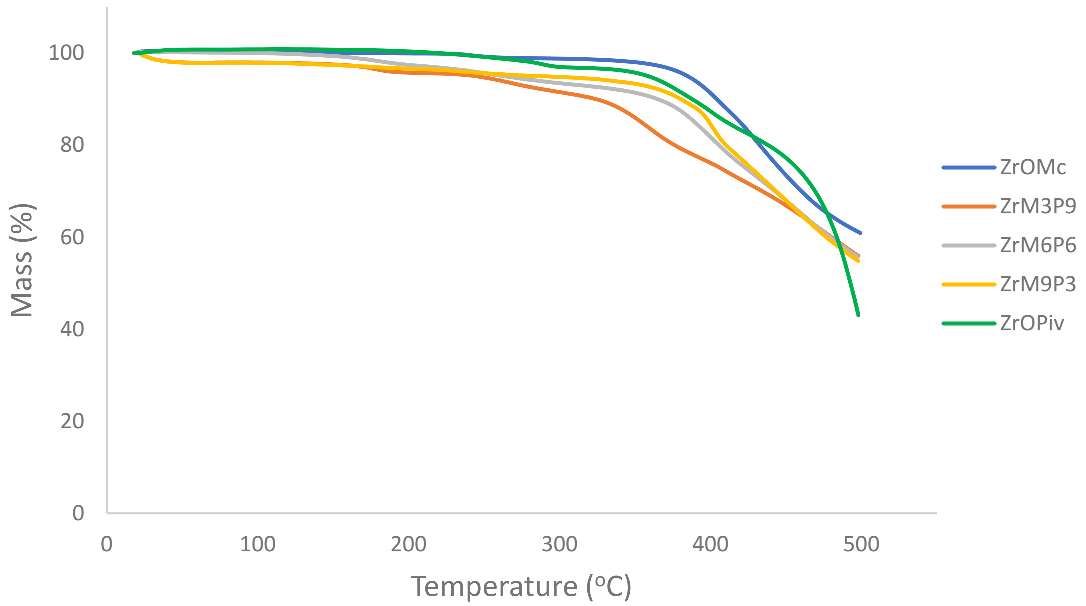

*Figure 4-11: TGA results of* $Zr_4O_2(OMc)_{12}$*,* $Zr_4O_2(OPiv)_{12}$ *and mixed-ligand Zr oxo clusters.*

### 4.2.2 Zirconium Oxo Clusters with Various Ligands

$Zr_4O_2(OVinac)_{12}$ and $Zr_4O_2(ODiMc)_{12}$ have a comparable TGA thermal behaviour to that of $Zr_4O_2(OMc)_{12}$ attributed to high similarity in core and ligand structures (Figure 4-12). Degradation temperatures of these two clusters could both reach above 350 °C, enabling them to sustain through PAB and PEB processes. Only a small trace of impurity resulted from the reactants was observed in the TGA experiment of $Zr_4O_2(OVinac)_{12}$. On the other hand, the degradation of $Zr_{12}O_8(OH)_8(OMc)_8(OAc)_{16}\cdot 6HOAc$ appear at a much lower temperature. Since the crystal is mainly composed of two $Zr_6O_4(OH)_4$ cores bridged with acetates, the disintegration of structure is expected to take place with increasing temperature, leading to the loss of acetate ligands. In contrast, the methacrylate ligands remain on the core until reaching approximately the same degradation temperature as other zirconium oxo clusters. Therefore, in order to maintain the material properties of $Zr_{12}O_8(OH)_8(OMc)_8(OAc)_{16}\cdot 6HOAc$, it is recommended to conduct PAB and PEB within manufacturing process at a temperature below 100 °C.

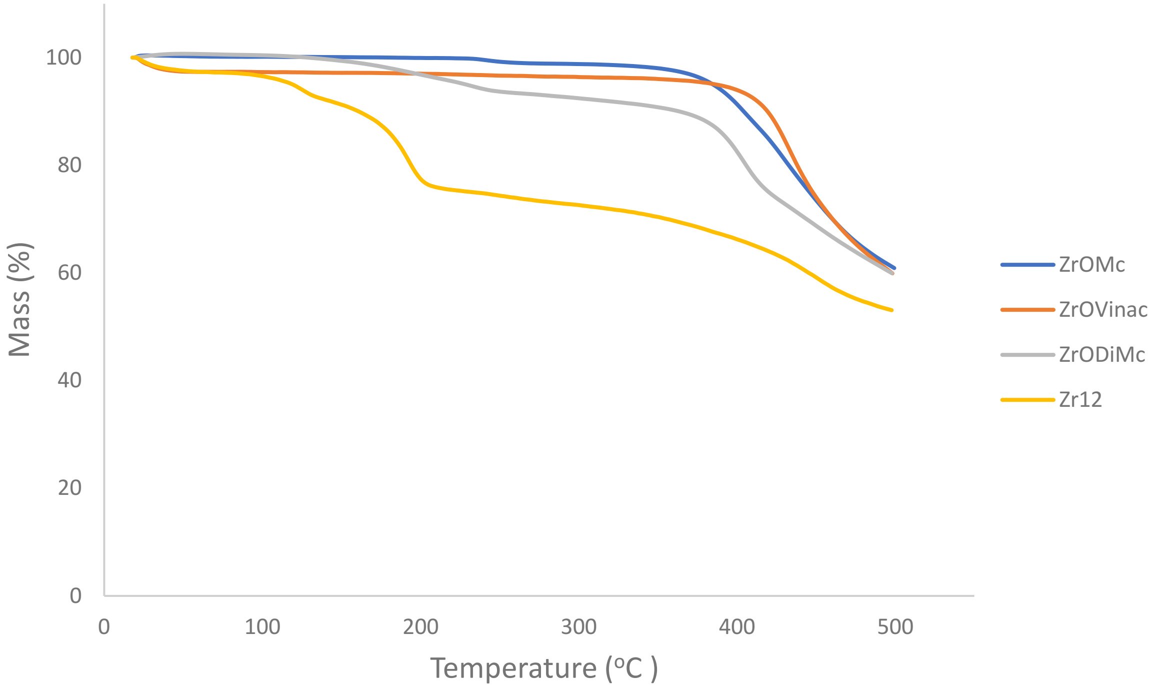

*Figure 4-12: TGA results of $Zr_4O_2(OMc)_{12}$, $Zr_4O_2(OPiv)_{12}$ and mixed-ligand Zr oxo clusters.*

## 4.3 Degradation Test

Requirements for the purity of photoresist material are very high since lithography of integrated circuits is an extremely delicate procedure. The lines should be perfectly positioned to prevent malfunctions and short circuits. Any degradation issue within resist materials would lead to considerable defects of the printed patterns. Therefore, it is crucial to understand the durability and degrading period for zirconium oxo clusters. In the work, $Zr_4O_2(OMc)_{12}$ was taken for degradation test to set a benchmark for the other oxo clusters.

The degradation test was carried out by directly exposing the crystal to air and then measuring the relative intensity of hydrolysed and pure $Zr_4O_2(OMc)_{12}$ via $^1$H NMR. $Zr_4O_2(OMc)_{12}$ clusters started to degrade fast as soon as it exposed to air but gradually slowed down after 24 hours (Figure 4-13). The final proportion of hydrolysed product containing in $Zr_4O_2(OMc)_{12}$ sample was 13.8% after one week. In the semiconductor industry, lithography procedure is usually conducted in clean rooms that have strict control over moisture, temperature and dust particle number per cubic metres. With appropriate preservation and organised system, these metal oxo clusters should be able to last longer in contrast to direct exposure to air.

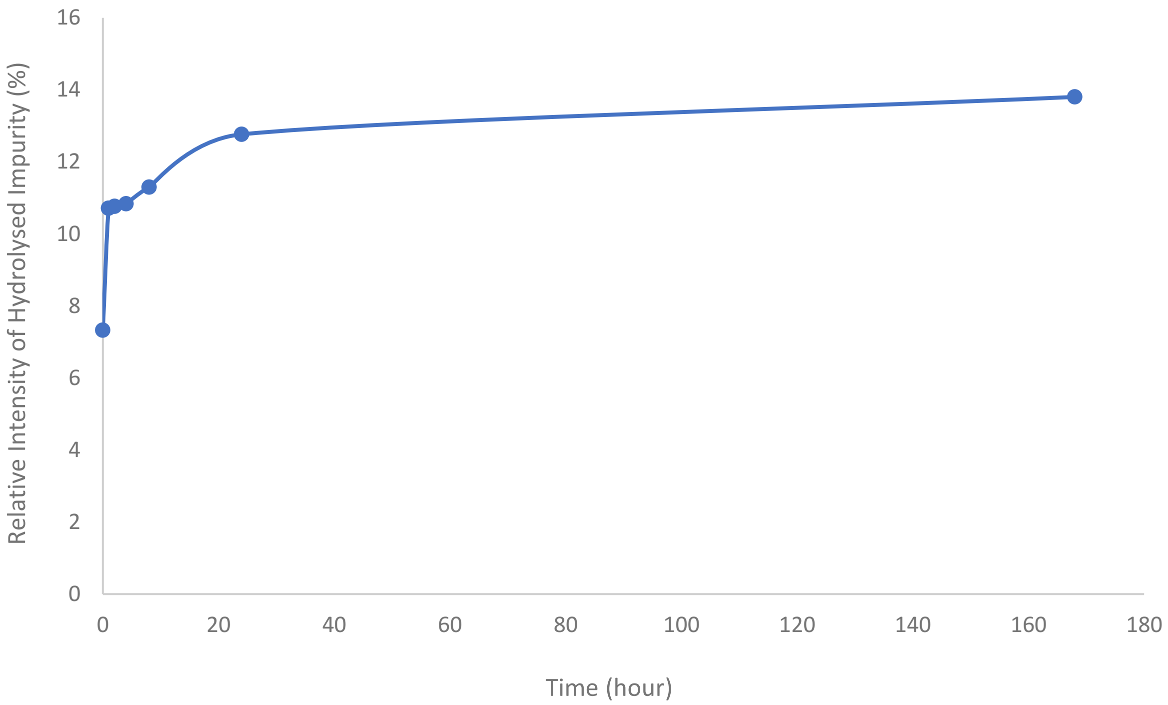

| **Time (Hour)** | **Relative Intensity of Hydrolysed Impurity (%)** |
|---|---|
| **0** | 7.333 |
| **1** | 10.714 |
| **2** | 10.769 |
| **4** | 10.843 |
| **8** | 11.304 |
| **24** | 12.766 |
| **168** | 13.804 |

*Figure 4-13: Degradation curve of $Zr_4O_2(OMc)_{12}$ up to 1 week.*

## 4.4 Summary

In order to synthesis zirconium oxo clusters with various ligands, two different approached have been applied. Carboxylic acid route was conducted for the formation of $Zr_4O_2(OMc)_{12}$, $Zr_4O_2(OPiv)_{12}$, $Zr_4O_2(OVinac)_{12}$, $Zr_4O_2(ODiMc)_{12}$ and $Zr_{12}O_8(OH)_8(OMc)_8(OAc)_{16}\cdot 6HOAc$. It generally showed very high yields except for $Zr_4O_2(OVinac)_{12}$ and $Zr_4O_2(ODiMc)_{12}$ clusters, which was potentially due to low reactivity of the reactants employed. On the other hand, ligand exchange measure was carried out on the synthesis of mixed-ligand oxo clusters. For replacing a partial of methacrylic ligands, non-crosslinkable pivalic acid was used as reactant to react with pristine $Zr_4O_2(OMc)_{12}$ cluster to generate three different clusters including

$Zr_4O_2(OMc)_3(OPiv)_9$, $Zr_4O_2(OMc)_6(OPiv)_6$ and $Zr_4O_2(OMc)_9(OPiv)_3$ that have the identical nucleus as well as similar geometry as their benchmark $Zr_4O_2(OMc)_{12}$. The yield of ligand exchange route is relatively low compared with carboxylic acid approach. It is possibly caused by an incomplete ligand exchange process that leads to a lower amount of product. Despite of the fast reaction rate of ligand exchange, the much bulkier pivalic acid would need more time to form an attachment to the zirconium core.

Purification has also been optimised for obtaining higher purity and providing more potentials to the industry by meeting requirements of high volume manufacturing. The original purification process was performed via recrystallization of cluster. This method was tried in this work but the products obtained at last still contained traces of reactants. It was also more time-consuming and expensive considering the solvents required for a small amount of cluster. New purification approach was done by direct rinsing with appropriate solvents (dry n-hexane in this case). It has been proven to be not only a much efficient and cheaper process but able to be applied for various zirconium oxo clusters at high quantities, with just minor impurities appearing in the NMR spectra as well as TGA results. Therefore, this measurement method was also used for the latter cluster syntheses. TGA data also revealed all the synthesised zirconium oxo clusters are capable of sustaining through the PAB and PEB processes under inert atmosphere without further degradation which would degrade the material properties, making them potentially appropriate candidates for being utilised as photoresist materials.

# 5 Multi-Metallic Oxo Clusters

The application of multi-metallic oxo clusters as photoresists is beneficial in terms of combining the advantages from the metal elements. For instance, despite of having a higher EUV absorption cross section, Ti oxo clusters are notorious for generating inhomogeneous layers on silicon wafers, deteriorating its value as EUV photoresists. The addition of extra Zr or Hf moieties can not only substantially improve the quality of thin films, but increase material sensitivity towards EUV photons. The reaction mechanism of multi-metallic oxo clusters synthesis is identical to that of zirconium oxo cluster syntheses. These clusters are essentially formed in high yields by reacting $Zr(OR)_4$ and/or $Ti(OR)_4$ with a defined excess amount of methacrylic acid. One or more alkoxide are initially replaced by carboxylate groups. Esterification reaction then takes place by the liberated alcohol to generate water. The produced ester along with water are prone to hydrolyse the remaining alkoxide groups and then become the source of oxide or hydroxide groups in the cluster. The highly-controlled growth of carboxylate-substituted oxometallate clusters is mainly resulted from the slow production of water [57].

Three of multi-metallic oxo clusters selected are based on Ti and Zr (9, 10, 11) (Table 4). By modifying the molar ratio of $Ti(OBu)_4$ and $Zr(OBu)_4$, the number of metals can be altered for creating various clusters with different linear absorption coefficients towards EUV. A noteworthy fact is that instead of zirconium n-butoxide, zirconium n-propoxide was employed as reactant for $Ti_4Zr_2O_4(OBu)_6(OMc)_{10}$ synthesis. The reason is using zirconium n-butoxide for $Ti_4Zr_2O_4(OBu)_6(OMc)_{10}$ would also give rise to the formation of $Ti_2Zr_6O_6(OMc)_{20}$, which leads to a rather complicated and time-consuming separation process. Previous evidence has indicated the relative reactivity of Ti and Zr alkoxides plays an important role and the reactivity of Zr alkoxide remarkably dominates in terms of forming cluster nucleus, resulting in the final cluster geometric [57]. Therefore, the more reactive zirconium n-propoxide with a molar ratio of 1:1:8 was used to solely synthesising $Ti_4Zr_2O_4(OBu)_6(OMc)_{10}$ to enable a simpler purification process.

*Table 4: List of multi-metallic oxo clusters for comparing the influence of metal core on patterning performance.*

| Cluster | Precursor | Carboxylic Acid | Remark | Reference |
|---|---|---|---|---|
| **$Ti_4Zr_4O_6(OBu)_4(OMc)_{16}$**<br>**(9)** | $Ti(OBu)_4$<br>$Zr(OBu)_4$ | Methacrylic Acid<br>(HOMc) | Molar Ratio:<br>1:1:8.5 [a] | 57 |

| | | | | |
|---|---|---|---|---|
| **$Ti_2Zr_4O_4(OBu)_2(OMc)_{14}$**<br>**(10)** | $Ti(OBu)_4$<br>$Zr(OBu)_4$ | Methacrylic Acid<br>(HOMc) | Molar Ratio:<br>1:2:13.5 [a] | 57 |
| **$Ti_4Zr_2O_4(OBu)_6(OMc)_{10}$**<br>**(11)** | $Ti(OBu)_4$<br>$Zr(OPr)_4$ | Methacrylic Acid<br>(HOMc) | Molar Ratio:<br>1:1:8 [a] | 57 |
| **$Ti_4Hf_4O_6(OBu)_4(OMc)_{16}$**<br>**(12)** | $Ti(OBu)_4$<br>$Hf(OBu)_4$ | Methacrylic Acid<br>(HOMc) | Molar Ratio:<br>1:1:8.5 [a] | 67 |
| **$Ti_2Zr_5HfO_6(OMc)_{20}$**<br>**(13)** | $Ti(OBu)_4$<br>$Zr(OBu)_4$<br>$Hf(OBu)_4$ | Methacrylic Acid<br>(HOMc) | Molar Ratio:<br>1:1:1:12 [a] | 67 |

[a] prepared by carboxylic acid route

The type of metal can also be changed by replacing the metal alkoxide reactant to the one of interest. Hafnium n-butoxide was taken as reactant for the synthesis with molar ratio the same as that for $Ti_4Zr_4O_6(OBu)_4(OMc)_{16}$. The generated oxo cluster, $Ti_4Hf_4O_6(OBu)_4(OMc)_{16}$, has resembling structural properties as $Ti_4Zr_4O_6(OBu)_4(OMc)_{16}$, both containing 16 methacrylate ligands. However, the crystallising time for $Ti_4Hf_4O_6(OBu)_4(OMc)_{16}$ was much longer considering the reactivity difference between zirconium and hafnium n-butoxide.

Moreover, given the chemical and structural similarity of Ti, Zr and Hf, the formation of a mixed-metal oxo cluster has been proven feasible [67]. Three metal n-butoxides were used as reactants and reacted with methacrylic acid in order to synthesise $Ti_2Zr_5HfO_6(OMc)_{20}$. The multi-metallic oxo clusters selected in this work should provide a clear overview in terms of nucleus composition influence on lithographic performance. Ti and Hf have higher optical sensitivity than Zr, while Zr showed excellent coatability as well as developability in previous studies, indicating these hybrid oxo clusters might have potential to combine the advantages of both ends and create an optimised version of resist material.

## 5.1 Synthesis

All multi-metallic syntheses were carried out with conventional Schlenk approach to secure a complete exclusion of water and oxygen. Reactants employed were either stored inside the glovebox or distilled over drying agents prior to reactions. Solvents involved in purification process had to be dried and distilled beforehand. The water contents should be lower than 15 ppm measured by Karl Fischer titration.

### 5.1.1 Synthesis of $Ti_4Zr_4O_6(OBu)_4(OMc)_{16}$ (9)

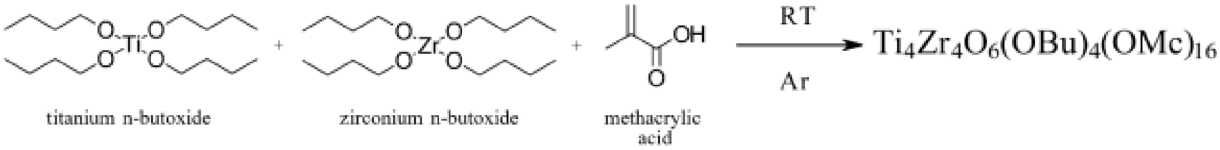

*Figure 5-1: Synthesis of $Ti_4Zr_4O_6(OBu)_4(OMc)_{16}$ oxo cluster via carboxylic acid route.*

$Ti_4Zr_4O_6(OBu)_4(OMc)_{16}$ was synthesised via carboxylic acid route (Figure 5-1). 1.00 eq. of titanium n-butoxide and 1.00 eq. of zirconium n-butoxide were weighed into a clean Schlenk flask that was sealed properly inside the glovebox before being connected to the Schlenk line. The solution was kept stirring for ten minutes to ensure a complete mixing. 8.50 eq. of methacrylic acid, which was weighed into a properly-sealed glass vial inside the glovebox beforehand, was added to the mixture under intensive stirring with argon flow. After mixing for one hour, the solution was allowed to stand at room temperature under argon atmosphere.

Colourless crystals formed after 7 days. To purify, the solids were first separated from the mother liquor. 10 mL of dry-hexane was used to rinse the product before being removed by a syringe. The process was repeated for three times and the crystalline fraction was eventually dried over high vacuum for 6 hours.

As previously mentioned, a recrystallization approach for purifying was not used afterwards so as to achieve higher purity and shorter processing time. However, the yield for $Ti_4Zr_4O_6(OBu)_4(OMc)_{16}$ in this work was slightly lower than that reported in the literature [57]. A possible explanation is that the reaction time may differ from different conditions, including ambient temperature, purity of reactants and water content. NMR spectra indicated minor traces of methacrylic acid remaining in the product, yet it could be removed with further n-hexane rinsing.

### 5.1.2 Synthesis of $Ti_2Zr_4O_4(OBu)_2(OMc)_{14}$ (10)

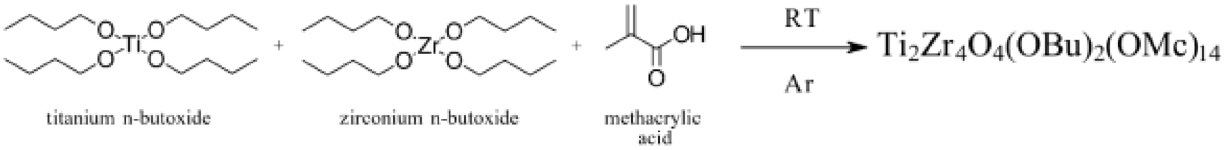

*Figure 5-2: Synthesis of $Ti_2Zr_4O_4(OBu)_2(OMc)_{14}$ oxo cluster via carboxylic acid route.*

The synthesis of $Ti_2Zr_4O_4(OBu)_2(OMc)_{14}$ followed carboxylic acid route (Figure 5-2). By changing the reactant molar ratio, the composition and geometric could vary to form a different

Ti-Zr oxo cluster even though the reactants employed were the same as $Ti_4Zr_4O_6(OBu)_4(OMc)_{16}$. 1.00 eq. of titanium n-butoxide and 2.20 eq. of zirconium n-butoxide were weighed into a Schlenk flask, which was sealed properly inside the glovebox and attached to the Schlenk line afterwards. The solution was left mixing for ten minutes before 13.50 eq. of methacrylic acid that was weighed into a properly-sealed glass vial inside the glovebox beforehand added into the flask under vigorous stirring. After an hour, the mixing was interrupted and the mixture was allowed to stand at room temperature under argon atmosphere. Colourless crystalline product could be obtained after 7 days.

To purify $Ti_2Zr_4O_4(OBu)_2(OMc)_{14}$ cluster, the mother liquor was first removed from the Schlenk flask. 10 mL of dry n-hexane was employed for thoroughly rinsing the product and removed via a syringe subsequently. The process was repeated for three times and the cluster was eventually dried under high vacuum for 6 hours. Similar to $Ti_4Zr_4O_6(OBu)_4(OMc)_{16}$, $Ti_2Zr_4O_4(OBu)_2(OMc)_{14}$ also had a slightly low yield according to published literature. The conditions that can affect reaction rate as well as yield might also make an impact on $Ti_2Zr_4O_4(OBu)_2(OMc)_{14}$ since the two reactions were conducted in approximately the same period. Yet the purity still achieved a high level, leaving nearly no trace of methacrylic acid remaining in the product.

### 5.1.3 Synthesis of $Ti_4Zr_2O_4(OBu)_6(OMc)_{10}$ (11)

Zirconium n-propoxide was utilised as reactant to replace zirconium n-butoxide concerning the complication of product separation and a potential purity issue (Figure 5-3). The reactivity of Zr alkoxide theoretically have a significant influence on the final geometric and composition. Even with similar reactant molar ratio to that of $Ti_4Zr_4O_6(OBu)_4(OMc)_{16}$, the reaction with zirconium n-propoxide can still lead to the formation of $Ti_4Zr_2O_4(OBu)_6(OMc)_{10}$. But in this case, changing the alkoxide only resulted in the inability of generating $Ti_2Zr_6O_6(OMc)_{20}$ cluster in order to avoid a much time-consuming purification process.

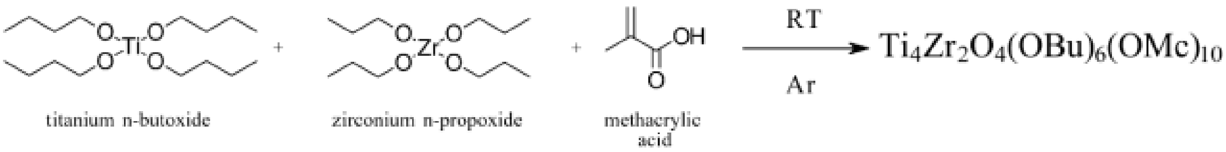

*Figure 5-3: Synthesis of $Ti_4Zr_2O_4(OBu)_6(OMc)_{10}$ oxo cluster via carboxylic acid route.*

The synthesis of $Ti_4Zr_2O_4(OBu)_6(OMc)_{10}$ was via carboxylic acid route. 1.00 eq. of titanium n-butoxide and 0.95 eq. of zirconium n-propoxide were weighed into a clean Schlenk flask inside the glovebox, which was sealed properly and connected to the Schlenk line afterwards for mixing. 8.06 eq. of methacrylic acid, packed in a properly-sealed glass vial inside the glovebox, was added to the mixture under intensive stirring with argon flow. After an hour, the solution was left still at room temperature under argon atmosphere to ensure no further hydrolysis takes place. Colourless crystals were obtained after 7 days.

For purification, the mother liquor was first removed from the Schlenk flask. 10 mL of dry n-hexane was injected for rinsing the crystalline product and withdrawn via a syringe subsequently. The process was repeated three times before the cluster being dried under high vacuum for 6 hours. A low yield was observed in the synthesis of $Ti_4Zr_2O_4(OBu)_6(OMc)_{10}$, which should be caused by the resembling issues as those of $Ti_4Zr_4O_6(OBu)_4(OMc)_{16}$ and $Ti_2Zr_4O_4(OBu)_2(OMc)_{14}$. Nevertheless, the purification was proven to be successful as no trace of methacrylic acid was observed in the NMR spectra.

### 5.1.4 Synthesis of $Ti_4Hf_4O_6(OBu)_4(OMc)_{16}$ (12)

In order to modify the composition of the nucleus, hafnium n-butoxide was taken as a substituent for zirconium n-butoxide with the similar molar ratio as $Ti_4Zr_4O_6(OBu)_4(OMc)_{16}$ (Figure 5-4). It should lead to the formation of Ti-Hf oxo cluster with identical composition and similar geometric. The synthesis of $Ti_4Hf_4O_6(OBu)_4(OMc)_{16}$ took a substantially longer time relative to Ti-Zr oxo clusters. Given the fact that hafnium alkoxide has lower reactivity and the cluster requires crystallising at low temperature, the crystalline products were observed after 30 days.

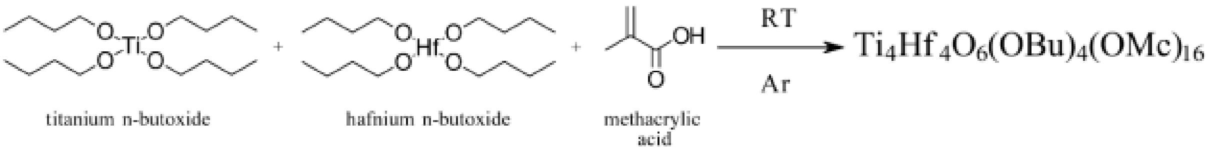

*Figure 5-4: Synthesis of $Ti_4Hf_4O_6(OBu)_4(OMc)_{16}$ oxo cluster via carboxylic acid route.*

The synthesis of $Ti_4Hf_4O_6(OBu)_4(OMc)_{16}$ also followed carboxylic acid route. 1.00 eq. of titanium n-butoxide and 0.89 eq. of hafnium n-butoxide were weighed into a clean Schlenk flask inside the glovebox, which was sealed properly and attached to the Schlenk line. The solution was mixing for 10 minutes before 7.95 eq. of methacrylic acid that was weighed into a properly-sealed glass vial inside the glovebox beforehand being added into the flask under vigorous stirring with argon flow. The stirring was stopped after one hour and the mixture was allowed to stand still at 4 °C under argon atmosphere for 30 days.

To purify the crystalline product, the mother liquor had to be removed from the flask while it was still at low temperature. 10 mL of dry n-hexane was utilised to thoroughly rinse the solids and withdrawn afterwards with a syringe. The process was repeated three times and the cluster was eventually dried under high vacuum for 6 hours.

The yield of $Ti_4Hf_4O_6(OBu)_4(OMc)_{16}$ was relatively low even if the reaction time in this work was longer than that in the previous studies. It was possibly related to the reaction process. Since the flask was stored in a conventional refrigerator instead of the fridge inside the glovebox for 30 days, the humid ambient environment would bring about serious influence on the crystallization of cluster. Concerning the time the Schlenk flask stayed in a moist area, the amount of water penetrating the flask remained considerable, even though it was sealed in an appropriate manner. This potential issue directly affected the rate of reaction as well as cluster crystallising, leading to a much lower yield eventually.

### 5.1.5 Synthesis of $Ti_2Zr_5HfO_6(OMc)_{20}$ (13)

The further modification of multi-metallic nucleus involved incorporating titanium, zirconium and hafnium in a single metal oxo cluster. Metal alkoxides of Ti, Zr and Hf were employed as reactants with an excess amount of methacrylic acid for the synthesis of target compound, $Ti_2Zr_5HfO_6(OMc)_{20}$. Despite of using the same equivalent of alkoxides, the composition and geometric of the final oxo cluster were still defined by the relative reactivity of reactants, leading to a core containing various number of metals. Besides high optical sensitive Ti and Hf, the oxo cluster also consists of more and only crosslinkable methacrylate ligand. Therefore, the expected linear absorption coefficient should be much higher, meaning this resist material would be quite sensitive towards EUV photons.

The synthesis of $Ti_2Zr_5HfO_6(OMc)_{20}$ was carried out via carboxylic acid route (Figure 5-5). 1.00 eq. of titanium n-butoxide, 1.00 eq. of zirconium n-butoxide as well as 0.95 eq. of hafnium n-butoxide were weighed into three glass vials, respectively. A clean Schlenk flask attached to the Schlenk line underwent pumping-venting cycles with argon for three times to remove moisture and oxygen prior to the reaction. Three metal alkoxides were added in sequence into the flask under stirring for ten minutes before 11.84 eq. of methacrylic acid that was previously packed into a glass vial inside the glovebox being added into the mixture. The vigorous stirring was continued for one hour and the solution was subsequently kept still at 4 °C under argon atmosphere.

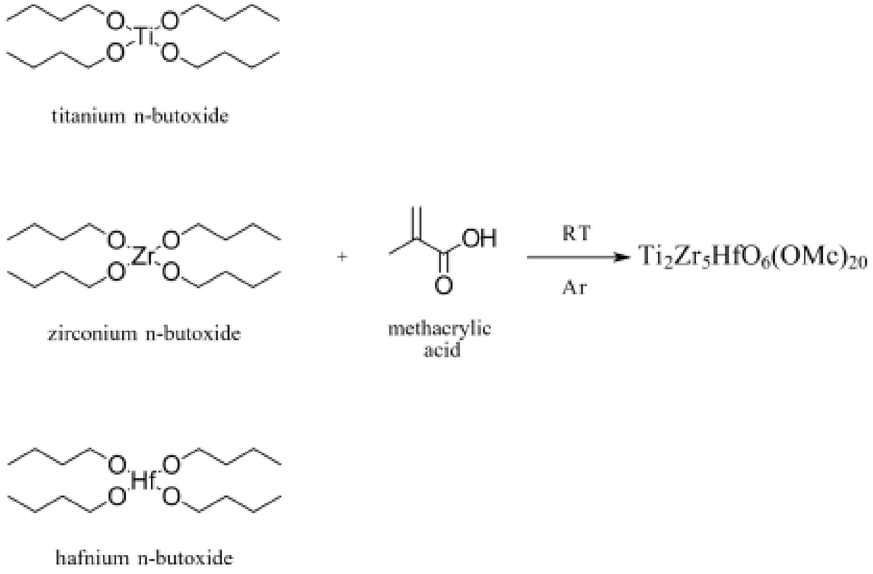

*Figure 5-5: Synthesis of $Ti_2Zr_5HfO_6(OMc)_{20}$ oxo cluster via carboxylic acid route.*

Colourless crystals were observed after 30 days. To purify, mother liquor was removed from the Schlenk flask while it was still at low temperature via a syringe. 10 mL of dry n-hexane was then injected for rinsing the solids for three times. Eventually the crystalline product was dried over high vacuum for 6 hours.

Low yield issue also existed in the work of $Ti_2Zr_5HfO_6(OMc)_{20}$ synthesis. The possible reason was similar to that for $Ti_4Hf_4O_6(OBu)_4(OMc)_{16}$. Given the time the reaction flask stayed in a highly humid refrigerator rather than the one in the glovebox, water from the ambient environment kept penetrating the container to slowed down and inhibited the crystallization of oxo cluster. This could also explain the phenomenon of longer formation time in this work in comparison with that in the published results. Traces of methacrylic acid were indeed observed from the NMR spectra yet the remaining amount was relatively low.

## 5.2 Thermogravimetric Analysis (TGA)

As previously mentioned, the main purpose of conducting TGA measurement on the metal oxo clusters is to study their sustainability during manufacturing process, especially for PAB and PEB. It can also reveal the purity of synthesised materials by comparing the results with NMR spectrum as well as the thermal properties published in the literature. The TGA measurements were carried out under nitrogen atmosphere with a temperature ramping rate at 10 K/min. Each sample was weighed inside the glovebox and packed into an aluminium crucible with a lib covered for analysis. It was loaded to the sample deck shortly before the finishing of the previous measurement.

TGA results of the synthesised multi-metallic oxo clusters were depicted in Figure 5-6. There were two steps of mass loss in each material if not considering the influence from the impurities. Essentially, the first mass loss is related to a structural degradation of the material, while the major mass loss is arisen from char formation of the organic entities. Three Ti-Zr-based oxo clusters were showing similar onset temperatures for the first mass loss. Despite the core structures are just slightly different, higher Zr moiety seems to have the ability of increasing the degradation temperature. $Ti_2Zr_5HfO_6(OMc)_{20}$, however, has a relatively lower onset temperature for the first degradation at 162 °C, which is resulted from its crystal structure and ligand formation. The multi-metallic oxo clusters all reached similar onset temperatures of the major mass loss at 365 °C. The first and second degradation temperatures they performed have indicated these oxo clusters are able to remain intact through the baking process under inert atmosphere without further damage on the material properties.

In principle, purity of the synthesised multi-metallic oxo clusters was excellent, showing just 2% of impurity within the products of $Ti_4Zr_4O_6(OBu)_4(OMc)_{16}$, $Ti_2Zr_4O_4(OBu)_2(OMc)_{14}$ and $Ti_4Zr_2O_4(OBu)_6(OMc)_{10}$, respectively. The TGA results are corresponding to those of NMR spectra in terms of purity and the source is primarily from the unreacted methacrylic acid.

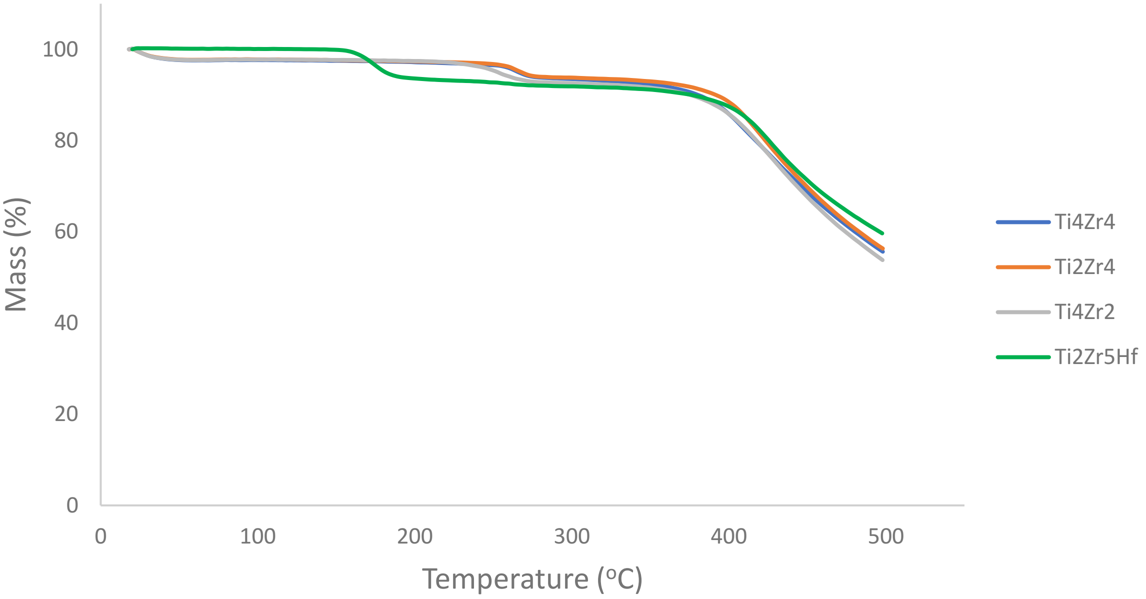

*Figure 5-6: TGA results of the Ti-, Zr- and Hf-based multi-metallic oxo clusters.*

## 5.3 Summary

The Di- and tri-metallic oxo clusters based on Ti, Zr and Hf were successfully conducted via carboxylic acid route. By either changing the molar ratio of reactants or employing different reactant with reactivity, the geometry and composition could be altered and tuned in a required manner. The optimised purification approach through dry n-hexane rinsing enabled the products to reach high purity with rather less time-consuming and cheap procedure, despite some clusters showed slightly lower yields according to the literature, which might be resulted from mistakes carried out during the reaction process.

TGA data revealed a high purity level of each synthesised multi-metallic oxo cluster. The impurities mainly based on unreacted methacrylic acid as the reactants, which can be removed via further purification steps. High onset temperatures for two degradation steps, all reaching above 160 °C, have also proven the sustainability of these materials through the baking procedures, making them suitable for photoresist applications.

These multi-metallic oxo clusters are expected to combine the advantages of each metal element and demonstrate a superior patterning performance. In contrast to zirconium and hafnium oxo clusters, their sensitivities towards EUV photons should be higher because not only more optical sensitive metals are incorporated but also more crosslinkable methacrylic ligands are attached. Even though the sizes would potentially cause deterioration upon line edge roughness or even resolution, these materials remain enthralling since no research so far has reported results on multi-metallic substance as EUV photoresist. The detailed mechanism of the oxo clusters will also be studied in this work via thin-film IR spectroscopy and outgassing approach.

# 6 Hafnium Oxo Cluster

Hafnium as constituent in oxo clusters is known for its excellent atomic absorption coefficient at 92 eV. Some hafnium-based resist materials have also been studied and even used in the industry [52, 54, 59]. Nonetheless, it is still quite intriguing to understand the detailed mechanism and patterning performance of two Zr and Hf oxo clusters with high structural similarity. Being in the same group, the chemical nature theoretically enables hafnium to form a cluster containing identical metal/organic moiety composition as well as resembling crystal structure as a zirconium derivative. In this work, $Zr_4O_2(OMc)_{12}$ was selected as the target for hafnium-based resist material (Table 5). The reaction mechanism is expected to follow the pathway for zirconium and multi-metallic oxo clusters syntheses. Through replacing zirconium n-propoxide with hafnium n-butoxide, the synthesis should eventually lead to the construction of $Hf_4O_2(OMc)_{12}$.

*Table 5: List of Hf oxo cluster for comparing the influence of metal optical sensitivity with the benchmark $Zr_4O_2(OMc)_{12}$.*

| Cluster | Precursor | Carboxylic Acid | Remark | Reference |
|---|---|---|---|---|
| **$Zr_4O_2(OMc)_{12}$ (1)** | $Zr(OPr)_4$ | Methacrylic Acid (HOMc) | Molar Ratio: 1:4, propanol[a] | [71] |
| **$Hf_4O_2(OMc)_{12}$ (14)** | $Hf(OBu)_4$ | Methacrylic Acid (HOMc) | Molar Ratio: 1:4, butanol[a] | [71, 67] |

[a] prepared by carboxylic acid route

Despite of being more optically sensitive towards EUV photon, Hf-based resist materials may have some drawbacks concerning its atom size. As the feature size decreasing down to single-digit nanometres, the influence from the size of photoresist on line edge roughness will become more significant. Castellanos et al. published a paper regarding the EUV lithographic capability of Ti-, Zr- and Hf-based resist materials, where they compared patterning performance of $Ti_8O_8(OMc)_{16}$, $Zr_6O_4(OH)_4(OMc)_{12}$ and $Hf_6O_4(OH)_4(OMc)_{12}(HOBu)$ [54]. The AFM images of line/space patterns at 50 and 22 nm half-pitch already revealed an evident difference between $Zr_6O_4(OH)_4(OMc)_{12}$ and $Hf_6O_4(OH)_4(OMc)_{12}(HOBu)$, as shown in Figure 6-1. Hexameric structures of their resist materials also deteriorated the line edge roughness obtained. The sizes of $Zr_4O_2(OMc)_{12}$ and $Hf_4O_2(OMc)_{12}$ oxo clusters are relatively small owing to the tetrameric nucleus, which can potentially improve the roughness of resulted pattern.

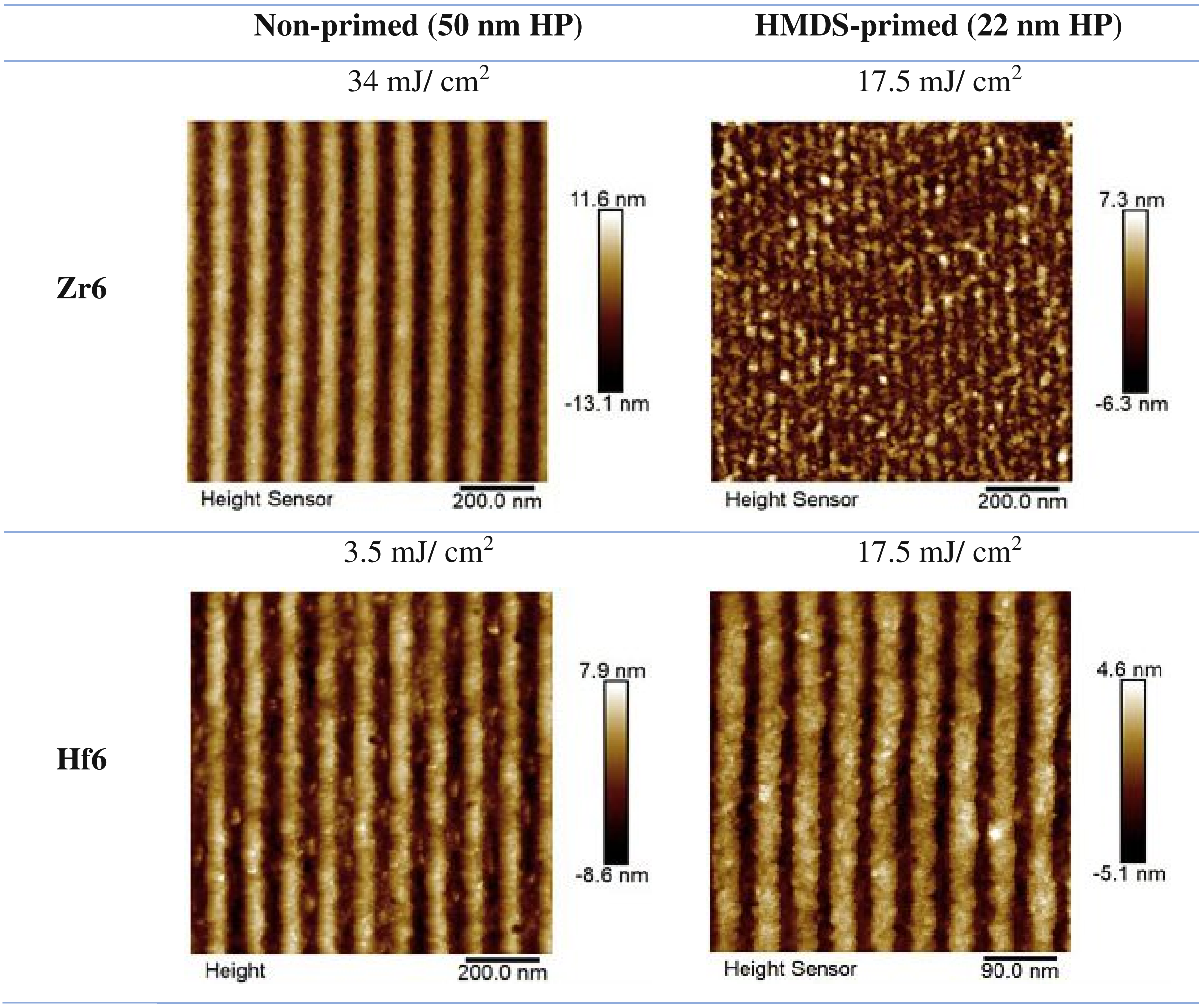

*Figure 6-1: AFM images of line/space patterns at 50 and 22 nm half-pitch by $Zr_6O_4(OH)_4(OMc)_{12}$ and $Hf_6O_4(OH)_4(OMc)_{12}(HOBu)$ (re-edited)* [54].

## 6.1 Synthesis

The reaction was conducted with conventional Schlenk technique. The reactants employed were either stored inside the glovebox or distilled prior to reaction. Solvents involved in the purification process were distilled over drying agent shortly before use.

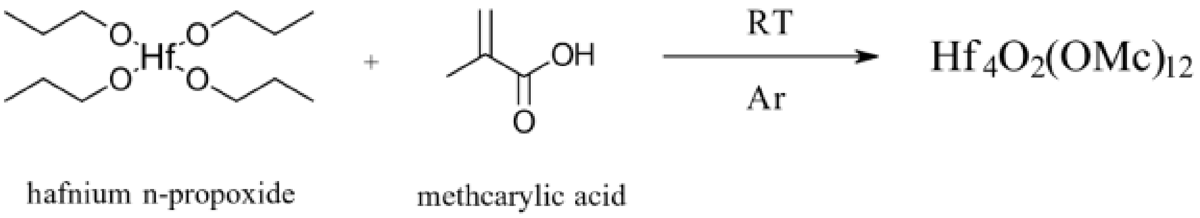

*Figure 6-2: Synthesis of $Hf_4O_2(OMc)_{12}$ oxo cluster via carboxylic acid route.*

The synthesis of $Hf_4O_2(OMc)_{12}$ cluster was carried out via carboxylic acid route with same reactant molar ratio as that of $Zr_4O_2(OMc)_{12}$ synthesis (Figure 6-2). 1.00 eq. of hafnium n-butoxide and 4.01 eq. of methacrylic acid were weighed into two properly-sealed glass vials respectively inside the glovebox. A clean Schlenk flask was connected to the Schlenk line and underwent pumping-venting cycles for three times to secure a complete exclusion of water and oxygen. Methacrylic acid and hafnium n-butoxide were then transferred into the flask via syringes with argon flow while stirring. The mixing was stopped after an hour and the solution was allowed to stand at room temperature under argon atmosphere. Colourless crystals were obtained after 3 days. To purify, the crystalline product was separated from its mother liquor before being rinsed with 10 mL of dry n-hexane to remove the reactants. The process was repeated for three times and the cluster was eventually dried under high vacuum for 6 hours.

Single crystal XRD analysis has revealed the isotypic nature of $Hf_4O_2(OMc)_{12}$ to the Zr analogue (see Chapter 12.4), with the structural properties and composition corresponding to those of $Zr_4O_2(OMc)_{12}$ oxo cluster. The yield of $Hf_4O_2(OMc)_{12}$ cluster was comparable with that of $Zr_4O_2(OMc)_{12}$, both reaching above 80% in 2-3 days of reaction time. Moreover, the purity of $Hf_4O_2(OMc)_{12}$ also achieved a high level via the optimised purification process, showing only minor traces of methacrylic acid existing in the $^1H$ NMR spectrum (Figure 6-3).

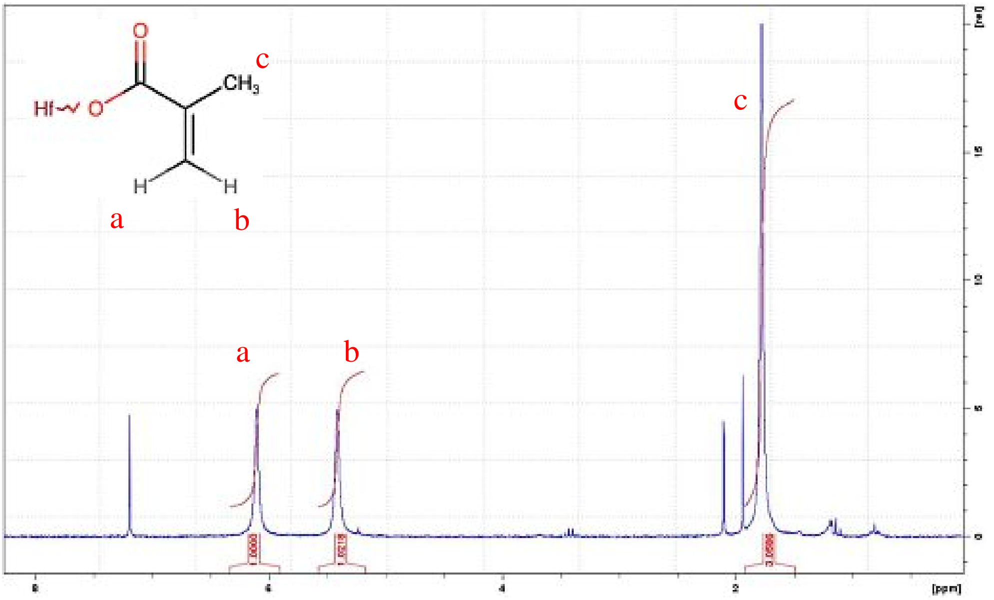

*Figure 6-3: $^1H$ NMR spectrum of $Hf_4O_2(OMc)_{12}$.*

## 6.2 Thermogravimetric Analysis (TGA)

TGA measurements for $Hf_4O_2(OMc)_{12}$ was conducted under nitrogen atmosphere with a temperature ramping rate at 10 K/min. The material was weighed inside the glovebox and packed into an aluminium crucible with a lid covered for the analysis. The crucible was loaded to the sample deck shortly before the finish of previous measurement to prevent further hydrolysis issue.

TGA result of $Hf_4O_2(OMc)_{12}$ was depicted in Figure 6-4 including that of $Zr_4O_2(OMc)_{12}$ as a comparison. Attributed to high structural similarity, the thermal properties of these two oxo clusters are nearly identical, with an onset temperature of the major mass loss at 365 °C. Hafnium entity has more influence on delaying the degradation at higher temperature compared to zirconium. Nonetheless, the analysis still revealed the potential of $Hf_4O_2(OMc)_{12}$ to remain intact through the baking process within semiconductor manufacturing.

Impurity with 2.2% mass was observed in the hafnium oxo cluster, which was mainly due to the unreacted methacrylic acid. TGA result is in line with that of NMR spectra regarding the entity of methacrylic acid. Further n-hexane rinsing step could be taken in order to obtain a pristine product.

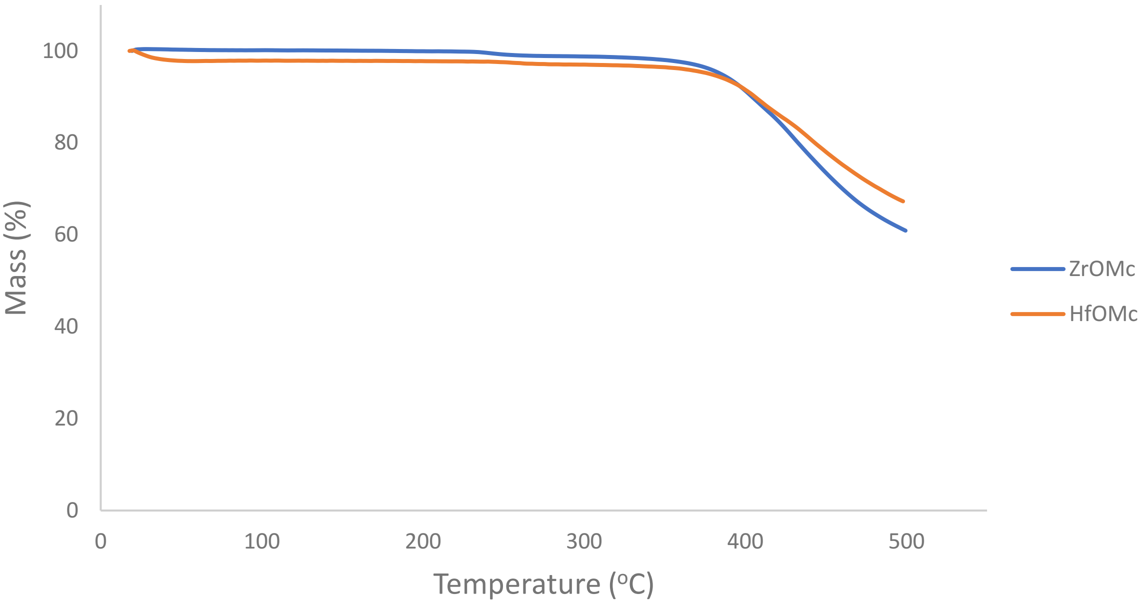

*Figure 6-4: TGA results of $Zr_4O_2(OMc)_{12}$ and $Hf_4O_2(OMc)_{12}$ oxo clusters.*

## 6.3 Summary

Having high chemical and structural similarity as $Zr_4O_2(OMc)_{12}$, $Hf_4O_2(OMc)_{12}$ has been proven feasible of being synthesised via carboxylic acid pathway. The yield and purity could both reach approximately the same level to those of $Zr_4O_2(OMc)_{12}$, with a slightly longer reaction time. The optimised rinsing purification process was also applied to a three-time scaling-up synthesis of $Hf_4O_2(OMc)_{12}$ and the purity obtained was comparable to that of the smaller batch, indicating once again the potential for this approach to be utilised in high volume manufacturing with relatively shorter processing time as well as lower production cost.

The thermal properties of $Zr_4O_2(OMc)_{12}$ and $Hf_4O_2(OMc)_{12}$ are essentially resembling, both reaching an onset temperature for the major mass loss above 360 ºC. This performance enables $Hf_4O_2(OMc)_{12}$ to be utilised as photoresist applications because of the sustainability it showed at high temperature that makes it stay intact through the PAB as well as PEB processes.

Previous studies revealed some of the defects Hf-based resists have, one of which was higher line edge roughness in the resulted line/space pattern due to the larger size of molecule. Identified as a tetrameric structure, the smaller size of $Hf_4O_2(OMc)_{12}$ can potentially reduce the negative influence on line edge roughness and even improve resolution, making it a more efficient photoresist material. The comparison with the lithographic performance of $Zr_4O_2(OMc)_{12}$ will also be studied in this work.

# 7 Coatability and Developability Tests

Coatability and developability are two crucial indices for defining the feasibility of a resist material at an early stage. Coatability indicates the ability of a material to form a homogenous and uniform film that has good adhesion on a silicon wafer surface via a simple coating approach. In the semiconductor manufacturing plants, coating of photoresist is mostly carried out by spin-coating (Figure 7-1). A casting solution is prepared prior to the coating by dissolving or diluting a resist material in a specific type of casting solvent before being applied to the centre of a silicon wafer that has already been mounted on the plate holder. The plate then starts spinning to evenly distribute the photoresist on the wafer and partially dry the solvent through evaporation at the same time. A post-apply bake is conducted in the end to ensure a complete evaporation of casting solvent. Temperature and time of baking are dependent on the type of solvent. Therefore, the selection of casting solvents is relatively important. It should be not only volatile to enable an efficient and straightforward removal, but less viscous to offer an effortless processability.

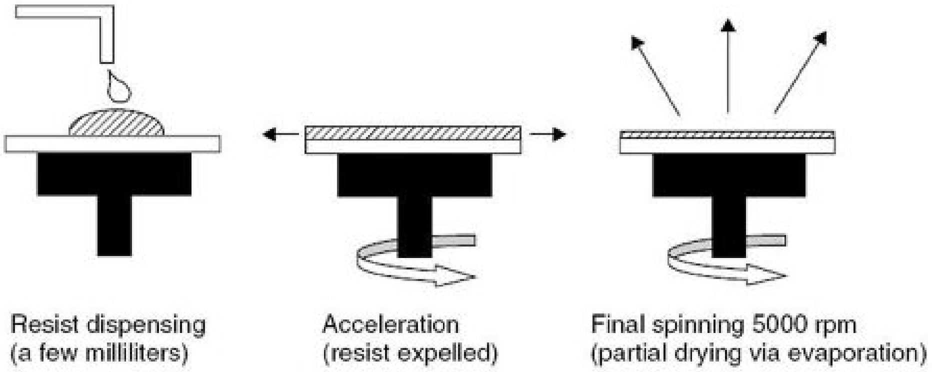

*Figure 7-1: Schematic illustration of spin-coating process* [79].

Furthermore, developability means the ability of a material to be removed from a silicon wafer surface without leaving traces and defects using a conventional developing process. There are two different development approaches that are primarily used in the industry (Figure 7-2). In spray development, a nozzle is employed to dispense fine mist of developing solvent onto a silicon wafer while it is being spun using an identical equipment as that in spin-coating. This technique can reduce the usage of solvent as well as give a more uniform developer coverage. Puddle development, on the other hand, is conducted by applying a specific developer onto a stationary silicon wafer that remains motionless for a period of time. The silicon wafer is spun afterwards to distribute the solvent and dried. Developer should essentially be able to dissolve the unexposed resist material and have a moderate volatility to ensure a good control during development process.

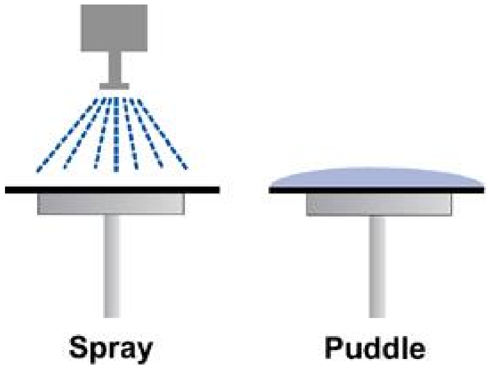

*Figure 7-2: Two different types of conventional developing processes* [80].

## 7.1 Preliminary Coatability and Developability Test (Conducted in TU Wien)

### 7.1.1 Solubility Test of Casting and Developing Solvents

A preliminary solubility test was carried out involving some of the most commonly-used casting solvents in the semiconductor industry for their solubility with $Zr_4O_2(OMc)_{12}$ that was utilised as a benchmark for the other zirconium oxo clusters. The concentration of each casting solution was formulated at 1% w/v, i.e. 10 mg of sample was dissolved in 1 mL of respective solvent (or solvent mixture). The solutions were further mixed via ultrasonic bath at room temperature for 5 minutes.

The results (Table 6) revealed that propylene glycol methyl ether (PGME), the mixture of PGME and propylene glycol methyl ether acetate (PGMEA) with a ratio of 7:3 by weight, as well as 2-heptanone are the most appropriate among the tested solvents for $Zr_4O_2(OMc)_{12}$, giving clear and fully-dissolved solutions. The other solvents, including propylene glycol methyl ether acetate (PGMEA), isopropyl alcohol (IPA), anisole, and methyl isobutyl ketone (MIBK), could not fully dissolve the zirconium cluster at the same concentration and hence are not ideal as the casting solvent for $Zr_4O_2(OMc)_{12}$.

*Table 6: Results of solubility test for commercially-used casting solvents with $Zr_4O_2(OMc)_{12}$.*

| **Solvent** | **Structure** | **Usage ($W_{cluster}/V_{solvent}$)** | **Result** |
|---|---|---|---|
| **Propylene glycol methyl ether** | 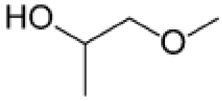 | 10 mg/ 1 mL | ○ |

| | | | |
|---|---|---|---|
| **(PGME)** | | | |
| **Propylene glycol methyl ether acetate (PGMEA)** | 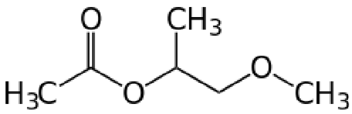 | 10 mg/ 1 mL | Δ |
| **PGME+PGMEA (7:3 by volume)** | - | 10 mg/ 1 mL | ○ |
| **Isopropyl Alcohol (IPA)** | 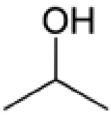 | 10 mg/ 1 mL | Δ |
| **Anisole** | 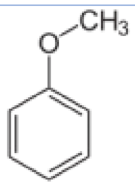 | 10 mg/ 1 mL | Δ |
| **2-Heptanone** | 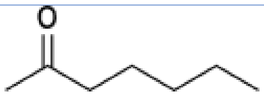 | 10 mg/ 1 mL | ○ |
| **Methyl isobutyl ketone (MIBK)** | 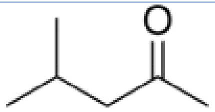 | 10 mg/ 1 mL | x |

*(○ Fully Dissolved, Δ Partially Dissolved, x Not Dissolved)*

### 7.1.2 Spin-Coating Test for Parameter Determination

#### 7.1.2.1 Spin-coating with 2-Heptanone as Casting Solvent

A series of spin-coating tests was performed in order to formulate a process with defined parameters including rotational speed and time. The ramping time, meaning the time from stationary to desired rotational speed, was set at 1 second. Ideal process conditions should eventually lead to a homogenous coating film with a flat topography and a moderate thickness for pattern printing. According to the solubility results, 2-heptanone was initially used as the solvent for preparing casting solution. The concentration remained at 1% w/v and the solution was further mixed in ultrasonic bath before being filtered with 0.2 µm PTFE syringe filters to ensure no particles existing. Silicon wafers with an approximate dimension of 1 cm x 1 cm were cleaned with acetone as well as IPA and baked in 100 °C oven for 5 minutes subsequently prior to spin-coating. After the wafer cooled down and was transferred to the spin-coater, 30 µL of the casting solution was then applied to the middle and an overflow should be avoided. The target thickness was set between 20 to 25 nm for meeting the requirements in the industry. The ellipsometer was utilised for thickness measurement. Different rotational speed and amount of casting solution were employed for thickness comparison. The results were depicted in Figure 7-3.

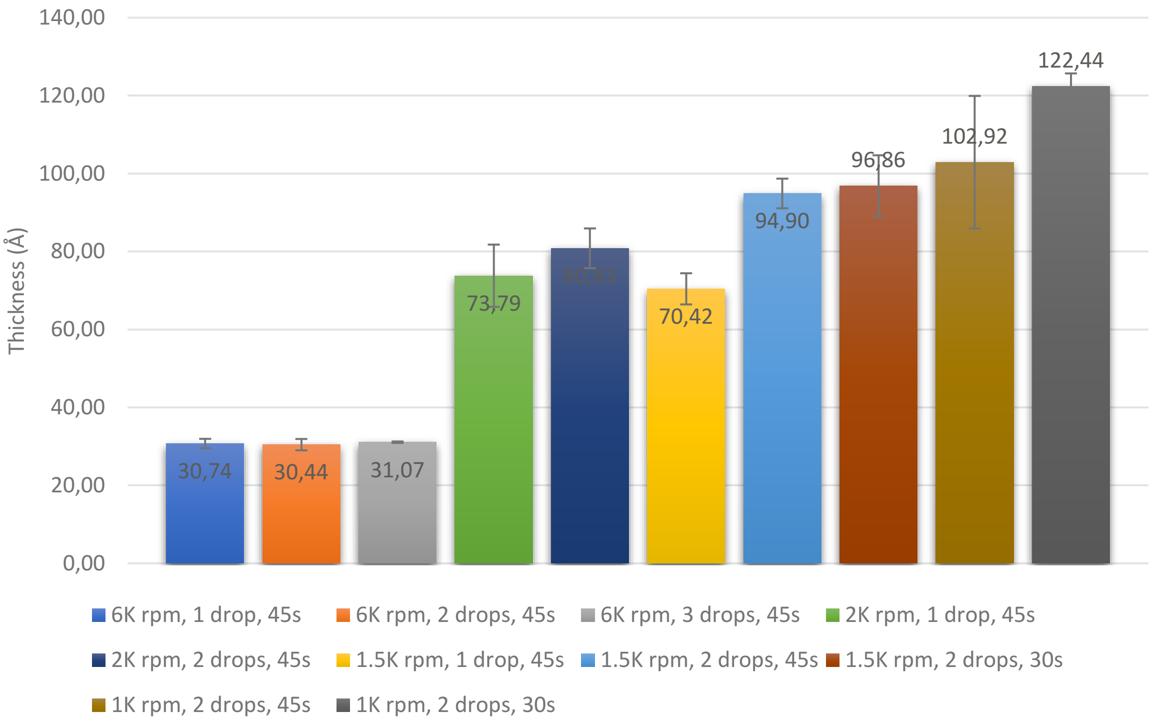

*Figure 7-3: Thickness of $Zr_4O_2(OMc)_{12}$ layer using different spin-coating parameters and 2-heptanone as casting solvent.*

Rotational speed started from 6000 rpm with various amounts of casting solution. Yet the coated layers could only reach 3 nm in thickness. As a result, the rotational speed was reduced to 2000 rpm and 1000 rpm with identical amounts of solution. The highest thickness that could be achieved was only 12 nm, which is far below the target thickness. Moreover, edge effect has also become more significant when the rotational speed went down to 1000 rpm. Edge effect is a common issue taking place in spin-coating process (Figure 7-4). As casting solution being spun from the middle to the edge, the excess material is prone to accumulate at the edge of the substrate, leading to a rough surface close to the edge. Although an additional procedure will be carried out in the industry for cleaning after spin-coating, it is still preferred to control the rugged edges to be as narrow as possible.

Atomic force microscopy (AFM) was employed for examining surface topography of the spin-coated layers at nanoscale (Figure 7-5). Three spots of each silicon wafer sample would be selected, which were the centre point (a), a spot locating in between centre and the edge (b) as well as a spot at the edge of the silicon wafer (c).

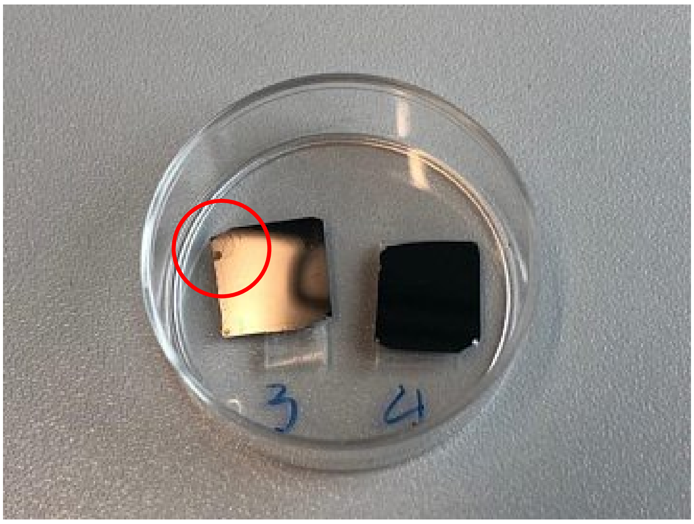

*Figure 7-4: Image of coated silicon wafers with 1000 rpm rotational speed showing severe edge effect.*

In general, the surface of centre area (point a) was relatively flat since it was the point where the casting solution was dropped and the centrifugal force of the spinning helped the solution to disperse towards the edge in a circular trend. The height deviation of each sample was below 5 nm if the large unknown particles were excluded. However, the roughness has gradually become obvious with the decrease in rotational speed. As can be seen from the images in Figure 49, the height deviation of the 1000-rpm sample reached over 200 nm, which is unacceptable for EUV nanopatterning.

Another issue needed to be addressed was the aggregation and striation of the cluster particles. It may be due to the undissolved clusters remaining in the casting solution even after filtration since the size was too small to be observed before spin-coating, which suggests that the solubility of 2-heptanone for $Zr_4O_2(OMc)_{12}$ is possibly not enough and therefore corresponds to the insufficient layer thickness formed.

| **1** | | |
|---|---|---|
| | 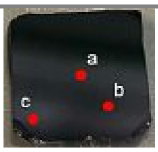 | |
| **1a** | 1b | 1c |
| 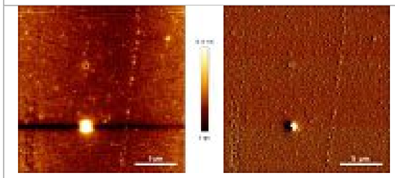 | 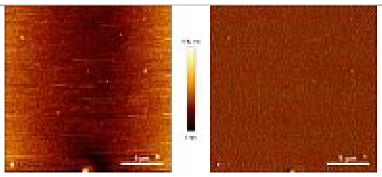 | 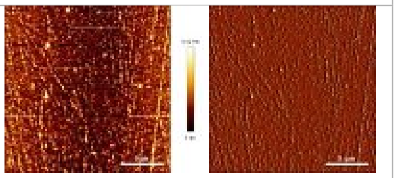 |
| **2** | | |

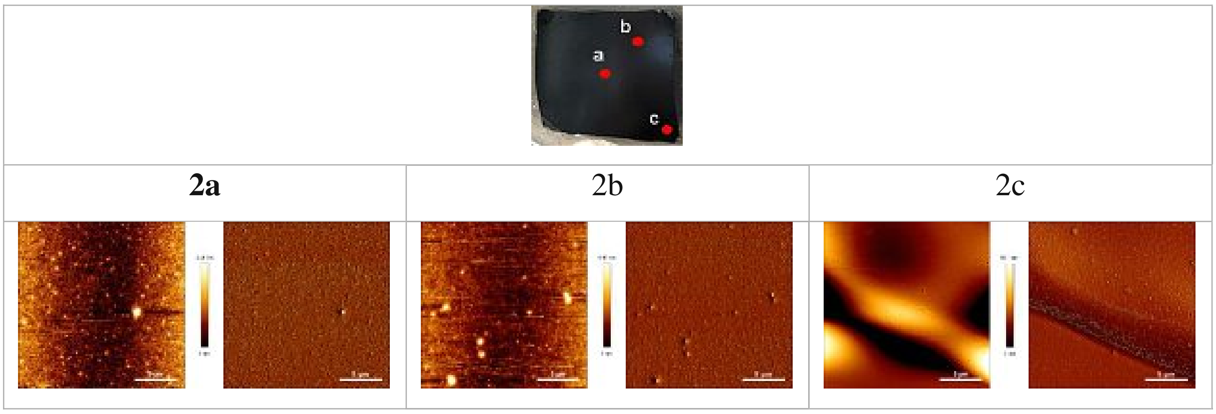

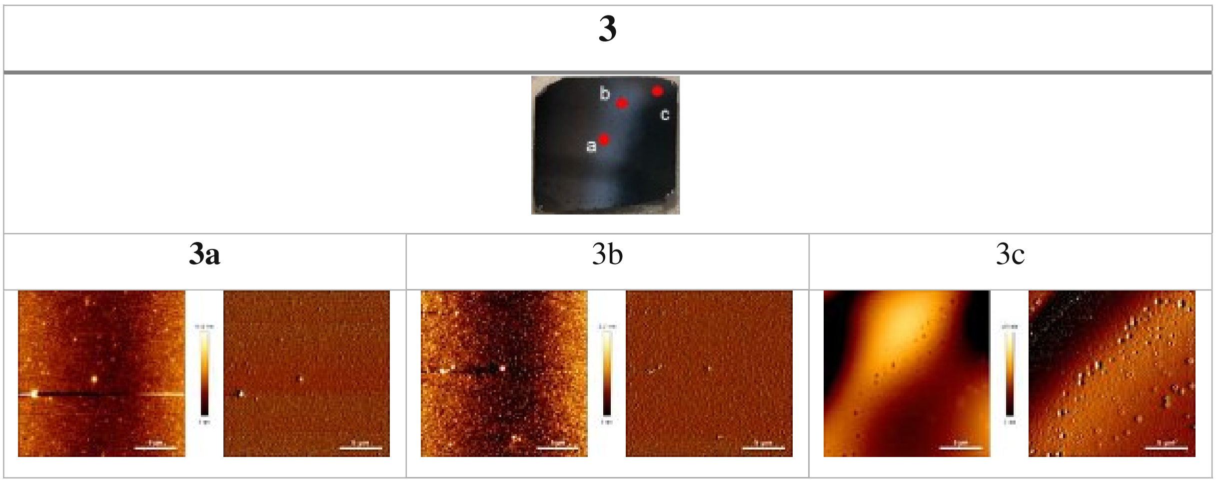

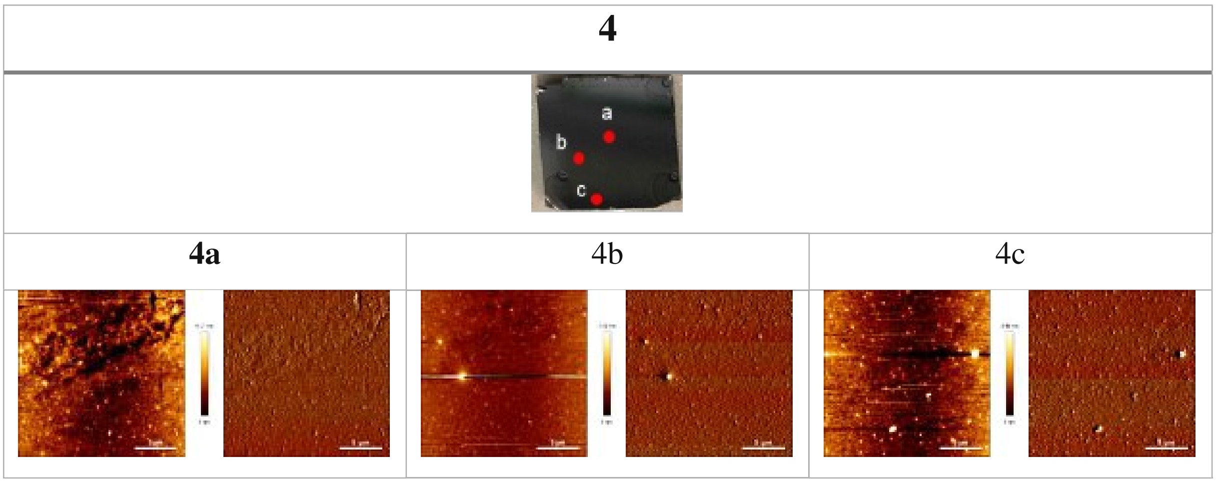

| Sample | Rotating Speed/ rpm | Time/ s | Concentration of Casting Solution |
|---|---|---|---|
| **1** | 2000 | 45 | 1% w/v (in 2-heptanone) |
| **2** | 1500 | 45 | |
| **3** | 1000 | 45 | |
| **4** | 1000 | 30 | |

*Figure 7-5: AFM images of surface topography of $Zr_4O_2(OMc)_{12}$ spin-coated layers with different parameters.*

#### 7.1.2.2 Spin-coating with PGME and PGMEA Mixture as Casting Solvent

The explanation for insufficiency in layer thickness using 2-heptanone as casting solvent was resulted from the deficient solubility 2-heptanone has upon $Zr_4O_2(OMc)_{12}$. Therefore, another casting solvent mixture consisting of PGME and PGMEA (7:3 by volume) was utilised to replace 2-heptanone as the casting solvent for $Zr_4O_2(OMc)_{12}$ cluster. The preparation of casting solution was identical to the abovementioned procedure. Two different rotating speeds (2000 and 1500 rpm) were employed, while the amount of casting solution per sample and coating time remained unchanged. The ellipsometry results (Figure 7-6) revealed that the PGME+PGMEA samples had dramatic increase in layer thickness, both of which could reach above 20 nm. This thickness is more realistic for semiconductor manufacturing.

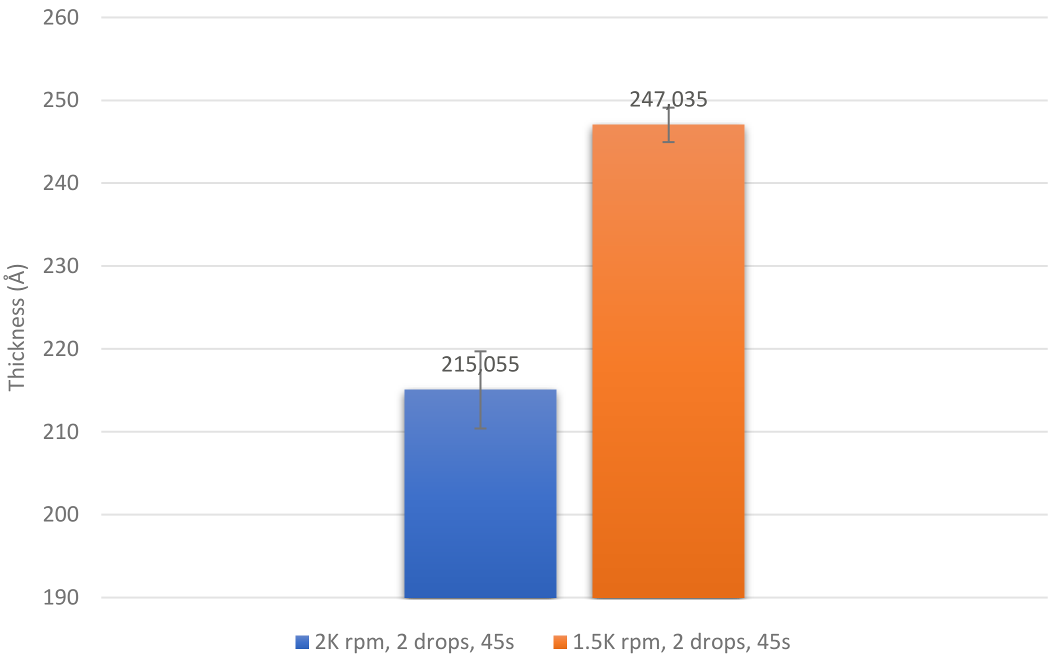

*Figure 7-6: Thickness of photoresist layer using different spin-coating parameters and PGME+PGMEA mixture as casting solvent.*

#### 7.1.2.3 Spin-coating with PGME and Chloroform Mixture as Casting Solvent

The previous results and parameters were provided to the collaboration partners at IMEC for further analysis including contrast curve and outgassing analysis. Nevertheless, they could not get homogeneous coating layers above 25 nm on 4-inch silicon wafers, which stopped them from proceeding to other measurements. Water content of the solvent they employed for preparing the casting solution was considered as the main issue. Since the clusters are prone to hydrolyse and precipitate when encountering water, the concentration will consequently be reduced, leading to a thinner layer. Moreover, the precipitates can also cause inhomogeneity issue attributed to some tiny particles that cannot be removed by syringe filters.

Therefore, to optimise the spin-coating procedure, over 30 different solvents and solvent mixtures were utilized for dissolving the clusters, aiming to reach a higher solubility. Eventually, the mixture of PGME+chloroform (3:2) was chosen to perform as the casting solvent for spin-coating $Zr_4O_2(OMc)_{12}$ and $Ti_4Zr_4O_6(OBu)_4(OMc)_{16}$ from each category (Zr-oxo-clusters and Ti-Zr-oxo-clusters) on 4-inch silicon wafers. The concentration of the casting solution was still set at 1% w/v, trying to reach the target thickness of 30 nm.

Besides spin-coating, a PGME+PGMEA (7:3) solvent mixture was selected after a series of testing, as the developing solvent to strip off the coating layers. The developing process was conducted by spattering 120 mL of developing solvent onto the coating layer with syringes and then rinsing with 20 mL of isopropanol (IPA) before baking the silicon wafer at 150 °C in the oven for 3 minutes.

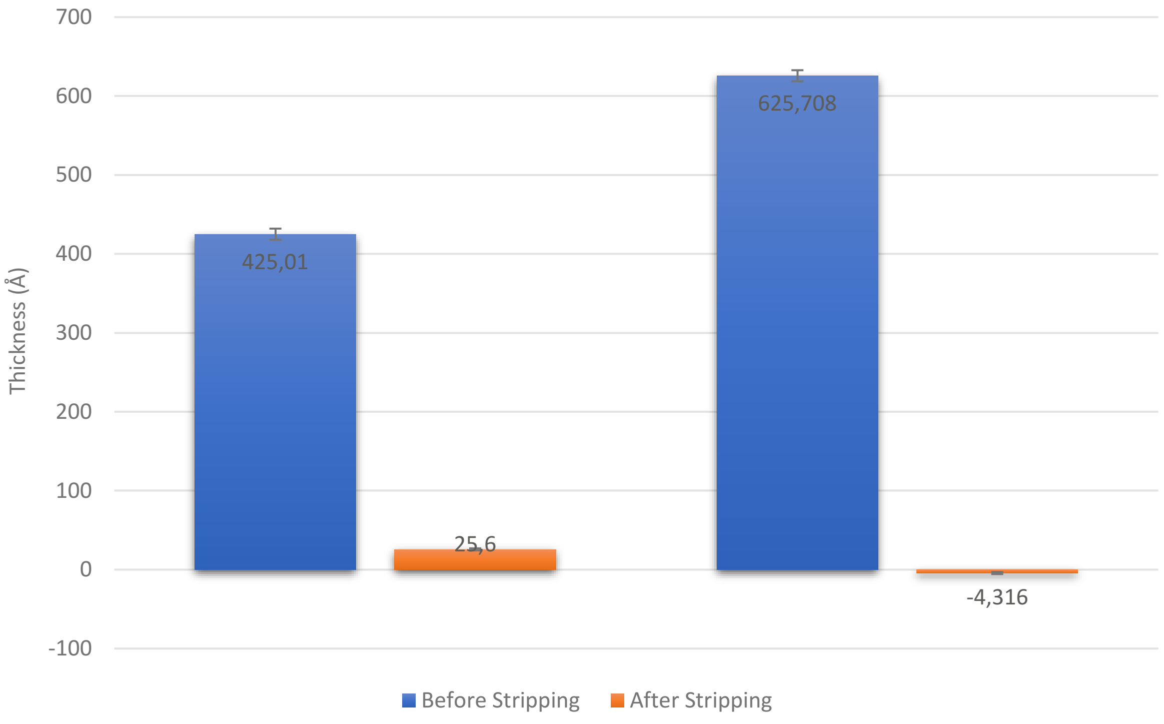

*Figure 7-7: Thickness of coating layers before and after stripping process for $Zr_4O_2(OMc)_{12}$ and $Ti_4Zr_4O_6(OBu)_4(OMc)_{16}$ clusters.*

The results of ellipsometry were depicted in Figure 7-7. Film thicknesses of $Zr_4O_2(OMc)_{12}$ and $Ti_4Zr_4O_6(OBu)_4(OMc)_{16}$ could both reach above 40 nm with high homogeneity on the coating surfaces, which were confirmed by AFM imaging. The minor defects on the coating layers were possibly caused by the evaporation of casting solvent that contained 40% of high volatile chloroform. However, it can be reduced by simply lowering down the chloroform entity within the solvent mixture. In addition, the ellipsometry results also indicated that the coating layers of both clusters could be stripped off almost entirely (over 94%) via PGME+PGMEA (7:3) mixture, exhibiting its potentials as developing solvents for the metal oxo clusters (Figure 7-8).

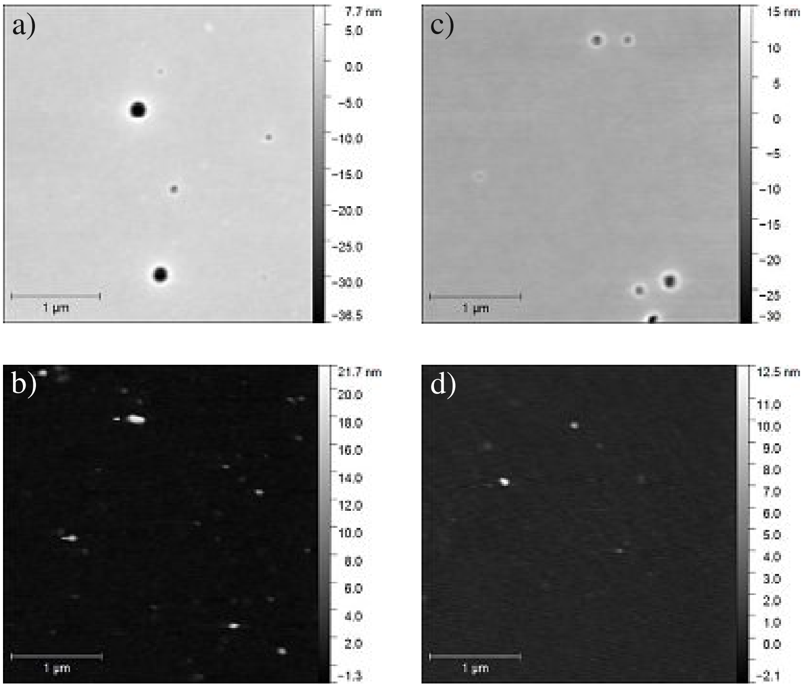

*Figure 7-8: AFM images of $Zr_4O_2(OMc)_{12}$ and $Ti_4Zr_4O_6(OBu)_4(OMc)_{16}$ before (a, c) and after stripping (b, d).*

Despite the parameters were provided to IMEC, they were still unable to develop the pattern using PGME+PGMEA (7:3) mixture since with their facility they could not perform the same developing process. Instead, they were using puddle developing, meaning the silicon wafer was submerged in 30 mL of developer solvent without any mechanical involved before being rinsed by ethanol and baked in the oven. The problem may still be resulted from hydrolysis of the cluster. Once either the material was exposed to air for too long or the water content of the solvents employed was too high, the metal oxo clusters could no longer function properly. Hence, extending durability of these metal oxo clusters has become the top priority.

## 7.2 Approaches for Cluster Sustainability Improvement

Hydrolysis has been the most troublesome issue for many metal-containing resists including the metal oxo clusters synthesised in this work [81]. After forming a thin film, the material yet becomes more sensitive to moisture. Water existing in both ambient environment as well as solvents employed are so hardly avoided that a more realistic option is to improve the lifetime of resist formulation under air atmosphere.

To solve this problem, two different measures were applied for comparing the effect in terms of slowing down or even inhibit the cluster hydrolysis. Bis (2,6-diisopropylphenyl) carbodiimide (BDICDI) is a type of anti-hydrolysis agent that has been commonly-used as additive in biocompatible composite research [82, 83]. The reaction kinetic of hydrolysis can be influenced by these nucleation agents that incline to react with water or other carboxylic groups. Therefore, the oxo clusters themselves can potentially be stabilised for a period of time, giving an appropriate processing window before exposure.

However, there is a concern of using BDICDI as anti-hydrolysis agent. Since it is a relatively bulky nucleation agent and preferably react also with carboxylic group, possibilities are the mechanism of cluster solubility switch would be affected, leading to a deterioration in patterning performance. As a result, another approach was also applied for testing, which employed methacrylic acid to replace BDICDI. Like BDICDI, methacrylic acid has a tendency of reacting with water. But it would be more suitable for this occasion because instead of forming nucleates, methacrylic acid can act as monomer that distributes uniformly within the resist materials and then be part of the composition in the resulted crosslinked network. The lithographic performance in the end would not be affected too significantly.

For comparing the anti-hydrolysis effects, both measures were tested using $Zr_4O_2(OMc)_{12}$ as resist materials and a pure $Zr_4O_2(OMc)_{12}$ thin film sample was also made. The casting solution were prepared via previous procedure and parameters yet the casting solution was changed from PGME+$CHCl_3$ (3:2) to toluene for excluding the influence of moisture since chloroform is prone to contain water. 0.01 g of $Zr_4O_2(OMc)_{12}$ was dissolved in 1 mL of dry toluene with additional 20% w.t. (relative to the weight of resist material employed) of dry methacrylic acid and BDICDI, respectively. The solutions were mixed in ultrasonic bath for 5 minutes and filtered before being spin-coated on 2 cm x 2 cm silicon wafers at 2000 rpm for 45 seconds. The film thickness measured by ellipsometer reached 30 nm for each sample.

IR-spectrometer was utilised to monitor the material variation with respect to time. The sample was simply exposed to air and measured after specific intervals. Results of the three different formulations were depicted in Figure 7-9. As can be observed in the pure $Zr_4O_2(OMc)_{12}$ spectra, the peak at 3100 to 3500 $cm^{-1}$, which is the response of OH-stretching, kept on increasing after it was exposed to air. The integral of the peak at 3600 seconds was about ten times higher than that at 0 second, indicating the water absorption of pure $Zr_4O_2(OMc)_{12}$ was quite fast and therefore leads to the cluster degradation.

On the other hand, the addition of methacrylic acid as well as BDICDI have effectively suppressed the hydrolysis issue, showing no OH response even after one hour. The only obvious change in the two spectra was resulted from O=C=O stretching, which is reasonable considering the time they were exposed and the influence of ambient carbon dioxide. These results have revealed the potential application of both methacrylic acid and BDICDI being employed as anti-hydrolysis agent for the metal oxo clusters. Nevertheless, given the fact that BDICDI tends to form nucleates within the system, methacrylic acid approach will be the primary option for lithographic trials afterwards.

a) Pure $Zr_4O_2(OMc)_{12}$

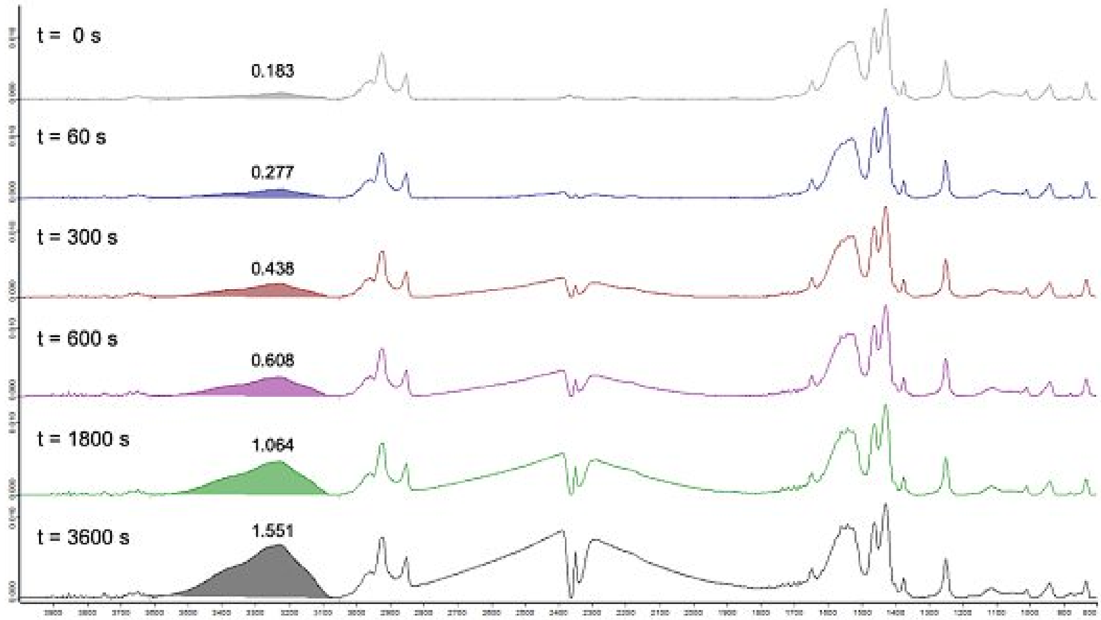

b) $Zr_4O_2(OMc)_{12}$ with 20% w.t. Methacrylic Acid

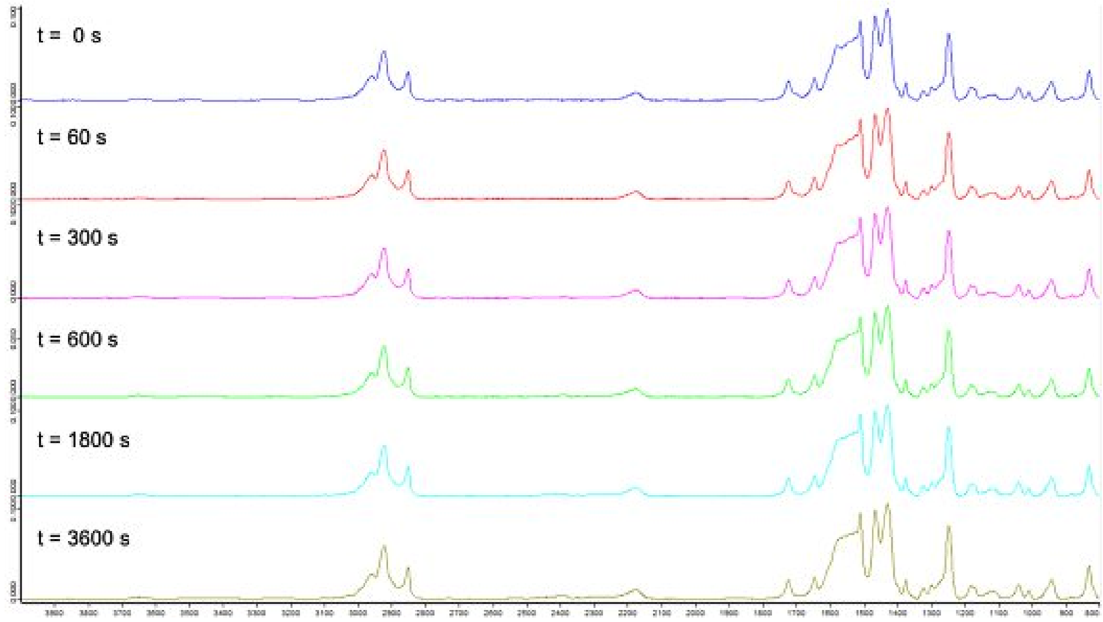

c) $Zr_4O_2(OMc)_{12}$ with 20% w.t. BDICDI

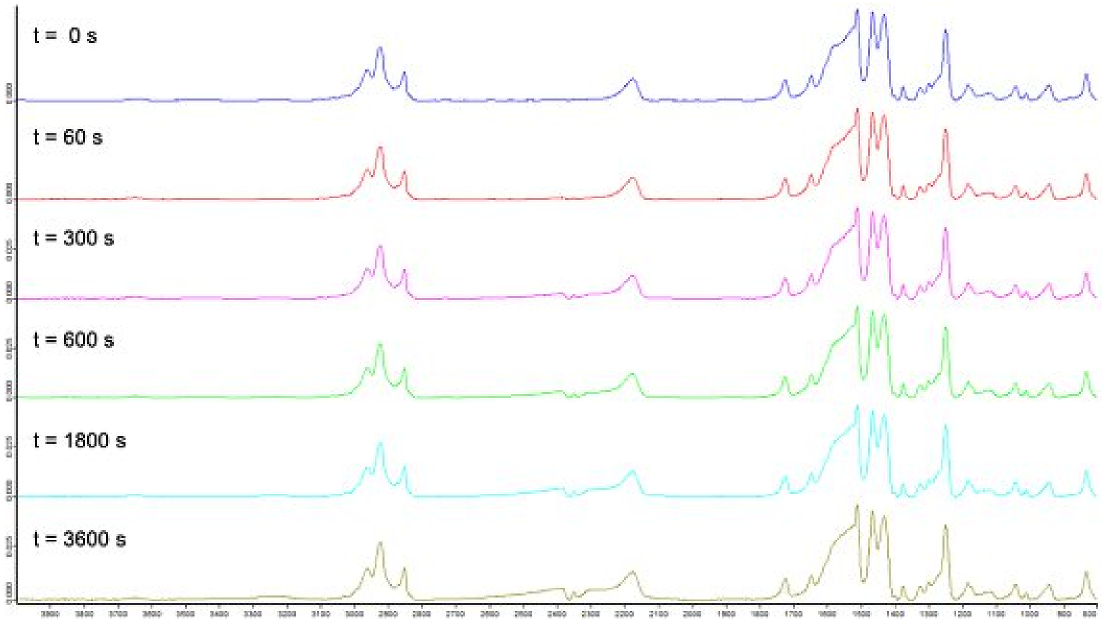

*Figure 7-9: Thin-film IR spectra of a) pure $Zr_4O_2(OMc)_{12}$ b) $Zr_4O_2(OMc)_{12}$ with 20% w.t. methacrylic acid and c) $Zr_4O_2(OMc)_{12}$ with 20% w.t. BDICDI at t=0, 60, 300, 600, 1800 and 3600 seconds.*

## 7.3 Determination of Coatability and Developability (Conducted at ARCNL)

Since methacrylic acid was added to the formulations as an anti-hydrolysis agent, the casting solvents and developers were required to be re-defined in order to achieve homogeneous topography as well as reasonable film thicknesses. Some specifically targeted solvents were tested again for their compatibility with new metal oxo cluster formulations before being employed for spin-coating with identical parameters as previously used.

The casting solvents and developers utilised for the metal oxo clusters should reach a certain dry condition for preventing materials from hydrolysis (water content below 15 ppm via Karl Fischer titration). Sample preparation for spin-coating was performed inside the glovebox. The casting solution was filtered using 0.2 µm syringe filters after mixing in the ultrasonic bath and sealed in a clean sample vial. The silicon wafers were pre-treated with base piranha solution for cleaning and 120 µL of the casting solution was required for a 1 cm x 1 cm wafer. Piranha solution employed was a mixture of hydrogen peroxide (30%) and ammonium hydroxide (28-30%), which can clean organic materials from wafers and oxidize most metals. Before adding the solution, the silicon wafer was heated at 150 °C for 60 s to remove moisture. Spin-coating was initiated immediately after the wafer cooled down by nitrogen flow, with a rotation speed at 2000 rpm for 45 s. The coated wafers were kept under inert atmosphere constantly before being analysed or patterned. Table 7 listed the specific casting solvents and developers (explain in the later chapters) for each metal oxo clusters, which were actually used for the following DUV, E-beam, and EUV lithography.

*Table 7: List of casting solvents and developer for each metal oxo cluster.*

| Materials | Casting Solvent | Developer |
|---|---|---|
| **$Zr_4O_2(OMc)_{12}$** | Toluene and PGME (4:1 by volume) | Chloroform and EtOAc (3:1 by volume) |
| **$Zr_4O_2(OPiv)_{12}$** | Toluene and PGME (4:1 by volume) | N/A |
| **$Zr_4O_2(OMc)_x(OPiv)_{12-x}$ (x=3, 6, 9)** | Toluene and PGME (4:1 by volume) | Chloroform |
| ***$Zr_4O_2(OVinac)_{12}$** | Toluene and PGME (4:1 by volume) | Chloroform and EtOAc (3:1 by volume) |
| ***$Zr_4O_2(ODiMc)_{12}$** | Toluene and PGME (4:1 by volume) | Chloroform and EtOAc (3:1 by volume) |
| **$Zr_{12}O_8(OH)_8(OMc)_8(OAc)_{16} \cdot 6HOAc$** | Toluene | Chloroform |
| **$Hf_4O_2(OMc)_{12}$** | Toluene and PGME (4:1 by volume) | Chloroform and EtOAc (3:1 by volume) |
| **$Ti_4Zr_4O_6(OBu)_4(OMc)_{16}$** | PGME and Chloroform (3:2 by volume) | Chloroform and EtOAc (1:3 by volume) |
| **$Ti_2Zr_4O_4(OBu)_2(OMc)_{14}$** | PGME and Chloroform (3:2 by volume) | Chloroform and EtOAc (1:3 by volume) |
| **$Ti_4Zr_2O_4(OBu)_6(OMc)_{10}$** | PGME and Chloroform (3:2 by volume) | Chloroform and EtOAc (1:3 by volume) |

| | | |
|---|---|---|
| *** $Ti_4Hf_4O_6(OBu)_4(OMc)_{16}$** | PGME and Chloroform (3:2 by volume) | Chloroform and EtOAc (1:3 by volume) |
| ***$Ti_2Zr_5HfO_6(OMc)_{20}$** | PGME and Chloroform (3:2 by volume) | Chloroform and EtOAc (1:3 by volume) |

**Casting and developing solvents were determined after ARCNL secondment at TU Wien*

A J.A. Woollam VB-400 variable angle spectroscopic ellipsometer (VASE) was initially utilised to measure the thickness of spin-coated thin-film materials on the silicon wafer. Nevertheless, due to the fact that the optical constants of the metal oxo clusters are unknown, the result from ellipsometry had a significant deviation. Therefore, AFM was employed eventually for thickness measurement by scanning the notches made purposely on different parts of the silicon wafer surface (Figure 7-10).

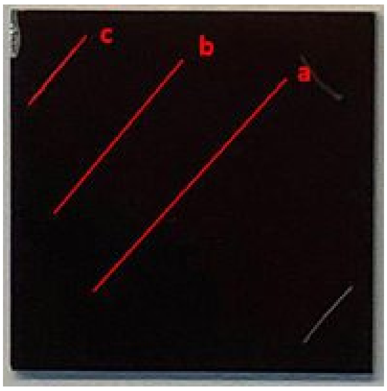

*Figure 7-10: Notch positions on a silicon wafer.*

The results of film thickness for each metal oxo cluster were depicted in Figure 7-11. The coated films could all reach above 20 nm, which are sufficient for nano-patterning and Critical Dimension Scanning Electron Microscopy (CD-SEM) imaging. Besides, the deviation of thickness in the centre and edge of the silicon wafer was relatively small, indicating the surface finish was homogeneous.

However, $Zr_4O_2(OPiv)_{12}$ cluster failed to form a thin film on silicon wafer attributed to low solubility issue of the pivalate clusters that resulted in a very rough surface. Furthermore, some of the clusters had not been synthesised including $Zr_4O_2(OVinac)_{12}$, $Zr_4O_2(ODiMc)_{12}$, $Ti_4Hf_4O_6(OBu)_4(OMc)_{16}$ and $Ti_2Zr_5HfO_6(OMc)_{20}$ by the time these experiments were conducted at ARCNL. These metal oxo clusters consequently did not proceed to DUV exposure as well as E-beam patterning stage.

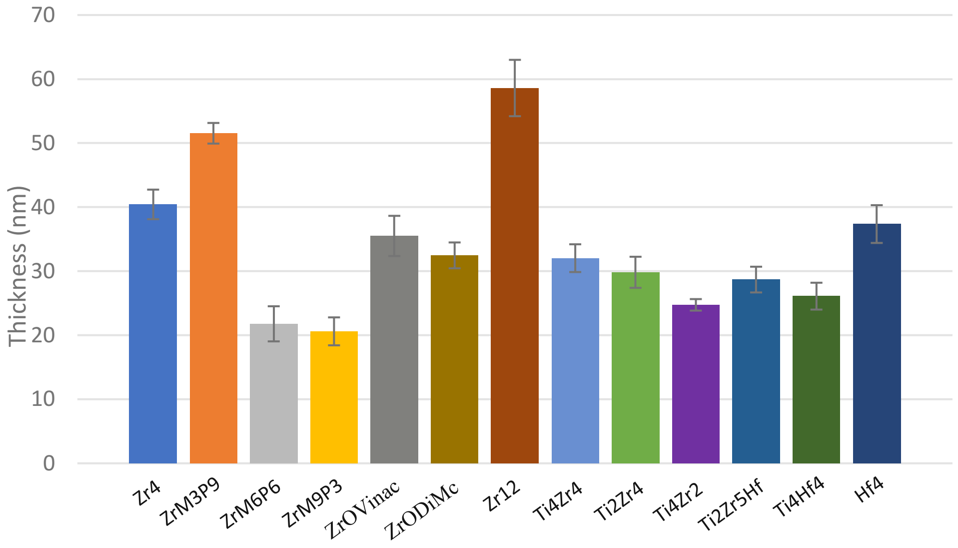

*Figure 7-11: AFM results for thickness measurements of the thin-film materials.*

### 7.3.1 UV/Vis Spectroscopy for Defining Developers

UV/Vis spectroscopy in this work has been employed for different objectives. A time-resolved femtosecond transient spectroscopy was originally planned within the secondment structure at ARCNL. Since the wavelength of the laser implemented for the setup was at 266 nm, the clusters should have high absorption at this wavelength for providing sufficient signal response. To evaluate the material capability, UV/Vis measurement on saturated solution sample was carried out. Furthermore, a more diluted set of cluster solutions were prepared in order to examine the consistency between the solution phase and thin film on quartz plate. Interaction of material with quartz plate surface could possibly result in a variation of absorption, which is able to be revealed via UV/Vis spectroscopy.

The other two applications were more related to patterning and material durability. Solvents were tested for their ability to strip off coated films from quartz plates. The stripping procedure was meant to simulate developing step after light exposure and therefore conducted via the puddle approach. By comparing the signals in UV/Vis spectrum before and after development, the appropriate developer can then be defined for each metal oxo cluster. Last part of UV/Vis analysis was focused on the study of thin-film material degradation. Apart from $Zr_4O_2(OMc)_{12}$, the other metal oxo clusters had not yet been tested in terms of sustainability. Through monitoring the deviation of signal response, it enables the understanding of material degradation behaviour as a function of time, providing a general overview on determining process window of each cluster.

#### 7.3.1.1 Solution Phase

As mentioned, the solution samples for UV/Vis spectroscopy were divided into two categories, saturated and diluted, for different research purposes. The saturated sample was prepared by dissolving 0.01g of the metal-oxo-cluster in 1 mL of anhydrous isopropanol, leading to a concentration of 1% w/v, while the diluted sample was obtained via mixing 0.1 mL of saturated solution with 10 mL of anhydrous IPA for a concentration of 0.01%. The measurement was performed via a Shimadzu UV2700 spectrophotometer.

**Saturated Solution**

Measurements for saturated samples were performed on the chosen metal-oxo-clusters including $Zr_4O_2(OMc)_{12}$, $Ti_4Zr_4O_6(OBu)_4(OMc)_{16}$, $Ti_2Zr_4O_4(OBu)_2(OMc)_{14}$, $Ti_4Zr_2O_4(OBu)_6(OMc)_{10}$, and $Hf_4O_2(OMc)_{12}$. UV/Vis spectroscopy on high concentration solution can reveal the potential of the materials being excited at 266 nm with sufficiently high absorbance, which is beneficial for the femtosecond transient spectroscopy analysis. The wavelength range was set from 450 nm to 205 nm due to the cut-off threshold for IPA at 205 nm.

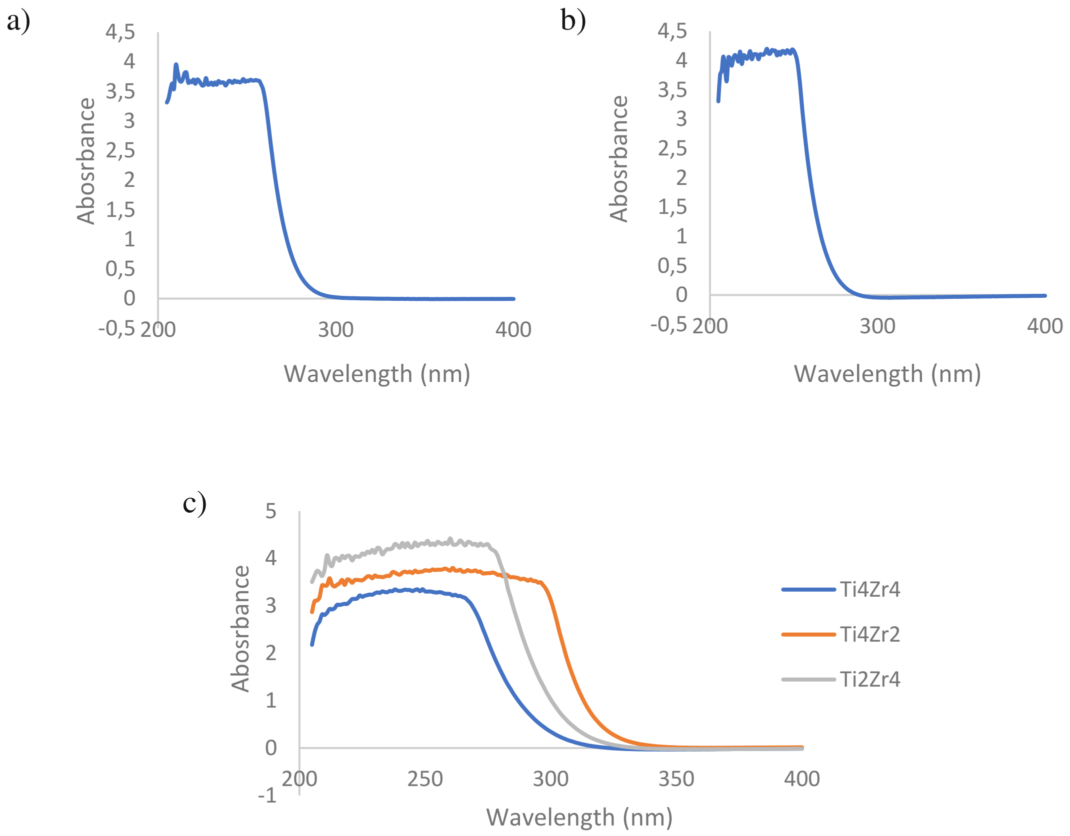

*Figure 7-12: UV/Vis spectra of saturated solutions of a) $Zr_4O_2(OMc)_{12}$, b) $Hf_4O_2(OMc)_{12}$ and c) Ti-Zr Clusters.*

The results in Figure 7-12 showed that clusters containing titanium atom essentially have higher absorptions compared with those of zirconium and hafnium clusters, which is mainly resulted from the orbital interactions. Via computational modelling from the metal-oxo-cluster structures, a strong interaction between the d orbital of titanium and the lone pair on p orbital of the oxygen on methacrylate ligand has been discovered, meaning electrons were able to be excited from the highest occupied molecular orbital (HOMO) of methacrylate ligands to the lowest unoccupied molecular orbital (LUMO) and therefore showed a lower excitation energy. Zirconium and hafnium, on the other hand, have relatively weak or no interaction with methacrylate ligands since the difference between energy level of the orbitals is too considerable. As a result, the femtosecond transient spectroscopy will be carried out primarily on the three Ti-Zr clusters.

## Diluted Solution

UV/Vis spectroscopy on diluted solutions was conducted on all the metal-oxo-clusters obtained at that time. Diluted sample measurement is more favourable for providing characteristic absorption of individual material, giving the highest absorbance at specific wavelength. Despite of $Zr_4O_2(OPiv)_{12}$ and $Zr_{12}O_8(OH)_8(OMc)_8(OAc)_{16} \cdot 6HOAc$ showing an unreasonable behaviour to the negative absorbance, which might be resulted from the dirty quartz cuvette employed, the other metal-oxo-clusters have absorption bands at approximately 250 nm, as shown in Figure 7-13. The onset of Ti-Zr clusters was slightly higher than those of zirconium and hafnium clusters as explained previously, which is correspond to the result of saturated samples. High absorption of the clusters below 250 nm is also an advantage for them to be utilised as the photoresist for DUV and EUV in terms of nanofabrication, which helps to increase the sensitivity towards the patterning.

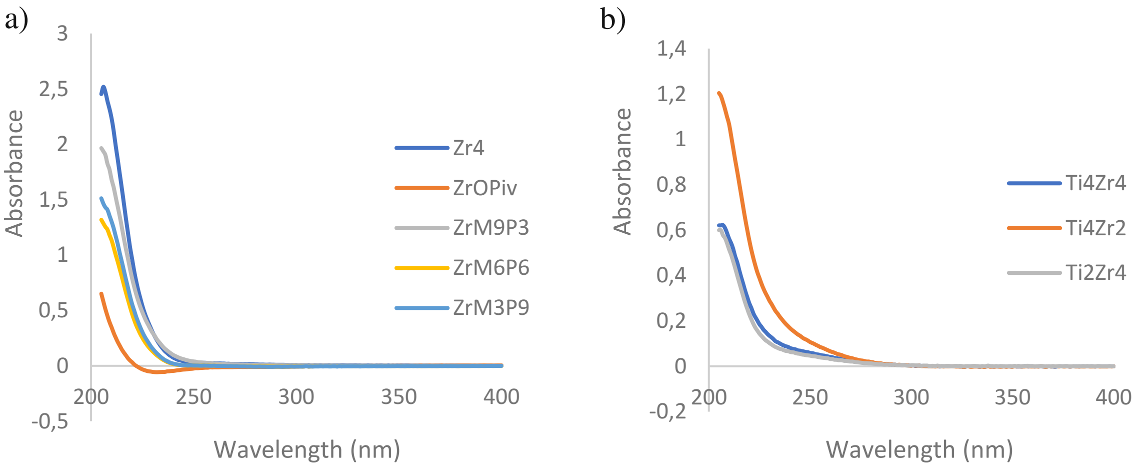

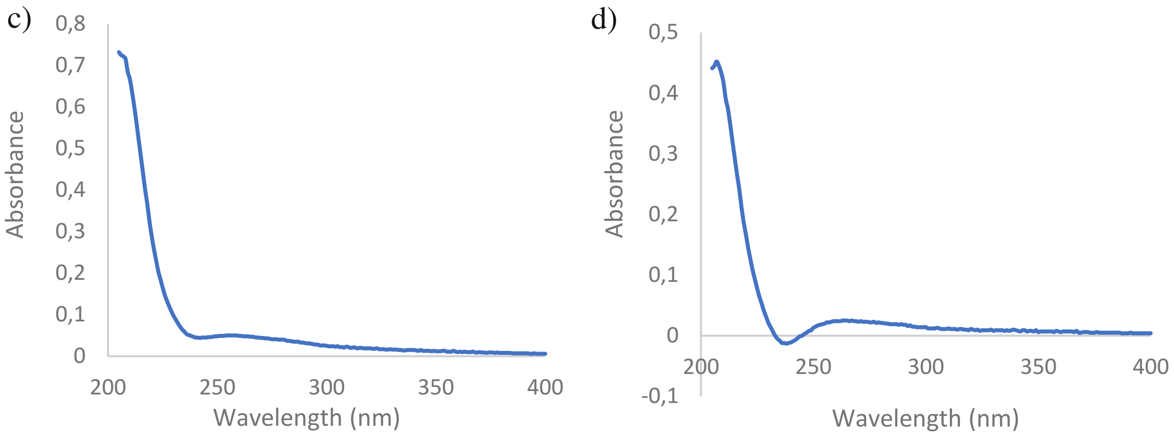

*Figure 7-13: UV/Vis spectra of diluted solutions of a) $Zr_4O_2(OMc)_x(OPiv)_{12-x}$ (x=0, 3, 6, 9, 12), b) Ti-Zr Clusters, c) $Hf_4O_2(OMc)_{12}$ and d) $Zr_{12}O_8(OH)_8(OMc)_8(OAc)_{16}\cdot 6HOAc$.*

### 7.3.1.2 Thin Film

Thin-film UV/Vis spectroscopy on quartz plate can provide a solid evidence in terms of coatability and developability of the metal-oxo-clusters on silicon wafer, which was also conducted via a Shimadzu UV2600 spectrophotometer. Quartz plates employed were treated with the same piranha cleaning procedure for silicon wafers in order to remove the organic layer or impurities on the surface.

Preparation for thin films was identical as those employed for film thickness analysis. A 1% w/v casting solution was made for each material and spin-coated at 2000 rpm on a quartz plate to form a thin layer with film thickness above 20 nm. The developing test was carried out by immersing the quartz plates in respective developer of each cluster (Table 7) for 60 s before being blown dry with nitrogen. Most of the metal-oxo-clusters showed significant developability in their developer with just one exception, the $Zr_4O_2(OPiv)_{12}$ cluster. Since the solubility of $Zr_4O_2(OPiv)_{12}$ is quite low, it did not have a sufficiently thick layer after the spin-coating and showed literally no contrast after developing (Figure 7-14).

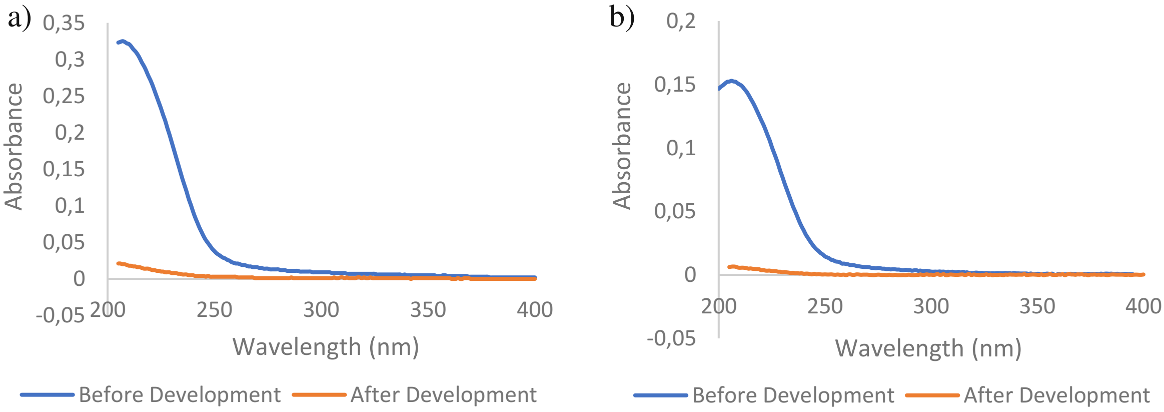

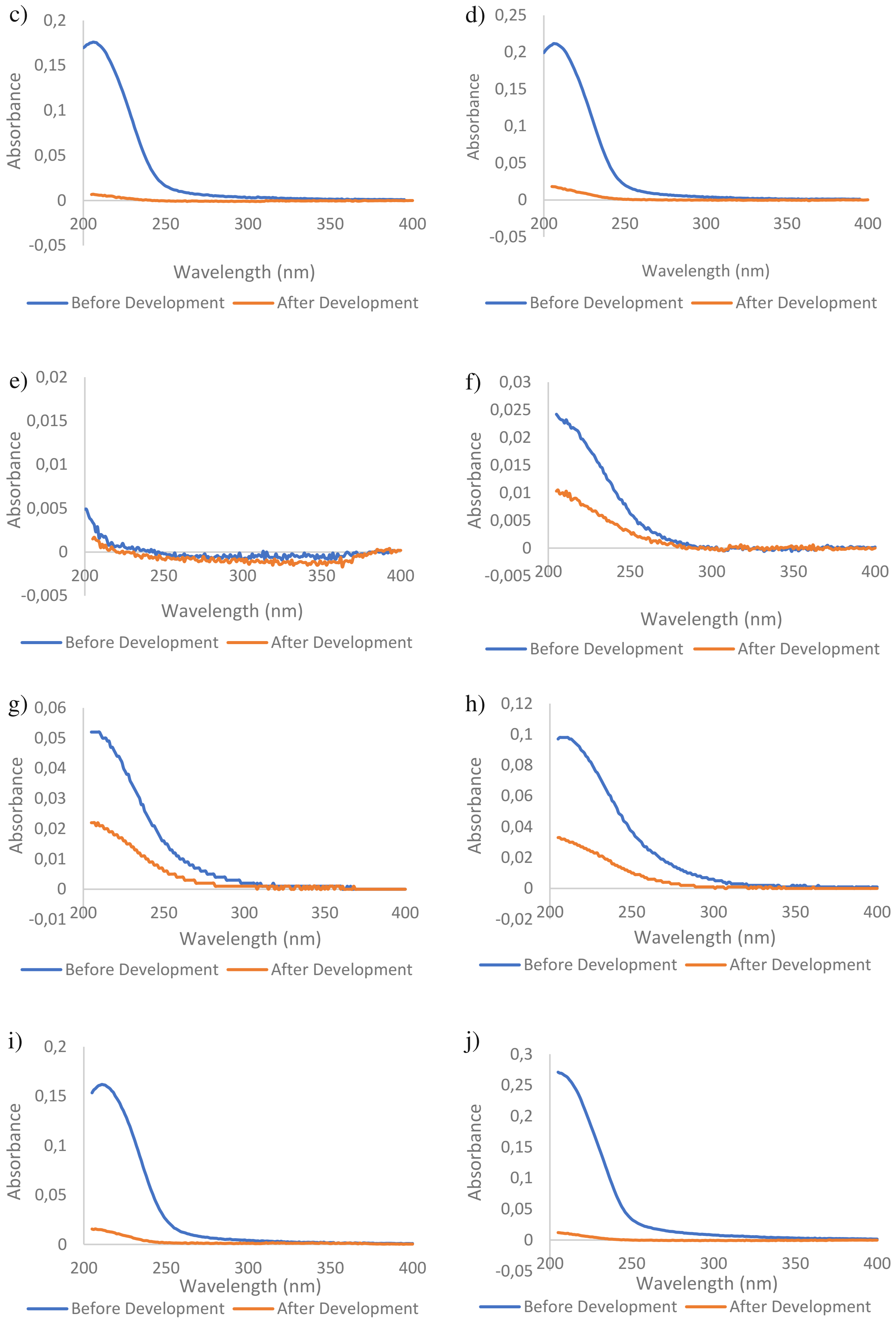

*Figure 7-14: UV/Vis spectra of thin-film materials a) $Zr_4O_2(OMc)_{12}$ with 20% w.t. methacrylic acid, b) $Zr_4O_2(OMc)_3(OPiv)_9$, c) $Zr4O2(OMc)_6(OPiv)_6$, d) $Zr_4O_2(OMc)_9(OPiv)_3$, e) $Zr_4O_2(OPiv)_{12}$, f)*

*$Ti_4Zr_4O_6(OBu)_4(OMc)_{16}$ with 20% w.t. methacrylic acid, g) $Ti_2Zr_4O_4(OBu)_2(OMc)_{14}$ with 20% w.t. methacrylic acid, h) $Ti_4Zr_2O_4(OBu)_6(OMc)_{10}$ with 20% w.t. methacrylic acid, i) $Hf_4O_2(OMc)_{12}$ with 20% w.t. methacrylic acid and j) $Zr_{12}O_8(OH)_8(OMc)_8(OAc)_{16}\cdot 6HOAc$ on quartz plates before and after development.*

### 7.3.1.3 Degradation Test via Thin-Film UV/Vis Spectroscopy

Most of the metal-oxo-clusters are prone to hydrolysis under ambient atmosphere. To determine the stability of the materials for providing a proper process window, a degradation test has been performed simply by exposing the coated quartz plates under air and monitoring via UV/Vis spectroscopy (Figure 7-15).

10%-20% of the metal-oxo-clusters degraded or hydrolysed within 30 minutes as indicated in the results. Despite of inevitability of hydrolysis, the spin-coated silicon wafers should be able to be loaded into the track at PSI for EUV exposure with a minor hydrolysed content. But line-edge roughness and resolution might be affected in the end. The possible reason why the metal-oxo-clusters are sensitive to air might arise from the size of the material. For comparison, as $Zr_6(OH)_4O_4(OMc)_{12}$ has a longer lifetime under air, the smaller pure $Zr_4O_2(OMc)_{12}$ starts to hydrolyse severely after 5 minutes. It is likely the higher surface tension and smaller bond angle make it so unstable that it disintegrates when being confronted by moisture. Nevertheless, this hypothesis still requires more experimental evidence to be confirmed. It is therefore recommended to keep the spin-coated silicon wafers under inert atmosphere before loading samples for obtaining better results.

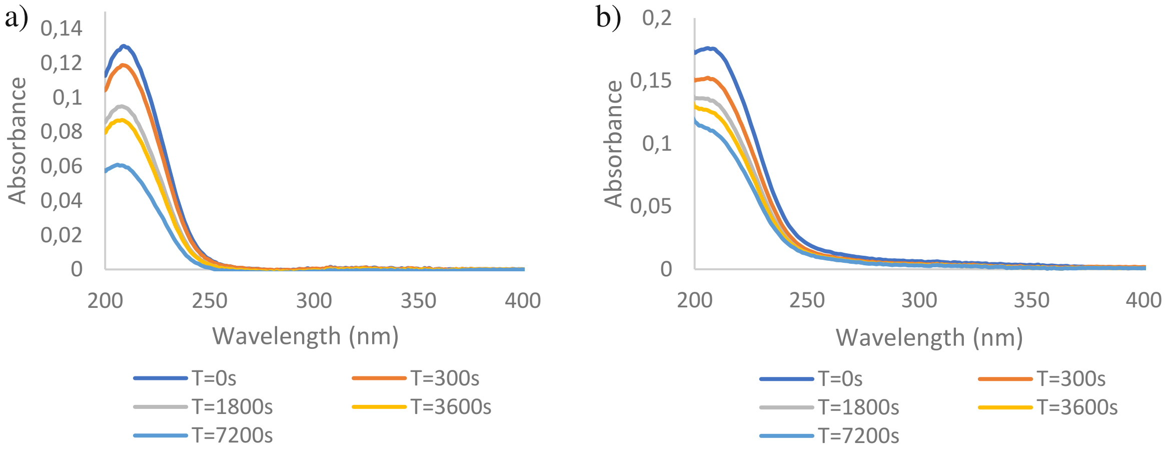

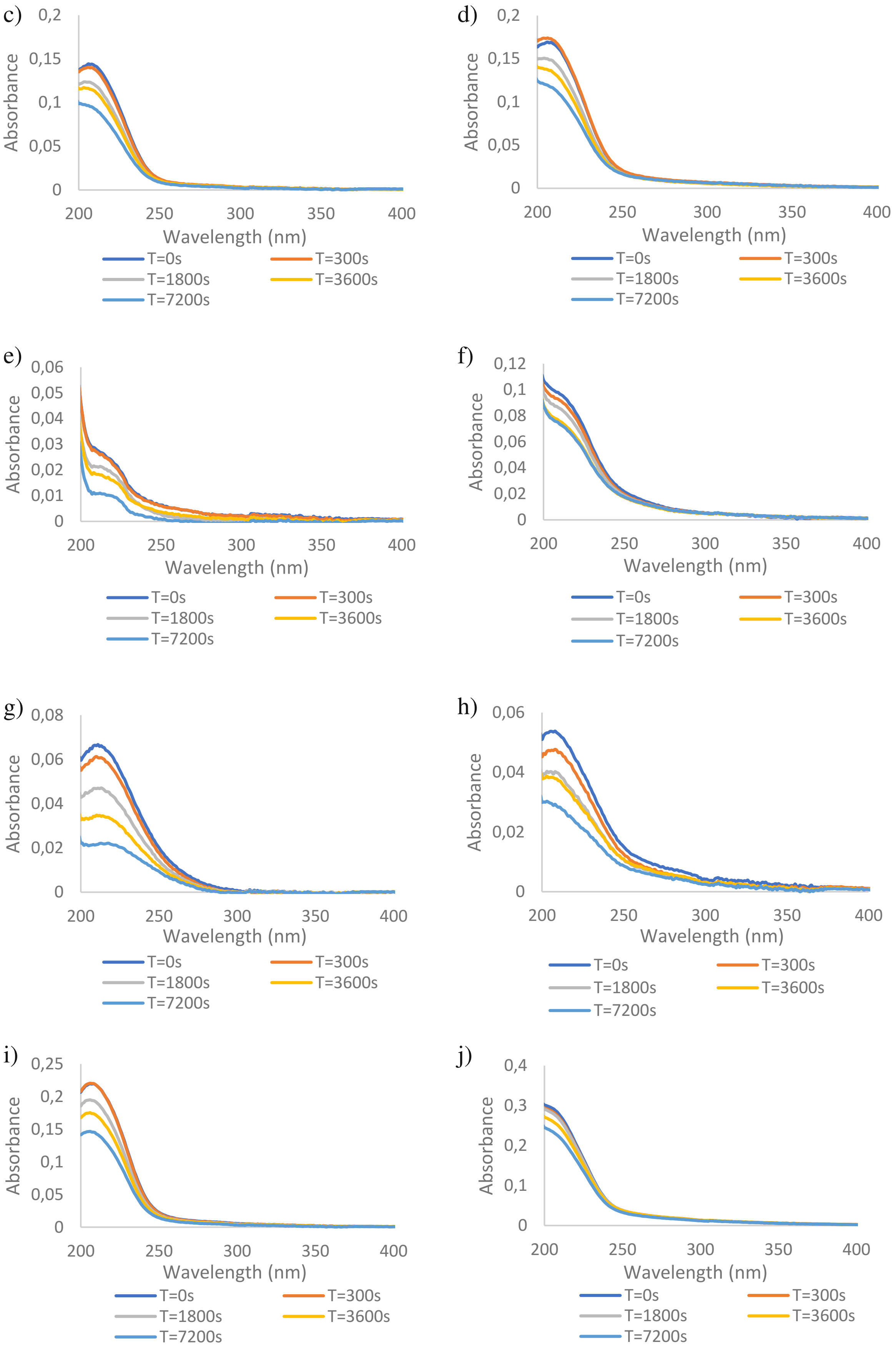

*Figure 7-15: UV/Vis spectra of the thin-film a) $Zr_4O_2(OMc)_{12}$ with 20% w.t. methacrylic acid, b) $Zr_4O_2(OMc)_3(OPiv)_9$, c) $Zr4O2(OMc)_6(OPiv)_6$, d) $Zr_4O_2(OMc)_9(OPiv)_3$, e) $Zr_4O_2(OPiv)_{12}$, f)*

*$Ti_4Zr_4O_6(OBu)_4(OMc)_{16}$ with 20% w.t. methacrylic acid, g) $Ti_2Zr_4O_4(OBu)_2(OMc)_{14}$ with 20% w.t. methacrylic acid, h) $Ti_4Zr_2O_4(OBu)_6(OMc)_{10}$ with 20% w.t. methacrylic acid, i) $Hf_4O_2(OMc)_{12}$ with 20% w.t. methacrylic acid and j) $Zr_{12}O_8(OH)_8(OMc)_8(OAc)_{16}\cdot 6HOAc$ under ambient atmosphere for up to 2 hours.*

### 7.3.2 Preliminary DUV Exposure

The interaction between EUV photons and photoresist material is much more complicated in detail. Nevertheless, if the solubility switch of a material can be triggered by DUV, there is a high possibility that the resist material can also work via a EUV source. DUV exposure is also beneficial in terms of determining proper developers for different metal oxo clusters. Some solvents like isopropanol are so hydrophilic that can remove both exposed and unexposed metal oxo clusters, leaving no patterns after development. A good developer should have a clear solubility margin for exposed and unexposed materials so as to separate completely the two phases. As a result, the DUV exposure can ideally leave a feature on the surface of a silicon wafer after being developing with the selected solvent. It was reckoned as a crucial indication in this work before proceeding to the actual E-beam lithographic patterning.

A YAG-pumped OPA laser (Ekspla NT342B), delivering nanosecond pulses at 225 nm at 10 Hz (2.5 mJ/pulse), was used as the irradiation source. The metal-oxo-clusters including $Zr_4O_2(OMc)_{12}$, $Zr_4O_2(OMc)_6(OPiv)_6$, $Ti_2Zr_4O_4(OBu)_2(OMc)_{14}$, $Ti_4Zr_2O_4(OBu)_6(OMc)_{10}$ and $Hf_4O_2(OMc)_{12}$ were spin-coated on 1 cm x 1 cm pre-treated silicon wafers beforehand with the same parameters as employed previously and installed in a special sample holder respectively with constant nitrogen flow (Figure 7-17). DUV laser was irradiated on the surface of the wafer with a dose of 1.4 J/cm$^2$ without a photomask. The samples were then developed via being immersed in 20 mL of dry developer for 60 seconds. The exposed feature can be clearly observed on every cluster sample tested by eyes as shown in Figure 7-16. SEM imaging also revealed a flat surface finish after development on both the exposed and unexposed areas.

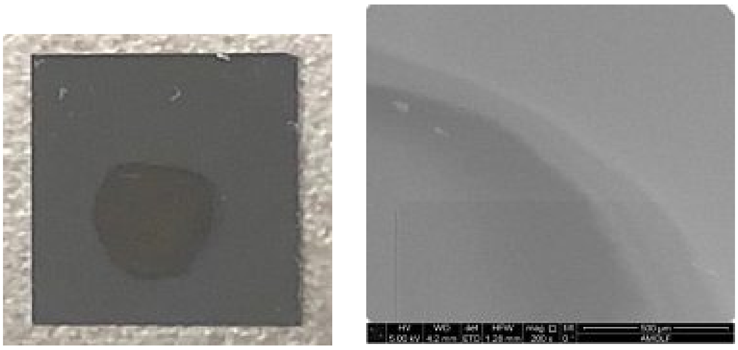

*Figure 7-16: Photo and SEM image of DUV-irradiated $Zr_4O_2(OMc)_{12}$ on a silicon wafer.*

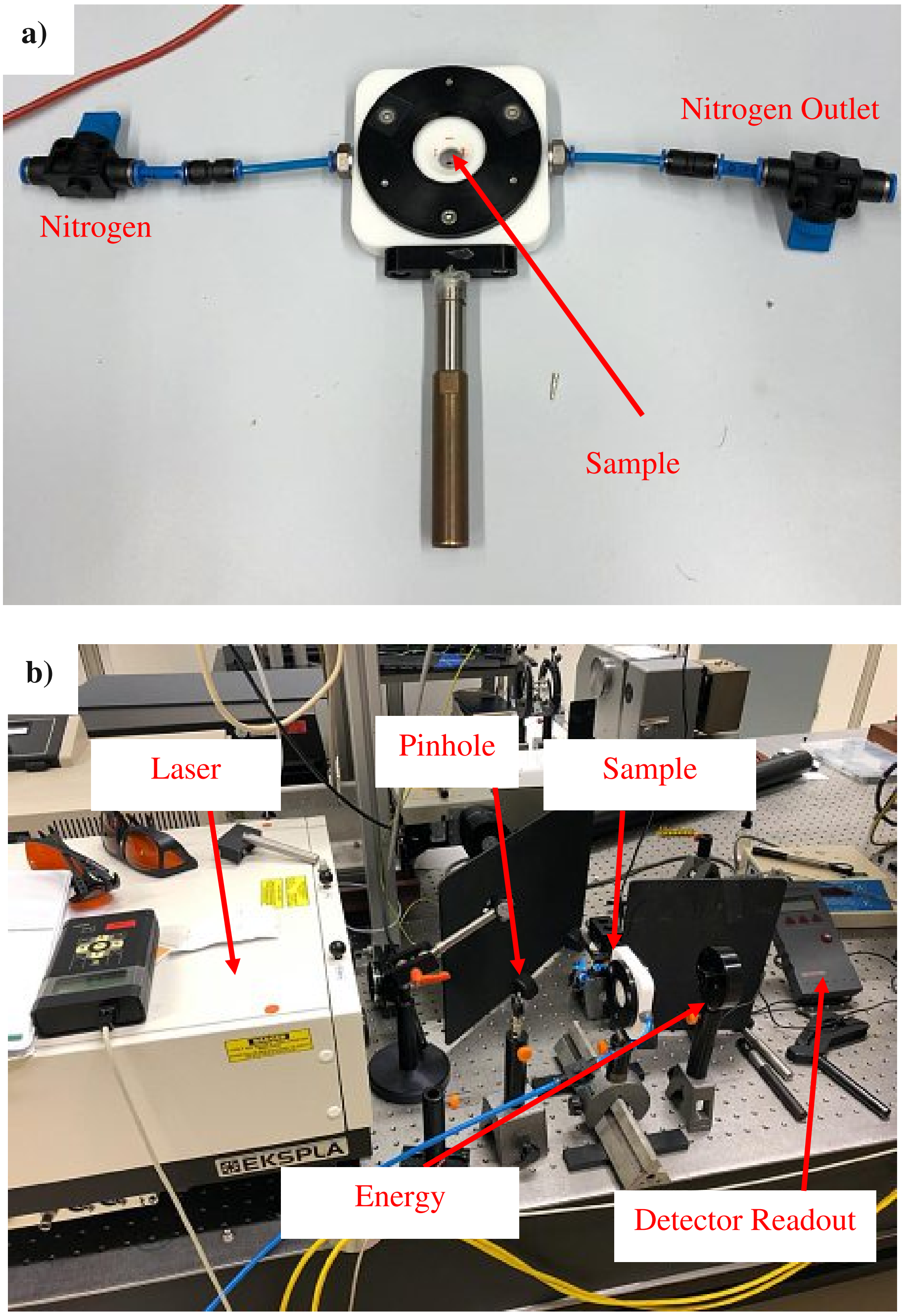

*Figure 7-17: a) Gas-purging sample holder; b) DUV laser setup (located at Spectroscopy and Photonic Materials laboratory at University of Amsterdam).*

## 7.4 Summary

In order to determine coatability and developability as well as define process conditions, multiple experiments have been conducted in sequence. Initially, various organic solvents were tested their solubility for the metal oxo clusters in the cause of spin-coating. Measured by ellipsometer and AFM, film thicknesses could reach above 20 nm, which is reckoned as a sufficient value for patterning in semiconductor industry, for all the clusters using the chosen casting solvents with a rotating speed at 2000 rpm for 45 seconds. High surface homogeneity with limited defects was able to achieve and consistent on 1 cm x 1cm and 2 cm x 2 cm silicon wafers. Moreover, since the metal oxo clusters are prone to hydrolyse under air and hence cause a serious degradation with respect to patterning performance, two different approaches were tested for their anti-hydrolysis ability on $Zr_4O_2(OMc)_{12}$ thin film. Transmission FTIR results indicated both methods could delay cluster hydrolysis up to one hour, meaning a proper process window can be provided for manufacturing. Yet water remains the biggest threat for the metal oxo clusters in terms of patterning capability. Thin-film UV/Vis spectroscopy also revealed a fast degrading speed in most of the cluster materials. Therefore, solvents employed for spin-coating as well as developing are required to be in dry condition and long exposing time for coated thin films to air should be avoided.

Defining appropriate developers for the metal oxo clusters was conducted in stepwise experiments. Thin-film UV/Vis was utilised to examine absorption intensity of the materials before and after developing in different kinds of developer. Following preliminary UV/Vis analysis, A maskless DUV exposure was carried out on $Zr_4O_2(OMc)_{12}$, $Zr_4O_2(OMc)_6(OPiv)_6$, $Ti_2Zr_4O_4(OBu)_2(OMc)_{14}$, $Ti_4Zr_2O_4(OBu)_6(OMc)_{10}$ and $Hf_4O_2(OMc)_{12}$ to initiate solubility switch on the exposed area. The wafers were developed after exposure using developers selected according to UV/Vis results and a clear contrast could be observed. Some aggressive developing solvents were able to wash away even the exposed materials, leaving no patterning on the surface. These solvents were considered as inappropriate developers for these clusters.

In this chapter, the metal oxo clusters have proven not only they have a good coatability, showing ideal surface finish after spin-coating, but their solubility switch can be triggered via DUV with nice contrast if proper developed is employed. These results have set a solid foundation regarding the process conditions for these materials, which is crucial and beneficial to actual electron beam and EUV lithography afterwards.

# 8 Electron Beam Lithography

E-beam lithography (EBL) has also been considered as one the most promising nanofabrication techniques towards sub-10 nm patterning. Unlike DUV or EUV lithography, it is a markless approach that directly employs a focus electron beam for resist exposure, meaning instead of a photomask containing required design, the patterns are written straightforward on the surface. This advantage enables it to be utilised for patterning photomasks for other lithographic techniques. Electrons of EBL used to be generated by tungsten thermionic emission cathode, which has been gradually replaced with field electron emission sources in order to achieve lower energy spread and enhanced brightness for high resolution patterning [84].

Among the various kinds of lithographic methods widely-employed nowadays, EBL is recognised to be capable of reaching the highest resolution attributed to its high-energy primary electrons ranging from 50 to above 100 keV. The flexibility makes it possible for any arbitrary structures or patterns to be generated via E-beam lithography with highest resolution down to 5 nm [85]. However, the major issue that retrains EBL from implementing high volume manufacturing in semiconductor industry still lies in its relatively low throughput. It generally takes several hours to pattern a silicon wafer with EBL, whereas DUVL can produce over a hundred wafers in an hour at a proper manufacturing plant [4]. Needless to mention that downsizing of ICs will even lead to a much longer exposing time using EBL. This significant drawback limits the application of E-beam lithography mainly on photomask manufacturing and research and development purposes. However, more studies have been focused on optimising EBL throughput recently including device architecture, multiple e-beam, shape-variable and reflective beam [86-89].

The real scenario of radiation-photoresist interaction in EUVL is much resembling to E-beam Lithography. While DUV is introducing a direct photon absorption to temporarily excite resist molecules to an excited state, the matter that triggers chemical reaction in EUV and E-beam lithography is primarily secondary electrons instead of primary electrons. In EBL, when high energy primary electrons being projected into the surface of photoresist thin-film, a series of elastic and inelastic collision take place and lead to electron scattering through the material. Inelastic collision then results in a substantial energy loss and generates numerous secondary electrons. These secondary electrons can undergo similar mechanism as primary electrons to form more free electrons. Each primary electron is capable of generating a cloud of electron that has a teardrop-shaped interaction volume within resist material. The simulation of secondary electron formation and incident angle can be calculated by Monte Carlo approach [4, 90, 91].

Since EUVL and EBL both employ high energy radiation-induced sources and secondary electron plays a crucial role in terms of initiating solubility switch in these two techniques, if a resist material can be patterned by either EUVL or EBL, it should also be feasible by applying the other lithographic approach. Conventional photoresists for EBL application, e.g. hydrogen silsesquioxane (HSQ) and poly methyl methacrylate (PMMA), have been studied for their capability in EUVL and some of them showed eminent patterning performance [92, 93]. Therefore, the more accessible E-beam lithography has become a beneficial tool for determining potential EUVL photoresists with respect to the material design as well as process conditions. But this does not mean the resist material would have identical patterning performance in EUVL and EBL. Occasionally, a photoresist that performs well in EUVL has inferior EBL capability and vice versa.

For this reason, E-beam lithography was conducted on the metal oxo clusters to define their patternability as well as optimise the process conditions prior to the final EUV lithography at Paul Scherrer Institute.

## 8.1 Experimental and Process Conditions

E-beam lithography was performed via Raith e-LiNE lithography system (Voyager) in the cleanroom at Institute for Atomic and Molecular Physics (AMOLF), the sister institute of ARCNL. Metal-oxo-clusters including $Zr_4O_2(OMc)_{12}$, $Zr_4O_2(OMc)_x(OPiv)_{12-x}$ (x=3, 6, 9), Ti-Zr clusters, $Hf_4O_2(OMc)_{12}$ and $Zr_{12}O_8(OH)_8(OMc)_8(OAc)_{16} \cdot 6HOAc$ were spin-coated on 1 cm x 1 cm silicon wafers for testing. Preparation of the casting solutions at 1% w/v for each material was carried out inside the glovebox. Wafers employed were treated with piranha solution for cleaning prior to spin-coating. A Suss Delta 80 Spin-coater was utilised for film preparation in the cleanroom with identical parameters as those as previously mentioned, while the development followed the puddling method, i.e. a wafer sample was immersed in 20 mL of a developer for 60 seconds without mechanical assistance and blown dry with nitrogen afterwards. Coated samples were stored under nitrogen atmosphere constantly before being loaded into the Voyager. Respective casting and developing solvents (Table 7) for each cluster were employed for spin-coating and development. Each of the metal oxo cluster was irradiated with dose factors from 1 to 9, meaning there were 9 areas in total on a single silicon wafer that was irradiated from 1 x (initial dose), 2 x (initial dose) to 9 x (initial dose) µC/cm2, respectively, as shown in Figure 8-1.

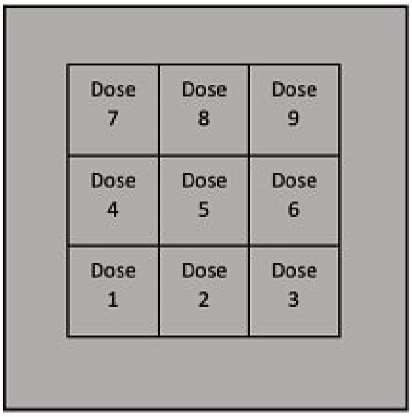

| | | |
|---|---|---|
| Dose 7 | Dose 8 | Dose 9 |
| Dose 4 | Dose 5 | Dose 6 |
| Dose 1 | Dose 2 | Dose 3 |

*Figure 8-1: Schematic diagram of doses and alignment on the sample of E-beam lithography.*

### 8.1.1 $Zr_4O_2(OMc)_{12}$

E-beam lithography started from $Zr_4O_2(OMc)_{12}$ to set as a benchmark for the other clusters in terms of operational procedure and conditions such as required dose and time. The initial dose set at the first trial was 100 µC/cm$^2$ for area dose, 100 ρC/cm for line dose and 0.01 ρC for dot dose, respectively. Dry isopropanol (IPA) was initially used as the developer. However, no pattern was observed on the silicon after development. The possible reason might be caused by the high polarity of alcohol that dissolved the exposed area along with unexposed material. Therefore, in order to determine the proper developer, different solvents and solvent mixtures were also employed for comparing their performance upon development under the same conditions.

The dose was reduced to 50% and 25% of the original dose respectively in the latter trials after suitable developers were chosen. More details are described in the following chapters.

#### 8.1.1.1 Toluene and Chloroform Mixture as Developer

Given that polar solvents are capable of removing also the exposed materials, the developer test started from the least polar solvent mixture. Dry Toluene and chloroform were mixed with a volume ratio of 4:1 as developer. Despite that the mixture could slightly dissolve the unexposed material, it could not generate a sufficient contrast and many particles aggregates were left on the surface after development, as shown in Figure 8-2.

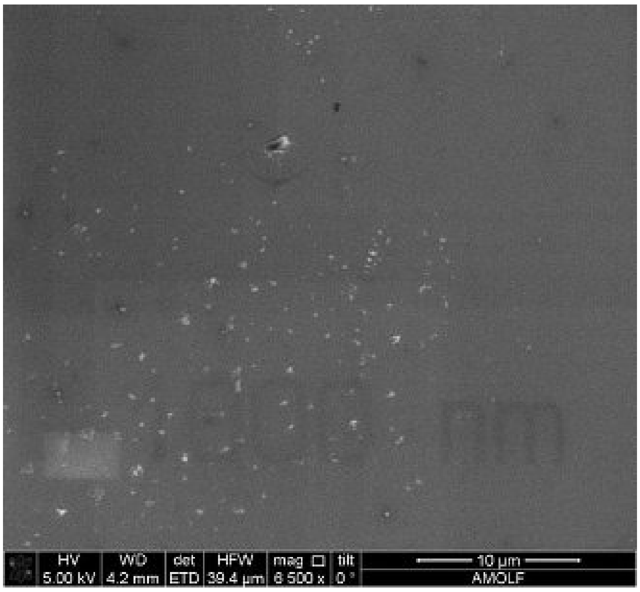

*Figure 8-2: SEM image of $Zr_4O_2(OMc)_{12}$ developed via toluene and chloroform mixture (4:1) on a silicon wafer.*

### 8.1.1.2 Chloroform as Developer

The result of toluene and chloroform mixture indicated developer polarity should be increased with respect to improving pattern contrast. Hence, 20 mL of pure and dry chloroform was employed for developing $Zr_4O_2(OMc)_{12}$ pattern via puddle process. SEM images in Figure 8-3 have revealed the E-beam lithographic patterns.

Chloroform can be reckoned as a suitable developer for $Zr_4O_2(OMc)_{12}$ cluster as the patterns were clearly developed with high contrast. The lines were perfectly aligned without any distortion that resulted from evaporation of high volatile solvent. The radiant pattern did not have pattern collapse or any defect as the lines are getting concentrated. Overflown squares in the dose test indicated the dose area dose at 100 µC/cm$^2$ was too high for $Zr_4O_2(OMc)_{12}$ patterning, which was reduced afterwards.

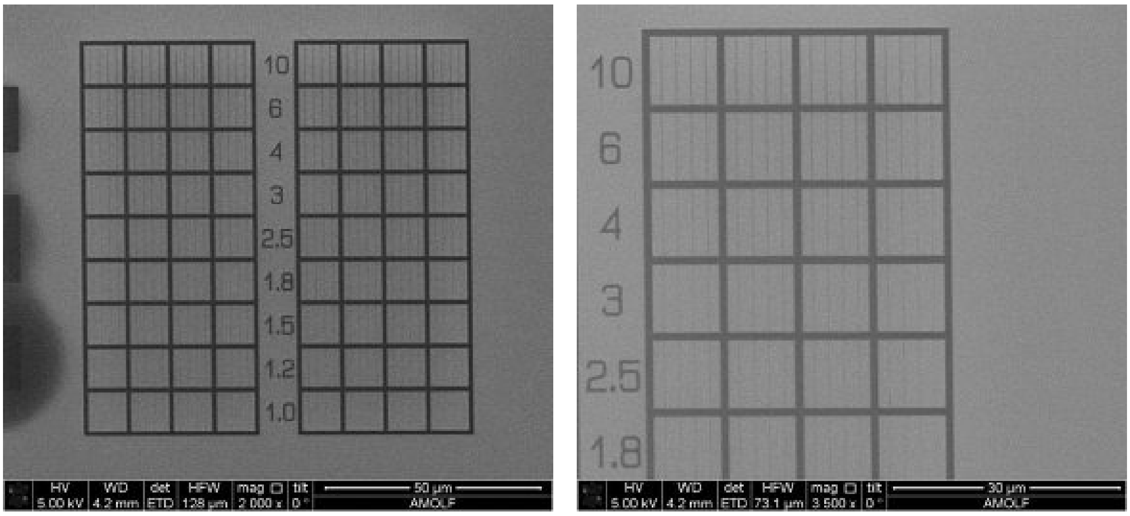

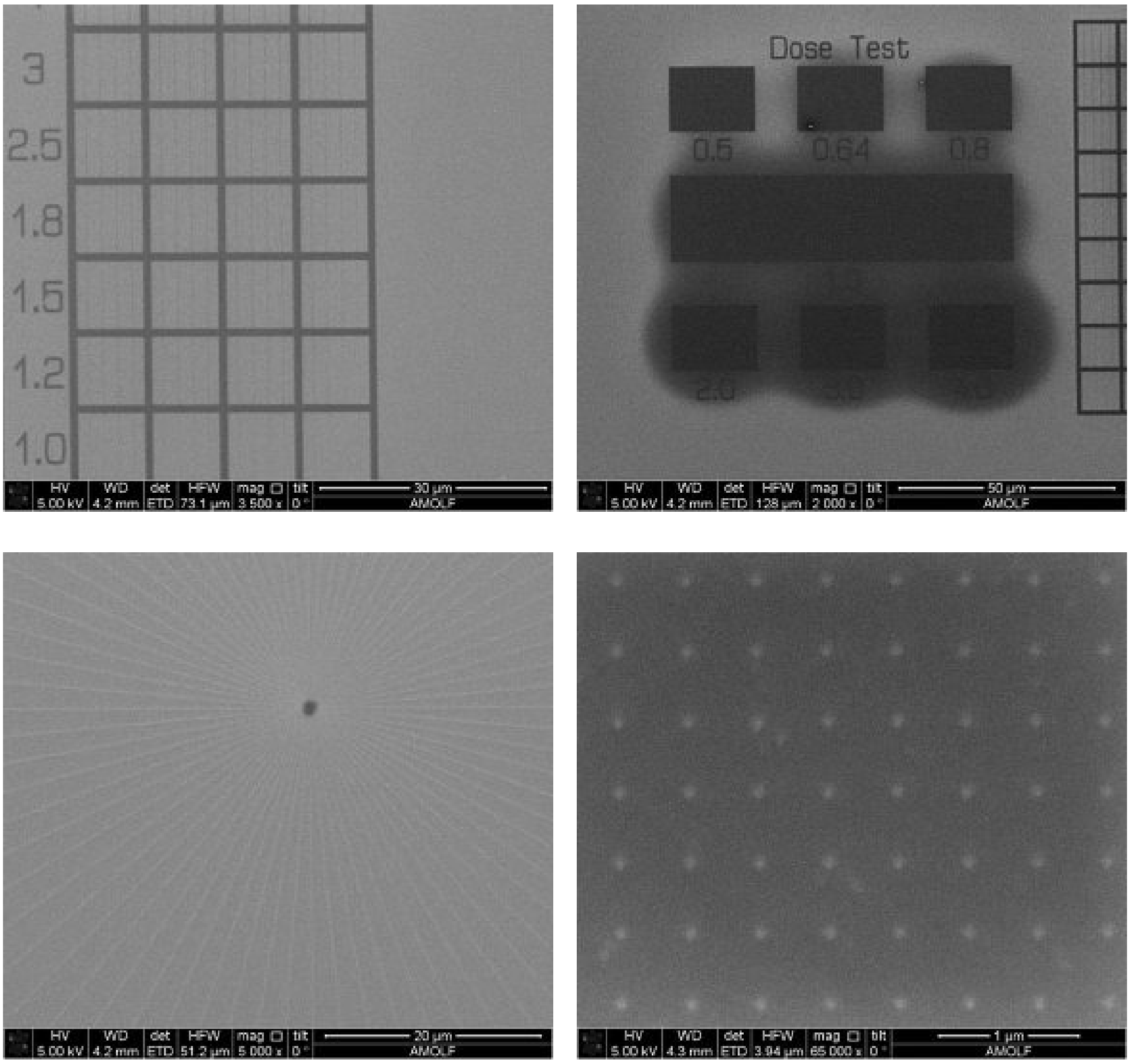

*Figure 8-3: SEM images of $Zr_4O_2(OMc)_{12}$ EBL samples developed by chloroform.*

### 8.1.1.3 Chloroform and Ethyl Acetate Mixture as Developer

Addition of 25% by volume ethyl acetate to chloroform was for the sake of increasing developer polarity and resulted in a better contrast after development. This mixture is preferred in comparison with chloroform due to a lower vapour pressure ethyl acetate has. For the case of chloroform, the developer evaporated very fast once the silicon wafer left the puddle, leaving just a limited period for applying nitrogen flow. High vapour pressure of the developer may give rise to some defects including striation as well as bubbles after development. Introducing ethyl acetate into the developer is able to delay solvent evaporation rate, providing more room for processing.

The E-beam lithographic patterns of $Zr_4O_2(OMc)_{12}$ using chloroform and ethyl acetate mixture (3:1) as developer were depicted in Figure 8-4. At a first glance, they were relatively similar to those developed by pure chloroform.

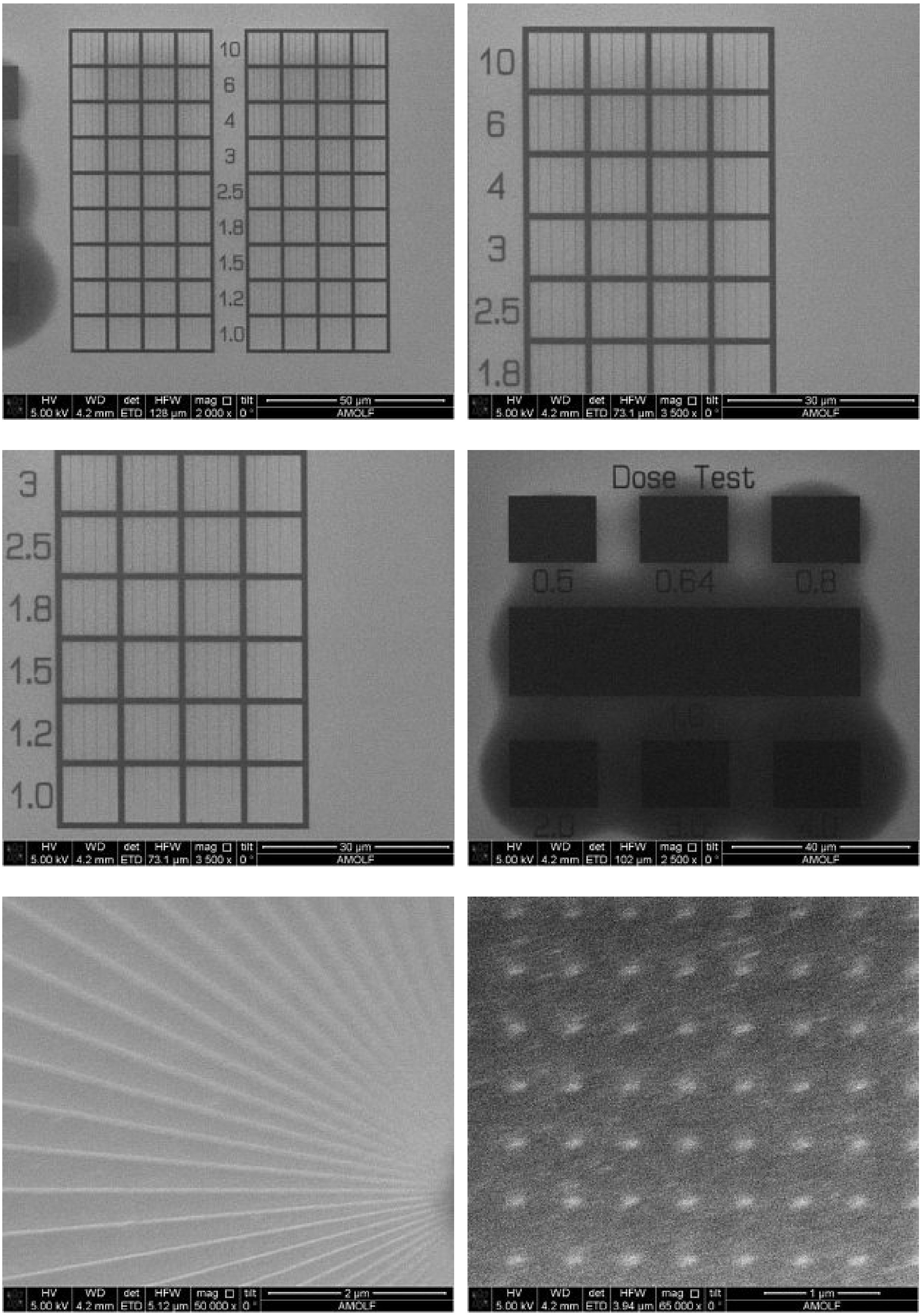

*Figure 8-4: SEM images of $Zr_4O_2(OMc)_{12}$ EBL samples developed by chloroform and ethyl acetate mixture (3:1).*

However, higher magnification SEM images revealed the difference between the two. Lines with a width at a single pixel size (approximately 10 nm) can be clearly observed after the sample being developed by the mixture of chloroform and ethyl acetate, whereas there is a partial pattern collapse for lines developed by chloroform (Figure 8-5). This could be related to the high vapour pressure of chloroform. The radiant patterns developed from two developers were also different. Lines of the solvent mixture sample are very distinct even at the centre of the radiant. However, the chloroform sample did not have an obvious separation between line closing to the centre although they were quite perfectly formed in the outer area.

Moreover, since the area dose test in $Zr_4O_2(OMc)_{12}$ results indicated a clear overdose with initial doses at 100 and 50, patterning with reduced area and line doses was carried out afterwards. Electron beam with an energy of 25 $\mu C/cm^2$ for area dose and 25 $\rho C/cm$ for line dose was employed using chloroform and ethyl acetate mixture for developing the patterns.

SEM images clearly reveal a remaining area overdose phenomenon with the reduced energy, meaning the area sensitivity of $Zr_4O_2(OMc)_{12}$ is potentially below 12.5 $\mu C/cm^2$, as recorded in Figure 8-6. Line dose, however, requires higher digits since the single-pixel lines can no longer be observed below dose factor 4. Pattern collapse and defects also exist within the radiant printing, which is attributed to insufficient energy input.

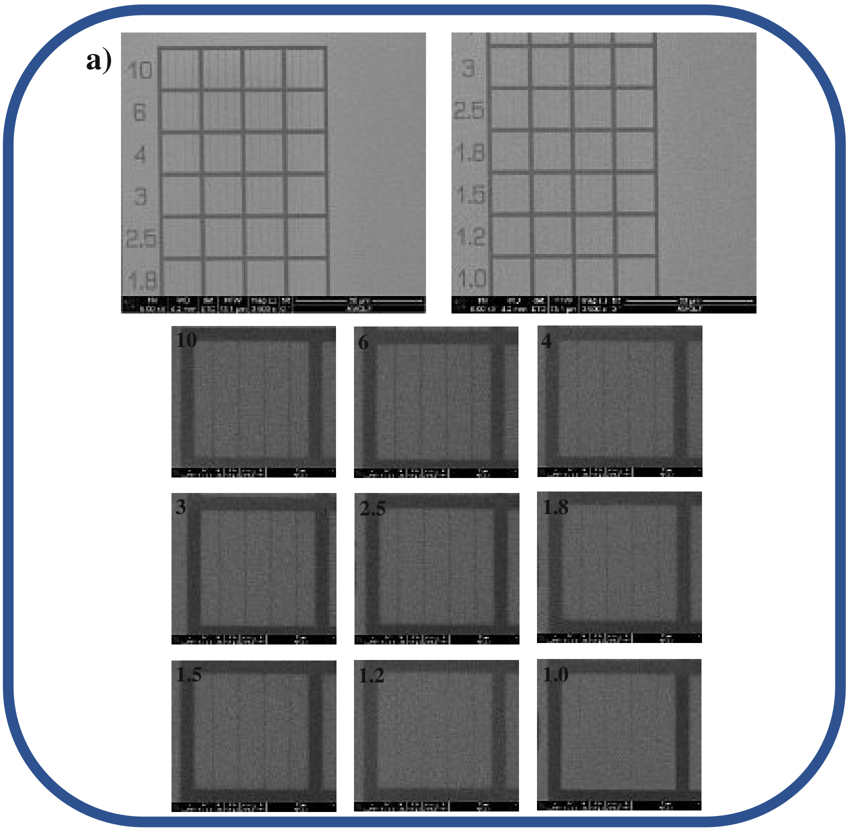

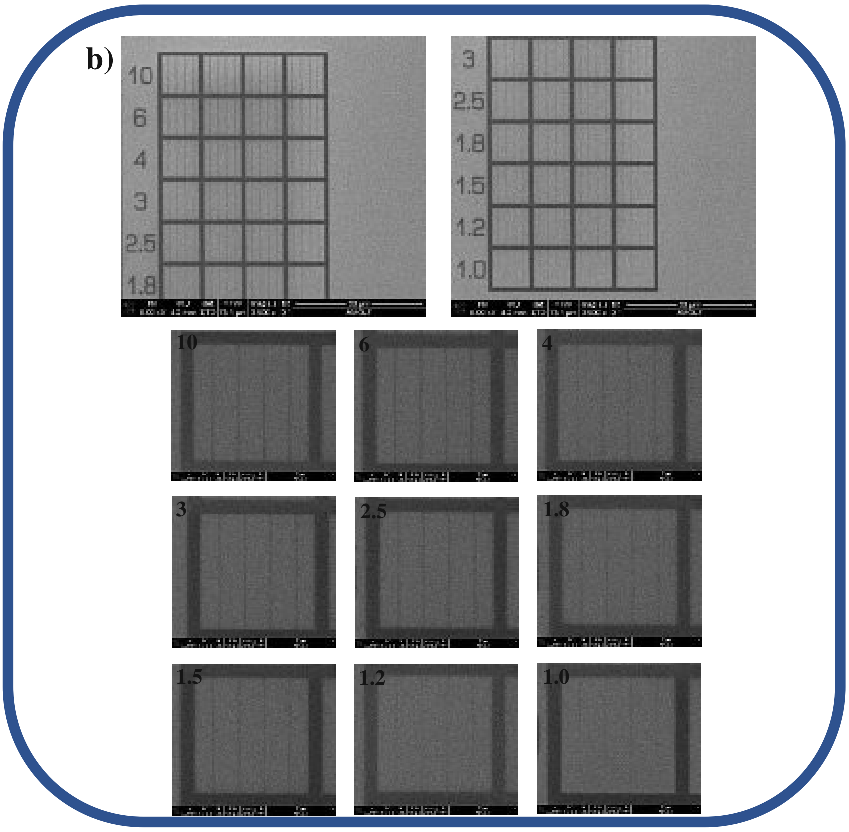

*Figure 8-5: Comparison of resolution on $Zr_4O_2(OMc)_{12}$ samples developed by a) chloroform and b) mixture of chloroform and ethyl acetate (Line dose: 100 ρC/cm).*

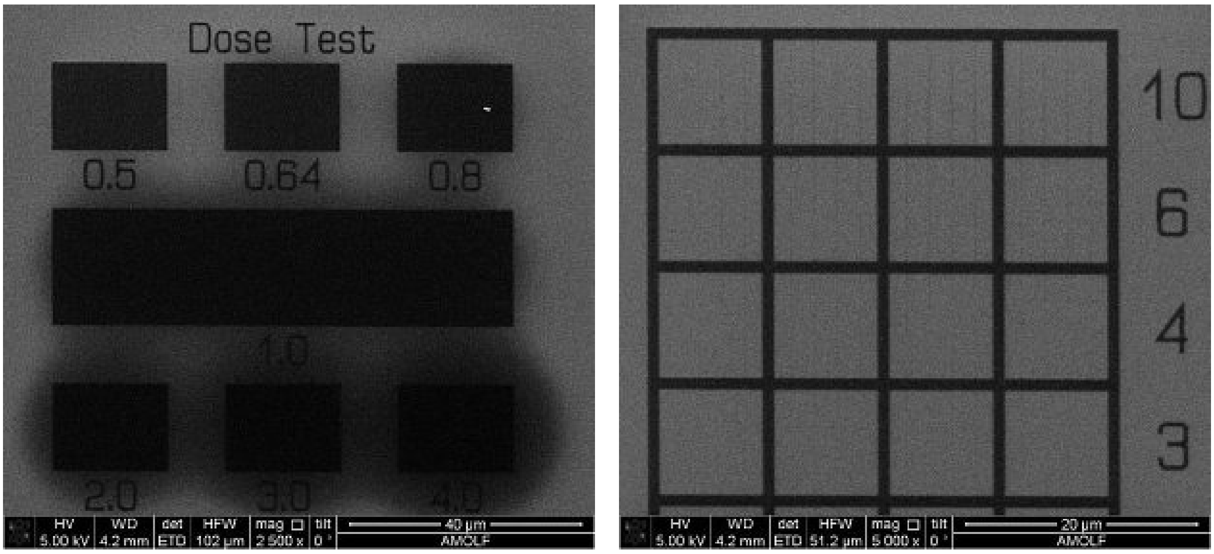

*Figure 8-6: SEM images of $Zr_4O_2(OMc)_{12}$ EBL samples developed by chloroform and ethyl acetate mixture (3:1) with area dose at 25 µC/cm² and line dose at 25 ρC/cm.*

#### 8.1.1.4 Chloroform and Propionic Acid Mixture as Developer

The last solvent mixture that has been tested as developer for $Zr_4O_2(OMc)_{12}$ was chloroform with additional 0.5% vol. of propionic acid. The purpose of adding carboxylic acid was to react with unexposed metal oxo clusters rather than increase solvent polarity. Propionic acid can theoretically coordinate with metal cation via different binding modes and substitute the original ligands for promoting dissolution of the material [94]. SEM images of $Zr_4O_2(OMc)_{12}$ developed by chloroform and propionic acid mixture were recorded and depicted in Figure 8-7.

Despite this mixture indeed could develop patterns by dissolving unexposed area, reactivity of propionic acid was too intense that even the exposed materials reacted with it and were washed away by the solvent mixture in the end. The resulted patterns therefore became blur and unrecognisable. Only areas with higher doses could have more exposed materials left, whereas limited exposed materials could remain on the silicon wafer surface at lower dose regions and for lines. Chloroform and propionic acid mixture eventually were reckoned as an inappropriate developer for these metal oxo clusters and did not proceed to other EBL patterning.

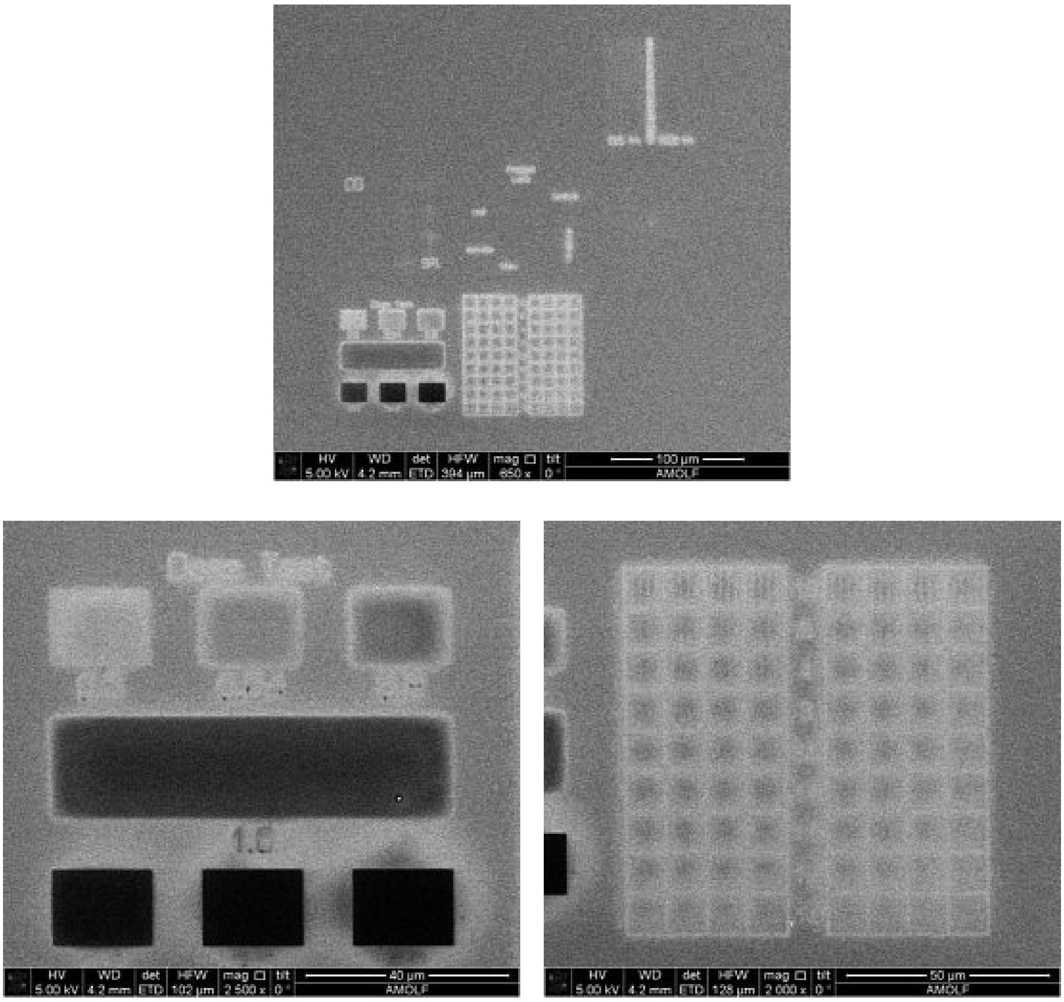

*Figure 8-7: SEM images of $Zr_4O_2(OMc)_{12}$ EBL samples developed by chloroform and 0.05% vol. propionic acid mixture.*

### 8.1.2 $Zr_4O_2(OMc)_x(OPiv)_{12-x}$ (x=3, 6, 9)

The three mixed-ligand zirconium clusters were expected to perform distinctly upon E-beam exposure with respect to sensitivity, line-edge roughness and resolution due to different crosslinking density. Despite that the potential mechanism proposed could undergo condensation reaction or crosslinking, crosslinkable methacrylate ligand still plays a crucial role in both pathways. In the condensation mechanism, the existence of methacrylates containing free radicals can help to improve sensitivity by traveling through the material system and crosslinking with other ligands [66]. On the other hand, crosslinking density of metal oxo clusters can also increase sensitivity by providing more active and crosslinkable sites.

The casting solutions of $Zr_4O_2(OMc)_3(OPiv)_9$, $Zr_4O_2(OMc)_6(OPiv)_6$, $Zr_4O_2(OMc)_9(OPiv)_3$ were prepared at the same time using the same bottle of solvent and stored under identical conditions before being loaded into the E=beam Voyager in order to exclude any possible external influences. The clusters were patterned with 100 μC/cm$^2$ area dose, 100 ρC/cm line dose, and 0.01 ρC for dot dose since the patterning performance below these doses were unfavourable and the sensitivity decreased in comparison with $Zr_4O_2(OMc)_{12}$. This phenomenon is possibly resulted from lower methacrylate portion on a single cluster shell.

The area and line dose tests have revealed a significant effect resulted from crosslinking density. $Zr_4O_2(OMc)_3(OPiv)_9$, which has the lowest methacrylate content among the three, showed no obvious overdose with an initial dose at 100 μC/cm$^2$. As the crosslinking density increased, $Zr_4O_2(OMc)_6(OPiv)_6$ pattern clearly presented an overdose at the highest dose factor (4.0), whereas most areas in $Zr_4O_2(OMc)_9(OPiv)_3$ went overdose with identical initial dose.

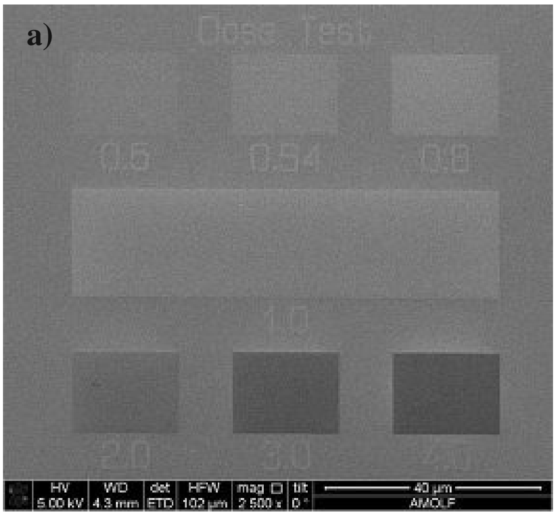

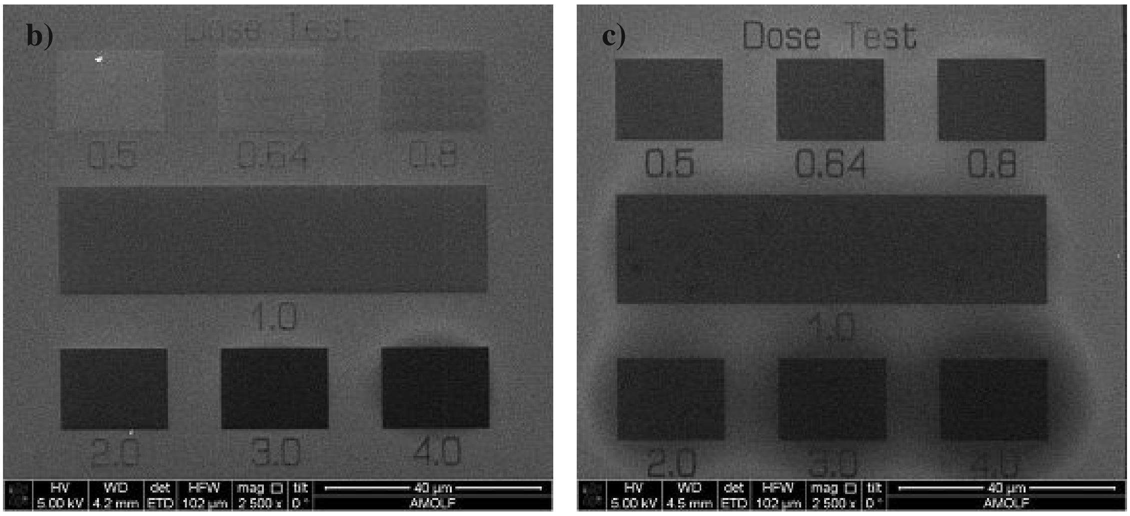

*Figure 8-8: SEM images of dose test patterning for a) $Zr_4O_2(OMc)_3(OPiv)_9$, b) $Zr_4O_2(OMc)_6(OPiv)_6$, c) $Zr_4O_2(OMc)_9(OPiv)_3$ (Area dose: 100 $\mu C/cm^2$).*

Amount of materials remaining on the silicon wafer surface after development also varied with crosslinking density, as can be observed in both area and line dose tests (Figure 8-8 and Figure 8-9). Only a shallow layer of $Zr_4O_2(OMc)_3(OPiv)_9$ formed a relatively compact network that made it insoluble in the developer employed (chloroform and ethyl acetate mixture) and some areas as well as lines are barely seen even at high dose factor. $Zr_4O_2(OMc)_6(OPiv)_6$ has an intermediate methacrylate content among these three clusters. Its SEM image of line dose test evidently showed the influence from crosslinkable ligand, with the dose enough for just the frame while the single-pixel lines were underdosed. The scenario in $Zr_4O_2(OMc)_9(OPiv)_3$ is much closer that of $Zr_4O_2(OMc)_{12}$ but only with a much higher dose utilised. Therefore, embedding a higher proportion of crosslinkable ligand in a single cluster can not only improve its sensitivity towards the exposing light source, but potentially reduce line edge roughness since a highly crosslinked and homogeneous system is generated. These benefits are true for both electron beam and EUV lithography.

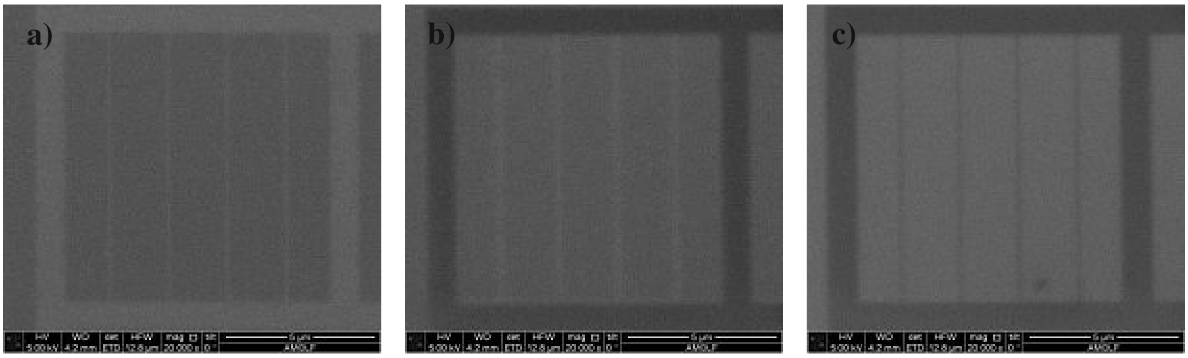

*Figure 8-9: SEM images of single-pixel line patterning for a) $Zr_4O_2(OMc)_3(OPiv)_9$, b) $Zr_4O_2(OMc)_6(OPiv)_6$, c) $Zr_4O_2(OMc)_9(OPiv)_3$ (Line dose: 100 $\rho C/cm$).*

### 8.1.3 Ti-Zr Clusters

$Ti_4Zr_4O_6(OBu)_4(OMc)_{16}$, $Ti_2Zr_4O_4(OBu)_2(OMc)_{14}$ and $Ti_4Zr_2O_4(OBu)_6(OMc)_{10}$ were patterned via E-beam lithography with an initial dose started from 50 µC/cm$^2$ for area dose and 50 ρC/cm for line dose. Unlike EUVL photoresists, metal moieties do not make a significant impact on material sensitivity towards electron beam. In the case of EUV, orientation of metal orbitals can help to capture EUV photons and then initiate chemical reactions within resist layer, meaning the sensitivity can be improved if the metal moiety is properly selected. Yet for EBL, there is no such interaction between metal orbitals and incident electrons. Therefore, these Ti-Zr oxo clusters were expected to have similar sensitivity in EBL patterning.

Attributed to the insufficient amount of $Ti_4Zr_4O_6(OBu)_4(OMc)_{16}$ remaining by the time EBL was conducted, $Ti_4Zr_4O_6(OBu)_4(OMc)_{16}$ was not involved in the first three lithography trials. $Ti_4Zr_2O_4(OBu)_6(OMc)_{10}$ and $Ti_2Zr_4O_4(OBu)_2(OMc)_{14}$ have been proved their feasibility of being patterned. However, the initial resolution of both clusters was not ideal using chloroform and ethylacetate mixture (1:1 by volume) as developer. The SEM images remained obscure even with higher dosage (450 µC/cm$^2$ area dose and 450 pC/cm line dose) and single-pixel lines could hardly be observed with dose factor below 10, as shown in Figure 8-10.

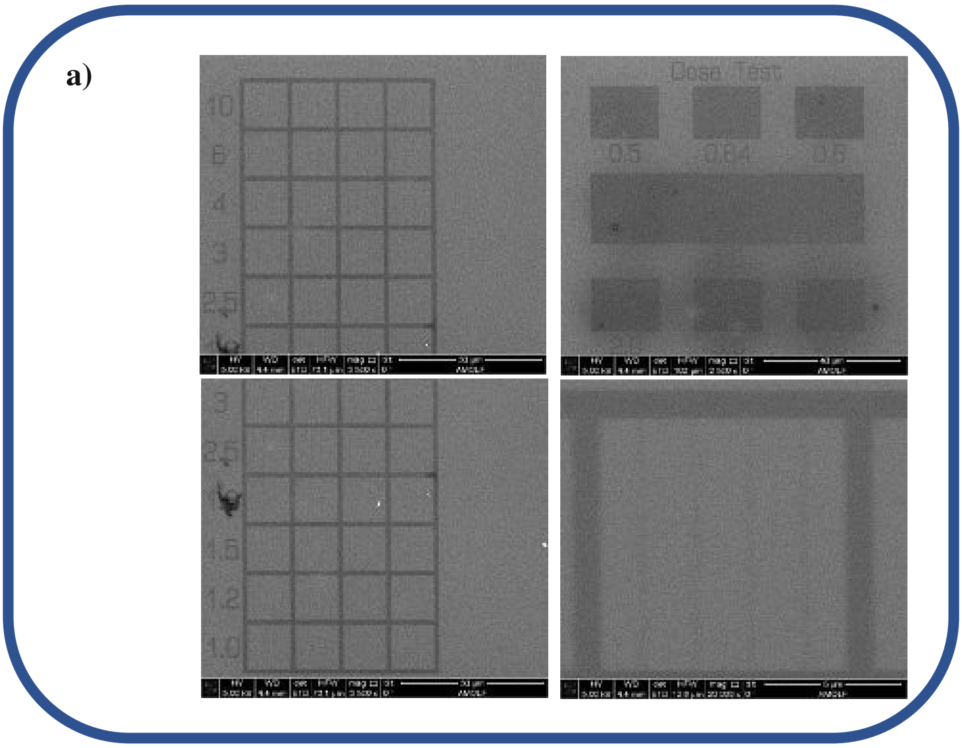

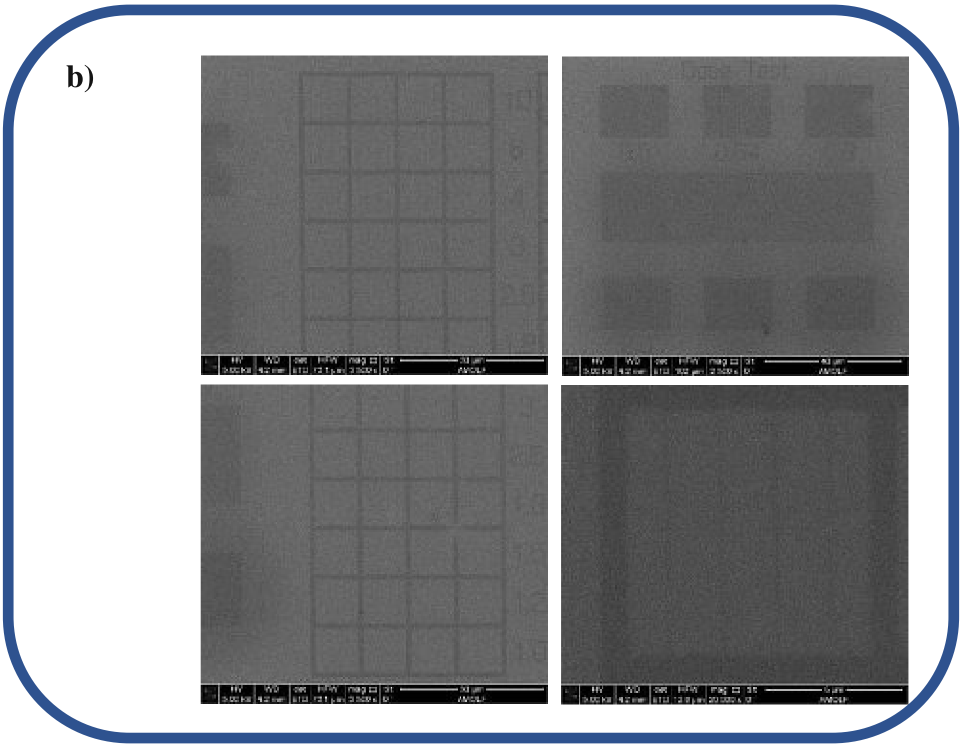

*Figure 8-10: SEM images of dose test for a) $Ti_4Zr_2O_4(OBu)_6(OMc)_{10}$ and b) $Ti_2Zr_4O_4(OBu)_2(OMc)_{14}$ (Area dose: 450 $\mu$C/cm$^2$; Line dose: 450 $\rho$C/cm).*

There are two possible reasons that leads to low contrast for Ti-Zr clusters. The first aspect is insufficient dose employed. But considering the crosslinking density of these Ti-Zr clusters are comparable with that of $Zr_4O_2(OMc)_{12}$, they should essentially have similar capability in electron beam lithography in terms of sensitivity and resolution. Moreover, the area dose test of $Ti_4Zr_2O_4(OBu)_6(OMc)_{10}$ and $Ti_2Zr_4O_4(OBu)_2(OMc)_{14}$ both indicated an overdose phenomenon when the dose factor went above 1.0 even though it is slightly hard to observe. As a result, it is sensible to assume that the initial dose employed was appropriate for patterning these two Ti-Zr clusters.

Another possibility is the influence of developer. If the materials are not soluble enough in the selected developer, they cannot be completely removed from the silicon wafer surface, which results in low contrast after development. In order to figure out and find a better developing solvent for Ti-Zr clusters, three solvents (or solvent mixtures) with different polarity including chloroform, a mixture of chloroform and ethyl acetate (1:1 by volume), and a mixture of chloroform and ethyl acetate (1:3 by volume) were utilised to develop the exposed $Ti_2Zr_4O_4(OBu)_2(OMc)_{14}$.

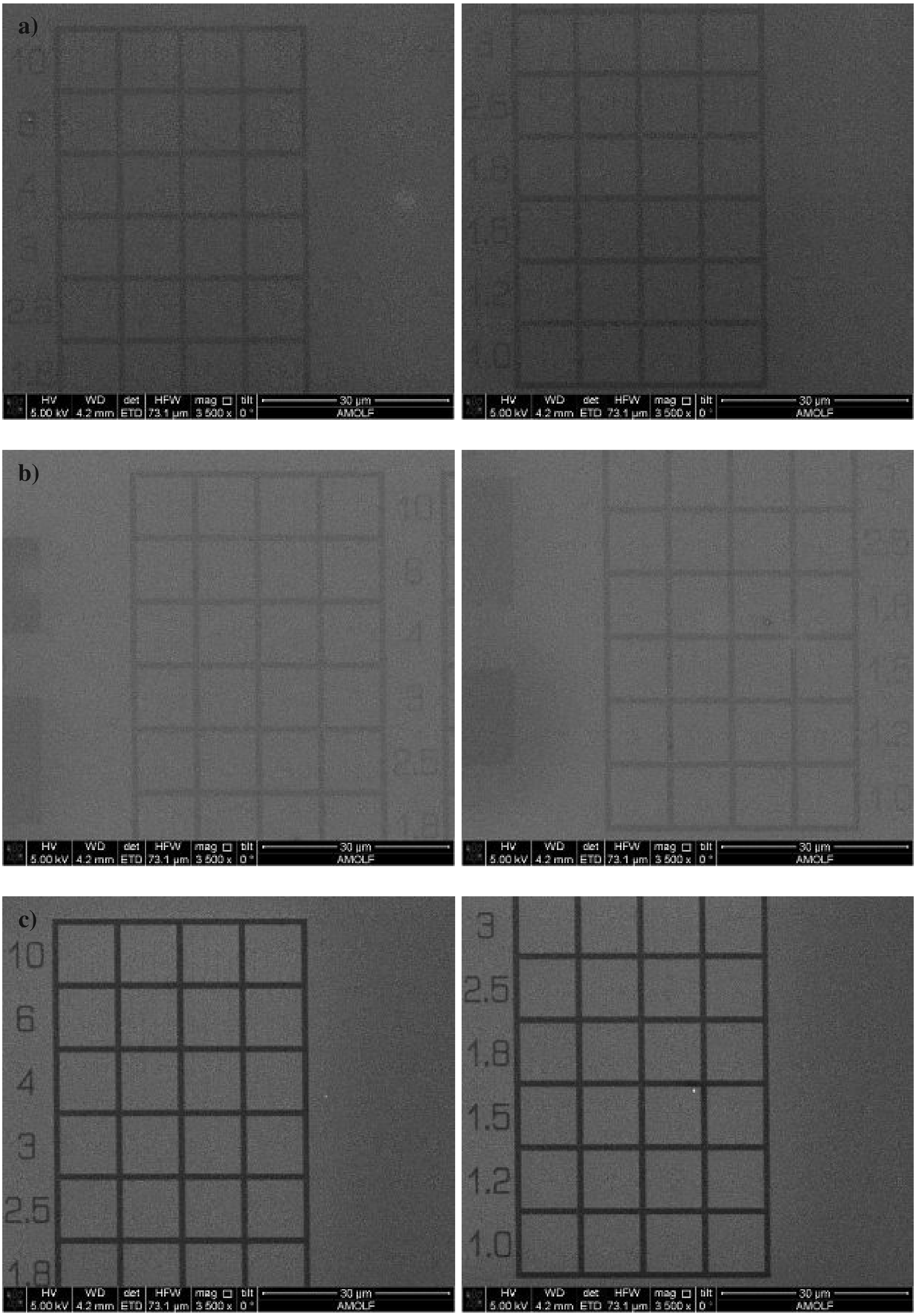

*Figure 8-11: SEM images of $Ti_2Zr_4O_4(OBu)_2(OMc)_{14}$ developed by a) $CHCl_3$, b) $CHCl_3$+EtOAc (1:1 by volume), and c) CHCl3+EtOAc (1:3 by volume) (Line dose: 450 ρC/cm).*

SEM images in Figure 8-11a and b shown that the contrast after development with pure chloroform and the 1:1 ratio solvent mixture was relatively insignificant. With the increase of developer polarity by raising the proportion of ethyl acetate to 75%, the contrast was indeed improved yet the single-pixel lines were still scarcely visible, which might be due to insufficient line dosage (Figure 8-11c). The mixture of chloroform and ethyl acetate (1:3 vol.) was also applied to $Ti_4Zr_4O_6(OBu)_4(OMc)_{16}$ and $Ti_4Zr_2O_4(OBu)_6(OMc)_{10}$ after E-beam lithography as developer. A substantial melioration on contrast can both be observed in both materials (Figure 8-12).

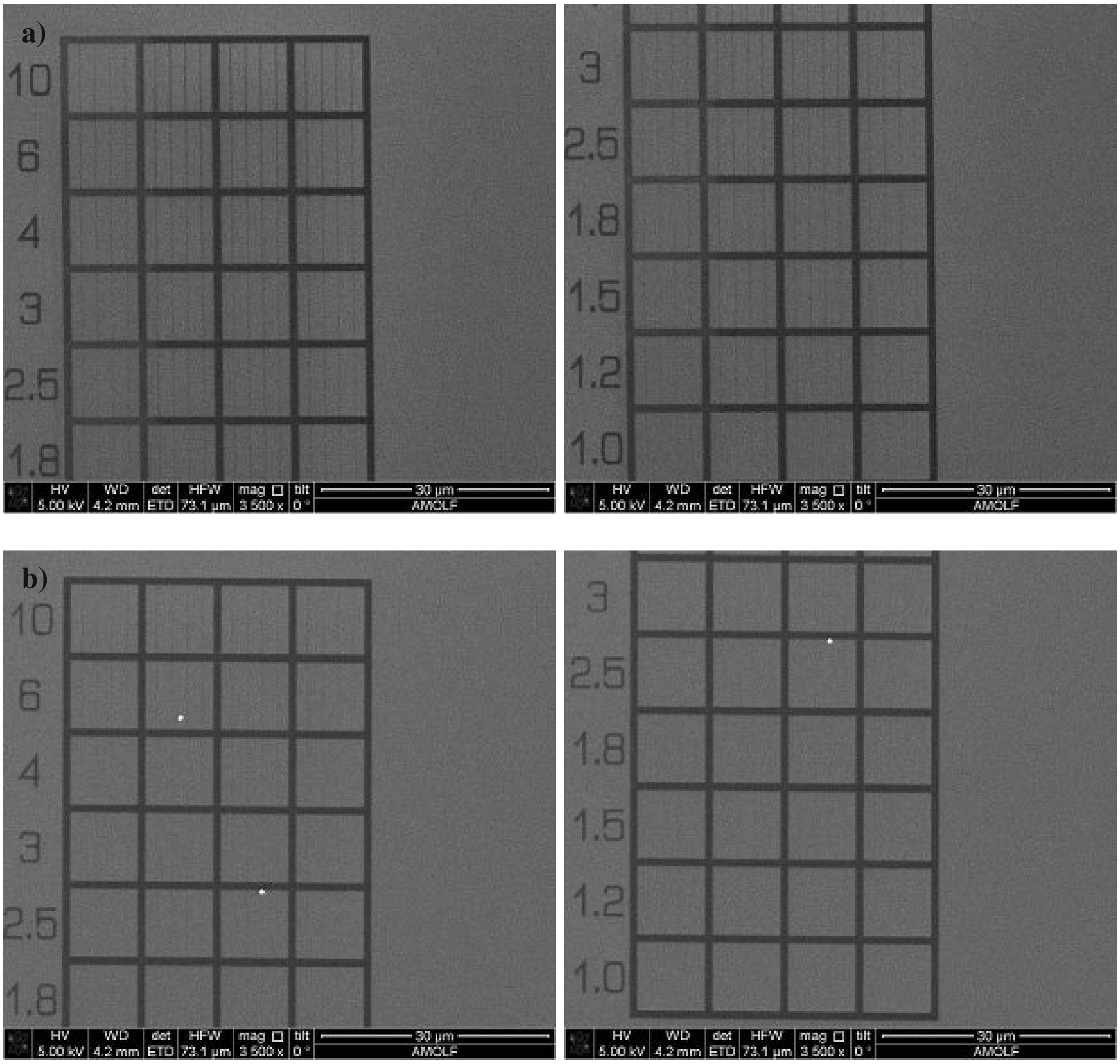

*Figure 8-12: SEM images of a) $Ti_4Zr_4O_6(OBu)_4(OMc)_{16}$ and b) $Ti_4Zr_2O_4(OBu)_6(OMc)_{10}$ developed by $CHCl_3$+EtOAc (1:3 by volume) (Line dose: 450 $\rho$C/cm).*

### 8.1.4 $Hf_4O_2(OMc)_{12}$

The major difference between $Hf_4O_2(OMc)_{12}$ and $Zr_4O_2(OMc)_{12}$ is based on their metal species. Hafnium was originally employed so as to increase material sensitivity upon EUV exposure. Except the metal elements, bond angles, metal proportions and organic ligand arrangements of two clusters are very similar. As already mentioned, metal moiety in photoresist material do not play a crucial role in terms of improving sensitivity during electron beam lithography. As a result, $Hf_4O_2(OMc)_{12}$ was expected to have resembling patterning performance as $Zr_4O_2(OMc)_{12}$ since the composition as well as crystal structure are alike.

The initial dose for $Hf_4O_2(OMc)_{12}$ EBL patterning started from 50 μC/cm$^2$ area dose and 50 ρC/ cm line dose. The casting and developing solvent mixture employed were identical to those for $Zr_4O_2(OMc)_{12}$. $Hf_4O_2(OMc)_{12}$ appeared to have faster degradation rate in comparison with the zirconium oxo clusters. Therefore, the time of sample exposing under air has been well-controlled before being loaded into E-beam Voyager and the puddle development.

SEM images of area and line dose tests were depicted in Figure 8-13. An obvious overdose in the area dose test already took place at dose factor above 0.84, indicating a more proper area dose for $Hf_4O_2(OMc)_{12}$ EBL patterning should be around 25 μC/cm$^2$, which is the same as that for $Zr_4O_2(OMc)_{12}$. Single-pixel lines in the line dose test failed to form or started to collapse as dose factor went below 1.5. Nevertheless, pattern contrast using chloroform and ethyl acetate mixture (3:1 vol.) as developer is essentially satisfying.  Both results are comparable with those of $Zr_4O_2(OMc)_{12}$. Lines in the radiant pattern were clearly separated towards the centre and no aggregation as well as defects were detected. In general, EBL capability of $Hf_4O_2(OMc)_{12}$ are highly comparable with $Zr_4O_2(OMc)_{12}$ in terms of sensitivity and resolution.

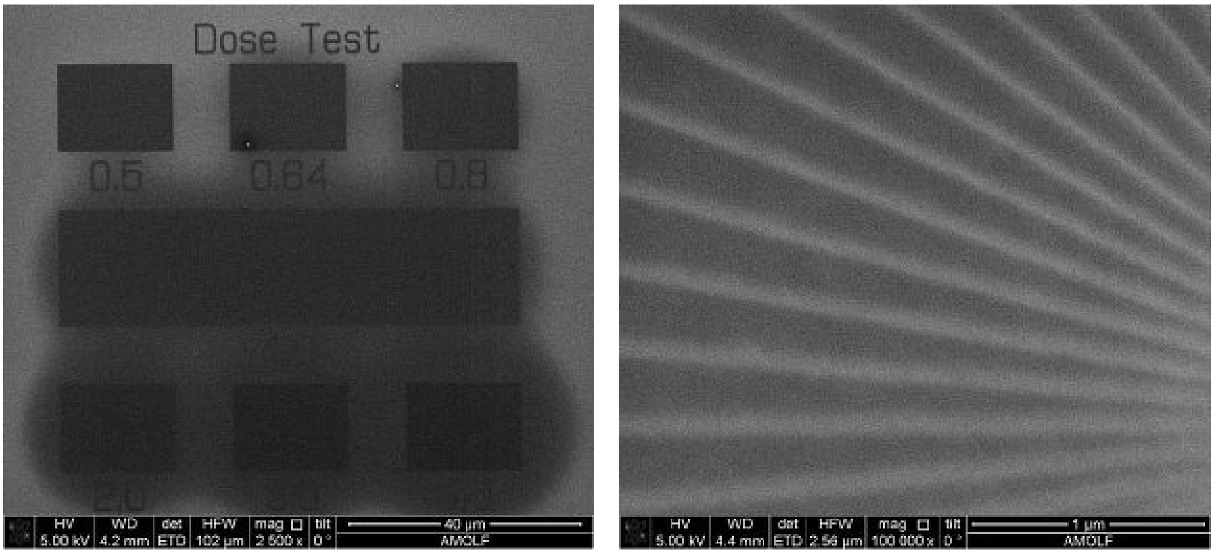

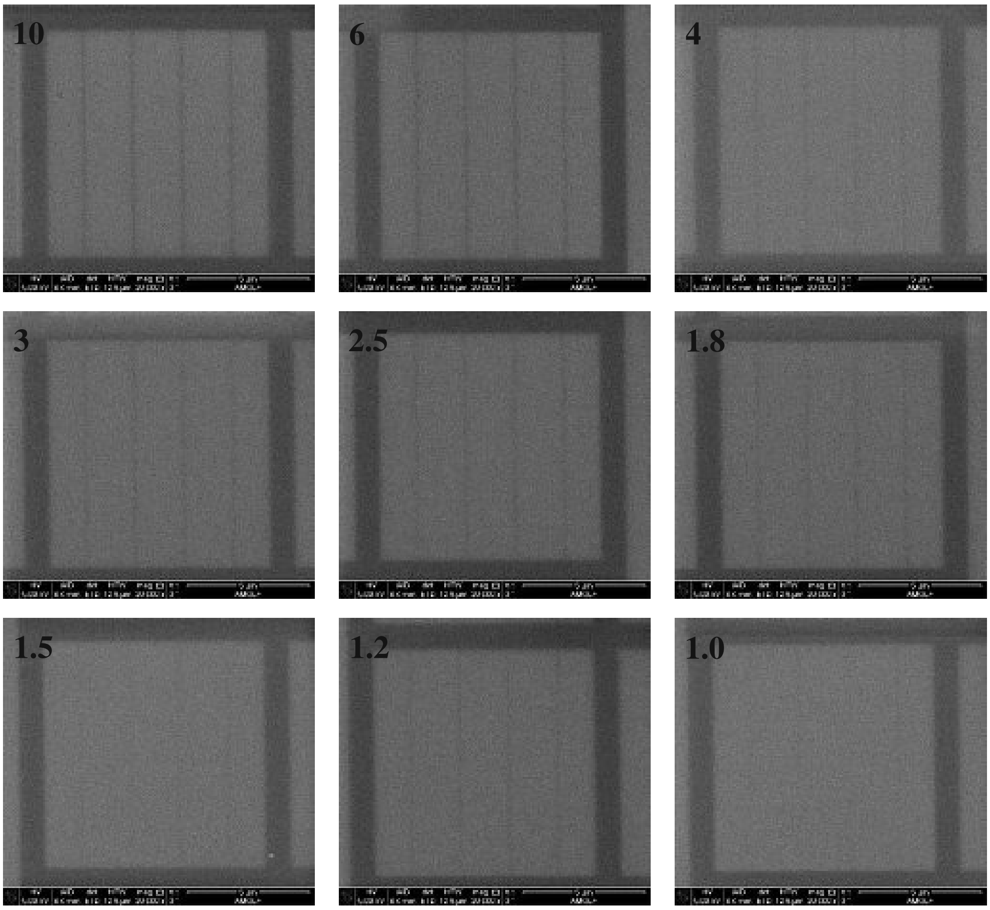

*Figure 8-13: SEM images of area dose test, single-pixel line patterning for* $Hf_4O_2(OMc)_{12}$ *from dose factor 10 to 1.0 as well as radiant patterning (Area dose: 50 µC/cm² and Line dose: 50 ρC/cm).*

### 8.1.5 $Zr_{12}O_8(OH)_8(OMc)_8(OAc)_{16} \cdot 6HOAc$

The last metal oxo cluster that was tested with electron beam lithography was $Zr_{12}O_8(OH)_8(OMc)_8(OAc)_{16} \cdot 6HOAc$. It is a dual-core structure consisted of two $Zr_6$ oxo clusters with acetate bridging in between. Given the fact that $Zr_{12}O_8(OH)_8(OMc)_8(OAc)_{16} \cdot 6HOAc$ has less crosslinkable ligands, its sensitivity should be lower than $Zr_4O_2(OMc)_{12}$. As the SEM results indicated the sensitivity of $Zr_{12}O_8(OH)_8(OMc)_8(OAc)_{16} \cdot 6HOAc$ towards e-beam was slightly lower in contrast to $Zr_4O_2(OMc)_{12}$ and $Zr_4O_2(OMc)_x(OPiv)_{12-x}$ clusters. At dosage above 150 µC/cm² and 150 pC/cm for area and line dose respectively could a visible set of patterns with good resolution be generated. Patterns developed with chloroform showed relatively high contrast with limited defects detected (Figure 8-14). However, a phenomenon that is worth mentioning is the exposed material is easily decomposed during SEM imaging. Once the pattern was exposed to electron beam of SEM for scanning, a disappearance of a significant amount of exposed $Zr_{12}O_8(OH)_8(OMc)_8(OAc)_{16} \cdot 6HOAc$ could be noticed.

Despite of requiring higher doses in electron beam lithography, different results in terms of sensitivity can potentially be obtained under EUV patterning since the metal moiety will become a critical feature. More metal components in a single cluster should increase linear absorption of the photoresist material and improve sensitivity towards EUV exposure. Consequently, $Zr_{12}O_8(OH)_8(OMc)_8(OAc)_{16} \cdot 6HOAc$ is expected to be more sensitive than $Zr_4O_2(OMc)_{12}$ and $Zr_4O_2(OMc)_x(OPiv)_{12-x}$.

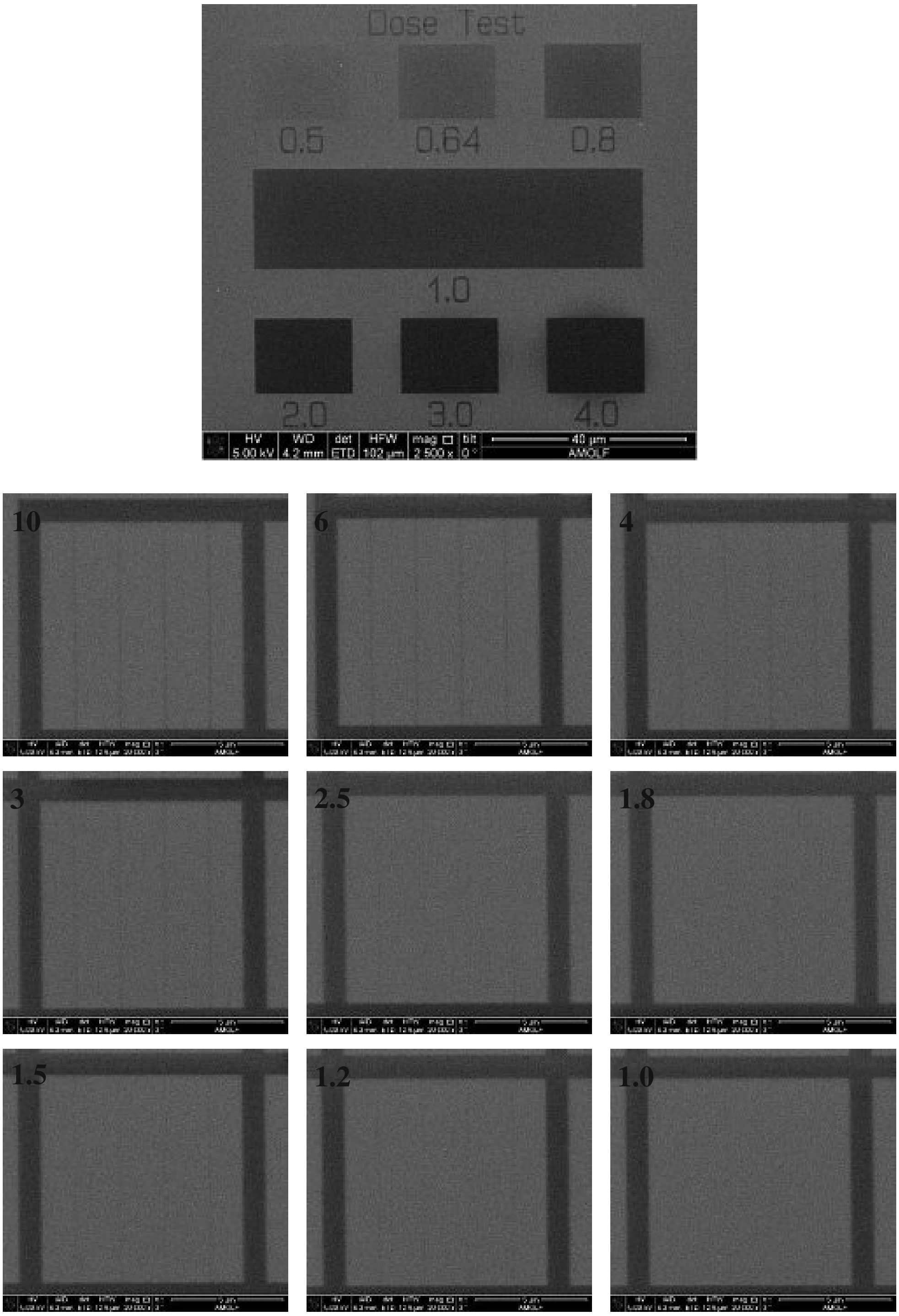

*Figure 8-14: SEM images of area dose test, single-pixel line patterning for $Zr_{12}O_8(OH)_8(OMc)_8(OAc)_{16} \cdot 6HOAc$ from dose factor 10 to 1.0 as well as radiant patterning (Area dose: 150 μC/cm$^2$ and Line dose: 150 ρC/cm).*

## 8.2 Summary

Attributed to resembling photochemical mechanism as well as more assessable facility, electron beam lithography is considered as a much similar technique that is used to evaluate photoresist capability towards EUV exposure. Secondary electron plays a crucial role in both lithography approaches in terms of triggering chemical reaction for resist solubility switch. $Zr_4O_2(OMc)_{12}$ was first test to set a benchmark for the other metal oxo clusters. Despite of few failures at the beginning resulted from inappropriate developers employed, it showed a good patternability. Defects such as pattern collapse or distortion were barely seen in the patterns. Its sensitivity upon electron beam is relatively high, with acceptable patterning quality down to area dose 25 $\mu C/cm^2$ and Line dose: 25 $\rho C/cm$.

On the other hand, the mixed-ligand clusters ($Zr_4O_2(OMc)_3(OPiv)_9$, $Zr_4O_2(OMc)_6(OPiv)_6$ and $Zr_4O_2(OMc)_9(OPiv)_3$) have very distinct lithographic properties. Besides the initial doses required for an acceptable pattern was higher than $Zr_4O_2(OMc)_{12}$, it is realised that crosslinking density of a cluster, namely methacrylate content in this case, can significantly influence material sensitivity in EBL. At the same dose, $Zr_4O_2(OMc)_3(OPiv)_9$ has the least exposed materials remaining on the silicon wafer surface, whereas $Zr_4O_2(OMc)_9(OPiv)_3$ has the most. The results indicate if a cluster with higher crosslinking density, electron beam can lead to a formation of crosslinked structure in an efficient manner. Cluster containing less crosslinkable ligands needs more electron input to reach a higher crosslinked system. This fact also applies to EUVL capability of these mixed-ligand clusters.

Unlike EUVL photoresist, metal moiety does not make a great impact on material sensitivity towards electron beam lithography. Yet Ti-Zr oxo clusters originally required a much higher dose to generate patterns with acceptable quality in contrast to $Zr_4O_2(OMc)_{12}$, which was unexpected since their crosslinking density is comparable to that of $Zr_4O_2(OMc)_{12}$. Until a more polar developer mixture (chloroform and ethyl acetate 1:3 by vol.) was employed, the patterns have shown pronounced contrast at low doses and pattern collapse as well as distortion defects did not occur.

Having a similar crystal structure as $Zr_4O_2(OMc)_{12}$, $Hf_4O_2(OMc)_{12}$ exhibited an identical patterning performance. Overdose started to take place above dose factor 0.64 with an initial area dose of 50 $\mu C/cm^2$, while formation of lines with a single-pixel width became struggle below dose factor 1.5 in line dose test (line dose: 50 $\rho C/cm$). But their sensitivities are expected to be different attributed to higher linear absorption coefficient hafnium has.

Furthermore, $Zr_{12}O_8(OH)_8(OMc)_8(OAc)_{16} \cdot 6HOAc$ showed an acceptable patterning capability with initial area dose of 150 μC/cm$^2$ and line dose of 150 ρC/cm. Its lower sensitivity in comparison with $Zr_4O_2(OMc)_{12}$ is mainly due to less crosslinkable ligand content as well as the bulky crystal structure that can potentially block the way of reactive species binding with adjacent active sites or ligands. Nevertheless, its higher metal moiety is capable of capturing more EUV photons and therefore should increase the sensitivity upon EUV exposure.

Electron beam lithography has provided an explicit understanding regarding patterning capability of these metal oxo clusters. Despite of different exposure source employed, process conditions should remain the same and feasible in EBL and EUVL. Metal element becomes a key constituent for EUV resist material. Hence, the sensitivity of some cluster is expected to be improved relative to EBL and reveal significant potentials with respect to downsizing feature sizes.

# 9 Extreme Ultraviolet Lithography

Due to low accessibility of EUV source, EUVL was conducted after successful patterning of the metal oxo clusters was achieved via electron beam lithography. The main experiments were carried out with the XIL-II (EUV-IL) beamline at Swiss Light Source (SLS) synchrotron facility of Paul Scherrer Institute (PSI) in Villigen, Switzerland, which included contrast curve analysis and line/space patterning in order to understand the material sensitivity as well as resolution limitation.

Resist contrast is an approach to study photoresist conversion of aerial image during exposure into spatial distribution as an actual physical image. Exposure of contrast curve is essentially open-framed, meaning no photomask is involved for creating patterns. Instead, it is performed by exposing a resist material coated on a silicon wafer to different doses of light source at multiple locations. The remaining film thickness of each position was measured after development and plotted as a function of exposing dose, as shown in Figure 9-1. Contrast of the material can be effectively indicated by the slope of diagram. Contrast can further be defined mathematically as:

$$\gamma = \left|\log(\frac{E_0}{E_1})\right|^{-1}$$

where γ is resist contrast; $E_0$ (or dose-to-clear) and $E_1$ are doses determined by extrapolated the slope to normalised thickness to 0 and 1, respectively [4].

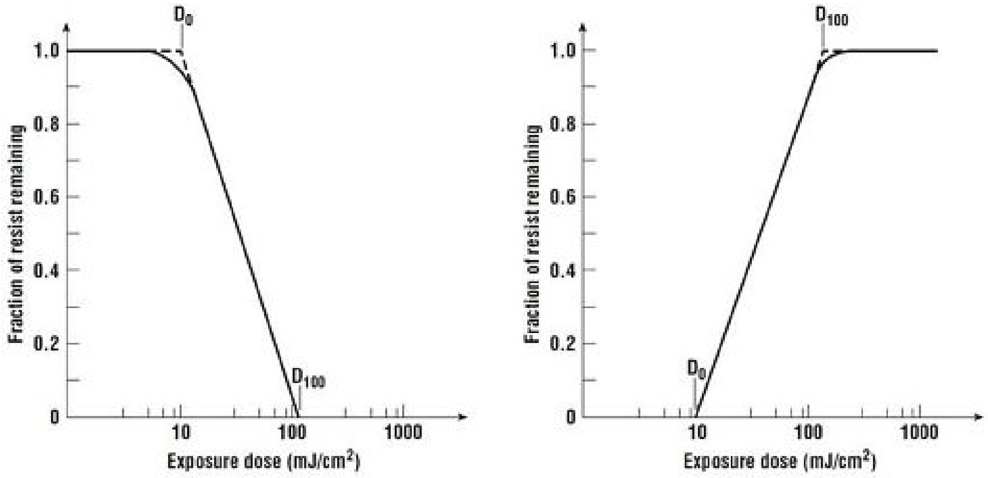

*Figure 9-1: Typical contrast curve diagrams of idealised a) positive tone resist and b) negative tone resist [95].*

On the other hand, line/space patterning is performed via interference mechanism, where two parallel gratings were employed for diffracting incident coherent synchrotron beam. The two beams will interfere in a specific distance from the mask and generate sinusoidal aerial image, which eventually leads to the formation of periodic and quasi-periodic nanopattern (Figure 9-2) [96, 97]. This setup has not just made evaluating existing and novel EUV photoresist with respect to resolution, line edge roughness and sensitivity more accessible for researchers of multiple fields, but helped semiconductor industry to optimise manufacturing process as well as tool design for high volume manufacturing.

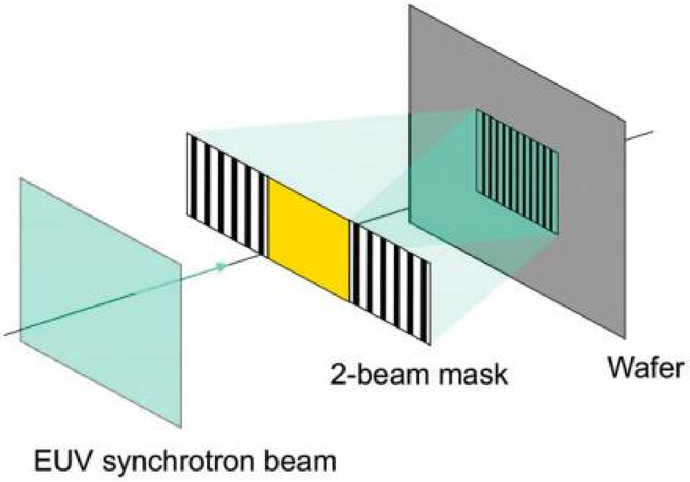

*Figure 9-2: Schematic illustration of the mechanism of line/space patterning at XIL-II beamline* [97].

## 9.1 Experimental and Process Conditions

The metal oxo clusters including zirconium oxo clusters ($Zr_4O_2(OMc)_{12}$, $Zr_4O_2(OMc)_3(OPiv)_9$, $Zr_4O_2(OMc)_6(OPiv)_6$, $Zr_4O_2(OMc)_9(OPiv)_3$, $Zr_4O_2(OVinac)_{12}$, $Zr_4O_2(ODiMc)_{12}$ and $Zr_{12}O_8(OH)_8(OMc)_8(OAc)_{16}\cdot 6HOAc$), multi-metallic oxo clusters ($Ti_4Zr_4O_6(OBu)_4(OMc)_{16}$, $Ti_2Zr_4O_4(OBu)_2(OMc)_{14}$, $Ti_4Zr_2O_4(OBu)_6(OMc)_{10}$ and $Ti_2Zr_5HfO_6(OMc)_{20}$) and hafnium oxo cluster ($Hf_4O_2(OMc)_{12}$) were packed in sealed HPLC glass vials inside the glovebox at TU Wien beforehand. Each vial contained 10 mg of material for the preparation of casting solution with 1% w/v concentration. Solvents for spin-coating and development were also pre-dried over 4 Å molecular sieves before being distilled at TU Wien. After distillation, these dry solvents were stored under argon and brought to PSI for the experiments.

Casting solutions of the metal oxo clusters were prepared on-site shortly before spin-coating without a glovebox. The casting solvents and spin-coating parameters employed were identical as mentioned in the previous chapter. Silicon wafers were cut into either 1 cm x 1cm or 2 cm x 2 cm squares. There was no pre-treatment on silicon wafers for cleaning. Except solution preparation, the rest of the procedure including spin-coating, exposure and development were conducted inside the cleanroom. After spin-coating was completed, the coated wafers were loaded onto a special sample holder that was then transferred into the exposing chamber immediately. An exposure map containing required doses was composed in advance. The positions of exposing points and EUV dose would also vary depending on the experiment (contrast curve or line/space patterning). The photomask employed contained line/space patterns with half-pitch size from 50, 40, 30 to 22 nm.

When the exposure finished, the silicon wafers were unloaded carefully from the sample holder. Developing process was carried out at once to prevent further hydrolysis of the unexposed materials. 20 to 30 mL of respective dry developer (or developer mixture) was employed for each exposed wafer. After being used, the solvent bottle was purged with nitrogen in case its water content increased. The developed silicon wafers were stored properly for AFM and SEM measurement at TU Wien.

## 9.2 Results

### 9.2.1 Zirconium Oxo Clusters

#### 9.2.1.1 $Zr_4O_2(OMc)_{12}$ and Mixed-Ligand Clusters

The previous E-beam patterning results have indicated that crosslinking density of metal oxo cluster has a crucial influence on the sensitivity towards electron beam. The same effect is also expected upon EUV exposure since crosslinking pathway is one of the possible mechanisms for initiating solubility switch. It is understandable that at the same EUV dose, if a metal oxo cluster has higher crosslinking density, there will be more allyl groups (C=C) in the system for free radicals to react and propagate to form a crosslinked structure. Whereas, a cluster with low crosslinking density has limited positions for free radicals to react, which also causes these free radicals to decay via different routes instead reacting with neighbouring molecules. Hence, the dose required to properly pattern a low crosslinking-density metal oxo cluster is relatively higher than the high cross-linking ones (Figure 9-3).

Except the ligand compositions, the core structures and formations of $Zr_4O_2(OMc)_{12}$ and $Zr_4O_2(OMc)_x(OPiv)_{12-x}$ (x=3, 6, 9) are nearly identical. It was believed that their sensitivity should correspond with the increase in the number of methacrylate ligand. The contrast curves indeed revealed that the slope of $Zr_4O_2(OMc)_{12}$ is the highest but very close to that of $Zr_4O_2(OMc)_9(OPiv)_3$, indicating their sensitivities are similar. Nevertheless, even though the solubility switch of $Zr_4O_2(OMc)_3(OPiv)_9$ started at higher doses compared with other the materials, the calculated contrast value of $Zr_4O_2(OMc)_6(OPiv)_6$ is slightly lower than that of

$Zr_4O_2(OMc)_3(OPiv)_9$ (1.098 and 1.357), which is unexpected considering the difference in crosslinking density. The major reason may lie in the development process and developer employed. Given the fact that there was no appropriate developing tool at PSI, the process was strongly depending on the operator. Once a step was delayed or varied, the result could also be influenced. The other reasonable explanation is related to the developer. Since the exposures of $Zr_4O_2(OMc)_6(OPiv)_6$ and $Zr_4O_2(OMc)_3(OPiv)_9$ were conducted in two separate batches, meaning the development also took place at different times, the increase of water content in the developing solvents could significantly affect development quality, as developing process was carried out under air rather than inert atmosphere.

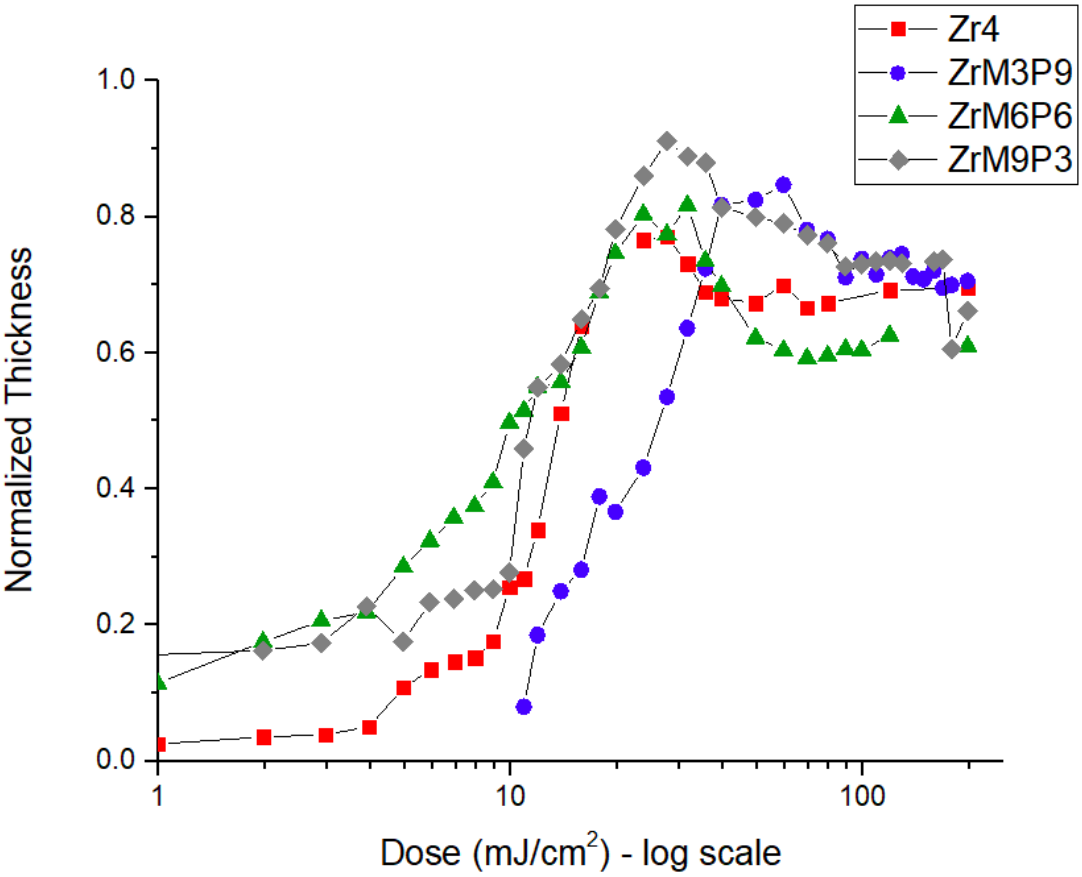

*Figure 9-3: Contrast curves of $Zr_4O_2(OMc)_{12}$ and Mixed-Ligand Cluster.*

The minimum dose required for line/space patterning can be estimated from the results of contrast curve. Essentially, the value is very close to the dose-to-clear of material multiplied by tool factor (usually between 2.5 to 3.0). SEM imaging has revealed that $Zr_4O_2(OMc)_{12}$ shows good EUVL patterning capability, with the feature clearly being observed from 50 nm to 22 nm HP (Figure 9-4). Distortion of lines becomes more obvious when feature size decreases. It is potentially attributed to the high thickness of coated resist film. The extreme aspect ratio of lines at smaller pitches can leads to deformation and even pattern collapse more easily. Another reason is connected to the developer. Due to its high vapour pressure and environmental concerns, chloroform is not being considered as a good developer in many cases. In order to compensate its high evaporating rate and increase polarity, additional ethyl acetate was added into the developer mixture. Even though this mixture was feasible in electron beam patterning, it is apparently required further optimisations in terms of EUV lithography, especially on smaller-feature patterning.

| **50 nm HP** | **40 nm HP** |
|---|---|
| 28 mJ/cm$^2$<br>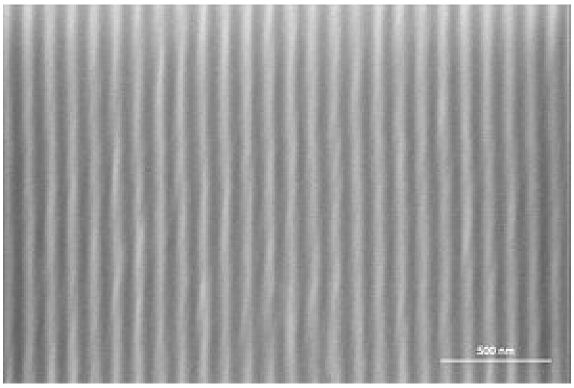<br> | 28 mJ/cm$^2$<br>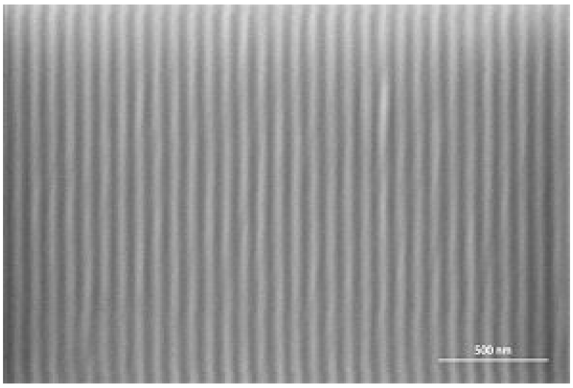<br> |
| **30 nm HP** | **22 nm HP** |
| 28 mJ/cm$^2$<br>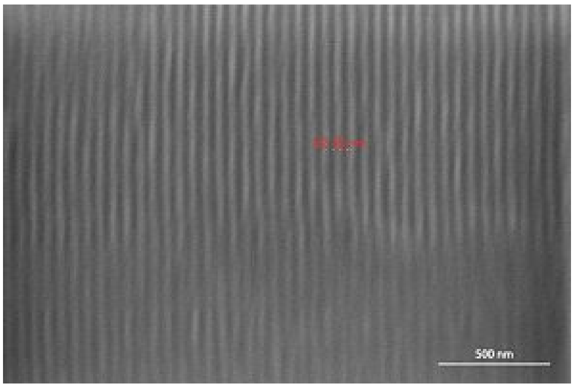<br> | 28 mJ/cm$^2$<br>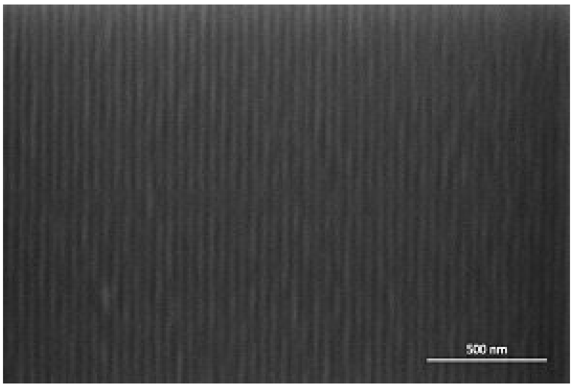<br> |

*Figure 9-4: SEM images of $Zr_4O_2(OMc)_{12}$ line/space patterns.*

The dose for successful $Zr_4O_2(OMc)_3(OPiv)_9$ line/space patterning is higher compared to that of $Zr_4O_2(OMc)_{12}$. Despite the feature was clearly developed at 50 nm and 40 nm HP using 30 mJ/cm$^2$, distortion of lines has started to appear already at 30 nm HP and the feature can be barely observed at 22 nm HP (Figure 9-5). These phenomena indicate that $Zr_4O_2(OMc)_3(OPiv)_9$ has its sensitivity upon EUV exposure lower than $Zr_4O_2(OMc)_{12}$ under the same processing condition. Quality of the pattern can possibly be improved via higher dose yet exposing time will substantially increase that leads to a lower throughput.

| **50 nm HP** | **40 nm HP** |
|---|---|
| 30 mJ/cm$^2$<br>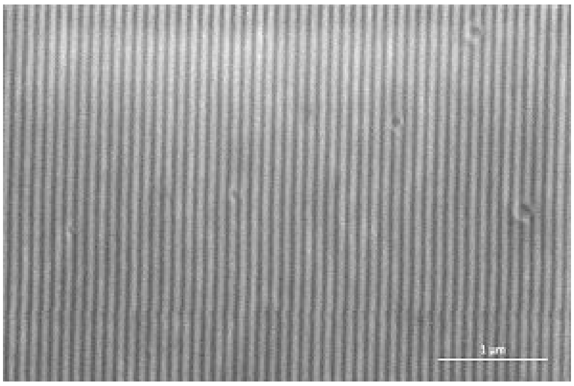<br> | 30 mJ/cm$^2$<br>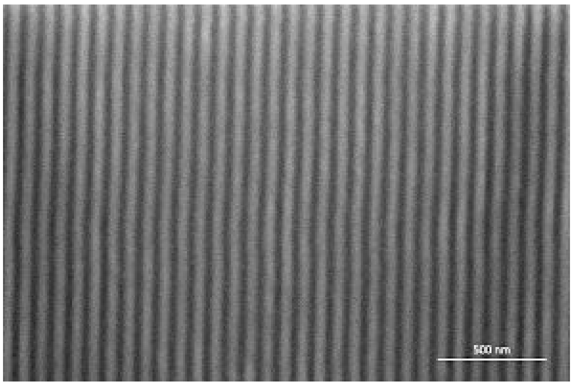<br> |
| **30 nm HP** | **22 nm HP** |
| 30 mJ/cm$^2$<br>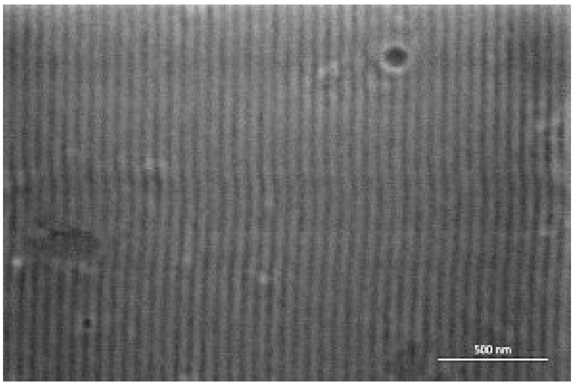<br> | 30 mJ/cm$^2$<br>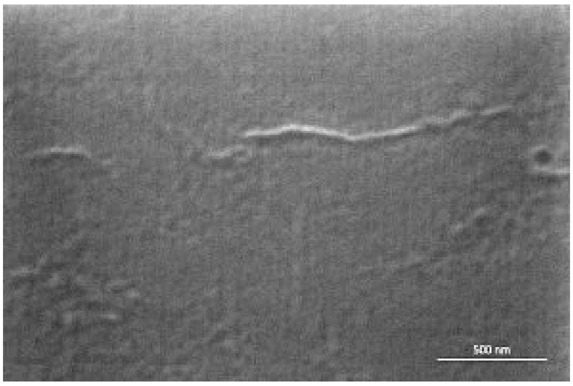<br> |

*Figure 9-5: SEM images of $Zr_4O_2(OMc)_3(OPiv)_9$ line/space patterns.*

Influence from thick coated film as well as developer mixture has become significant on patterning performance in the cases of $Zr_4O_2(OMc)_6(OPiv)_6$ (Figure 9-6) and $Zr_4O_2(OMc)_9(OPiv)_3$ (Figure 9-7). Besides deteriorating pattern collapse in low-pitch patterning resulted from unfavourable aspect ratio, the contrast between exposed and unexposed areas is also insufficient. The increasing water content within developing solvents is the major issue. Since the metal oxo clusters are sensitive to water, the developer mixture will fail to dissolve unexposed materials if containing too much water, leaving most of the metal oxo clusters on the surface of silicon wafer. It can not only result in low-contrast patterns but give rise to solid aggregates caused by hydrolysis of the clusters.

| **50 nm HP** | **40 nm HP** |
|---|---|
| 30 mJ/cm$^2$ | 30 mJ/cm$^2$ |

| | |
|---|---|
| 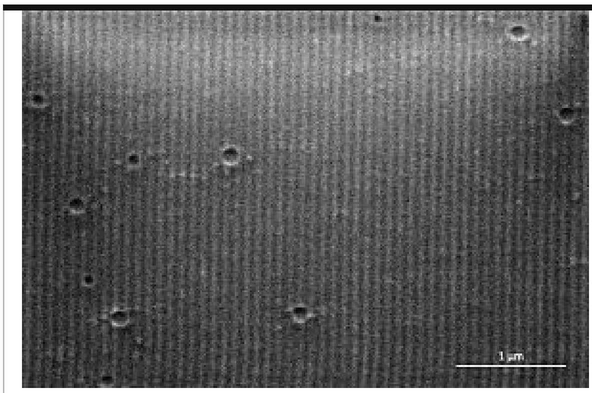<br> | 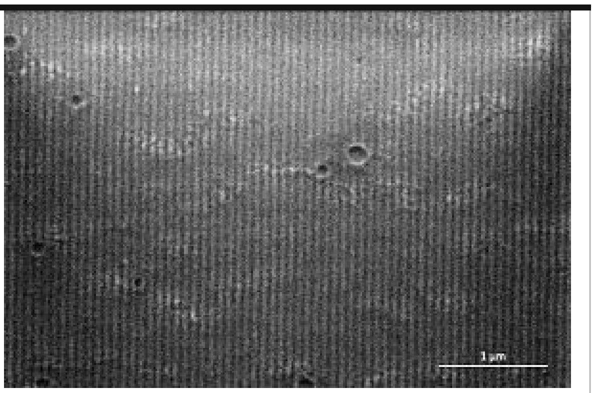<br> |
| **30 nm HP** | **22 nm HP** |
| 30 mJ/cm$^2$<br>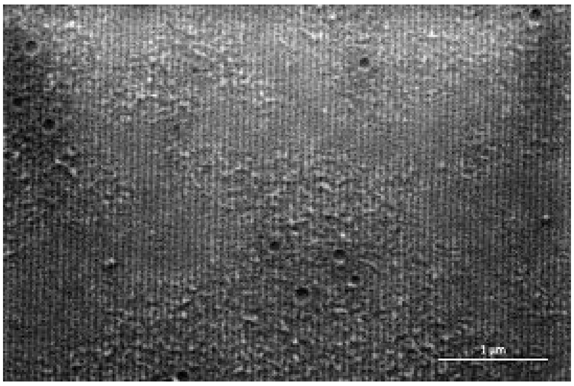<br> | 30 mJ/cm$^2$<br>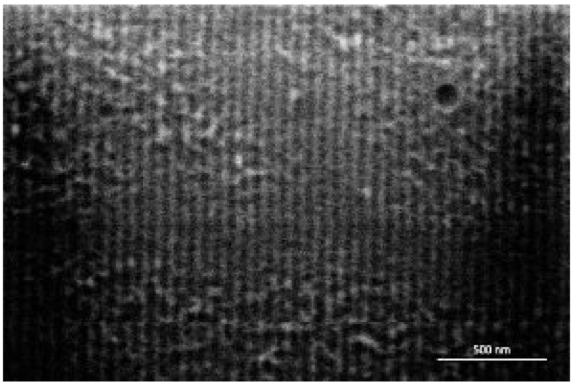<br> |

*Figure 9-6: SEM images of $Zr_4O_2(OMc)_6(OPiv)_6$ line/space patterns.*

Nevertheless, with respect to sensitivity, $Zr_4O_2(OMc)_6(OPiv)_6$ and $Zr_4O_2(OMc)_9(OPiv)_3$ have better performance in comparison to $Zr_4O_2(OMc)_3(OPiv)_9$. Despite of defects, the features in $Zr_4O_2(OMc)_6(OPiv)_6$ line/space patterns can be observed down to 22 nm HP with a dose of 30 mJ/cm$^2$. Whereas $Zr_4O_2(OMc)_9(OPiv)_3$ can be patterned with a dose identical to that of $Zr_4O_2(OMc)_{12}$, with the patterns being visible down to 30 nm HP via SEM imaging. In contrast, the line and space of $Zr_4O_2(OMc)_9(OPiv)_3$ 22-nm-HP pattern are hardly distinguished at 28 mJ/cm$^2$, indicating its sensitivity is still slightly lower than that of $Zr_4O_2(OMc)_{12}$.

From contrast curve as well as line/space patterning of $Zr_4O_2(OMc)_{12}$ and the mixed-ligand clusters, crosslinking density, namely methacrylate content in this case, does have an impact on resist material sensitivity towards EUV photons. However, methacrylate is prone to hydrolyse and leads to material degradation if the process and water content of solvents are not well controlled. As a result, how to reach an agreement on the trade-off between EUV sensitivity and material shelf life becomes an issue for these metal oxide photoresists.

| **50 nm HP** | **40 nm HP** |
|---|---|
| 28 mJ/cm$^2$ | 28 mJ/cm$^2$ |

| 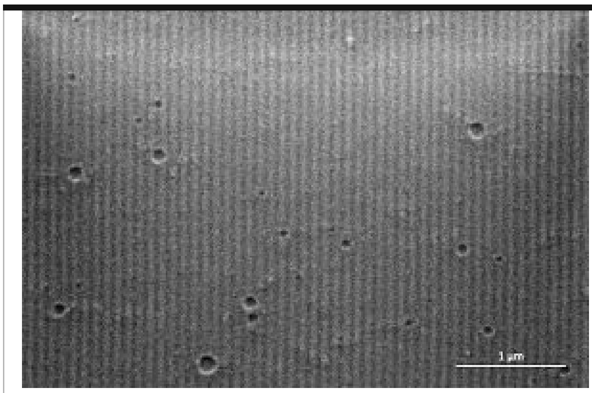 | 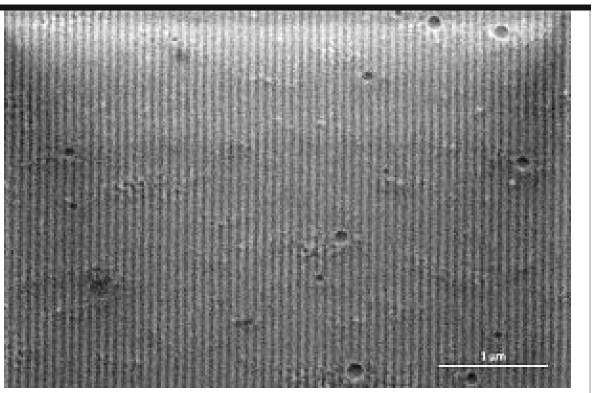 |
|---|---|
| **30 nm HP** | **22 nm HP** |
| 28 mJ/cm$^2$<br>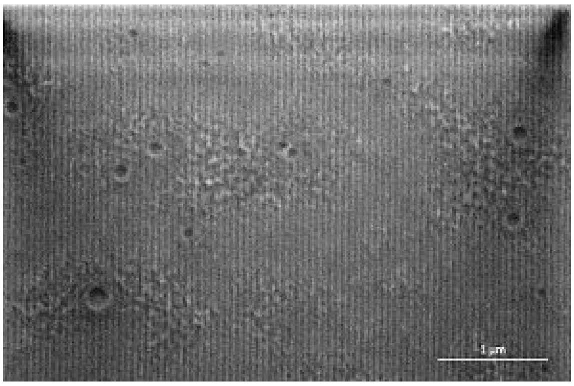 | 28 mJ/cm$^2$<br>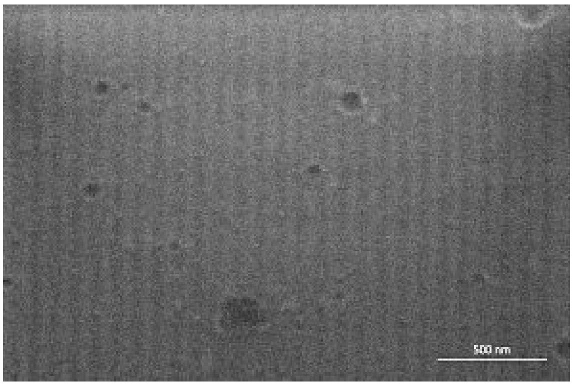 |

*Figure 9-7: SEM images of $Zr_4O_2(OMc)_9(OPiv)_3$ line/space patterns.*

#### 9.2.1.2 Zirconium Oxo Clusters with Different Crosslinkable Ligands

The previous results have indicated that the crosslinking density is closely related to material sensitivity towards both EBL and EUVL. Yet influence of the position of crosslinkable allyl group on the ligand that leads to various steric hindrance during photochemical reactions remains unknown. Having highly resembling crystal structures, $Zr_4O_2(OMc)_{12}$, $Zr_4O_2(OVinac)_{12}$ and $Zr_4O_2(ODiMc)_{12}$ contain three different types of crosslinkable ligands respectively for comparison of patterning performance, helping to evaluate the selection of crosslinkable moiety when designing resist materials.

However, $Zr_4O_2(ODiMc)_{12}$ only showed a limited contrast upon EUV exposure, even though the exposed patterns are physically visible on the silicon wafer. The surface has become very rough with solid aggregates accumulating after development, as shown in Figure 9-8. It is primarily resulted from the inappropriate process conditions employed. The developer chosen for $Zr_4O_2(ODiMc)_{12}$ was chloroform and ethyl acetate (3:1) mixture. Since it has not been patterned by either DUV or electron beam beforehand, this developer mixture was merely tested for its ability to strip off $Zr_4O_2(ODiMc)_{12}$ layer coated on a silicon wafer. Judging from the

AFM imaging, it is highly possible that the developer was too polar to wash away most of the exposed materials as well, leaving a rough and thin layer afterwards. Unfortunately, there was no other opportunity for another trial and therefore successful contrast curve as well as line/patterning of $Zr_4O_2(ODiMc)_{12}$ have not been obtained.

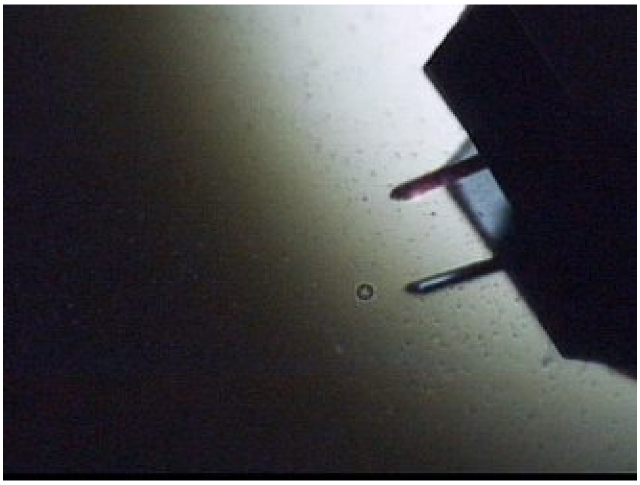

*Figure 9-8: Surface image of $Zr_4O_2(ODiMc)_{12}$ contrast curve analysis acquired via CCD camera of AFM.*

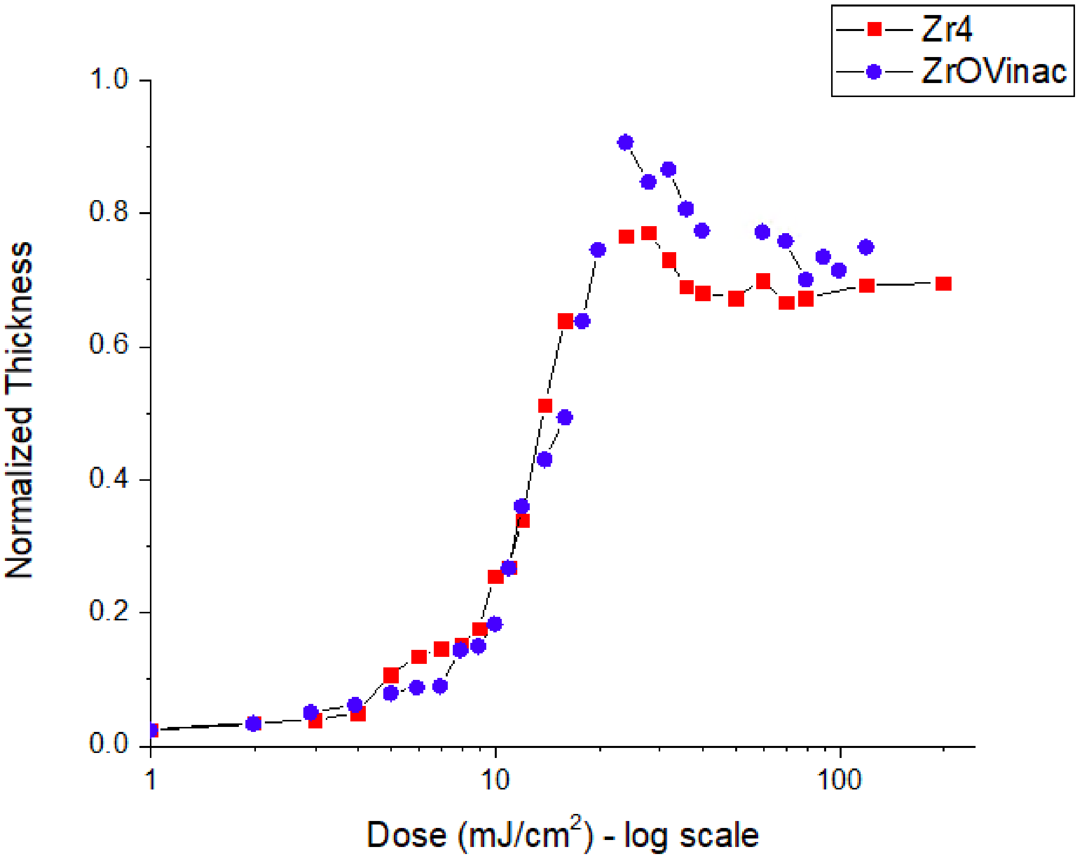

*Figure 9-9: Contrast curves of $Zr_4O_2(OMc)_{12}$ and $Zr_4O_2(OVinac)_{12}$.*

The contrast curve results of $Zr_4O_2(OMc)_{12}$ and $Zr_4O_2(OVinac)_{12}$ have revealed very similar responses upon EUV exposure (Figure 9-9). Considering the two ligand structures, the allyl group of vinylacetic acid has a steric hindrance different from that of methacrylate because of the additional methyl group and the distance with carboxylic group. It turns out these discrepancies only have a slight influence in terms of EUV patterning capability. The doses required for line/space patterning are also identical. Features can be rendered from 50 nm down to 30 nm HP at 28 mJ/cm$^2$. Some deformations are observed in the image of 22 nm HP yet the quality can still be optimised with higher EUV doses (Figure 9-10).

From the comparison of $Zr_4O_2(OMc)_{12}$ and $Zr_4O_2(OVinac)_{12}$ performance, it can be presumed that a minor variance with respect to ligand structure leads to no major effects on EUV lithographic capability of the metal oxo clusters. Nevertheless, more samples with resembling core formations are required to establish a data group that is large enough for giving rise to a convincing conclusion.

| **50 nm HP** | **40 nm HP** |
|---|---|
| 28 mJ/cm$^2$<br>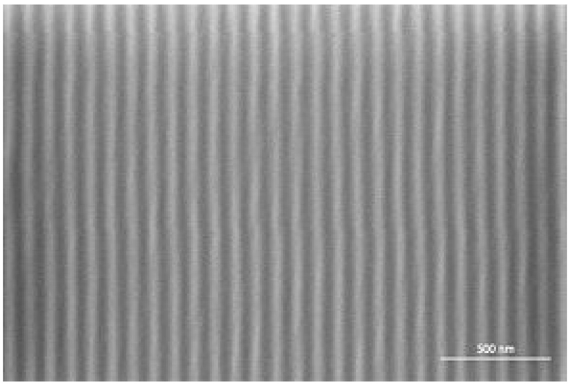<br> | 28 mJ/cm$^2$<br>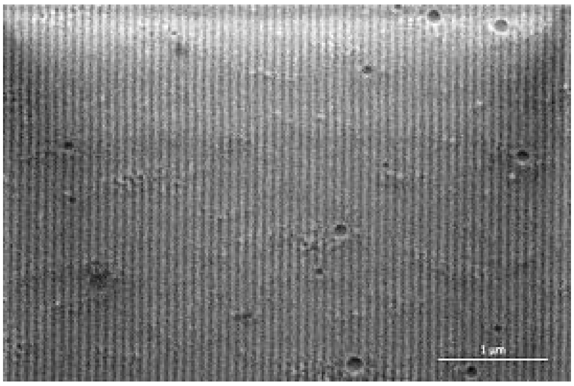<br> |
| **30 nm HP** | **22 nm HP** |
| 28 mJ/cm$^2$<br>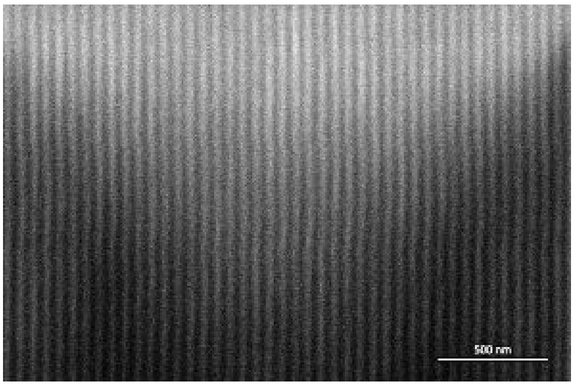<br> | 28 mJ/cm$^2$<br>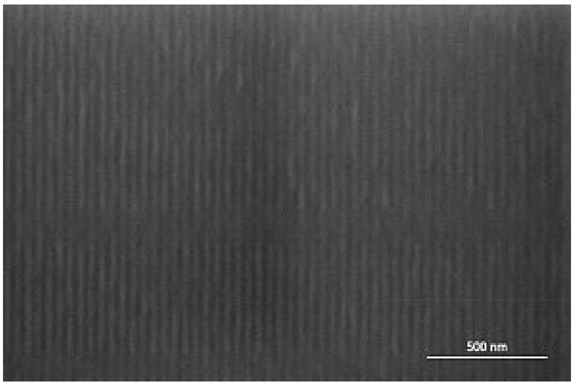<br> |

*Figure 9-10: SEM images of $Zr_4O_2(OVinac)_{12}$ line/space patterns.*

### 9.2.1.3 Zirconium Oxo Clusters with Different Core Formation

The crystal structures of $Zr_4O_2(OMc)_{12}$ and $Zr_{12}O_8(OH)_8(OMc)_8(OAc)_{16}\cdot6HOAc$ are quite different. $Zr_4O_2(OMc)_{12}$ is essentially a single-core crystal with methacrylate ligands attached, while $Zr_{12}O_8(OH)_8(OMc)_8(OAc)_{16}\cdot6HOAc$ is a dual-core cluster that contains two $Zr_6O_4(OH)_4$ with acetate bridging. In terms of crystal size and EUV sensitivity, $Zr_{12}O_8(OH)_8(OMc)_8(OAc)_{16}\cdot6HOAc$ should be theoretically higher than $Zr_4O_2(OMc)_{12}$ considering the number of Zr metal in each material. Yet the results of contrast curve indicate their sensitivities are relatively close under the employed process conditions (Figure 9-11). Additionally, the thickness shrinkage of $Zr_{12}O_8(OH)_8(OMc)_8(OAc)_{16}\cdot6HOAc$ has become substantial at higher doses, which is potentially attributed to its bulky structure. Since mechanisms of solubility switch could undergo either condensation or crosslinking route or both, the distance between neighbouring clusters will be significantly reduced, especially for crystals with larger structures. At higher EUV energy, a quantity of secondary electrons are able to initiate more photochemical reactions for solubility switch within the condensed resist film. Condensation and crosslinking can bring the metal oxo clusters closer to each other and form a much compact crosslinked structure. It is also possible that $Zr_{12}O_8(OH)_8(OMc)_8(OAc)_{16}\cdot6HOAc$ breaks into two $Zr_6O_4(OH)_4$ or smaller fragments upon high EUV exposure. This will be a serious disadvantage for it to be used as photoresist in actual HVM manufacturing.

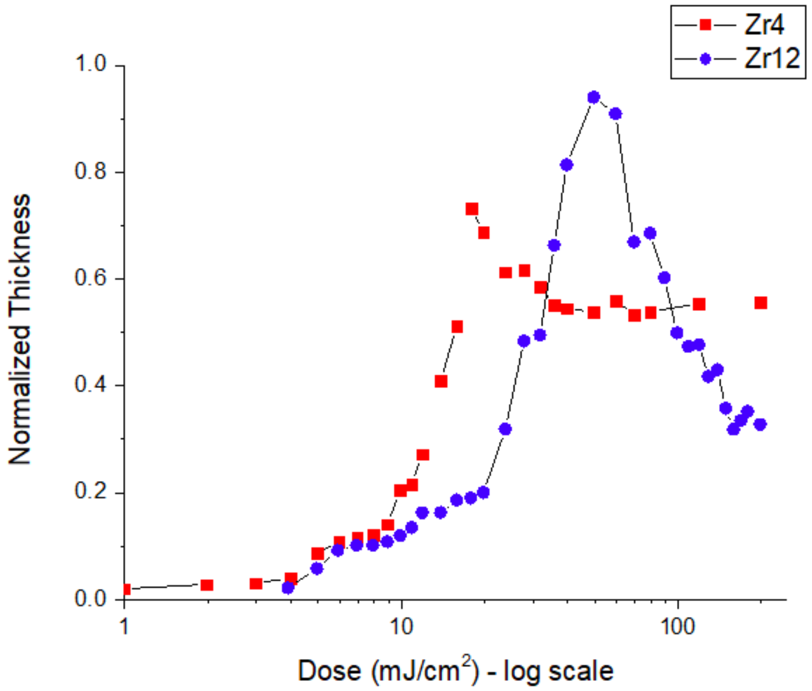

*Figure 9-11: Contrast curves of $Zr_4O_2(OMc)_{12}$ and $Zr_{12}O_8(OH)_8(OMc)_8(OAc)_{16}\cdot6HOAc$.*

On the other hand, line/space patterning of $Zr_{12}O_8(OH)_8(OMc)_8(OAc)_{16}{\cdot}6HOAc$ revealed an insufficient dose of EUV (Figure 9-12). Despite the contrast curves show the sensitivities of these two clusters are resembling, it is apparently $Zr_{12}O_8(OH)_8(OMc)_8(OAc)_{16}{\cdot}6HOAc$ requires a higher dose since the lines are either disconnected or deformed, indicating the solubility has not been completely switched throughout the exposed materials. Therefore, developer was capable of dissolving the areas that was not fully transformed, leaving defective patterns. In this regard, the EUV sensitivity of $Zr_{12}O_8(OH)_8(OMc)_8(OAc)_{16}{\cdot}6HOAc$ is potentially lower than that of $Zr_4O_2(OMc)_{12}$.

| **50 nm HP** | **40 nm HP** |
|---|---|
| 28 mJ/cm$^2$<br>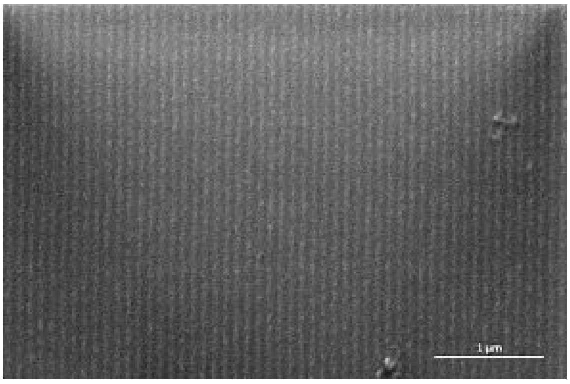<br> | 28 mJ/cm$^2$<br>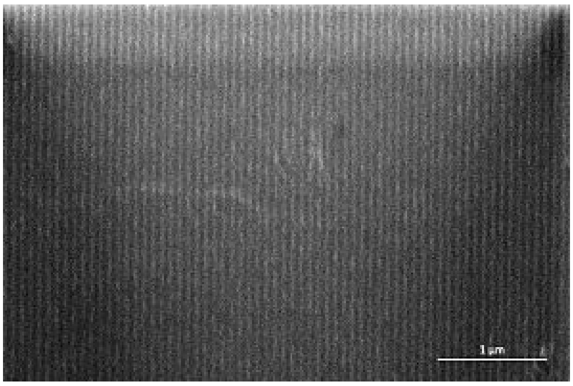<br> |
| **30 nm HP** | **22 nm HP** |
| 28 mJ/cm$^2$<br>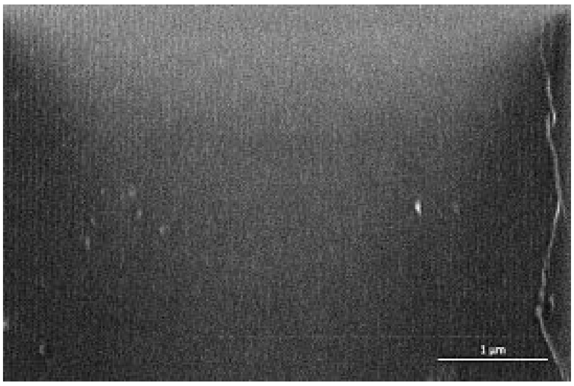<br> | 28 mJ/cm$^2$<br>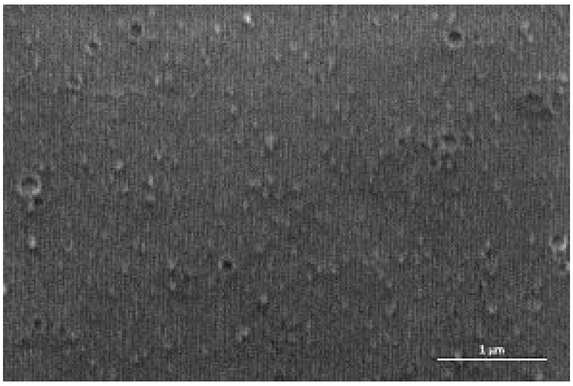<br> |

*Figure 9-12: SEM images of $Zr_{12}O_8(OH)_8(OMc)_8(OAc)_{16}{\cdot}6HOAc$ line/space patterns.*

### 9.2.2 Multi-Metallic Oxo Clusters

In multi-metallic system, the influence of additional metals with high EUV linear absorption coefficient is mainly studied for enabling the understanding on EUV lithographic capability of di- and tri-metallic clusters. In contrast to zirconium, titanium and hafnium have higher optical sensitivity towards EUV photons so the metal oxo clusters embedded with Ti and Hf should have improved sensitivity. Considering only the contrast curves of Ti-Zr clusters, the slope of $Ti_4Zr_4O_6(OBu)_4(OMc)_{16}$ is higher than those of $Ti_2Zr_4O_4(OBu)_2(OMc)_{14}$ and $Ti_4Zr_2O_4(OBu)_6(OMc)_{10}$ owing to its higher overall linear absorption (Figure 9-13). Its larger crosslinking density might also contribute to increasing the EUV sensitivity. On the other hand, $Ti_2Zr_5HfO_6(OMc)_{20}$ has a comparable slope with $Ti_4Zr_4O_6(OBu)_4(OMc)_{16}$, meaning their EUV sensitivities are close. But the surface of $Ti_2Zr_5HfO_6(OMc)_{20}$ is very rough after being developed, which leads to a significant thickness deviation. Moreover, the thickness shrinkage at higher dose is serious compared to Ti-Zr clusters attributed to its relatively bulk structure. This disadvantage will possibly be the reason for downgrading its value as EUVL photoresist unless some optimisations on both material and process can be applied.

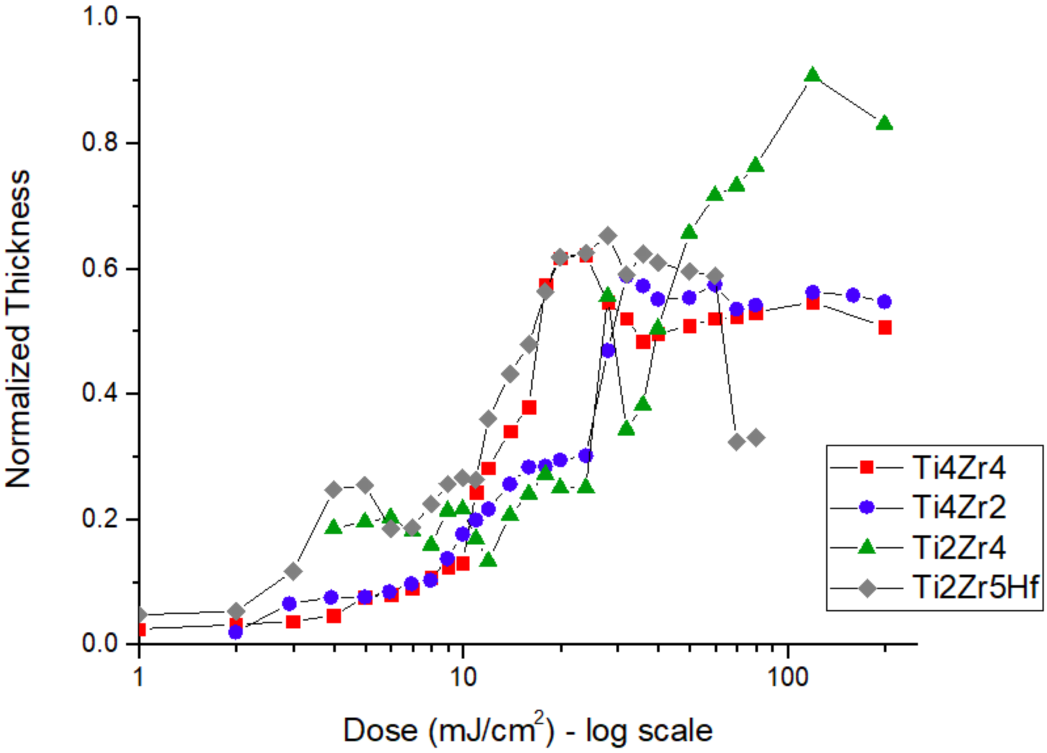

*Figure 9-13: Contrast curves of multi-metallic oxo clusters.*

Essentially, the doses required for line/space patterning of multi-metallic clusters are lower than those of the previous zirconium oxo clusters, revealing a EUV sensitivity improvement caused by additional Ti moieties. At 22.5 mJ/cm$^2$, the features of $Ti_4Zr_4O_6(OBu)_4(OMc)_{16}$ patterns can be clearly rendered from 50 to 30 nm HP (Figure 9-14). Despite the image of 22 nm HP is very blur, which is resulted from insufficient EUV dose or possibly reaching the limitation of SEM, the lines and spaces are still able to be distinguished.

With the same dose, patterns ranging from 50 to 30 nm HP can also be acquired using $Ti_4Zr_2O_4(OBu)_6(OMc)_{10}$ (Figure 9-15). Nevertheless, the dose could be higher for a more successful patterning concerning the fact of deformations and that 22 nm HP pattern is unable to be observed. It is expected the sensitivity of $Ti_4Zr_2O_4(OBu)_6(OMc)_{10}$ is lower yet the material indeed shows good developability and patternability with the process conditions employed.

| **50 nm HP** | **40 nm HP** |
|---|---|
| 22.5 mJ/cm$^2$<br>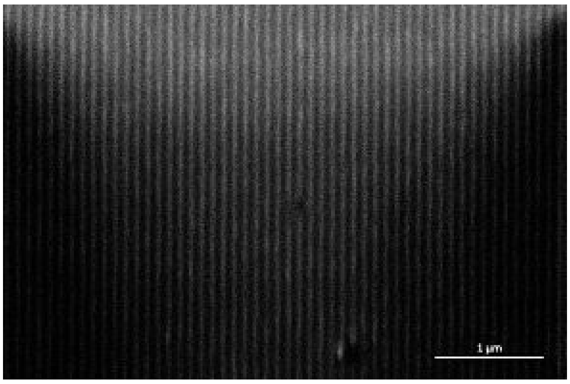 | 22.5 mJ/cm$^2$<br>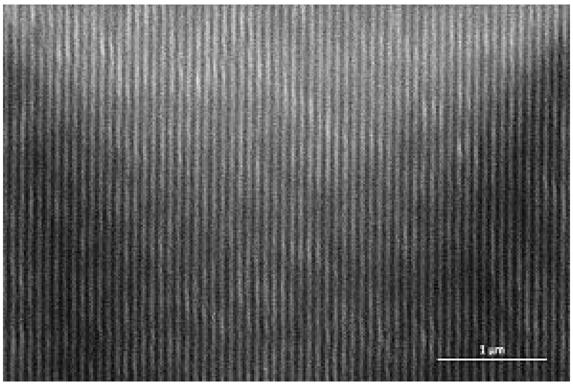 |
| **30 nm HP** | **22 nm HP** |
| 22.5 mJ/cm$^2$<br>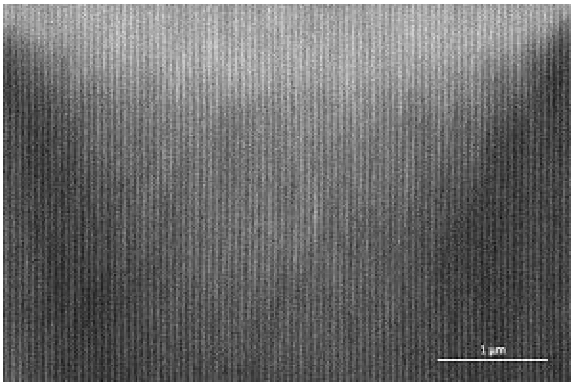 | 22.5 mJ/cm$^2$<br>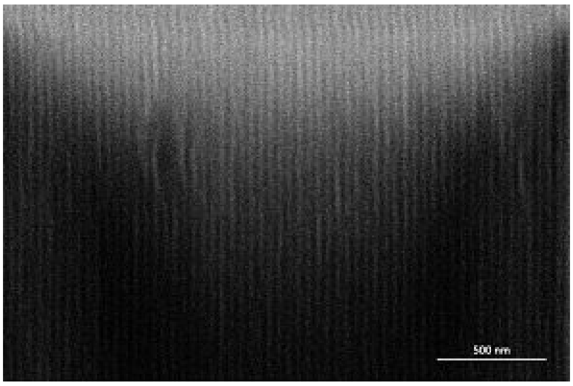 |

*Figure 9-14: SEM images of $Ti_4Zr_4O_6(OBu)_4(OMc)_{16}$ line/space patterns.*

| **50 nm HP** | **40 nm HP** |
|---|---|
| 22.5 mJ/cm$^2$ | 22.5 mJ/cm$^2$ |

| | |
|---|---|
| 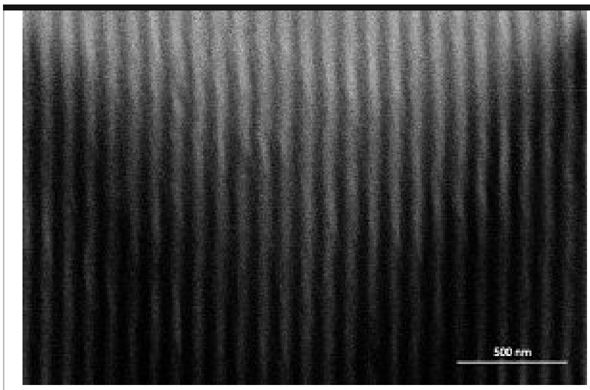 | 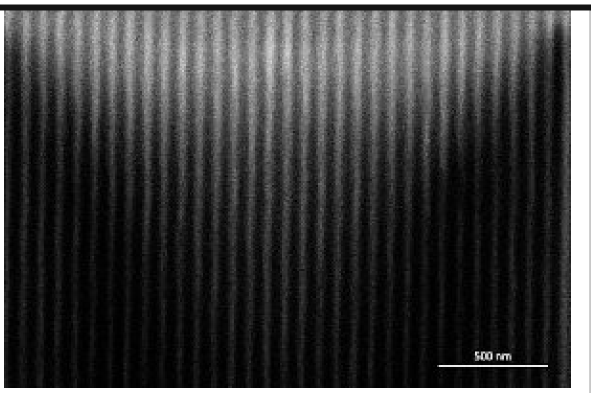 |
| **30 nm HP** | **22 nm HP** |
| 22.5 mJ/cm$^2$<br>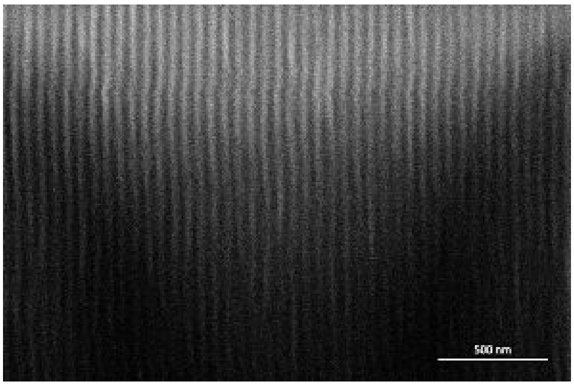 | 22.5 mJ/cm$^2$<br>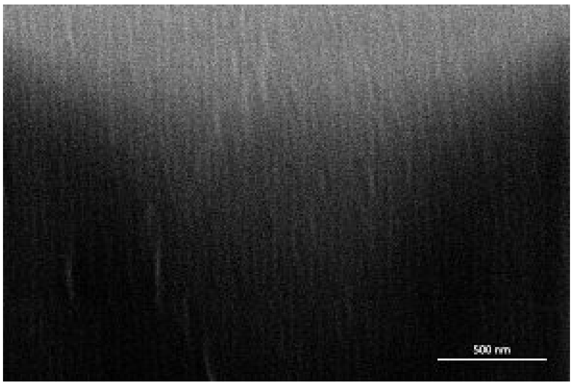 |

*Figure 9-15: SEM images of $Ti_4Zr_2O_4(OBu)_6(OMc)_{10}$ line/space patterns.*

In the case of $Ti_2Zr_4O_4(OBu)_2(OMc)_{14}$, doses needed for acquiring a successful line/space patterning are slightly higher, at 25 mJ/cm$^2$ (Figure 9-16). The pattern contrast is more obvious owing to a thicker coated film yet it also leads to deformations and distortions upon development of smaller HP patterns, which indicates controlling film thickness at in a moderate range (20 nm to 30 nm) is relatively crucial for high-quality patterning. Nevertheless, the defectivity in the $Ti_2Zr_4O_4(OBu)_2(OMc)_{14}$ patterns is still low and therefore it was taken for further investigations at IMEC in terms of mechanism study (outgassing, GATR-FTIR) and line/space patterning with commercially available ASML NEX:3400B lithography tool.

A significant amount of aggregates are observed with the decreasing of feature size in the line/space patterns of $Ti_2Zr_5HfO_6(OMc)_{20}$ (Figure 9-17). In addition, not only the lines have insufficient contrast but disconnectivity occurs throughout the entire patterns. All these phenomena have revealed the inappropriateness of the developer employed for $Ti_2Zr_5HfO_6(OMc)_{20}$ that leads to a failure in developing a successful pattern. The SEM images still show the potential of this trimetallic oxo cluster, but further optimisations are required before being put into HVM as resist material.

| **50 nm HP** | **40 nm HP** |
|---|---|
| 25 mJ/cm$^2$<br>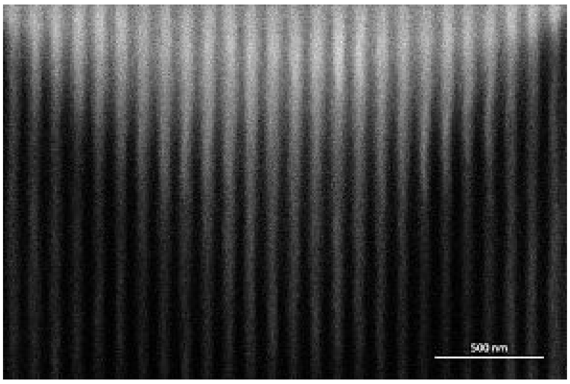 | 25 mJ/cm$^2$<br>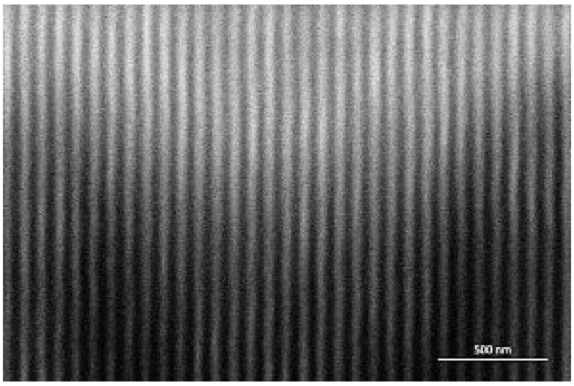 |
| **30 nm HP** | **22 nm HP** |
| 25 mJ/cm$^2$<br>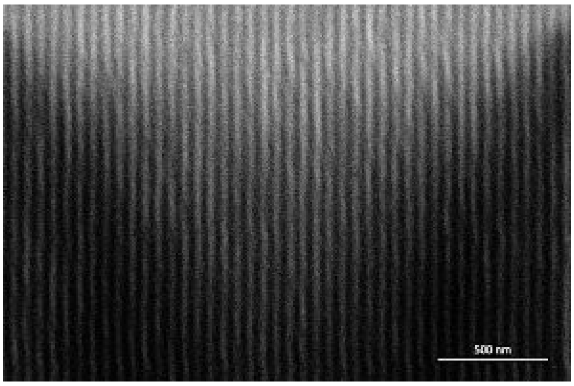 | 25 mJ/cm$^2$<br>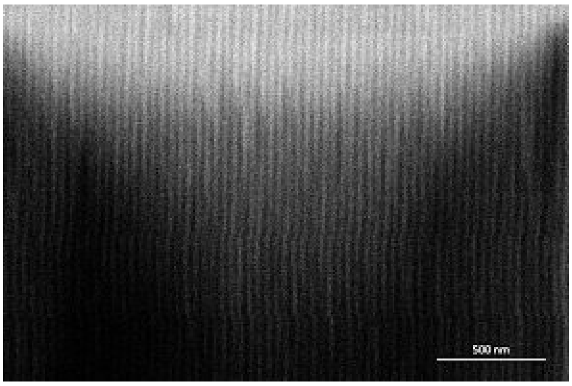 |

*Figure 9-16: SEM images of* $Ti_2Zr_4O_4(OBu)_2(OMc)_{14}$ *line/space patterns.*

| **50 nm HP** | **40 nm HP** |
|---|---|
| 22.5 mJ/cm$^2$<br>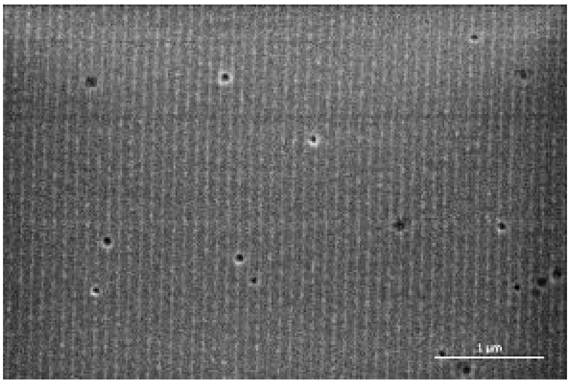 | 22.5 mJ/cm$^2$<br>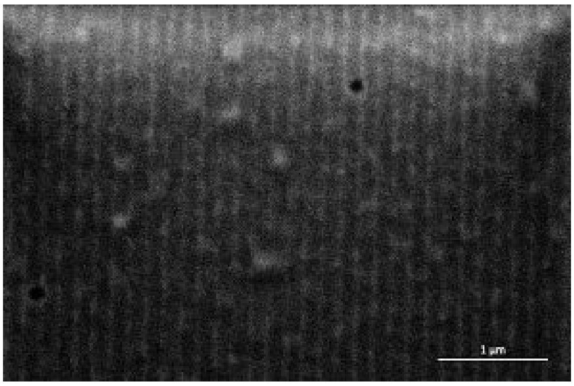 |
| **30 nm HP** | **22 nm HP** |
| 22.5 mJ/cm$^2$ | 22.5 mJ/cm$^2$ |

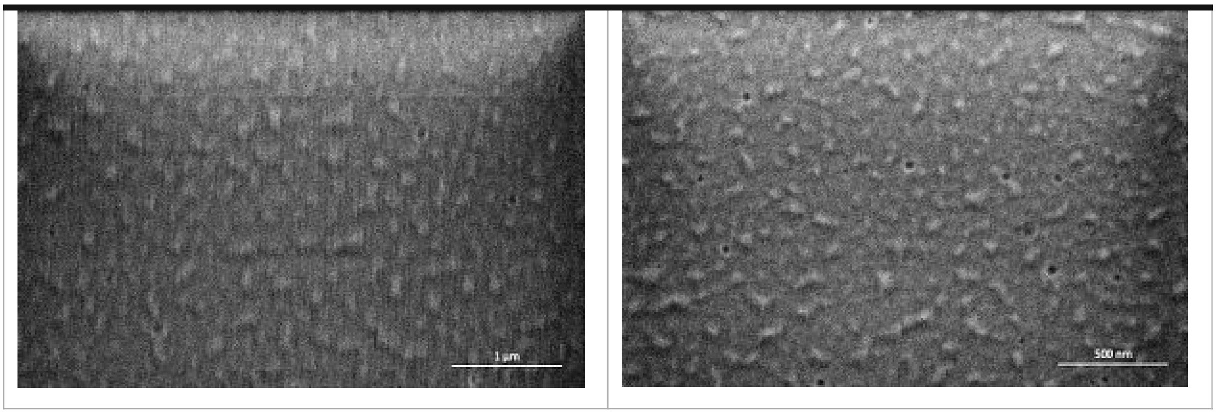

*Figure 9-17: SEM images of $Ti_2Zr_5HfO_6(OMc)_{20}$ line/space patterns.*

## 9.3 Summary

Open-framed contrast curve and interfered line/space patterning EUV exposure were conducted on the metal oxo clusters with SLS XIL-II beamline at PSI for studying their sensitivity and lithographic capability towards EUV photons. Operations including preparation of casting solutions, spin-coating, and developing was conducted on site under air so the influence from ambient moisture on patterning performance should be taken into consideration.

From the comparison of $Zr_4O_2(OMc)_{12}$ and the mixed-ligand clusters ($Zr_4O_2(OMc)_x(OPiv)_{12-x}$), crosslinking density, namely methacrylate proportion in this case, indeed plays a crucial role with respect to increasing resist sensitivity upon EUV exposure. Since there are more possible sites (allyl group) for polymerising in high crosslinking-density materials, crosslinking is more likely and easier to occur at the same dose in contrast to low crosslinking-density ones. On the other hand, effects from the position of allyl group on ligand in terms of material patterning performance remain unclear attributed to the fact that $Zr_4O_2(ODiMc)_{12}$ has not been developed properly in both contrast curve and line/space patterning. Having high structural ligand similarities and limited difference in steric hindrance, $Zr_4O_2(OMc)_{12}$ as well as $Zr_4O_2(OVinac)_{12}$ show close sensitivities and patterning capabilities in EUVL. Further investigations will be applied on comparing the performance of zirconium oxo clusters with identical core formation but various crosslinkable ligands. $Zr_{12}O_8(OH)_8(OMc)_8(OAc)_{16}{\cdot}6HOAc$ did not reveal an improved sensitivity as being expected from the beginning. Instead, it has a comparable sensitivity with that of $Zr_4O_2(OMc)_{12}$ yet inferior patternability with the decrease in feature size. Additionally, the shrinkage issue at high doses is also another serious disadvantage for $Zr_{12}O_8(OH)_8(OMc)_8(OAc)_{16}{\cdot}6HOAc$ to be used in EUVL photoresist applications.

Contrast curve has revealed the improvement resulted from additional metal moieties including titanium as well as hafnium in the system of multi-metallic oxo clusters and their sensitivities are corresponding to the overall EUV linear absorption of the components. Line/space patterning of the materials has also been proven feasible with lower doses in comparison with those of zirconium oxo clusters. Not only pattern contrast is higher owing to better sensitivity, but less distortions and deformations take place after development, both of which make them relatively appropriate for EUVL photoresist applications. Nonetheless, $Ti_2Zr_5HfO_6(OMc)_{20}$ has quite defective patterns with the process conditions employed. Further testings with other developers are required in order to optimise the patterning quality.

$Hf_4O_2(OMc)_{12}$ failed to have successful contrast curve and line/space patterns after being developed. The scenario is similar to that of $Zr_4O_2(ODiMc)_{12}$, as shown in Figure 82, indicating most of the exposed and unexposed materials were dissolved away and the developer employed could be improper. Therefore, the comparison on clusters with resembling structures but different metal moieties cannot be conducted in this research.

# 10 Study of EUVL Photoresist Mechanism

As EUV technology has been employed in semiconductor industry for high volume manufacturing, there still exist some major issues that diminish the production efficiency of EUVL than it is supposed to have. Resist material is one of them. Attributed to the current limitations in EUVL photoresist in terms of patterning capability, companies are forced to take alternative measures for the purpose of achieving narrower feature sizes. Approaches such as multiple patterning, meaning multiple exposures take place for generating patterns beyond its capability, has substantially complicated manufacturing procedure and increased the processing time. Increasing on budget as well as production cost also make products very expensive and unaffordable for most people.

The interactions between ionizing X-ray radiation with resist films in EUVL is essentially distinct in comparison with the resonant photochemistry on DUVL and the interaction of ionizing electrons with resist materials in E-beam lithography [98]. In order to optimise and solve the issues of photoresists, understanding detailed mechanisms on molecular scale of materials upon EUV photons is relatively crucial. However, it is very difficult to directly study the reactions induced in thin-film condensed materials by 92 eV EUV photons [39]. Prediction of secondary electron can neither be simulated by simple mathematical calculations since they undergo a series of complicated elastic and inelastic collision that results in various energy before being detected. Characterisation techniques that can monitor transient structural and energy changes are reckoned as powerful tools for resist mechanism study. Yet most of the measures are still restrained by technical issues of equipment at the moment. For instance, time-resolved transient spectroscopy that is capable of monitoring energy variation of material upon light exposure as a function of time has limited research input due to the lack of femtosecond-pulsed EUV sources [4]. Gas-phase photoemission experiment can be utilised to observe secondary electrons and radicals from isolated molecule [99] but its accessibility is low. More researches are ongoing in this area.

Other characterisations are considered as relatively indirect approaches, which mostly involve examination of structural difference before and after EUV exposure, outgassed species and material fragmentations via energy source with similar energy with EUV photons or secondary electrons. By assessing material behaviours afterwards, conjectures can be made with respect to the construction of a reasonable reactive pathways as well as light-matter interactions between resist materials and EUV photons.

In this work, three different approaches including dissociative electron attachment spectroscopy, outgassing analysis and thin-film IR spectroscopy on EUV-exposed material were conducted for studying detailed interactions of the metal oxo clusters upon EUV photons. The results were combined eventually to make a complete evaluation on the potential mechanisms.

## 10.1 Dissociative Electron Attachment (DEA) Spectroscopy

### 10.1.1 Introduction

Electron-induced chemistry plays a crucial role in the field of microlithography and nanolithography. Generally speaking, a molecule that interacts with high-energy radiation like X-ray and electron beam can be excited and/or ionised or low-energy electrons released are able to induce excitation or ionisation, which can further result in dissociation of the molecule. These fragments might continue reacting with surrounding molecules to generate new products [4]. Since in EUV regime the reaction of resist material is no longer like the case in DUV, which is photon-induced, the origin of solubility switch is primarily triggered by electrons. Electron scattering becomes dominant, leading to various electron energies instead of a well-defined one and these electrons are key to determining the dissociation pathways. The routes of electron travelling are also distinct that a mean free path in the thin film is required. Different chemical interactions in EUV have significantly influenced the capability of photoresists regarding resolution, line-edge roughness and sensitivity.

As mentioned previously, the incident EUV photons with 92 eV leads to formation of a quantity of secondary electrons having energy at 80 eV or below within a thin resist layer. These low energy electrons can cause molecular fragmentations via four main mechanisms, which are dissociative electron attachment (DEA), dissociative ionisation (DI), neutral dissociation (ND) and dipolar dissociation (DD) [100, 101]:

$$AB + e^- \rightarrow AB^{(\#)-} \rightarrow A^{(\#)-} + B^{(\#)} \qquad \text{(Dissociative Electron Attachment)}$$

$$AB + e^- \rightarrow AB^{(\#)+} + 2e^- \rightarrow A^{(\#)+} + B^{(\#)} + 2e^- \qquad \text{(Dissociative Ionisation)}$$

$$AB + e^-(\varepsilon_1) \rightarrow [AB]^* + e^-(\varepsilon_2 < \varepsilon_1) \rightarrow A^{(\#)} + B^{(\#)} \qquad \text{(Neutral Dissociation)}$$

$$AB + e^-(\varepsilon_1) \rightarrow [AB]^* + e^-(\varepsilon_2 < \varepsilon_1) \rightarrow A^{(\#)+} + B^{(\#)-} \qquad \text{(Dipolar Dissociation)}$$

where # indicates the fragment might be in a vibrationally and/or electronically excited state. * symbolises intermediate electronic excitation leads to ND and DD. $\varepsilon_1$ represents the incident energy electron while $\varepsilon_2$ represents the energy of the electron remaining after inelastic scattering.

The molecular dissociation through dipolar dissociation pathway is very limited in photoresist mechanism. Therefore, it is usually excluded from the discussion.

#### 10.1.1.1 Electron Attachment

In the case of electron attachment, a neutral molecule AB captures an electron that leads to the formation of either a transient anion ($AB^-$) or an excited transient anion ($AB^{*-}$) as depicted in Figure 10-1a. From the Franck-Condon theory, the electronic transition is much faster than nuclear motion, meaning the nuclei remain immobilised while molecule having interactions with the electron [102]. Only if the molecule can go from its ground state to the final state of transient ion can an electron be captured. The capturing is indicated as EC (electron capture) via a vertical transition within the Franck-Condon region. The resulted transient species is thermodynamically unstable attributed to not only the ground state can potentially be higher than that of original molecule, but the occupation of orbit can be accompanied by the excitation of the molecule.

The transient anion can relax through four different pathways including reemission of the electron (autodetachment, AD), dissociative electron attachment (DEA), associative attachment and radiative cooling [4] (Figure 10-1a). Among these routes, resist chemistry is predominantly affected by DEA. DEA takes place depends on whether the transient negative ion has its interaction potential preferable for dissociative and the electron affinity of fragmented species. Since the mechanism of EUV is significantly different in comparison with previous DUV technique where photo-induced reaction is irrelevant to the state from which the molecule is originally excited, the energy of incident electron is crucial in determining which orbital it should occupy and as a result affects interaction potential of the resonance as well as determines the dissociative pathways in the end. Previous studies indicated DEA is essentially initiated by electron with energy less than 10 eV [100, 101, 103].

#### 10.1.1.2 Electron Impact Ionisation

Electron impact ionisation starts from the incident electron ionises a neutral molecule by ejecting an electron from its orbital and give rise to an excited positively charged ion. The molecule jumps from the initial energy potential to the final interaction potential curve in just 100 attosecond [104], which results in two possible curves, $AB^{'*+}$ and $AB^{*+}$ (Figure 10-1b). Species generated after electron-molecule interactions are composed of an excited cation $AB^{*+}$ and two free electrons, which are incoming electron as well as the ejected electron. The excited species then undergoes relaxation via various decay pathways, especially in the case of multi-atomic molecules. Dissociative ionisation (DI) is one of the possibilities and preferred route in EUVL resist material mechanism since the threshold of electron impact ionisation is above 10 eV [100]. It eventually leads to the formation of a primary ion and a neutral (radical) fragment along with two free electrons.

Even though the determination of ionisation cross section of dissociative ionisation is relatively crucial for many industrial applications, the predictions cannot simply be made by mathematical calculations and neither direct measurements can achieve such evaluation for actual values of molecules.

### 10.1.1.3 Electron Impact Excitation

Mechanism of electron impact excitation is resembling to that of electron impact ionisation, which occurs by a passing electron excites molecule and gives rise to an excited neutral species in a short period of time, followed by a relaxation via three primary pathways. The molecule is able to decay through releasing a photon or transferring energy to neighbouring particles for returning to ground state. The other routes involve the dissociation of the excited molecule. In the case of neutral dissociation (ND), the molecule can dissociate and generate two neutral radicals, whereas in dipolar dissociation (DD) the molecule results in the formation a cation and an anion via dissociative relaxation. ND (4 to 6 eV) usually takes place in the energy range lower than dissociative ionisation since the molecule is not ionised [105]. On the other hand, higher energy (10-15 eV) is required for DD attributed to the production of ions [105].

a) DEA

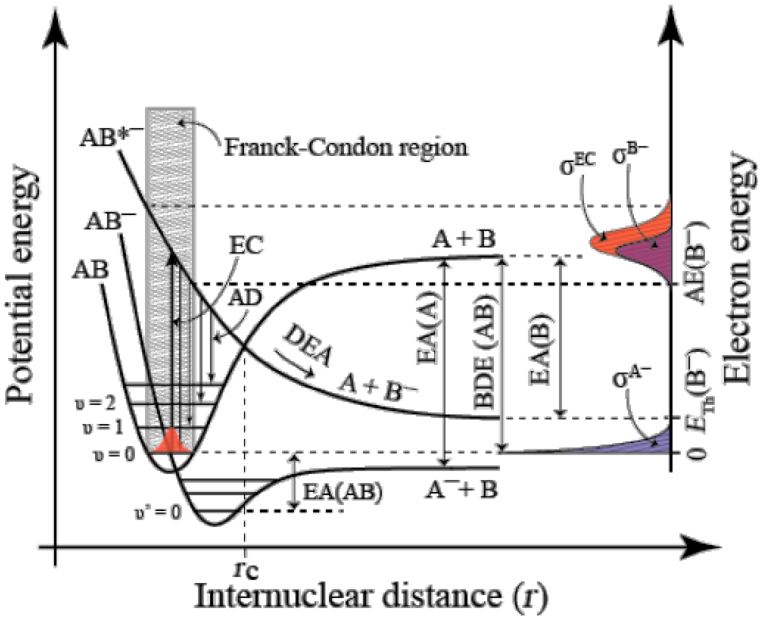

b) DI

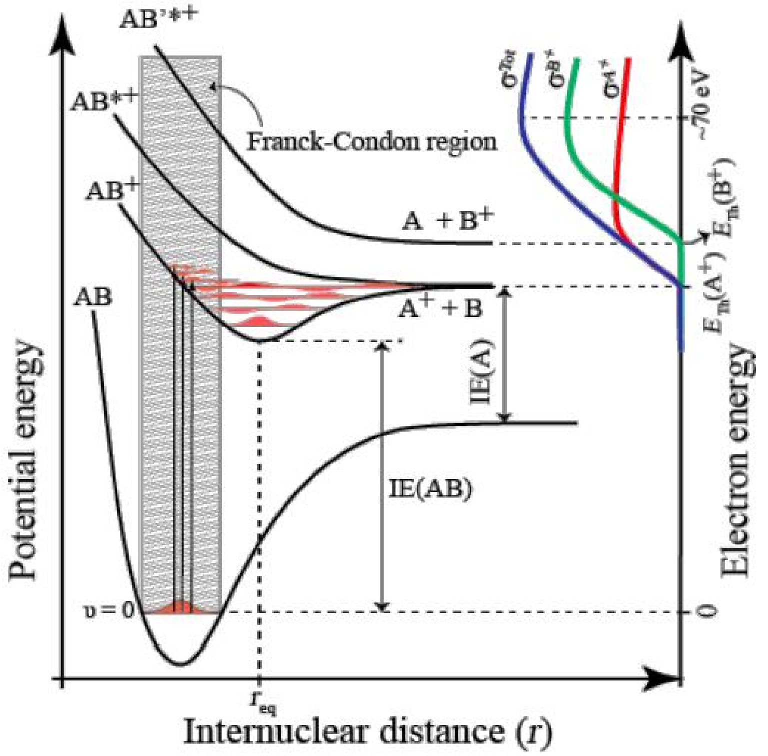

c) ND

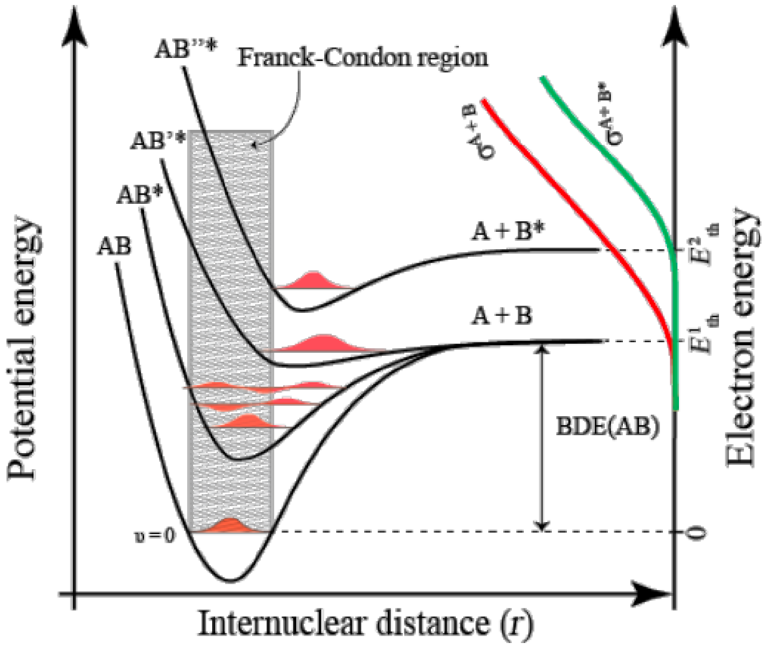

*Figure 10-1: Schematic potential energy diagrams of a) DEA, b) DI and c) ND through electronic excitations* [100].

Understanding of ND in multi-atomic system is rather opaque. Unlike the scenario in DEA, DI and DD, ND only gives rise to neutral products, which makes characterisations and quantification difficult. Therefore, the study regarding ND in electron-induced chemistry and resist material field remains limited and requires the assistance from optimised equipment or setup to enable the detecting of uncharged species.

### 10.1.2 Experimental and Setup

In this work, a dissociative spectroscopy attachment spectroscopy was conducted for the sake of simulating interaction of the photoresist ligands upon low energy electrons. The measurements were carried out in the laboratory of Prof. Janina Kopyra at Siedlce University of Natural Sciences and Humanities in Poland. Three ligand precursors and one of the zirconium oxo clusters ($Zr_4O_2(OMc)_{12}$) were tested in the energy range of 0 eV to 12 eV and fragments were recorded by channel, which was then transferred into molar mass. Details regarding the samples are depicted in Table 8.

*Table 8: Target samples for DEA spectroscopy experiment.*

| Material | Structure | Properties |
|---|---|---|
| **Methacrylic Acid** | 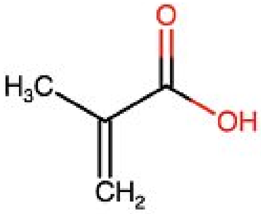 | **Molecular Weight:** 86.09 g/mol<br>**Melting Point:** 14-15 °C<br>**Boiling Point:** 161 °C |
| **3-Butenoic Acid** | 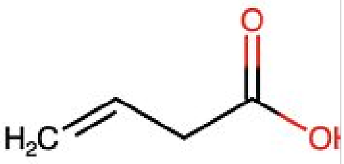 | **Molecular Weight:** 86.09 g/mol<br>**Melting Point:** -39 °C<br>**Boiling Point:** 163 °C |
| **Trans-2,3-dimethacrylic Acid** | 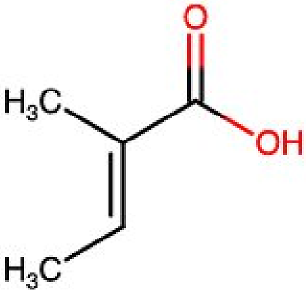 | **Molecular Weight:** 100.12 g/mol<br>**Melting Point:** 61-64 °C<br>**Boiling Point:** 95-96 °C (12 mmHg) |
| **Zirconium Oxo Cluster ($Zr_4O_2(OMc)_{12}$)** | 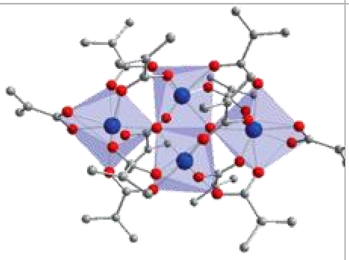 | **Molecular Weight:** 1416 g/mol<br>**Degradation Temperature:** 350 °C |

The DEA spectroscopy setup mainly consists of an electron source, an oven, and a quadrupole mass spectrometer (Figure 10-2). The components dwell in an ultrahigh vacuum (UHV) chamber with pressure level of $10^{-8}$ mbar. The introduction of sample is via either a glass capillary with a heating oven and inlet for liquid materials, or a sample holder directly installed into the chamber for solid materials. Electrons generated by the filaments are projected horizontally into the chamber after their energy being normalised and controlled by monochromator. Gas-phase sample that either sublimes or evaporates under ultrahigh vacuum and increasing temperature is introduced into the reaction chamber where it intersects orthogonally with the well-defined incident electron beam. Impact from the electrons will then results in fragmentation of target sample and turn them into negative charged species. The fragmented anions are extracted by an electric field into the quadrupole mass spectrometer where they are analysed and detected by a single-pulse counting technique [106].

The calibration of energy scale utilises the well-known resonance in sulphur hexafluoride ($SF_6$) as standard. In comparison with the short timescale of electron transition, the lifetime of $SF_6$ transient state is relatively long (at millisecond range). $SF_6$ not only has outstanding DEA cross-section, but also is capable of generating the metastable $SF_6^-$ near 0 eV, which makes it one of the perfect references for DEA experiment [107].

After calibration, the $SF_6$ gas inlet was switched off and a vacuum pump kicks in to remove $SF_6$ residue for at least 15 minutes. The samples were measured from 0 to 12 eV with a 2-second dwell time and different temperatures in order to reach a density that is high enough to yield reasonable anion signals. Additional heating at the inlet and sample holder were also required for avoiding the condensation of material as well as increasing intensity of analysis. The experimental conditions of each sample were list in Table 9.

*Table 9: Experimental conditions of the tested samples for DEA spectroscopy.*

| Material | Chamber Temperature (°C) | Chamber Pressure (mbar) |
|---|---|---|
| **Methacrylic Acid** | 50 | $8.0 \times 10^{-6}$ |
| **3-Butenoic Acid** | 50 | $2.0 \times 10^{-5}$ |
| **Trans-2,3-dimethacrylic Acid** | 65 | $3.0 \times 10^{-6}$ |
| **$Zr_4O_2(OMc)_{12}$** | 120 | $6.0 \times 10^{-6}$ |

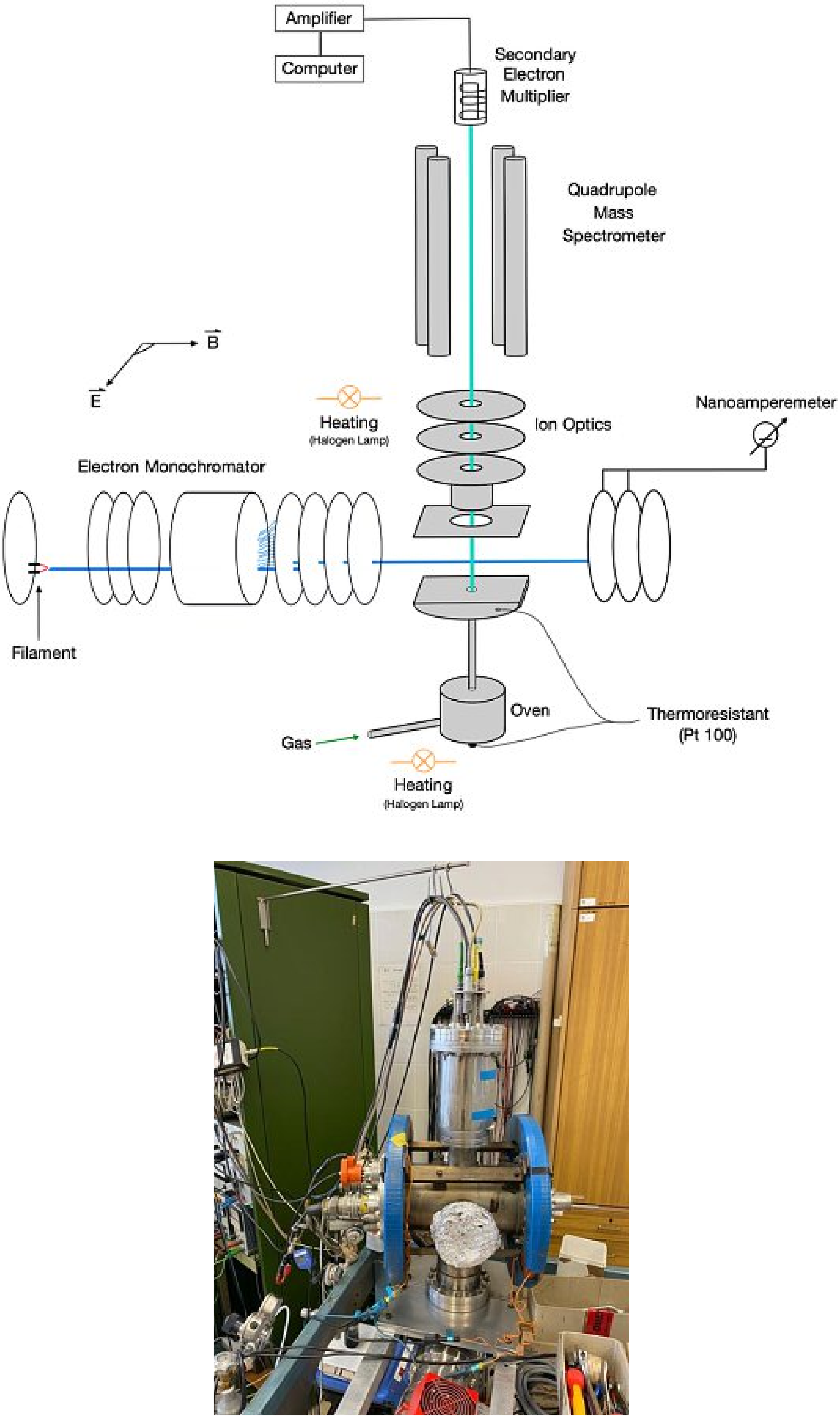

*Figure 10-2: Schematic diagram and picture of DEA experiment setup.*

### 10.1.3 Results

#### 10.1.3.1 Methacrylic Acid

It has been reported previously by Andrzej Pelc et al. in 2004 where propionic acid was studied via a series of DEA experiments [108]. They discovered that the most dominant fragment for carboxylic acids was resulted from the dehydrogenation of the target molecule, meaning a neutral hydrogen radical is expelled from the OH group and leads to formation of a respective molecule with negative charge.

As a liquid sample, methacrylic acid was introduced into the setup via a glass capillary with heating to increase the signal intensity. Temperature employed should be below 70 °C in general to prevent polymerisation. Similar results were also revealed in the measurement of methacrylic acid. Pronounced peaks with lower energy resonance (< 2 eV) at 85 amu indicated methacrylic acid tends to undergo dehydrogenation and the respective species is not just stable but has relatively high electron affinity (Figure 10-3).

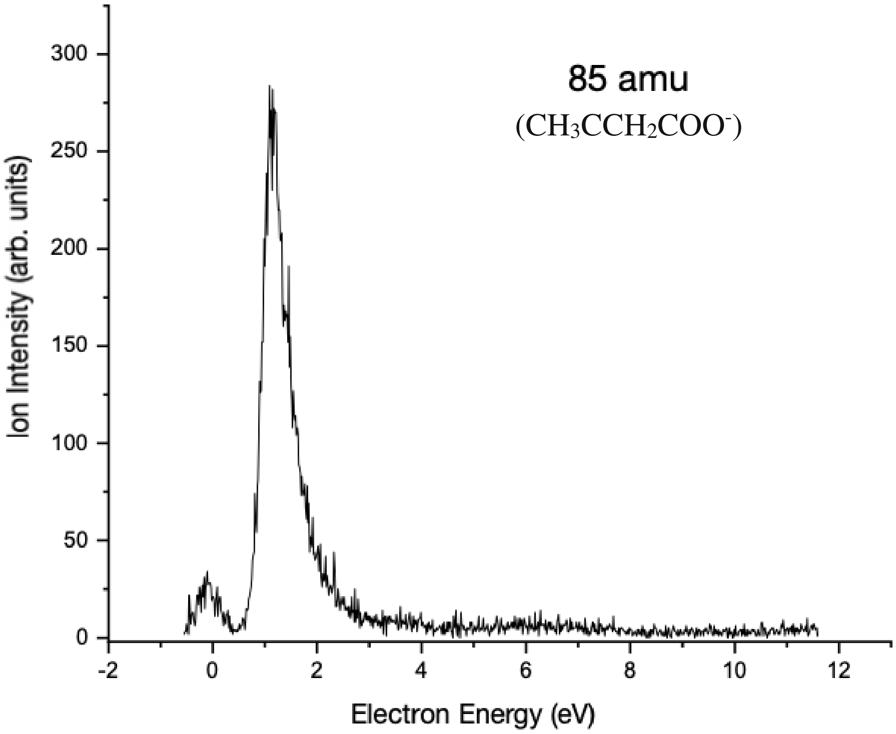

*Figure 10-3: Fragment ions observed at 85 amu from electron attachment to methacrylic acid.*

Several fragments with lower intensity were also detected with resonance at either high (> 7 eV) or low (< 2 eV) energy (Figure 10-4). It was suggested that most of the minor fragments essentially came from the dissociation of the carboxylic group, e.g. $O^-$, $CO^-$, $COO^-$, $HCOO^-$ [108].

The variety and number of fragment ions are related to electronic as well as geometrical structures of molecule. For instance, the C=C bond of methacrylic acid is too rigid to be broken within this energy region (0-12 eV). Therefore, the fragments involving dissociating C=C bond are hardly observed from DEA experiment. Yet, it is still under question and requires further evidence.

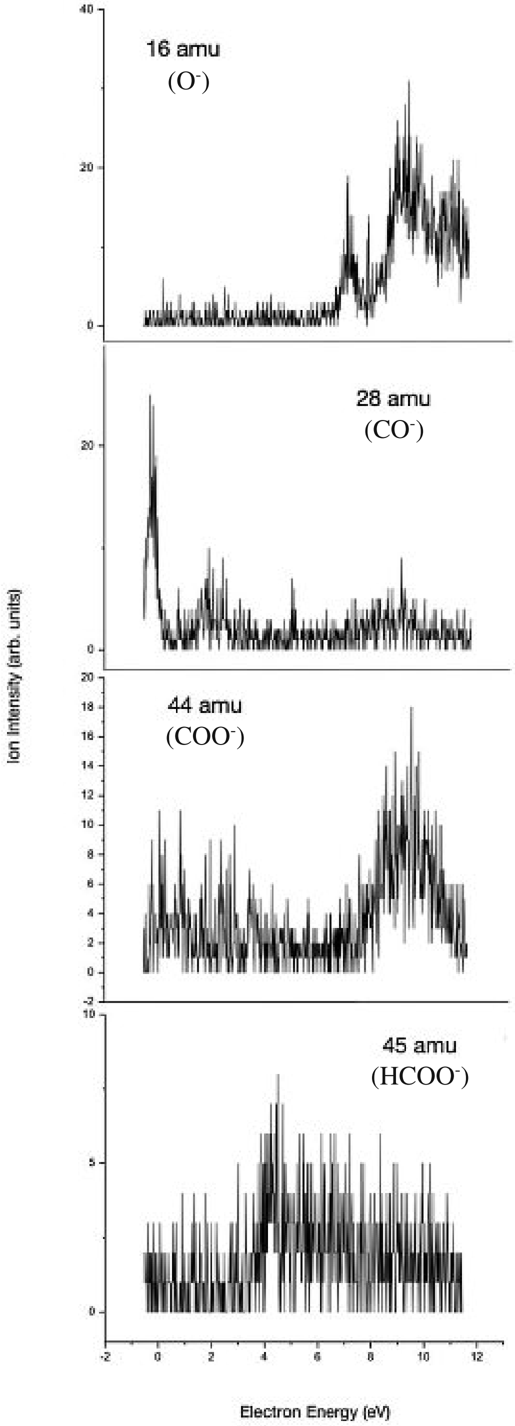

*Figure 10-4: Fragment ions observed at 16, 28, 44, 45 amu from electron attachment to methacrylic acid.*

Being the most abundant fragment after DEA, dehydrogenated methacrylic acid radical anion can potentially trigger chemical reactions that eventually leads to the solubility switch for resist materials. The result also suggests the originally proposed mechanisms for the metal oxo clusters might be feasible with respect to the initiation of solubility switch through DEA pathways. Minor fragments will not make a significant impact and possibly outgas from the condensed resist film, as outgassing analysis revealed a large amount of carbon dioxide released from photoresist layer after exposure of EUV. More details are included in the latter chapters.

#### 10.1.3.2 3-Butenoic Acid

The spectra of 3-butenoic acid were identical to those of methacrylic acid with more significant intensity due to higher pressure it could achieve during the measurements. The most pronounced signal was also at 85 amu, which was caused by the ejection of hydrogen from carboxylic group (Figure 10-5). Other evident responses could only be found at 16, 28, 44, 45 amu resulted from $O^-$, $CO^-$, $COO^-$and $HCOO^-$, respectively (Figure 10-6). The spectra have two lines where the red line is showing real intensity of the resonance peaks, while the black line is illustrating the intensity with arbitrary units, which is still comparable between different fragments.

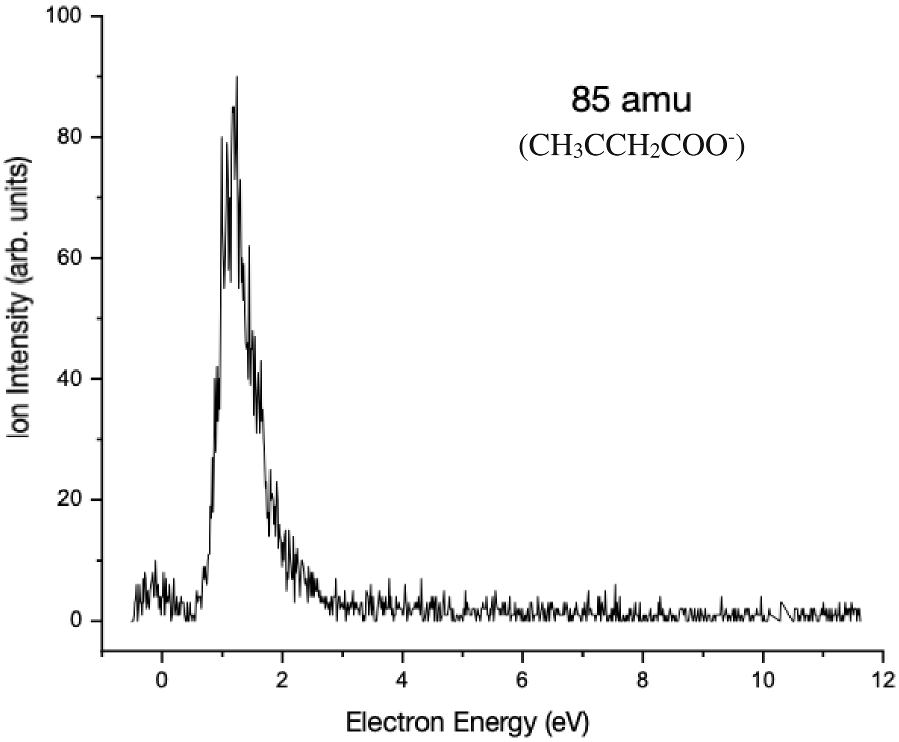

*Figure 10-5: Fragment ions observed at 85 amu from electron attachment to 3-butenoic acid.*

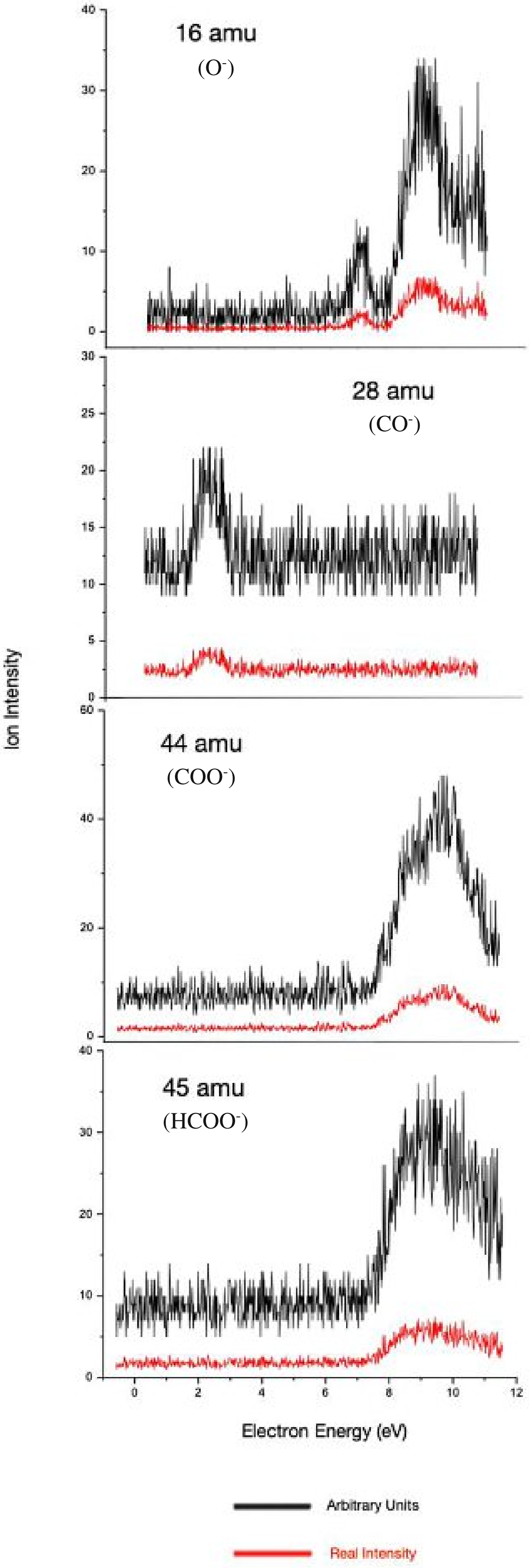

*Figure 10-6: Fragment ions observed at 16, 28, 44, 45 amu from electron attachment to 3-butenoic acid.*

Mass scans at 0, 1.6 and 9.0 eV were also conducted to ensure there was no peak missing in the energy scan measurements (Figure 10-7). The results essentially correspond to those of energy scans. In the scan of 0 eV, the responses at 28 and 85 amu were clearly detected. The most intense peak in the spectrum was at approximately 35 amu. Considering its high intensity, the peak was possibly from a high DEA cross section element, namely chlorine in this case. Nevertheless, given the fact that the sample came from a newly-purchased bottle opened and stored in the glovebox and that the setup was checked before introduction of the substance to make sure no impurities existing, the actual origin of this response remains unknown.

Trace of this impurity was also detected at energy level of 1.6 eV but with much lower intensity. Response of the dehydrogenated 3-butenoic acid was predominant in this energy range, showing an intensity closer to that in the energy scan spectrum. Most of the minor fragments including $O^-$, $COO^-$ and $HCOO^-$ have responses at around 9.0 eV. Owing to their low intensity, noise became significant in the spectrum yet corresponding peaks were still detected even though there was a slight shift in mass, which was possibly resulted from calibration issue of the mass detector.

Due to high structural similarity and the fragments detected, the zirconium oxo cluster ($Zr_4O_2(OVinac)_{12}$) with dehydrogenated 3-butenoic acid as ligands should undergo the same pathways as that of $Zr_4O_2(OMc)_{12}$ through a reactive dehydrogenated carboxylic acid species to initiate condensation and/or crosslinking reactions for achieving solubility switch. Other minor fragments only have limited influence with respect to the mechanism of solubility switch as some of them will potentially outgas from resist thin-film.

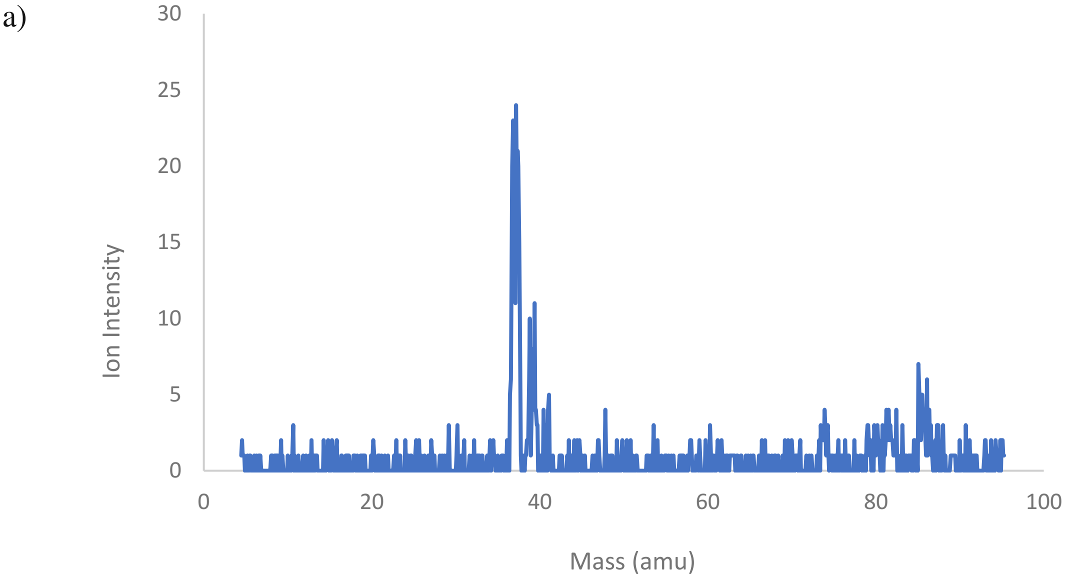

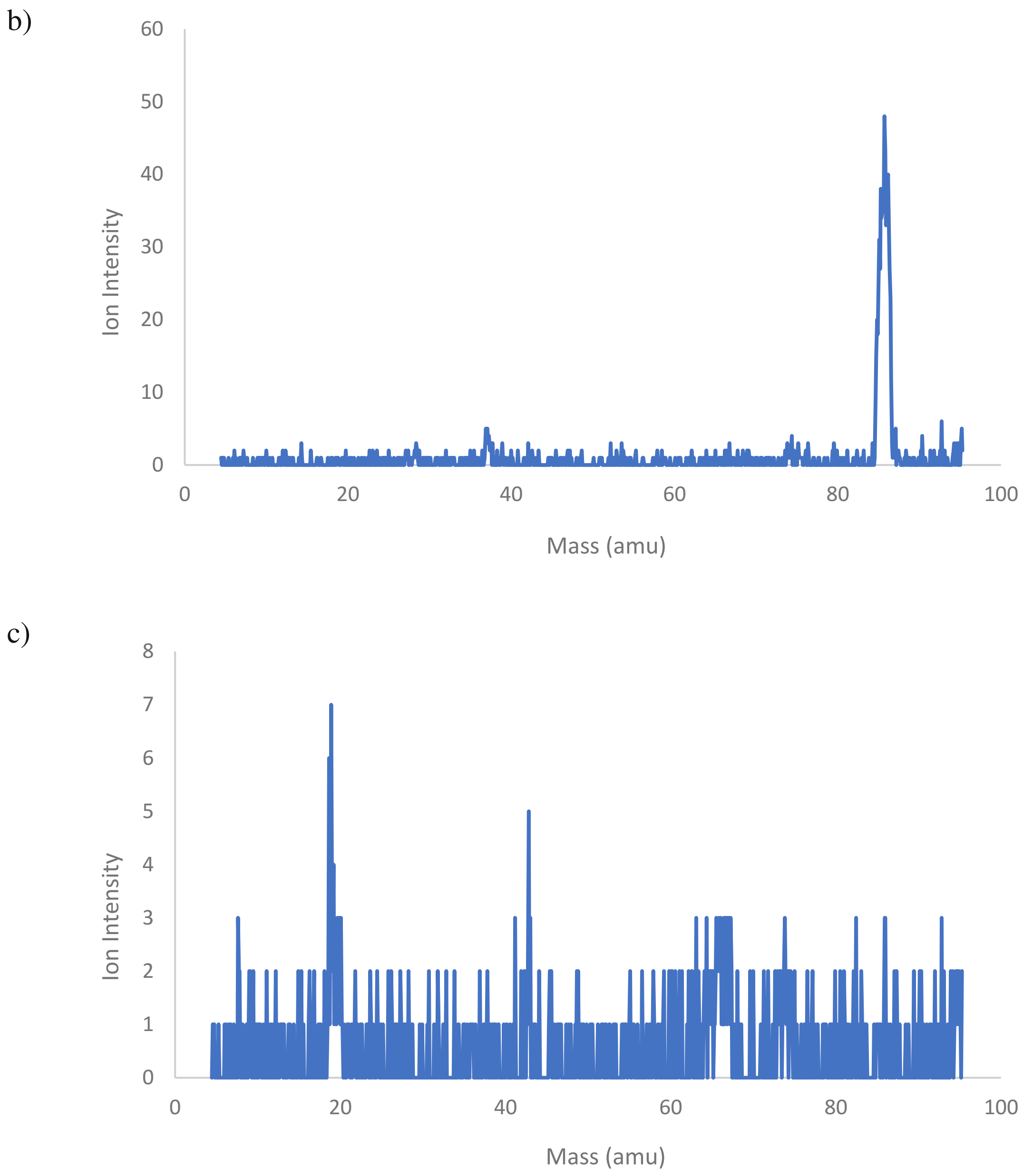

*Figure 10-7: Mass scans for 3-butenoic acid fragment ions at a) 0, b) 1.6 and c) 9.0 eV.*

### 10.1.3.3 Trans-2,3-dimethacrylic Acid

Dehydrogenation remains dominant among the DEA mechanism for trans-2,3-dimethacrylic acid (Figure 10-8). The shape and relative intensity of two pronounced peaks are similar to the results of methacrylic acid and 3-butenoic acid with identical resonance energy. It indicates the process of electron-induced dissociation electron attachment of carboxylic acid can generate same energy profile with limited influence from the rest of the structures.

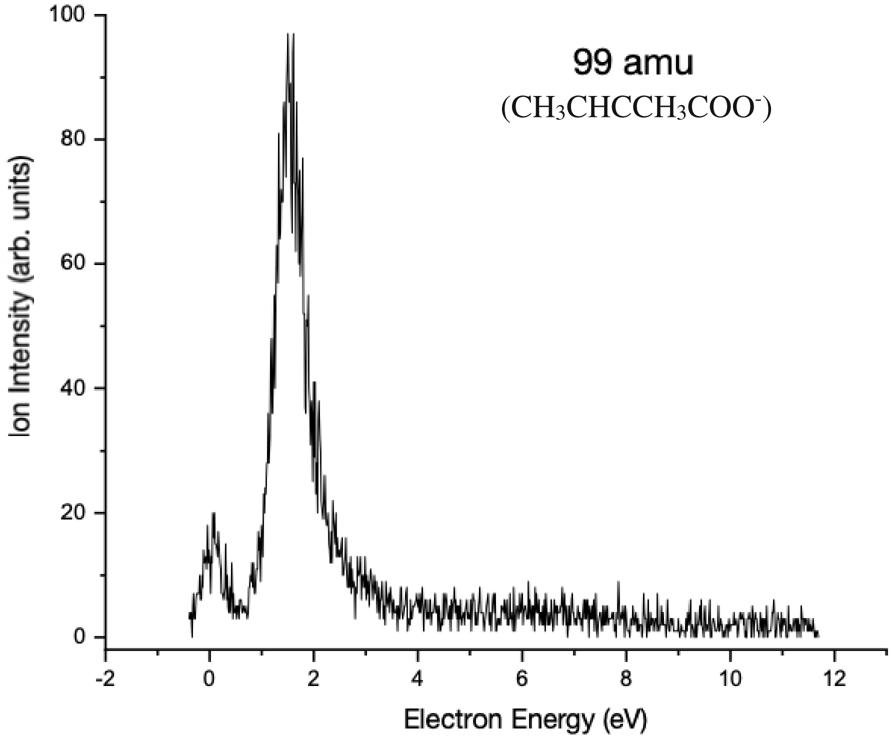

*Figure 10-8: Fragment ions observed at 99 amu from electron attachment to trans-2,3-dimethacrylic acid.*

However, concerning the other signals with the less intensive response, a new fragment was discovered at 73 amu and the one at 28 amu was unable to be detected (Figure 10-9). A possible explanation for this disappearance might be resulted from low pressure during the measurements, allowing only a small amount of sample entering the chamber. Therefore, the density of the target material was substantially reduced and caused the energy resonance too low to be detected.

On the other hand, existence of the fragment with 73 amu is difficult to be explained by the evidence obtained so far. The loss of 27 amu from the original compound seems unrealistic at this low energy range. There was potentially structural rearrangement taking place within the fragment after the electron attachment. Further experiments are required to evaluate the origin of this fragment.

Like the cases of methacrylic aid and 3-butenoic acid, $Zr_4O_2(ODiMc)_{12}$ should have its solubility switch initiated by the reactive dehydrogenated trans-2,3-dimethacrylic acid and through the pathways of condensation and/or crosslinking, while the rest of fragments with lower intensity make only insignificant impact with respect to chemical reaction. Dehydrogenation of the three ligand precursors take place at the identical energy and rather similar cross section, meaning $Zr_4O_2(OMc)_{12}$, $Zr_4O_2(OVinac)_{12}$ and $Zr_4O_2(ODiMc)_{12}$ clusters possessing the same nucleus composition should essentially have very close sensitivities towards EUV exposure.

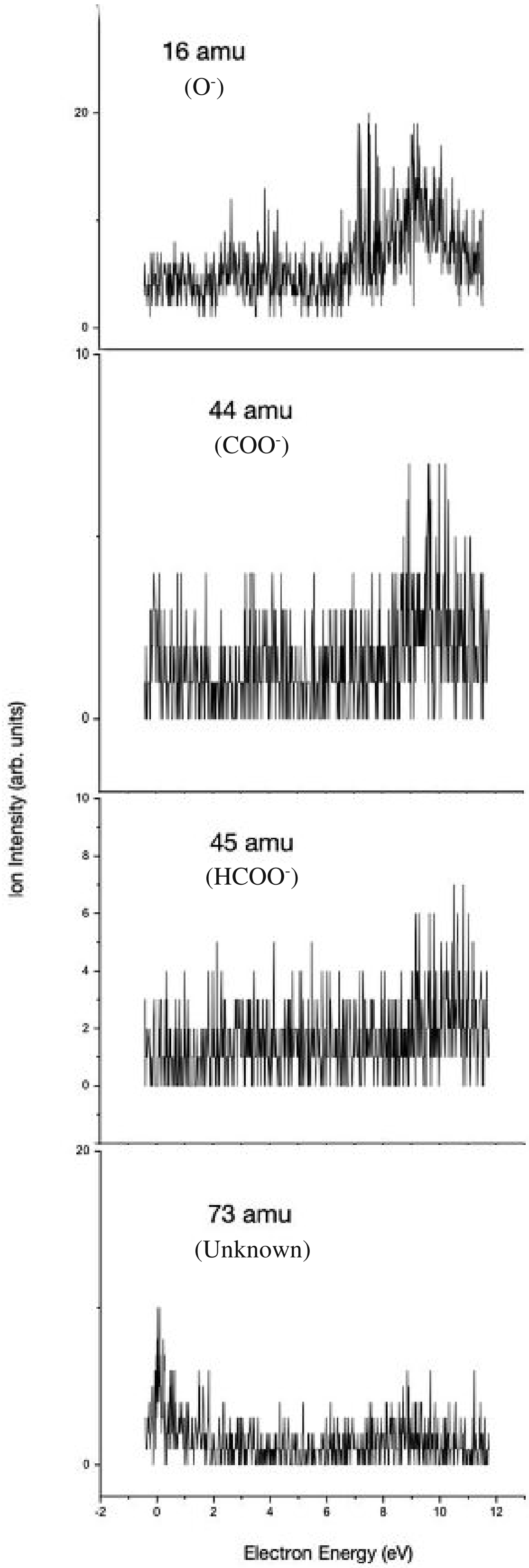

*Figure 10-9: Fragment ions observed at 16, 44, 45 and 73 amu from electron attachment to trans-2,3-dimethacrylic acid.*

### 10.1.3.4 $Zr_4O_2(OMc)_{12}$

Due to limitation of the setup, the measuring of mass can only range from 0 to 300 amu, which is insufficient for the metal oxo clusters. Moreover, the gasification of $Zr_4O_2(OMc)_{12}$ was hard to achieve. Originally, the cluster was directly transferred into the chamber, trying to gasify it under ultrahigh vacuum ($10^{-8}$ mbar) and a high chamber temperature (90 °C). The intensity remained low even though the temperature was increased to 120 °C. Approach changed after some trials to introduce the cluster material through a glass capillary with heating. The temperature at the capillary stayed constantly at 160 °C with extra heating employed on the inlet system at 90 °C, whereas the chamber remained at 120 °C. Despite the pressure was still relatively low in contrast to those of the previous carboxylic acids, it could provide sufficient intensity for measuring.

Three fragments were still managed to be recorded. The fragment of 16 amu and 85 amu were basically predictable since the cluster is mainly composed of methacrylate ligands (Figure 10-10). But there was no sign of other fragment from methacrylic acid. Existence of the fragment at 103 amu is lack of explanation. Structural rearrangement might have taken place involving one of the zirconium atoms on the cluster.

Regarding simulation of material behaviour upon EUV exposure, it can be assumed that original proposed mechanisms including condensation and crosslinking pathways are potential feasible, if combined with previous results from carboxylic acid measurements. Instead of breaking into smaller anions, the primary species of $Zr_4O_2(OMc)_{12}$ under DEA experiment is the reactive dehydrogenated methacrylic radical anion (85 amu), indicating secondary electrons generated by incident EUV photons with energy below 12 eV are prone to cleave the methacrylate ligands from the metal nuclei. The cleavage of a ligand will result in an active site on the surface of the metal core that can promote condensation reaction with adjacent metal oxo clusters and form a bond in between. This reaction is able to propagate and eventually lead to a undissolvable system within exposed materials. The other possibility is the cleavage of methacrylate ligand will give rise to a reactive radical anion that is capable of initiating a crosslinking reaction among other methacrylate ligands. The process can then propagate and form a undissolvable system in the end. The origin of solubility switch may go through either one of the routes or it is potentially the combination of these two. Furthermore, the intensity of 85 amu is relatively significant considering the pressure it could reach, indicating DEA is able to "functionalise" efficiently high amount of reactive species and therefore enables exposed materials to be more homogeneous in this case.

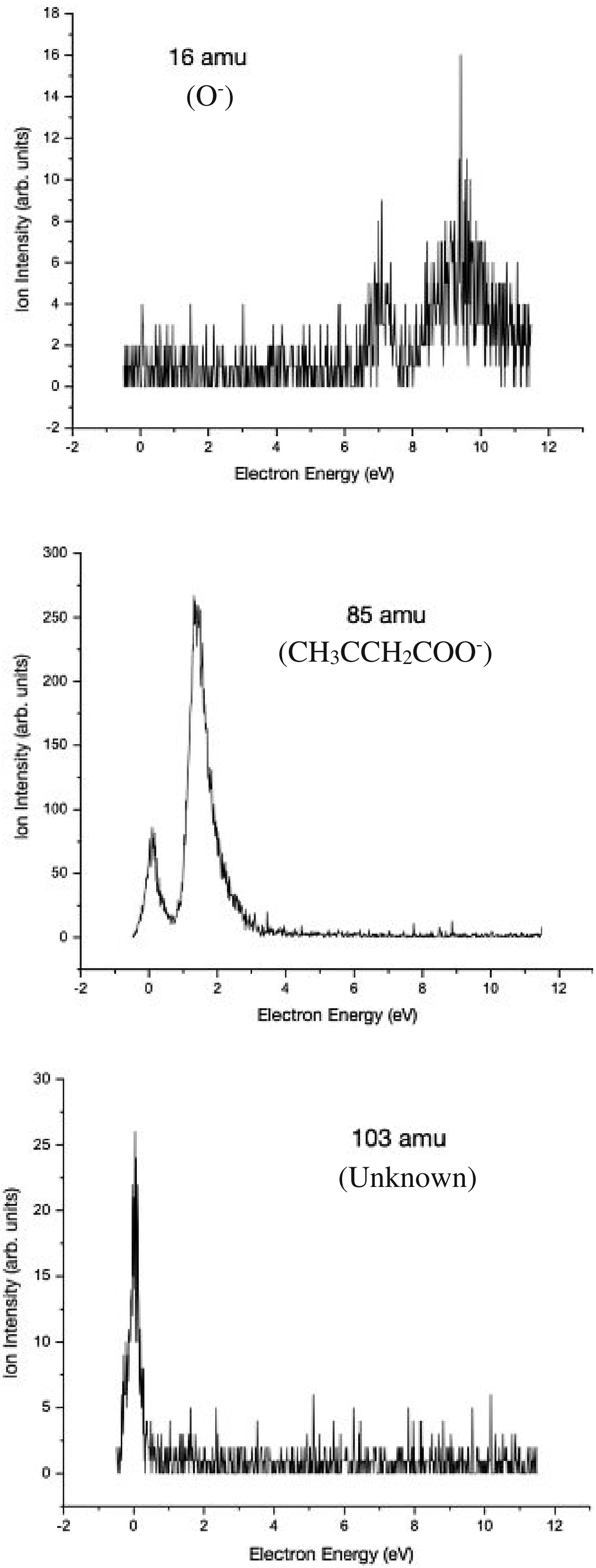

*Figure 10-10: Fragment ions observed at 16, 85 and 103 amu from electron attachment to* $Zr_4O_2(OMc)_{12}$.

## 10.2 Outgassing Analysis

### 10.2.1 Introduction

Outgassing analysis is mainly used to investigate resist-related outgassing after light exposure. These outgassed species can be a potential risk for optics especially in EUV exposure tools and results in serious degradation that substantially reduces the lifetime. Nevertheless, it is challenging because not only quantification and determination of hazardous elements are relatively complicated, but the result is strongly depending on experimental conditions as well as analysing equipment employed [109-111]. In order to achieve better understanding of outgassing composition, a residual gas analysis (RGA) is therefore embedded in the outgassing setup. RGA is basically like a gas chromatography-mass spectroscopy (GC-MS) device, which is able to collect the gas released from condensed resist thin-film after the EUV exposure and analyse the species intensity as a function of mass with careful calibrations required to avoid significant deviations. A so-called witness sample (WS), a representative sample for EUV optics, is also installed within the setup. It is a widely-accepted measure for evaluating resist materials before being employed in an actual EUV exposure tool.

In addition to contaminant determination, outgassing analysis has been considered as an useful tool with respect to resist mechanism studying in recent years [46, 112]. By analysing fragments outgassed after EUV exposure, it is feasible to understand the light-matter photochemical behaviours taking place within the condensed thin-film and furthermore deduce a possible mechanism pathway for the resist materials. Given that some fragments are not able to outgas from resist layer, this approach is usually accompanied with other measurements such as low energy electron (LEE) spectroscopy (DI and DEA) as well as thin-film IR spectroscopy for acquiring a more realistic overview regarding photochemical properties and mechanisms of resist materials.

### 10.2.2 RGA Setup and Experimental Conditions

The device used for outgassing analysis in this work was provided by EUV Technology in the US and is currently located in IMEC. A xenon-based Energetiq is embedded as the EUV source that is capable of producing 10W/2πsr EUV radiation. The radiation is filtered by a Zr spectral purity filter before reaching the multilayer (ML) mirror, which can move the projection on either silicon wafer surface or witness sample. Spot size on the wafer is approximately 10 mm$^2$ with the power density at around 4mW/cm$^2$, while the spot size at witness sample is 1-2 mm$^2$ in diameter and the maximum intensity in the centre of the spot is about 80 mW/cm$^2$. A Pfeiffer

QMG422 RGA is employed for collecting and analysing outgassed species inside the ultrahigh vacuum chamber with a pressure level of 1.5x10$^{-8}$mbar. 200 mm wafer sample can be loaded into the chamber with an automated loadlock, whereas WS has to be transferred manually (Figure 10-11) [109].

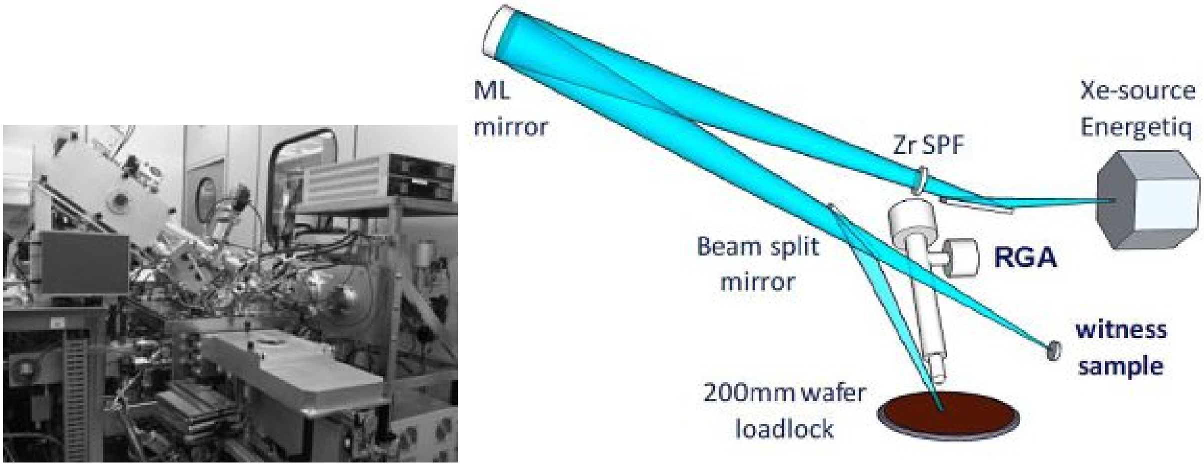

*Figure 10-11: A photo and a schematic illustration of the outgassing setup at IMEC* [113].

Due to constraint of time, outgassing measurement was only carried out on $Ti_2Zr_4O_4(OBu)_2(OMc)_{14}$ cluster in the cleanroom. Since approximately 3 mL of casting solution is required for spin-coating a 200-mm silicon wafer, a 1% w/v of sample solution was prepared by dissolving 0.03 mL of $Ti_2Zr_4O_4(OBu)_2(OMc)_{14}$ powder in a solvent mixture consisting of 1.8 mL of propylene glycol methyl ether (PGME) and 1.2 mL of 1.2 mL of chloroform. 0.02 µm syringe filters were utilised for removing undissolved particles. The solvents employed were dried beforehand over 4 Å of molecular sieves for at least 24 hours in the cleanroom. A TEL CLEAN TRACK™ ACT™ 8, namely a multi-step programmable 8-inch spin coater, blad and spray coaters, was used for depositing a thin layer sample on an 8-inch wafer. The spin-coating profile was set as follows:

| | **Procedure** | **Condition** | **Time** |
|---|---|---|---|
| **1** | Cooling | Temperature: 20 ºC | 30 seconds |
| **2** | Rotating | RPM: 2000 | 60 seconds |
| **3** | Edge Removing | RPM: 2000 | 5 seconds |
| **4** | Post Apply Bake | Temperature: 60 ºC | 60 seconds |

| | | | |
|---|---|---|---|
| **5** | Cooling | Temperature: 20 ºC | 30 seconds |

Inhomogeneity was observed closer to the edge of silicon wafer, which was possibly resulted from minor hydrolysis leading to precipitation in the casting solution. The resulted film thickness checked by a programmable ellipsometer that can automatically measure layer thickness at desired positions was 30 ± 3 nm.

The 8-inch silicon wafer was then loaded into RGA setup through the automated loadlock. After internal pressure reaching ultrahigh high vacuum level, EUV generated via Xe source was exposed on selected area of the wafer with a consistent dose at 15 mJ/cm$^2$. The outgassed elements were collected and analysed by RGA.

### 10.2.3 Results

The RGA analysis of $Ti_2Zr_4O_4(OBu)_2(OMc)_{14}$ outgassed species was shown in Figure 10-12, as it was depicted in the formation of outgassing rate (molecule/cm$^2$·s) as a function of mass (amu). The most predominant peak was at 44 amu that was primarily resulted from carbon dioxide. Possible origins of $CO_2$ lie in two folds. From DEA experiments, it has been proven that low energy electrons are capable of causing the dissociation upon methacrylic acid that gives rise to a significant amount of $COO^-$ fragment. These radical anions might outgas from the condensed thin-film resist and were detected by RGA. The other origin was related to crosslinking of the resist material. In the proposed mechanism, free radicals generated after EUV exposure can initiate crosslinking reaction among methacrylate ligands that potentially leads to the formation of carbon dioxide in the end.

Signal at 86 amu indicated the existence of methacrylic acid among outgassed species. In the proposed condensation mechanism pathway, EUV photons is able to cleave off methacrylate ligands and create active sites on the surface of metal core, which leads to binding with neighbouring oxo clusters. However, the rate of methacrylic acid is substantially lower than that of $CO_2$ at 44 amu. One of the explanations is the efficiency of secondary electrons cleaving off methacrylate ligands from $Ti_2Zr_4O_4(OBu)_2(OMc)_{14}$ cluster is lower than that of giving rise to active free radical, which favours the crosslinking pathway instead of condensation reaction. Moreover, no post exposure bake (PEB) was applied during outgassing analysis.

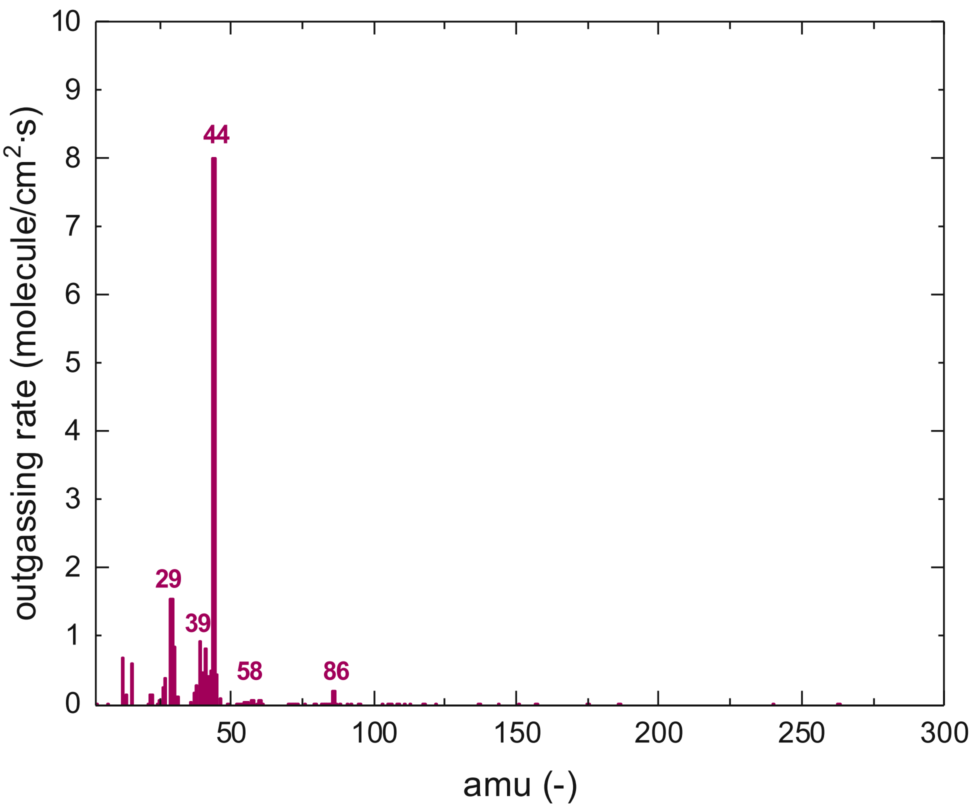

*Figure 10-12: Outgassing result of $Ti_2Zr_4O_4(OBu)_2(OMc)_{14}$ with a EUV dose at 15 mJ/cm$^2$.*

Since baking can promote the condensation mechanism and improve patterning capability, there were less methacrylic acids condensed from the resist material in this case and therefore the outgassing rate was much slower. Another possibility is the methacrylate ligands cleaved from $Ti_2Zr_4O_4(OBu)_2(OMc)_{14}$ after EUV exposure were dissociated by secondary electrons via DEA in a very short timescale, resulting in the increase of $COO^-$ outgas through sacrificing methacrylic acids. Further analyses including DEA and DI spectroscopy of $Ti_2Zr_4O_4(OBu)_2(OMc)_{14}$ are recommended in order to understand this phenomenon.

Signals at 58, 39 and 29 amu came from outgas of butane and its fragmented derivatives, as butoxide ligands were contained in the shell of $Ti_2Zr_4O_4(OBu)_2(OMc)_{14}$. Cleavage of a carbon-carbon bond can generate a carbocation, namely an ethyl cation with a mass of 29 amu (Figure 10-13), which is the most abundant ion in the mass spectrum of propane [114]. Fragment at 39 amu appearing in propane mass spectrum potentially comes from $C_3H_3$. Yet its actual structure is still unknown. Propane MS analysis can give rise to 44 amu ($CO_2$), meaning the cleavage of butoxide ligands is also able to contribute to $CO_2$ outgas after EUV exposure. Multi-channels leading to the formation of fragments at 44 amu is the main reason that its outgassing rate is the highest among all species.

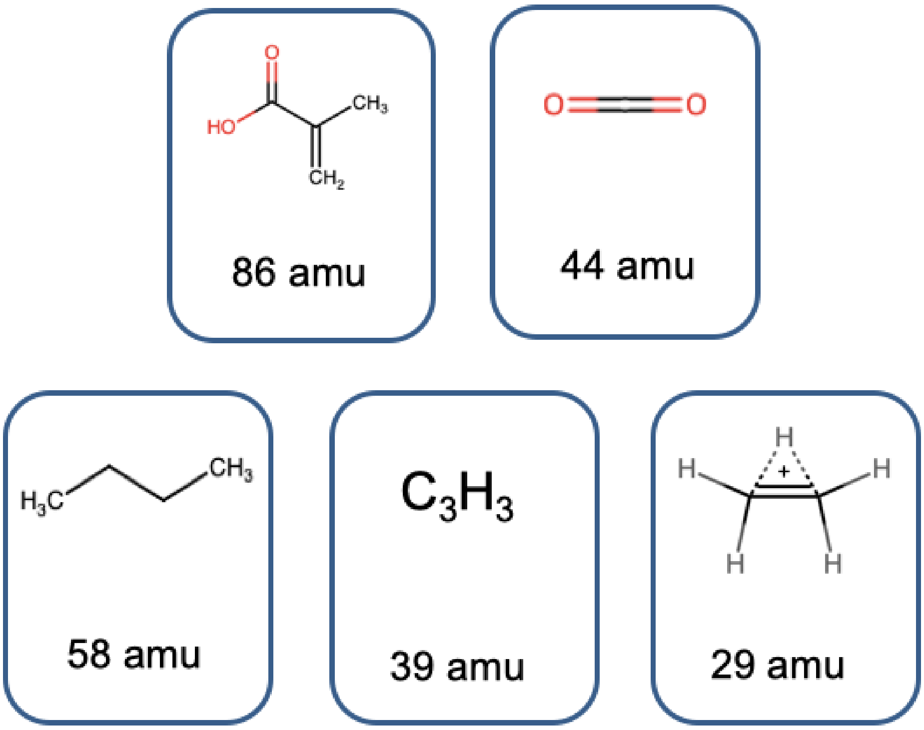

*Figure 10-13: Fragment structures of $Ti_2Zr_4O_4(OBu)_2(OMc)_{14}$ outgassing species.*

The overall outgassing result has provided sufficient evidence for mechanism deduction of $Ti_2Zr_4O_4(OBu)_2(OMc)_{14}$ and other similar metal oxo clusters. It clearly revealed the occurrence of methacrylate ligand cleavage as well as formation of $CO_2$ generated through ligand crosslinking and DEA of methacrylic acid upon exposure of EUV photons. Hence, the proposed condensation and crosslinking mechanism pathways can both be the origins of solubility switch and take place simultaneously. Nevertheless, the predominance of these two routes still depends on process conditions (e.g. PEB), which possibly affects material sensitivity towards EUV.

## 10.3 Thin-film FTIR

### 10.3.1 Introduction Experimental Conditions

IR spectroscopy is a relatively straightforward approach for understanding photochemical reaction resulted from EUV photons. By comparing variations of different chemical bodings before and after light exposure, it is beneficial to study the possible structural changes that eventually lead to solubility switch of resist materials [115-117]. In addition, IR can also be utilised to reveal the interaction between photoresist and silicon wafer surface [54]. Bonding formed after resist material being deposited on a wafer can have an evident influence on adhesion or developability. Those having bad adhesion with silicon wafer will require an extra priming layer such as Bis(trimethylsilyl)amine (HMDS) for the sake of increasing attachment before spin-coating photoresist.

In this work, IR spectroscopy was conducted in two separate approaches, transmission FTIR and grazing angle attenuated total reflectance FTIR (GATR-FTIR). Transmission FTIR measurement was carried out on $Zr_4O_2(OMc)_6(OPiv)_6$, $Zr_4O_2(OMc)_9(OPiv)_3$, $Zr_{12}O_8(OH)_8(OMc)_8(OAc)_{16}\cdot 6HOAc$, $Ti_4Zr_2O_4(OBu)_6(OMc)_{10}$, $Ti_2Zr_5HfO_6(OMc)_{20}$. The EUV exposure was performed via SLS XIL-II beamline at PSI. 1% casting solution for each metal oxo cluster was prepared with the conditions and procedure as stated in Table 7. Samples were spin-coated on 1 cm x 1 cm silicon wafers (single-sided polished with a substrate thickness of 500 ± 25 µm) shortly before being loaded into ultrahigh vacuum exposure chamber. Open-frame EUV source (no photomask involved) was exposed to the centre of a silicon wafer for 25 times to create a 5 mm x 5 mm area that is large enough for transmission FTIR measurement (Figure 10-14). Dose employed for all tested samples was 60 mJ/cm$^2$ to ensure sufficient structural changes for solubility switch. After exposure, samples were developed with respective developing solvents and blown dry with nitrogen.

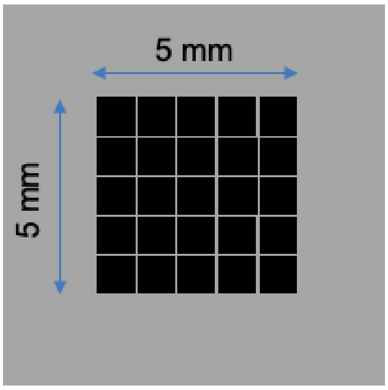

*Figure 10-14: Schematic illustration of EUV exposure for preparing transmission FTIR samples.*

GATR-FTIR was conducted only on $Ti_2Zr_4O_4(OBu)_2(OMc)_{14}$ cluster in the cleanroom of IMEC. 3mL of 1% casting solution was prepared through identical parameters and conditions as previously mentioned. The resist material was spin-coated on an 8-inch silicon wafer shortly before being loaded into the same setup for outgassing experiment. The Xenon Energetiq source was employed to generate EUV photons that exposed on different positions on the wafer surface. Exposing dose started from 10 mJ/cm$^2$ at position 1 to 50 mJ/cm$^2$ at position 5 with an interval of 10 mJ/cm$^2$ in order to understand the structural change as a function of EUV dose (Figure 10-15). Position 6 to 8 were not used in this experiment. The exposed areas were separated from the 8-inch wafer by a diamond cutter for fitting into the sample holder of GATR-FTIR.

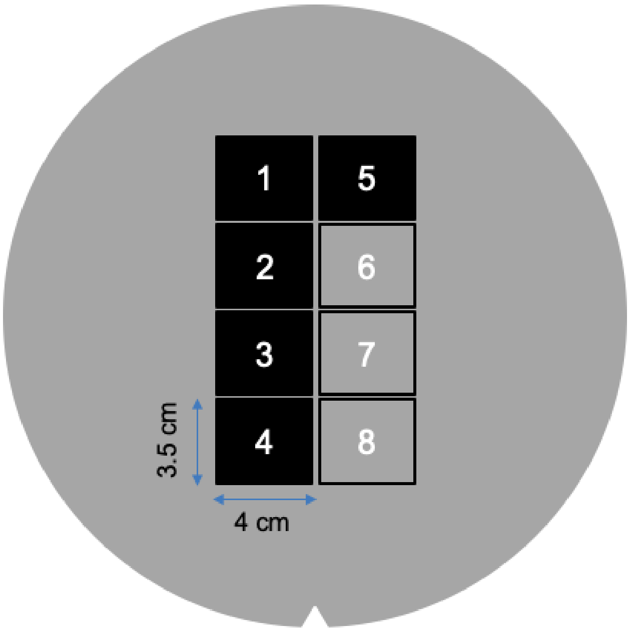

*Figure 10-15: Schematic illustration of EUV exposure for preparing the GATR-FTIR sample.*

### 10.3.2 Results of Transmission FTIR

#### 10.3.2.1 $Zr_4O_2(OMc)_9(OPiv)_3$

Thin-film FTIR measurements have revealed an evident difference of $Zr_4O_2(OMc)_9(OPiv)_3$ before and after EUV exposure (Figure 10-16). A predominant peak at 2350 $cm^{-1}$ indicates a large amount of $CO_2$ existing within the condensed film, which is corresponding to the results of dissociative electron attachment spectroscopy and outgassing analysis. It further confirms the formation of $CO_2$ resulted from not only fragmentation of DEA of resist material, but potentially crosslinking of the metal oxo clusters. It is the most abundant species in both the outgassing analysis as well as FTIR spectrum and not all molecules were able to escape from the photoresist layer afterwards.

Peaks at 1650 (C=C stretching, vinylidene), 1706 (C=O stretching, carboxylic acid) and 1750 $cm^{-1}$ (C=O stretching, ester) are originated from methacrylate ligands as well as its resulted derivatives. The wavenumber of these three peaks in the exposed sample seem to have shifted to higher value in contrast to the unexposed one. An explanation for this phenomenon is the intermolecular bonding is reduced substantially, meaning a significant amount of methacrylate ligands were possibly cleaved from the metal core of clusters and hence the distance between two molecules have increased that leads to less intermolecular interaction.

Peaks at 3700 and 1100 cm$^{-1}$ are attributed to existence of alcohol. As the DEA study indicates low energy electrons can procure the dissociation of methacrylic acid and create a $CO^{-}$ radical anion at 28 amu. These fragments can react with ambient hydrogen atoms and therefore give rise to alcohols. Peak at approximately 1600 cm$^{-1}$ is another pronounced signal after exposure of EUV. It is caused by the C=C stretching of cyclic alkene, which was potentially generated via crosslinking of methacrylic ligands.

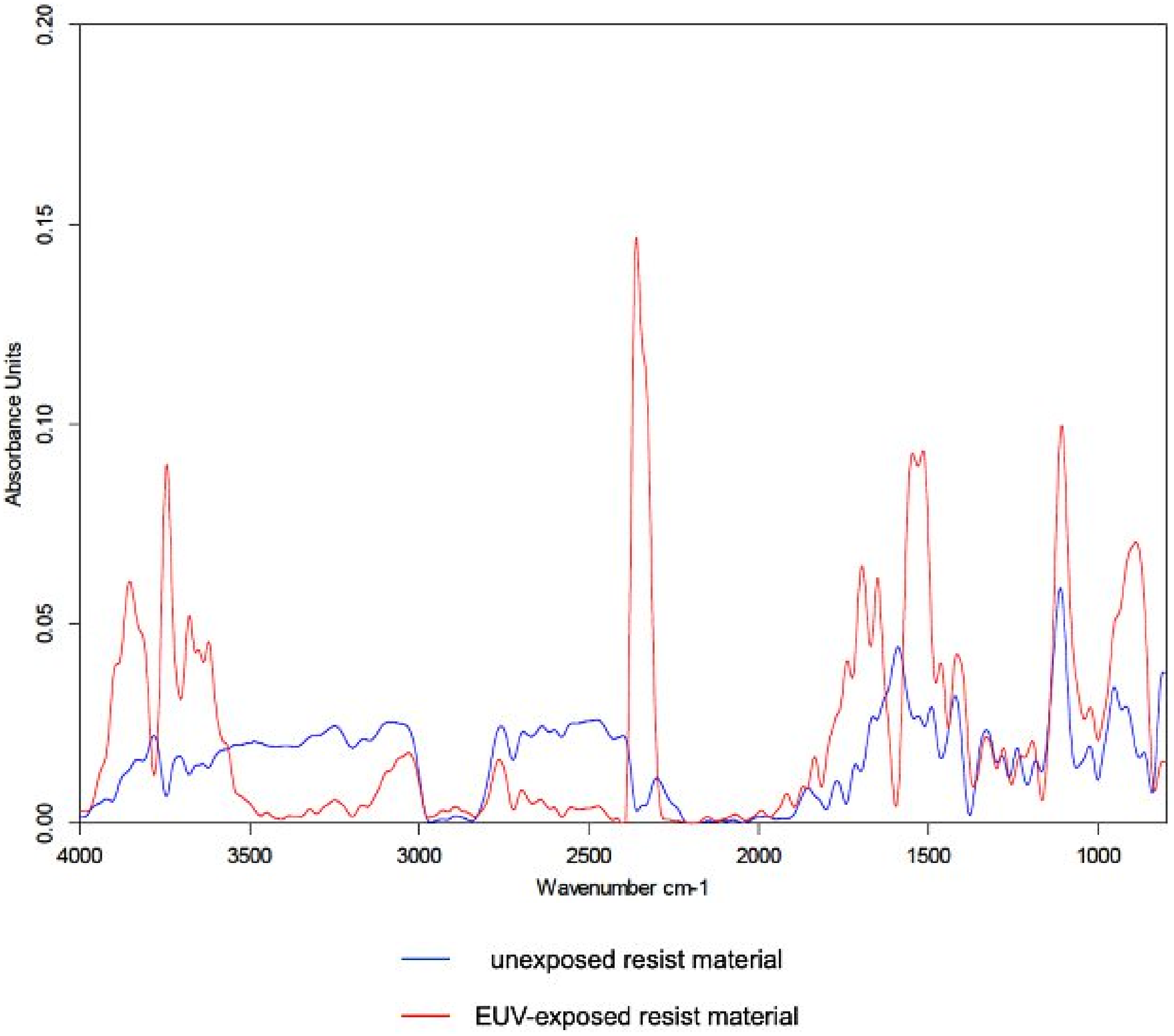

| Wavenumber (cm$^{-1}$) | Assignment | Wavenumber (cm$^{-1}$) | Assignment |
|---|---|---|---|
| **3700 - 3580** | O-H stretching (free alcohol) | 1650 | C=C stretching (vinylidene) |
| **3300 - 3200** | C-H stretching (carboxylic acid) | 1650 - 1560 | C=C stretching (cyclic alkene) |

| | | | |
|---|---|---|---|
| **3150 - 2980** | O-H stretching (carboxylic acid) | 1450 | C-H bending (methyl group) |
| **2800 - 2730** | C-H stretching (alkane) | 1440-1395 | O-H bending (carboxylic acid) |
| **2350** | O=C=O stretching (Carbon dioxide) | 1150 - 1085 | C-O stretching (aliphatic ether) |
| **1750 - 1735** | C=O stretching (ester) | 895 - 885 | C=C bending (vinylidene) |
| **1720 - 1706** | C=O stretching (carboxylic acid dimer) | | |

*Figure 10-16: FTIR spectrum of unexposed and EUV-exposed $Zr_4O_2(OMc)_9(OPiv)_3$* [118].

### 10.3.2.2 $Zr_4O_2(OMc)_6(OPiv)_6$

As can be observed from the spectrum of EUV-exposed $Zr_4O_2(OMc)_6(OPiv)_6$, the intensity ratio of $CO_2$ at 2350 $cm^{-1}$ to carboxylic O-H at 3100 cm-$^{1}$ has substantially reduced (Figure 10-17). Given the fact that proportion of methacrylate ligands is lower compared to $Zr_4O_2(OMc)_9(OPiv)_3$, the number of DEA-resulted $CO_2^-$ fragment caused by dissociation of methacrylic acid is therefore diminished. On the other hand, lower crosslinking density has also led to an inferior crosslinking efficiency in $Zr_4O_2(OMc)_6(OPiv)_6$, releasing less carbon dioxide after EUV exposure. In the meantime, higher pivalate ligand content enables the C-H bending at 1450 $cm^{-1}$ of methyl group to become more pronounced, yet C-H stretching at 3000 to 2800 $cm^{-1}$ are barely recorded.

Cleavage of methacrylate ligands that gives rise to free methacrylic acids or its ester derivatives has caused peaks at 1754, 1722 and 1668 $cm^{-1}$ to shift upwards to higher wavenumber due to less intermolecular interactions. C=C stretching from cyclic alkene are detected in the exposed sample, indicating a crosslinked system is potentially induced for solubility switch after exposure of EUV photons.

In contrast to $Zr_4O_2(OMc)_9(OPiv)_3$, the reason of $Zr_4O_2(OMc)_6(OPiv)_6$ having lower sensitivity is because less reactive species including radicals and radical ions can be dissociated from fewer methacrylate ligands. Active site that can be created by ligand cleavage has become insignificant. Therefore, higher dose is required for fabricating high contrast and small sizes of pattern. Yet this is relatively independent on the light source employed for lithography.

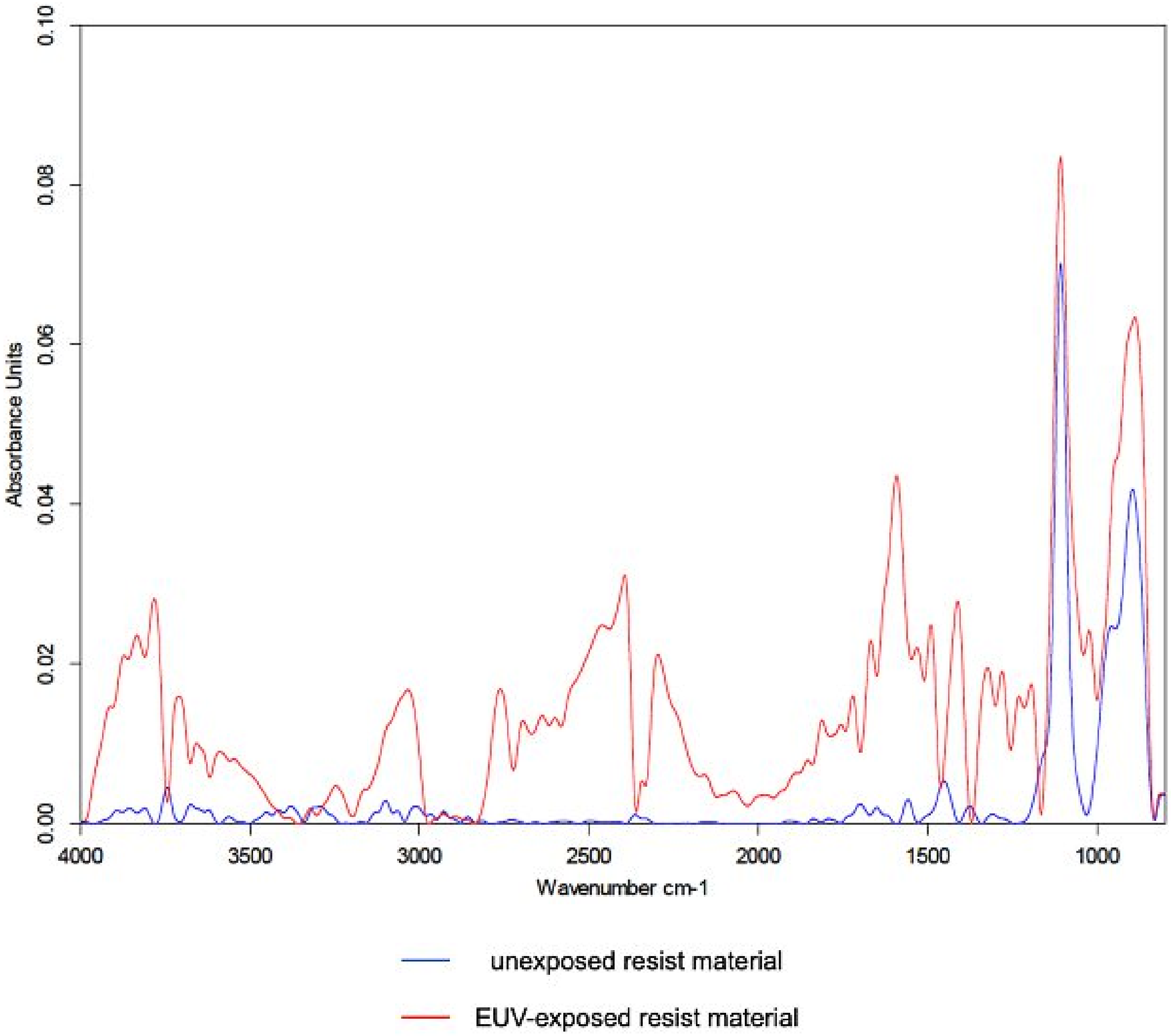

| Wavenumber (cm$^{-1}$) | Assignment | Wavenumber (cm$^{-1}$) | Assignment |
|---|---|---|---|
| **3700 - 3580** | O-H stretching (free alcohol) | 1650 | C=C stretching (vinylidene) |
| **3300 - 3200** | C-H stretching (carboxylic acid) | 1650 - 1560 | C=C stretching (cyclic alkene) |

| | | | |
|---|---|---|---|
| **3150 - 2980** | O-H stretching (carboxylic acid) | 1450 | C-H bending (methyl group) |
| **2800 - 2730** | C-H stretching (alkane) | 1440 - 1395 | O-H bending (carboxylic acid) |
| **2350** | O=C=O stretching (Carbon dioxide) | 1150 - 1085 | C-O stretching (aliphatic ether) |
| **1750 - 1735** | C=O stretching (ester) | 895 - 885 | C=C bending (vinylidene) |
| **1720 - 1706** | C=O stretching (carboxylic acid dimer) | | |

*Figure 10-17: FTIR spectrum of unexposed and EUV-exposed $Zr_4O_2(OMc)_6(OPiv)_6$.*

#### 10.3.2.3 $Zr_{12}O_8(OH)_8(OMc)_8(OAc)_{16}\cdot 6HOAc$

Since $Zr_{12}O_8(OH)_8(OMc)_8(OAc)_{16}\cdot 6HOAc$ is composed of two $Zr_6O_4(OH)_4$ with acetate bridging, an intermolecular-bonded O-H stretching is recorded by FTIR, as shown in Figure 10-18. Carboxylic O-H stretching at 3035 $cm^{-1}$ as well as the set of peaks at 1750, 1725 and 1665 $cm^{-1}$ resulted from methacrylic acid and its derivatives have all shifted to lower wavenumbers, revealing the cleavage of methacrylate ligands that leads to free methacrylic acid.

Relative intensity of O=C=O stretching at 2350 $cm^{-1}$ to carboxylic O-H stretching is insignificant attributed to lower methacrylate moieties, which deteriorates the material sensitivity upon light exposure. Nevertheless, higher metal content can compensate for sensitivity loss due to lower crosslinking density in the case of EUV lithography. Twelve zirconium atoms are capable of capturing EUV photons more efficiently that gives rise to more secondary electrons for initiating photochemical reactions within the resist layer. Hence, the EUV sensitivity of $Zr_{12}O_8(OH)_8(OMc)_8(OAc)_{16}\cdot 6HOAc$ cluster is even higher than those of $Zr_4$-based oxo clusters.

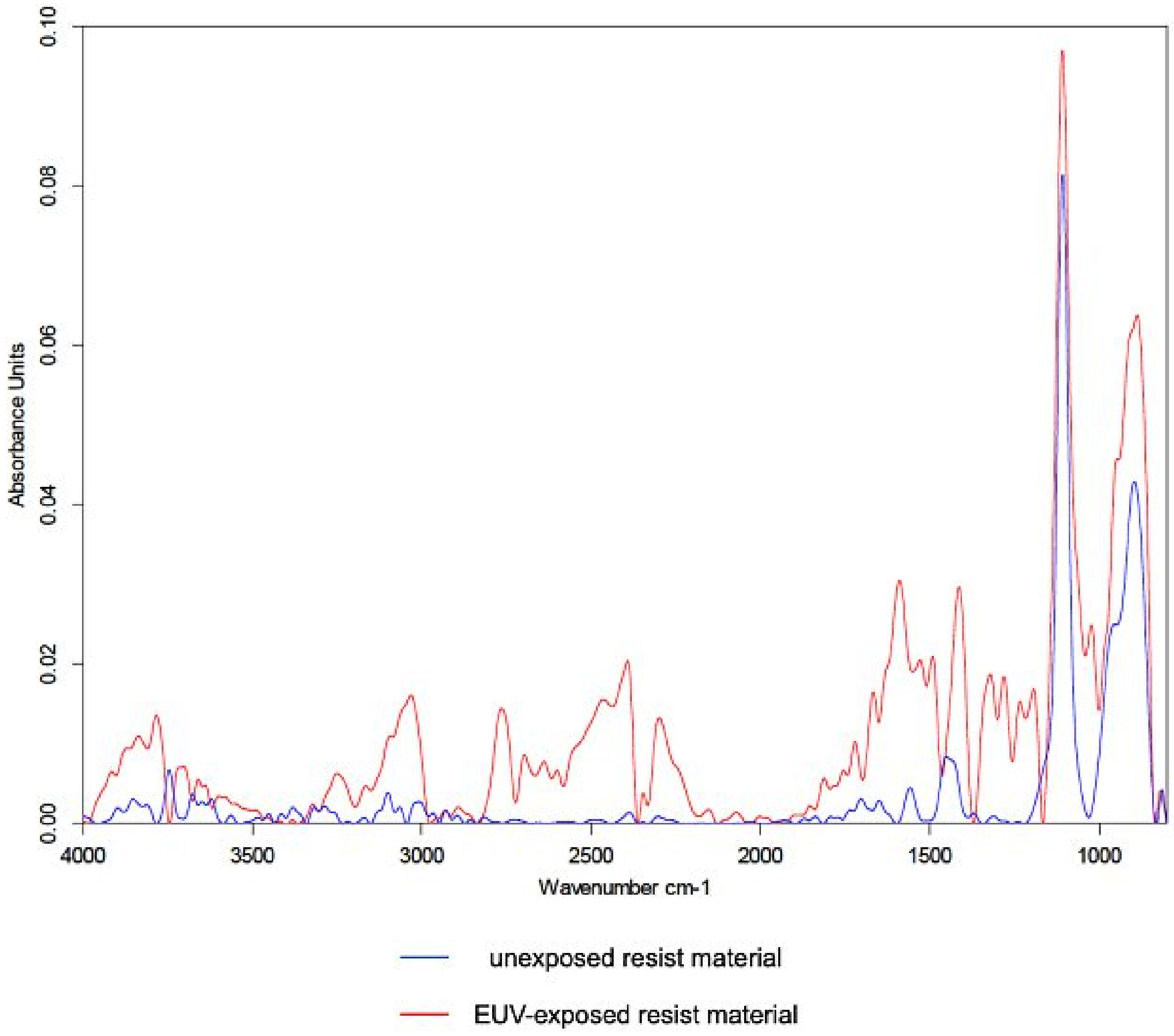

| Wavenumber (cm$^{-1}$) | Assignment | Wavenumber (cm$^{-1}$) | Assignment |
|---|---|---|---|
| **3700 - 3580** | O-H stretching (free alcohol) | 1720 - 1706 | C=O stretching (carboxylic acid dimer) |
| **3550 - 3200** | O-H stretching (intermolecular-bonded alcohol) | 1665 | C=C stretching (vinylidene) |
| **3300 - 3200** | C-H stretching (carboxylic acid) | 1650 - 1560 | C=C stretching (cyclic alkene) |
| **3150 - 2980** | O-H stretching (carboxylic acid) | 1490 | C-H bending (methyl group) |

|  |  |  |  |
|---|---|---|---|
| **2800 - 2730** | C-H stretching<br>(alkane) | 1440 - 1395 | O-H bending<br>(carboxylic acid) |
| **2350** | O=C=O stretching<br>(Carbon dioxide) | 1150 - 1085 | C-O stretching<br>(aliphatic ether) |
| **1750 - 1735** | C=O stretching<br>(ester) | 895 - 885 | C=C bending<br>(vinylidene) |

*Figure 10-18: FTIR spectrum of unexposed and EUV-exposed* $Zr_{12}O_8(OH)_8(OMc)_8(OAc)_{16}\cdot 6HOAc$.

#### 10.3.2.4 $Ti_4Zr_2O_4(OBu)_6(OMc)_{10}$

O=C=O stretching from $CO_2$ at 2350 cm$^{-1}$ becomes the most predominant peak again in $Ti_4Zr_2O_4(OBu)_6(OMc)_{10}$ spectrum since its high methacrylate moiety content (Figure 10-19). Cleavage of methacrylate ligands leading to the formation of free methacrylic acids also caused carboxylic O-H stretching and peaks at 1740, 1695 and 1650 cm$^{-1}$ to shift upwards to higher wavenumbers proving the feasibility of condensation pathway for solubility switch. DEA fragments of methacrylic acid yet contribute to the intensity of $CO_2$ peak.

Similarly, C=C stretching of cyclic alkene appears significantly as in $Zr_4O_2(OMc)_9(OPiv)_3$. A possible explanation is related to the crosslinking density of metal oxo clusters. Resist materials with more methacrylate ligands in a single cluster provide many positions for crosslinking. As a result, there are more possibilities to create cyclic structures after EUV exposure in this case. In the spectra of $Zr_4O_2(OMc)_6(OPiv)_6$ and $Zr_{12}O_8(OH)_8(OMc)_8(OAc)_{16}\cdot 6HOAc$, this cyclic formation is not very pronounced potentially due to their lower crosslinking density or relatively bulky structure.

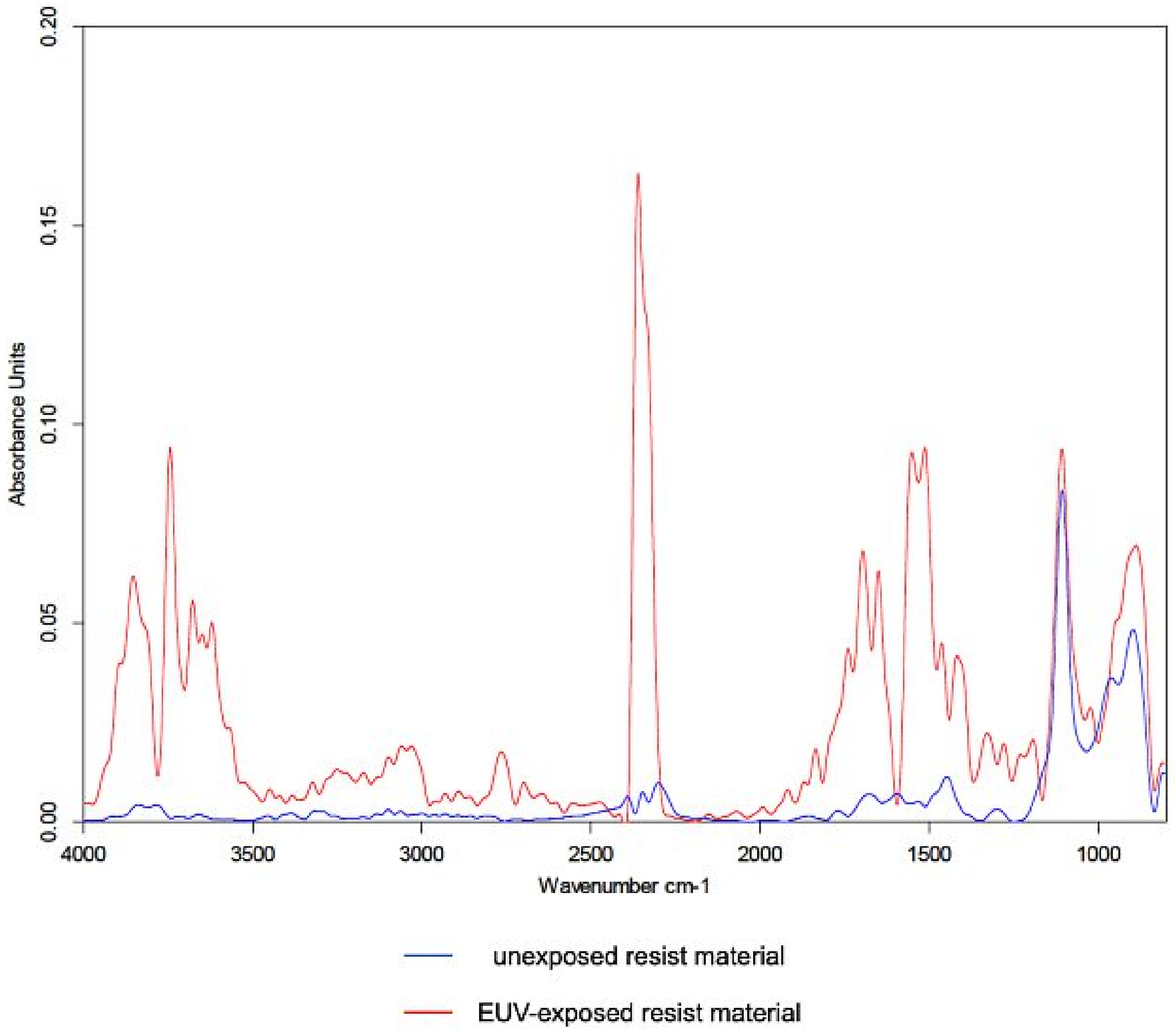

| **Wavenumber (cm$^{-1}$)** | **Assignment** | **Wavenumber (cm$^{-1}$)** | **Assignment** |
|---|---|---|---|
| **3700 - 3580** | O-H stretching (free alcohol) | 1720 - 1706 | C=O stretching (carboxylic acid dimer) |
| **3550 - 3200** | O-H stretching (intermolecular-bonded alcohol) | 1665 | C=C stretching (vinylidene) |
| **3300 - 3200** | C-H stretching (carboxylic acid) | 1650 - 1560 | C=C stretching (cyclic alkene) |
| **3150 - 2980** | O-H stretching (carboxylic acid) | 1440 - 1395 | O-H bending (carboxylic acid) |

| | | | |
|---|---|---|---|
| **2800 - 2730** | C-H stretching (alkane) | 1150 - 1085 | C-O stretching (aliphatic ether) |
| **2350** | O=C=O stretching (Carbon dioxide) | 895 - 885 | C=C bending (vinylidene) |
| **1750 - 1735** | C=O stretching (ester) | | |

*Figure 10-19: FTIR spectrum of unexposed and EUV-exposed $Ti_4Zr_2O_4(OBu)_6(OMc)_{10}$.*

#### 10.3.2.5 $Ti_2Zr_5HfO_6(OMc)_{20}$

The FTIR spectrum of $Ti_2Zr_5HfO_6(OMc)_{20}$ has most of the characteristic signals identical to those in $Ti_4Zr_2O_4(OBu)_6(OMc)_{10}$ (Figure 10-20). However, the intensity of O=C=O stretching at 2350 $cm^{-1}$ is not in proportional to methacrylate moiety content as expected. Peaks at 1760, 1725 and 1665 indeed shifted to higher wavenumber yet in a short distance. Both results indicate that cleaving off methacrylate ligands from $Ti_2Zr_5HfO_6(OMc)_{20}$ cluster does not seem to be efficient. Only a small amount of free methacrylic acid can be generated in contrast to that from $Ti_4Zr_2O_4(OBu)_6(OMc)_{10}$ cluster, even though $Ti_2Zr_5HfO_6(OMc)_{20}$ has a higher methacrylate content. And this phenomenon also leads to less amount of reactive DEA fragments that is capable of triggering crosslinking mechanism among the clusters.

According the contrast curve result, $Ti_2Zr_5HfO_6(OMc)_{20}$ still has a relatively good sensitivity towards EUV photons. It is mainly owing to the high optical sensitive metal moieties consisting of the metal core that helps capturing more EUV photons for inducing photochemical reactions. Yet its patterning capability for E-beam lithography can be potentially inferior.

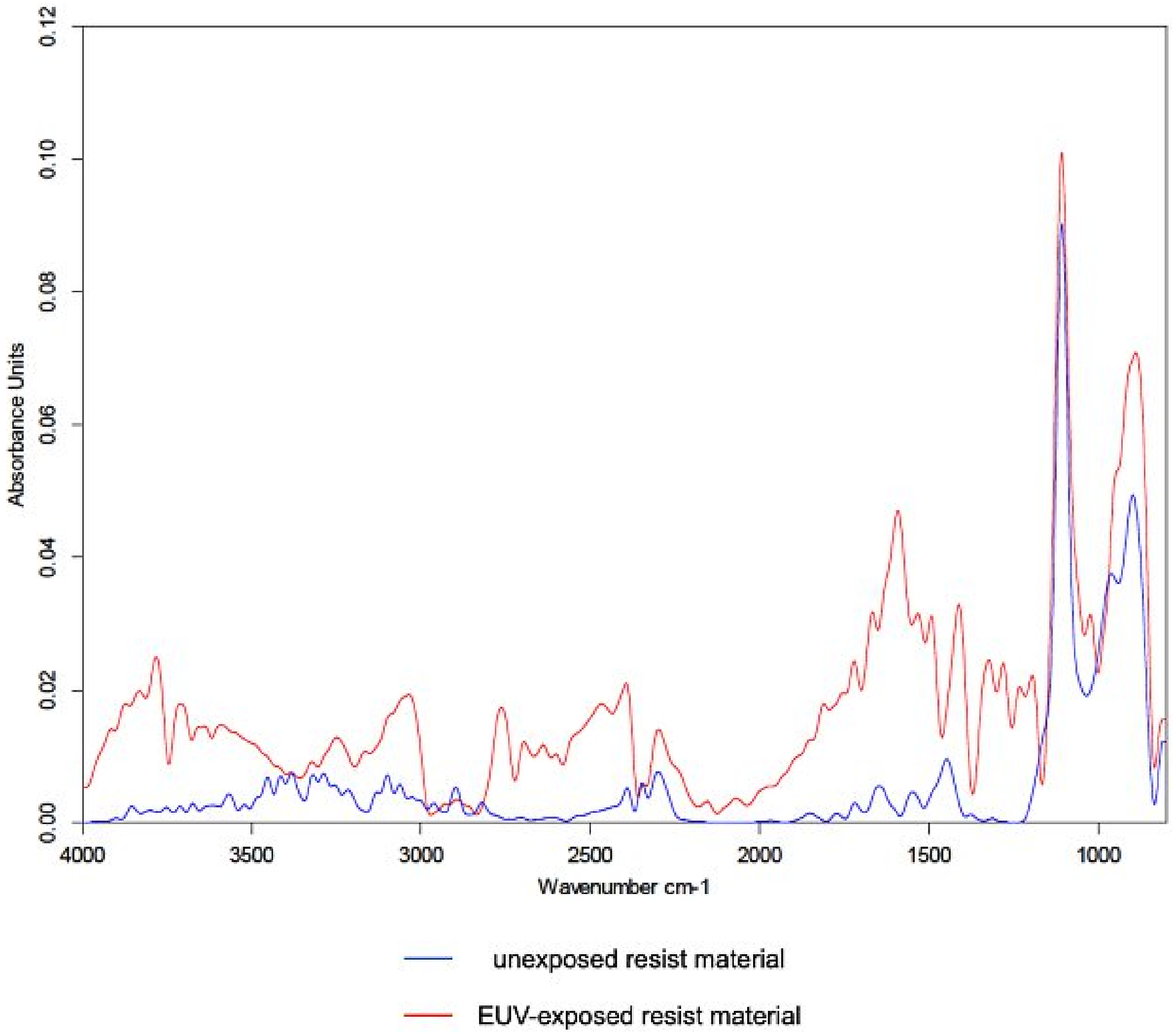

| **Wavenumber (cm$^{-1}$)** | **Assignment** | **Wavenumber (cm$^{-1}$)** | **Assignment** |
|---|---|---|---|
| **3700 - 3580** | O-H stretching (free alcohol) | 1720 - 1706 | C=O stretching (carboxylic acid dimer) |
| **3550 - 3200** | O-H stretching (intermolecular-bonded alcohol) | 1665 | C=C stretching (vinylidene) |
| **3300 - 3200** | C-H stretching (carboxylic acid) | 1650 - 1560 | C=C stretching (cyclic alkene) |
| **3150 2980** | O-H stretching (carboxylic acid) | 1440 - 1395 | O-H bending (carboxylic acid) |

| | | | |
|---|---|---|---|
| **2800 - 2730** | C-H stretching (alkane) | 1150 - 1085 | C-O stretching (aliphatic ether) |
| **2350** | O=C=O stretching (Carbon dioxide) | 895 - 885 | C=C bending (vinylidene) |
| **1750 - 1735** | C=O stretching (ester) | | |

*Figure 10-20: FTIR spectrum of unexposed and EUV-exposed* $Ti_2Zr_5HfO_6(OMc)_{20}$.

## 10.4 Summary

Studying mechanisms of EUV resist materials is complicated and lack of straightforward time-resolved approaches for characterising. In this work, multi-dimension analyses and experiments were employed in order to understand possible photochemical interactions and reaction pathways that eventually lead to solubility switch for lithographic patterning. Dissociative electron attachment (DEA) spectroscopy is a useful technique with respect to electron-induced chemistry research, where low energy electrons are projected to gas-phase material and excites the molecules. Decay then takes place through different routes including DEA that excited molecules dissociate into radical and radical anion depending on their electron affinity. DEA spectroscopy is able to provide an overview for simulating how secondary electrons formed after EUV exposure interacts with photoresist material and induce following reactions. The carboxylic acid precursors (methacrylic acid, 3-butenoic acid, and trans-2,3-dimethacrylic acid) and $Zr_4O_2(OMc)_{12}$ were tested via the setup in Siedlce University of Natural Sciences and Humanities. The results of carboxylic acids indicated that dehydrogenation dominates the relaxation pathways, leaving dehydrogenated carboxylic species as the most abundant fragment in DEA spectra. In $Zr_4O_2(OMc)_{12}$ experiments, dehydrogenated methacrylic radical anion was also predominant among all the fragments. This suggests cleavage of methacrylate ligands from $Zr_4O_2(OMc)_{12}$ is a preferred pathway, which results in active sites on the metal cores that promote condensation reaction with neighbouring clusters. Crosslinking of methacrylate ligands on the clusters can be initiated as well via radicals generated in DEA. Both routes could be the origin(s) of solubility switch for the metal oxo cluster.

Outgassing analysis is widely-used technique to define contamination source of resist materials before they are exposed in an actual exposure tool. Besides, it is beneficial to provide information regarding outgassed species that are related to solubility switch mechanism. $Ti_2Zr_4O_4(OBu)_2(OMc)_{14}$ was tested by an EUV Technology RGA setup at IMEC. The cluster was spin-coated on an 8-inch wafer to form a 30-nm thick layer. A Xe source was used for generating EUV photons that projected onto the wafer surface by a set of mirrors. RGA collected the outgassed species and analysed the outgassing rate as a function of mass. The results revealed predominance of 44 amu resulted from $CO_2$ and traces of methacrylic acid as well as fragments from butoxide ligands. As DEA and crosslinking of clusters can both contribute to the formation of $CO_2$, it is corresponding to the initial prediction. The outgassing rate of methacrylic acid is relatively low mainly attributed to secondary and low energy electrons that dissociate cleaved methacrylate ligands into smaller fragments. Furthermore, lack of post exposure bake also restrains condensation pathway and eventually gives rise to much less methacrylic acid.

Transmission thin-film FTIR spectroscopy is capable of revealing structural information of resist materials before and after EUV exposure. Sample preparation and EUV exposure of $Zr_4O_2(OMc)_6(OPiv)_6$, $Zr_4O_2(OMc)_9(OPiv)_3$, $Zr_{12}O_8(OH)_8(OMc)_8(OAc)_{16}\cdot 6HOAc$, $Ti_4Zr_2O_4(OBu)_6(OMc)_{10}$, $Ti_2Zr_5HfO_6(OMc)_{20}$ were conducted at Paul Scherrer Institute (PSI) and transmission FTIR was carried out at TU Wien. $CO_2$ formation is still quite pronounced in every exposed sample due to DEA fragments as well as crosslinking products. Downshift of wavenumber from methacrylic acid signals are observed, meaning intermolecular interaction has been reduced resulted from free methacrylic acids generated after exposing. Evident C=C stretching from cyclic alkene was also recorded in some of the spectra. This also suggests a potentially methacrylate crosslinking structure was created by EUV photons. Nevertheless, it is difficult to distinguish between two possible solubility switch pathways since evidences of both routes all appear in the spectra. Hence, the origin of solubility switch is conceivably the combination of the two.

# 11 Summary and Conclusions

As EUV technology has been employed for high volume manufacturing in semiconductor industry, photoresist materials require optimisations in various dimensions with the downsizing of IC feature size. Conventional chemically amplified resists that are being widely used have been confronted with serious resolution and line edge roughness issues in sub-30 nm patterning due to the diffusion of acid. The acids generated by photoacid generator after EUV exposure are capable of inducing chemical reactions to trigger the solubility switch. However, the diffusion path and photon stochastics have become significant with the decrease of feature sizes, resulting in rough pattern edges and defects. Additionally, the resolution is deteriorating as well.

Recently, the emerging of metal oxide for EUV resist applications has drawn much attention in academy and semiconductor industry. This type of materials utilises metal moiety that has good linear absorption coefficient towards EUV photons, namely inclination to attract EUV photons, to replace photoacid generator and increase sensitivity upon EUV exposure. Since the initiation of the solubility switch is not triggered via an acid, the line edge roughness is no longer affected by acid diffusion issue and can be improved in sub-30 nm patterning. In addition, a metal moiety is also able to increase the mechanical properties of the material and helps to avoid pattern collapse during development process. Both advantages can potentially lead to higher resolution and sensitivity eventually, if metal moiety and material are properly selected and structured.

The organometallic compounds developed in this work are primarily based on metal oxo clusters. In order to design the materials, EUV optical sensitive metals play the key role in core formation for increasing sensitivity. Whereas polymerisable organic moiety is included as ligand in order to form a crosslinked structure after exposure. Solubility switch can be feasible attributed to the photochemical reaction initiated by primary EUV photons and secondary electrons and therefore patterns from photomask can be transferred to the silicon wafer surface after development. Titanium, zirconium and hafnium are the main metallic composition of the developed metal oxo clusters, which leads to two different categories, the mono- and multi-metallic systems.

$Zr_4O_2(OMc)_{12}$ was selected as the benchmark. Optimisations with respect to synthesis, purification and characterisations were conducted within the study of $Zr_4O_2(OMc)_{12}$ and normalised for the other metal oxo clusters. Methacrylic acid precursor was then replaced with carboxylic acids including pivalic acid, vinylacetic acid and tiglic acid for creating clusters that have very high structural similarity yet with different ligand species. Additionally, a ligand exchange approach was then applied in order to substitute different proportions of crosslinkable methacrylate ligands with non-crosslinkable pivalic ligands. Along with $Zr_{12}O_8(OH)_8(OMc)_8(OAc)_{16}\cdot6HOAc$ and $Hf_4O_2(OMc)_{12}$ synthesised via carboxylic acid route, these materials enabled the investigation of influence from ligand crosslinking density as well as core and ligand structure on lithographic capabilities.

Multi-metallic compounds are metal oxo clusters that incorporates two or more different kinds of metals (Ti, Zr and Hf) in a single crystal. Ti-Zr clusters including $Ti_4Zr_4O_6(OBu)_4(OMc)_{16}$, $Ti_2Zr_4O_4(OBu)_2(OMc)_{14}$ and $Ti_4Zr_2O_4(OBu)_6(OMc)_{10}$ were synthesised via similar carboxylic acid route, while $Ti_4Hf_4O_6(OBu)_4(OMc)_{16}$ was generated by replacing the zirconium precursor in $Ti_4Zr_4O_6(OBu)_4(OMc)_{16}$ synthesis with hafnium n-butoxide. Moreover, Ti, Zr and Hf n-butoxide were employed in the synthesis together with methacrylic acid, which give rise to the formation of $Ti_2Zr_5HfO_6(OMc)_{20}$. Through investigations of their patterning performance, it was possible to evaluate and compare the influence of additional metal moieties as well as feasibility to pattern the dual and tri-metallic oxo clusters via electron beam, DUV and EUV.

Due to low accessibility of EUV exposure tool, the process conditions for each material required to be determined step by step and proven to be attainable by the actual electron beam lithographic patterning before proceeding to EUVL at PSI (Figure 11-1). Starting from a series of solubility tests with various organic solvents for spin-coating, the coated films had to achieve moderate film thicknesses (25 to 40 nm) and homogeneous surface finish to avoid pattern collapse and defectivity. The acquired spin-coating parameters and conditions were employed to coat each material onto quartz plates for sample preparation of thin-film UV/Vis spectroscopy. By comparing the intensity of absorption band before and after development along with a preliminary DUV exposure, it was straightforward to know if the coated film could be stripped off by the selected developer while leaving the exposed material on the surface of silicon wafer. Most of the metal oxo clusters revealed relatively good coatability as well as developability except $Zr_4O_2(OPiv)_{12}$, which precipitated in seconds in spin-coating process and could only result in inhomogeneous films. Therefore, it did not advance to the lithographic steps. Developers of several clusters were still modified depending on the results of EBL. Given that polarity of developing solvent is crucial for acquiring higher pattern contrast and even better resolution, several approaches including solvent mixtures and addition of carboxylic acid in developers have been tried on the clusters to compare patterning performance.

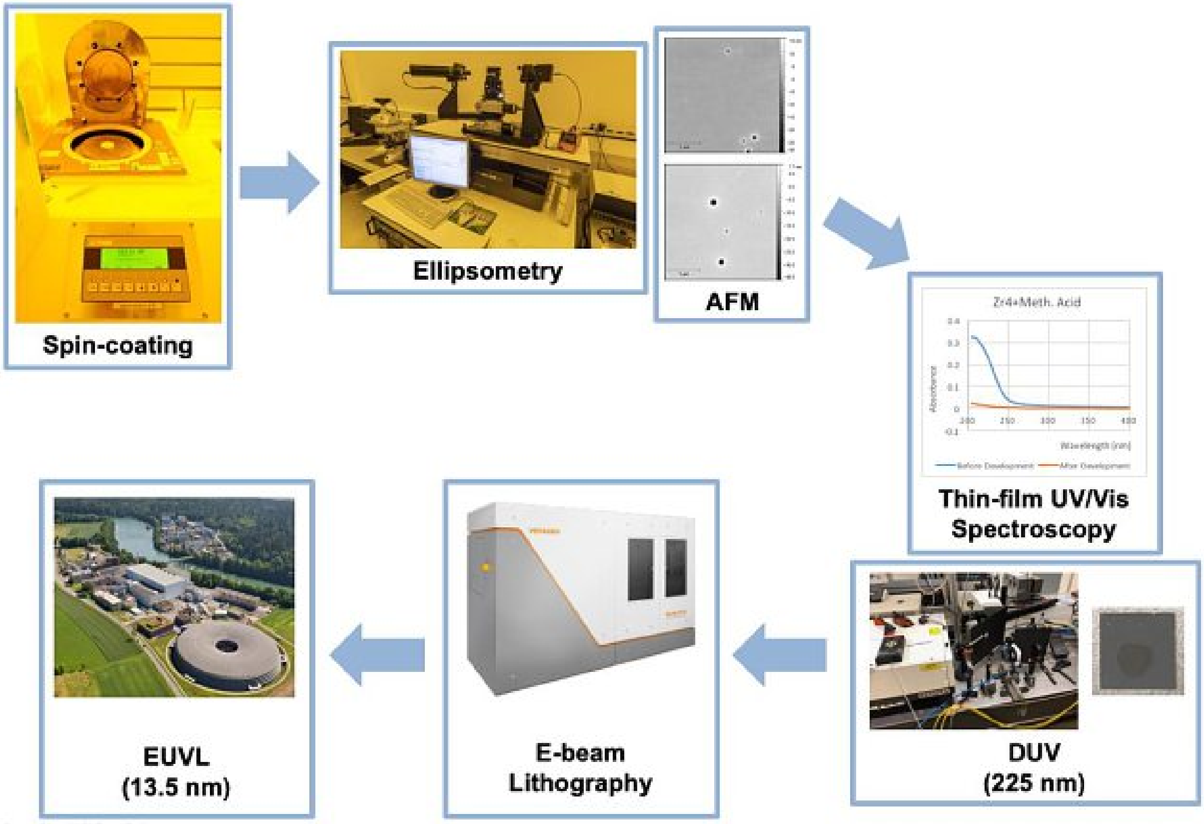

*Figure 11-1: Schematic diagram on the determination of process conditions for the metal oxo clusters.*

The performance of $Zr_4O_2(OMc)_{12}$ remained as the benchmark for the other clusters. It showed good patterning capabilities with area dose at 50 μC/cm$^2$ and line dose 50 ρC/cm. Different developers or developer mixtures were also tested to render high contrast and resolution results. Developing solvents, such as isopropanol and chloroform with propionic acid, were too polar to dissolve not just unexposed material but the polymerised clusters, making them non-ideal as developer. On the contrary, toluene was not able to create much contrast due to its low polarity. As a result, ethyl acetate was employed for addition to chloroform in order to tune the polarity to the moderate point where most of the unexposed area was washed away. This rule was also applied to defining developers for the other clusters.

Compared with $Zr_4O_2(OMc)_{12}$, the mixed-ligand clusters ($Zr_4O_2(OMc)_x(OPiv)_{12-x}$, x=3, 6, 9) required twice as much as the doses for $Zr_4O_2(OMc)_{12}$ to have good patterning results. It also has been revealed that crosslinking density of the metal oxo cluster have an impact on material sensitivity, namely the sensitivity increases with the rise of crosslinking density, as clearly indicated by the line dose comparison of the mixed-ligand clusters (Figure 11-2). The EBL patterning performance of $Hf_4O_2(OMc)_{12}$ is close to that of $Zr_4O_2(OMc)_{12}$, whereas multi-metallic system has also been proven feasible to be lithographically patterned yet their sensitivities are slightly lower. However, the scenario was different from that of EUVL since metal moieties do not affect material sensitivity towards electron beam as for EUV photons.

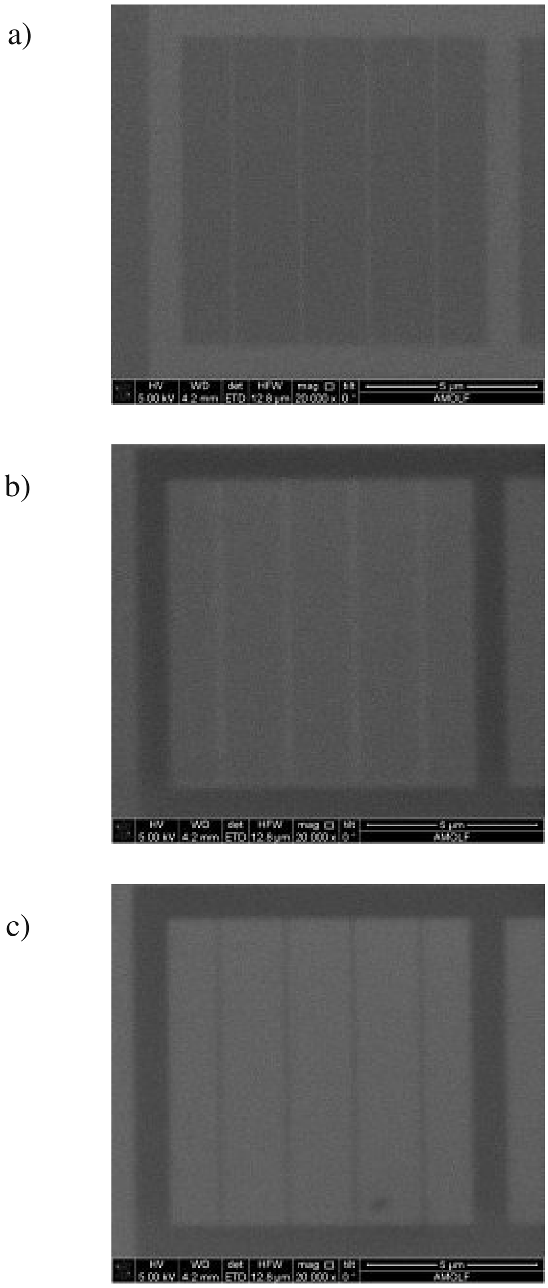

*Figure 11-2: Line dose patterning of a) $Zr_4O_2(OMc)_3(OPiv)_9$, b) $Zr_4O_2(OMc)_6(OPiv)_6$ and c) $Zr_4O_2(OMc)_9(OPiv)_3$.*

EUV exposure was conducted at PSI after the metal oxo clusters revealed the lithographic capabilities via EBL. Contrast curve analysis and line/space patterning were the primary experiments carried out for the investigation material properties. Contrast curve was an open-framed exposure, meaning no photomask was installed. It was conducted by exposing the coated material to different doses of EUV photons at multiple locations. The sample was developed afterwards and thicknesses of exposed area were measured. A contrast curve diagram can be plotted with dose as a function of remaining film thickness. Sensitivities of the materials are indicated by the value of slope. Line/space patterning was carried out via interference mechanism to generate line/space patterns with half-pitch of 50, 40, 30, 22 nm.

As expected from the results of EBL, sensitivities of $Zr_4O_2(OMc)_{12}$ the mixed-ligand clusters were positively correlated to crosslinking density of clusters even though $Zr_4O_2(OMc)_6(OPiv)_6$ is slightly less sensitive in comparison with $Zr_4O_2(OMc)_3(OPiv)_9$, which was potentially attributed to the developer employed. Line/space patterning has revealed that the solubility switch of each cluster could be successfully initiated by EUV photons and developed in high contrast with the developer (or developer mixture) defined from EBL patterning (Figure 11-3). Nevertheless, $Zr_4O_2(OMc)_6(OPiv)_6$ and $Zr_4O_2(OMc)_9(OPiv)_3$ have severe pattern collapse in small feature-size patterns (30 and 22 nm), which resulted mainly from a high film thickness. Development also gave rise to aggregates as well as bubbles distributing throughout the patterns. These facts indeed indicated the process conditions still require optimisations for EUVL.

| **$Zr_4O_2(OMc)_{12}$** | **$Zr_4O_2(OMc)_3(OPiv)_9$** |
|---|---|
| 28 mJ/cm$^2$<br>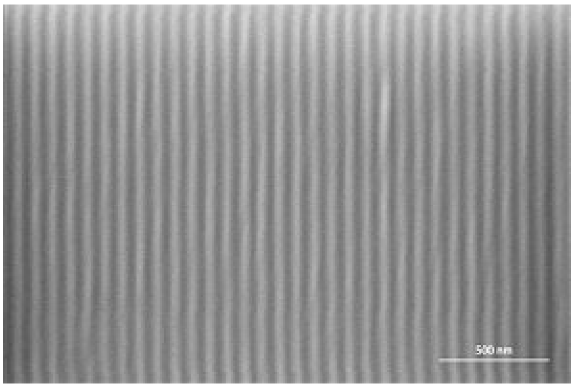<br> | 30 mJ/cm$^2$<br>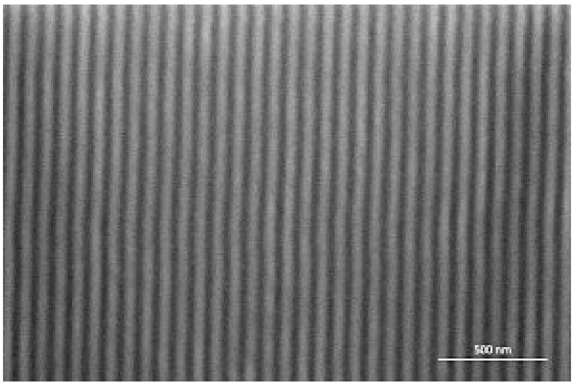<br> |
| **$Zr_4O_2(OMc)_6(OPiv)_6$** | **$Zr_4O_2(OMc)_9(OPiv)_3$** |
| 30 mJ/cm$^2$<br>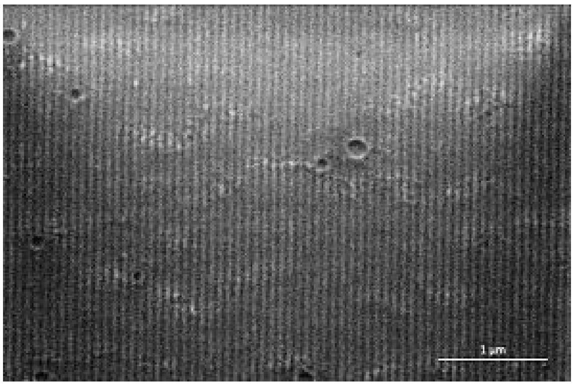<br> | 28 mJ/cm$^2$<br>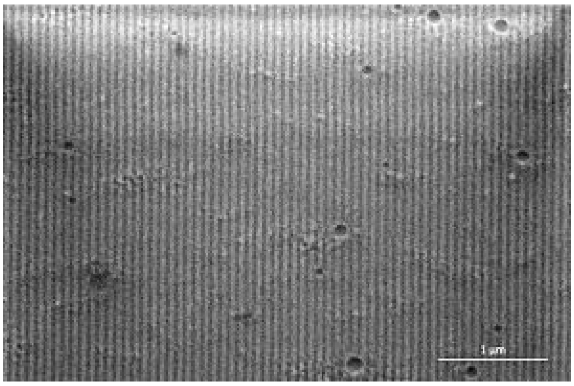<br> |

*Figure 11-3: Line/space patterning of $Zr_4O_2(OMc)_{12}$ and the mixed ligand clusters at 40 nm HP.*

Given the fact that $Zr_4O_2(ODiMc)_{12}$ failed to be patterned with the process conditions employed, the study on the influence of ligand allyl group position upon patterning performance has not been completed. $Zr_4O_2(OVinac)_{12}$ has comparable EUV lithographic capabilities as those of $Zr_4O_2(OMc)_{12}$ with respect to sensitivity and resolution due to their high structural similarity. Moreover, $Zr_{12}O_8(OH)_8(OMc)_8(OAc)_{16}{\cdot}6HOAc$ did not show a substantially improved sensitivity in contrast to $Zr_4O_2(OMc)_{12}$. Its high shrinkage has possibly led to a deteriorating resolution, which diminishes the potential of being used as EUVL photoresist.

Multi-metallic oxo clusters have revealed good patterning capabilities upon EUV exposure. Not only their sensitivities were improved compared with the zirconium oxo clusters by addition of high EUV optical sensitive Ti and Hf, but the line/space patterns were less defective owing to moderate film thicknesses as well as the developer mixture that is less volatile. High methacrylate content of $Ti_2Zr_5HfO_6(OMc)_{20}$ has made it very sensitive to moisture, which is possibly one of the reasons that aggregates are distributed throughout the patterns and low contrast. It can be a considerable disadvantage for photoresist applications.

EUVL patterning of $Hf_4O_2(OMc)_{12}$ resulted in rough patterns with most of the materials being dissolved by the developer, which is different from that of EBL. Therefore, the investigation on the effect of core formation could not be conducted.

In order to understand solubility switch mechanism of the metal oxo clusters upon incident EUV photons, three different approaches have been carried out to study detailed photochemical interactions after EUV exposure. Since the majority of reactions are activated by low energy secondary electrons, dissociative electron attachment spectroscopy utilised low energy electrons ranging from 0 to 12 eV to interact with gas-phase ligand precursors as well as $Zr_4O_2(OMc)_{12}$. The molecule can be disintegrated into fragments by electrons with certain energy via DEA pathway. Dehydrogenated carboxylic acid is the most predominant fragment in all precursor analyses (methacrylic acid, 3-butenoic acid and trans-2,3-dimethacrylic acid), indicating the structures are nearly unbreakable by electron energy between 0-12 eV. The other fragments including $O^-$, $COO^-$ and $HCOO^-$ are products from carboxylic group yet their intensities are relatively low. Similar results are also observed in $Zr_4O_2(OMc)_{12}$ experiment, with dehydrogenated methacrylic acid dominating. DEA spectroscopy has proven that low energy electrons are capable of cleaving methacrylate ligands from the metal core, giving rise to an active site on the surface for initiating condensation reaction. On the other hand, cleaved methacrylate ligands are so reactive that they are able to react with allyl groups of other methacrylate ligands remaining on the clusters.

Conducted at IMEC, outgassing analysis was carried out by projecting EUV photons generated by a Xe-based source onto an 8-inch, $Ti_2Zr_4O_4(OBu)_2(OMc)_{14}$-coated silicon wafer. The outgassed species were collected and analysed by a residual gas analyser and the mass of fragment was then revealed as a function of outgassing rate. Unlike the results of DEA spectroscopy, $CO_2$ (44 amu) is the most pronounced outgassed fragment. Since $CO_2$ is also one of the DEA products of methacrylic acid, it could contribute to the outgassing rate. Additionally, crosslinking of methacrylate ligands can potentially lead to the formation of $CO_2$ from carboxylic groups. Both pathways are considered as the main reasons that $CO_2$ has a high outgassing rate. Methacrylate was also outgassing but with much slower rate, meaning cleavage of methacrylate ligand still occurred and is feasible upon EUV exposure.

The last approach for mechanism study was thin-film transmission FTIR of the EUV exposed metal oxo clusters including $Zr_4O_2(OMc)_9(OPiv)_3$, $Zr_4O_2(OMc)_6(OPiv)_6$, $Zr_{12}O_8(OH)_8(OMc)_8(OAc)_{16}{\cdot}6HOAc$, $Ti_4Zr_2O_4(OBu)_6(OMc)_{10}$ and $Ti_2Zr_5HfO_6(OMc)_{20}$. Spectra of unexposed and exposed samples were compared the wavenumber and intensity changes of peaks. In most cases, an O=C=O stretching signal with high intensity appears in the exposed material. It has revealed the formation of a large quantity of $CO_2$, which is corresponding to the result of outgassing analysis. A C=C stretching of cyclic alkene was also recorded after EUV exposure. It proves crosslinking of methacrylate ligands forms a cyclic structure that results in solubility switch for development. Moreover, the peaks of C=O and C=C stretching of methacrylate have shifted to higher wavenumber, indicating the intermolecular interaction has been reduced. Cleavage of methacrylate ligands after EUV exposure is able to provide more degree of freedom for methacrylates and keep them from being restrained within the clusters. As a result, the intermolecular interaction decreases.

In this work, the metal oxo clusters were successfully synthesised and modified through different carboxylic acid. The products could reach high purity with an optimised process. Their coatability and developability were determined by a series of experiments in order to figure out superior process conditions for actual lithography. Despite patterning failed to be rendered on a few of the clusters, these state-of-the art resist materials have demonstrated improved EBL and EUVL patterning capabilities and in the meantime are exhibiting great potentials for further structural modifications with respect to reaching better patterning performance. In mechanism study, DEA spectroscopy, outgassing analysis and thin-film FTIR have proven both proposed condensation and crosslinking routes for solubility switch are feasible upon EUV exposure. Yet it is difficult to understand which pathway dominates the mechanism. The lack of direct technique remains an issue of providing convincing evidence on actual solubility switch scenario. Therefore, time-resolved spectroscopy will be a powerful and beneficial tool in terms of EUV resist mechanism study.

# Appendix 1: Synthesis Details

## 1 Preparation of Zirconium Oxo Clusters

### 1.1 Synthesis of $Zr_4O_2(OMc)_{12}$ (1)

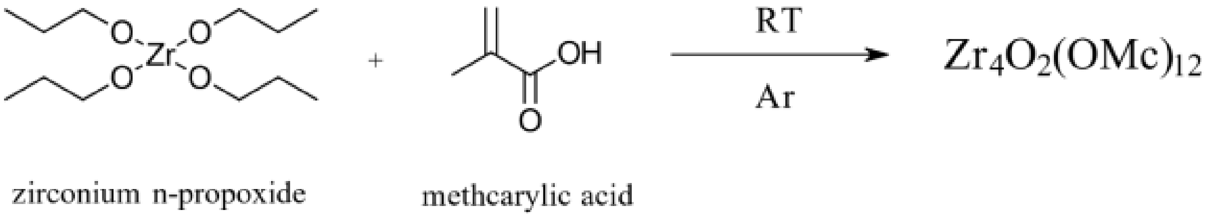

| Compound | Equivalents | n [mmol] | m [g] |
|---|---|---|---|
| Zirconium n-propoxide | 1.00 | 9.15 | 3.00 |
| Methacrylic acid | 4.07 | 37.20 | 3.20 |

The reaction and purification procedure were carried out with conventional Schlenk apparatus to exclude influence from oxygen and moisture. For the synthesis of $Zr_4O_2(OMc)_{12}$, 3.20 g (37.2 mmol, 4.07 eq.) of pre-distilled methacrylic acid and 4.28 g of a 70% zirconium propoxide solution (9.15 mmol, 1 eq.) in n-propanol were weighed into a Schlenk flask and a sealed container inside the glovebox, respectively. After the Schlenk flask being transferred to Schlenk line, zirconium propoxide was slowly added to methacrylic acid under argon. The reaction was exothermic. The solution was stirred for 1 hr and allowed to stand at room temperature. Colourless prismatic crystals were generated after 2 days [15].

To purify, the crystalline products were first separated from the mother liquor. 10 mL of dry n-hexane was added into the Schlenk flask to wash the crystals and then removed by a syringe. The process was repeated 3 times. Eventually, the crystals were dried at $10^{-6}$ bar to evaporate the solvent for 6 hrs before being stored inside the glovebox at room temperature.

| | |
|---|---|
| Yield: | 2.71 g (84%), M=1417.8 g·mol$^{-1}$ |
| $^1$H NMR: $\delta_H$ (ppm, 400 MHz, $CDCl_3$) | 6.13 (s, 12 H, $CH_2$, cis-H to the carboxylate group), 5.40 (s, 12 H, $CH_2$, trans-H to the carboxylate group), 1.76 (s, 36 H, $CH_3$) ppm |

| | |
|---|---|
| $^{13}$C NMR: $\delta_C$ (ppm, 400 MHz, $CDCl_3$) | 168.9 (COO), 137.4 ($CH_2C(CH_3)COO$), 125.5 ($CH_2$), 18.7 ($CH_3$) ppm |
| Elemental Analysis for $Zr_4C_{48}H_{60}O_{26}$ | (calc.) Zr, 25.67; C, 40.62; H, 4.23; O, 29.34 |
| | (founded) Zr, 25.72; C, 40.59; H, 4.29; O, 28.07 |
| FTIR (ATR): | 2978 (w, CH), 2957 (w, CH), 2925 (w, CH), 1692 (m, COO), 1644 (m, C=C), 1583 (s, br, asym. COO), 1511 (m) 1500 (w), 1456 (s, sym. COO), 1415 (s), 1371 (m), 1321 (w), 1301 (w), 1243 (m), 1204 (w, br), 1008 (w), 938 (m), 880 (w), 827 (w) cm$^{-1}$ |

## 1.2 Synthesis of $Zr_4O_2(OMc)_3(OPiv)_9$ (2)

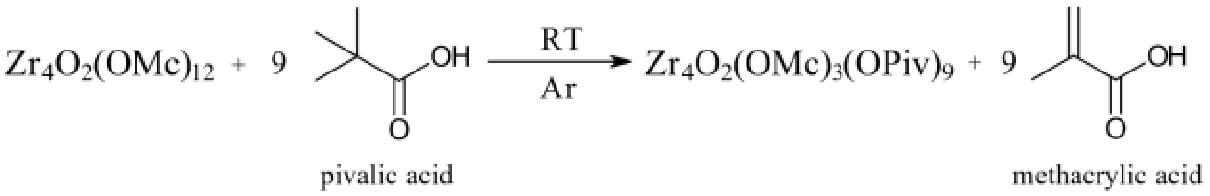

| Compound | Equivalents | n [mmol] | m [g] |
|---|---|---|---|
| $Zr_4O_2(OMc)_{12}$ | 1.00 | 0.35 | 0.50 |
| Pivalic acid | 9.23 | 3.23 | 0.33 |

The reaction and purification procedure were carried out with conventional Schlenk apparatus to exclude influence from oxygen and moisture. The zirconium oxo clusters with mixed ligands were synthesised via ligand-exchange pathway. For the synthesis of $Zr_4O_2(OMc)_3(OPiv)_9$, 0.5 g of $Zr_4O_2(OMc)_{12}$ crystal (0.35 mmol, 1 eq.) was weighed into a Schlenk flask and dissolved in 2 mL of dry dichloromethane (DCM) inside the glovebox before being transferred to Schlenk line. 0.33 g of pivalic acid (3.23 mmol, 9.23 eq.) was weighed into a sealed glass container inside the glovebox. Until a clear solution was obtained, pivalic acid was added dropwise to $Zr_4O_2(OMc)_{12}$ under argon at room temperature. The mixture was stirred for 1 day to ensure a complete exchange of the ligands.

To purify, the solvent was first evaporated via Schlenk line and cooling trap. 10 mL of dry n-hexane was utilised for washing the colourless solids and removed afterwards with a syringe.

The process was repeated 3 times. Eventually, the colourless powder was dried over high vacuum at $10^{-6}$ bar and stored in the glovebox.

| | |
|---|---|
| **Yield:** | 0.35 g (64%), M=1562.0 g·mol$^{-1}$ |
| **$^1$H NMR:** $\delta_H$ (ppm, 400 MHz, $CDCl_3$) | 6.09 (s, 3 H, $CH_2$, cis-H to the carboxylate group), 5.39 (s, 3 H, $CH_2$, trans-H to the carboxylate group), 1.78 (s, 9 H, $CH_3$), 1.03 (s, 81 H, $C(CH_3)_3$) ppm |
| **$^{13}$C NMR:** $\delta_C$ (ppm, 400 MHz, $CDCl_3$) | 170.1 ($COO_{(OPiv)}$), 166.7 ($COO_{(OMc)}$), 139.2 ($CH_2C(CH_3)COO_{(OMc)}$), 134.7 ($(CH_3)_3CCOO_{(OPiv)}$), 123.2 ($CH_{2(OMc)}$), 27.2 ($CH_{3(OPiv)}$), 18.0 ($CH_{3\ (OMc)}$) ppm |
| **FTIR (ATR):** | 2970 (w, CH), 2960 (w, CH), 2928 (w, CH), 1644 (m, C=C), 1560 (s, br, asym. COO), 1522 (m) 1503 (w), 1484 (s, $CH_2$), 1456 (s, sym. COO), 1418 (s), 1372 (m), 1360 (m), 1229 (m), 1117 (w), 1006 (w), 936 (m), 879 (w), 830 (w), 788 (w), 728 (m) cm$^{-1}$ |

### 1.3 Synthesis of $Zr_4O_2(OMc)_6(OPiv)_6$ (3)

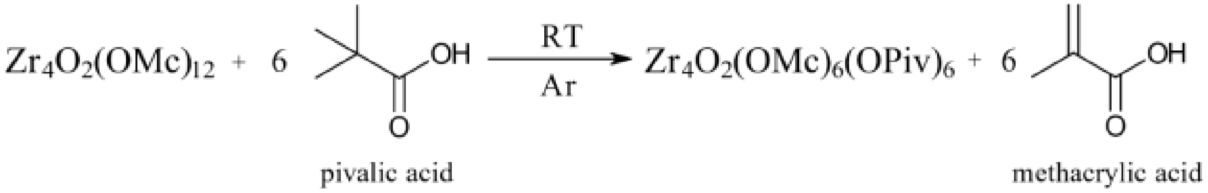

| Compound | Equivalents | n [mmol] | m [g] |
|---|---|---|---|
| $Zr_4O_2(OMc)_{12}$ | 1.00 | 0.35 | 0.50 |
| Pivalic acid | 6.14 | 2.15 | 0.22 |

The reaction and purification procedure were carried out with conventional Schlenk apparatus to exclude influence from oxygen and moisture. The zirconium oxo clusters with mixed ligands were synthesised via ligand-exchange pathway. For the synthesis of $Zr_4O_2(OMc)_6(OPiv)_6$, 0.5 g of $Zr_4O_2(OMc)_{12}$ crystal (0.35 mmol, 1 eq.) was weighed into a Schlenk flask and dissolved in 2 mL of dry dichloromethane (DCM) inside the glovebox before being transferred to Schlenk line. 0.22 g of pivalic acid (2.15 mmol, 6.14 eq.) was weighed into a sealed glass container inside the glovebox. Until a clear solution was obtained, pivalic acid was added dropwise to $Zr_4O_2(OMc)_{12}$ under argon at room temperature. The mixture was stirred for 1 day to ensure a complete exchange of the ligands.

To purify, the solvent was first evaporated via Schlenk line and cooling trap. 10 mL of dry n-hexane was utilised for washing the colourless solids and removed afterwards with a syringe. The process was repeated 3 times. Eventually, the colourless powder was dried over high vacuum at $10^{-6}$ bar and stored in the glovebox.

| | |
|---|---|
| **Yield:** | 0.37 g (70%), M=1513.6 g·mol$^{-1}$ |
| **$^1$H NMR:** $\delta_H$ (ppm, 400 MHz, $CDCl_3$) | 6.12 (s, 6 H, $CH_2$, cis-H to the carboxylate group), 5.39 (s, 6 H, $CH_2$, trans-H to the carboxylate group), 1.78 (s, 18 H, $CH_3$), 1.05 (s, 54 H, $C(CH_3)_3$) ppm |
| **$^{13}$C NMR:** $\delta_C$ (ppm, 400 MHz, $CDCl_3$) | 169.8 ($COO_{(OPiv)}$), 165.9 ($COO_{(OMc)}$), 141.7 ($CH_2C(CH_3)COO_{(OMc)}$), 134.9 ($(CH_3)_3CCOO_{(OPiv)}$), 126.4 ($CH_{2(OMc)}$), 26.9 ($CH_{3(OPiv)}$), 18.0 ($CH_{3\,(OMc)}$) ppm |
| **FTIR (ATR):** | 2970 (w, CH), 2961 (w, CH), 2928 (w, CH), 1644 (m, C=C), 1560 (s, br, asym. COO), 1483 (s, $CH_2$), 1456 (s, sym. COO), 1413 (s), 1378 (m), 1361 (m), 1227 (m), 1118 (w), 1006 (w), 935 (m), 899 (w), 879 (w), 830 (w), 786 (w), 727 (m) cm$^{-1}$ |

## 1.4 Synthesis of $Zr_4O_2(OMc)_9(OPiv)_3$ (4)

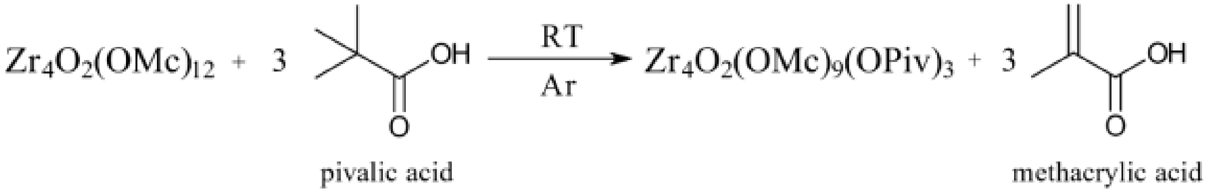

| Compound | Equivalents | n [mmol] | m [g] |
|---|---|---|---|
| $Zr_4O_2(OMc)_{12}$ | 1.00 | 0.35 | 0.50 |

| | | | |
|---|---|---|---|
| Pivalic acid | 3.00 | 1.05 | 0.11 |

The reaction and purification procedure were carried out with conventional Schlenk apparatus to exclude influence from oxygen and moisture. The zirconium oxo clusters with mixed ligands were synthesised via ligand-exchange pathway. For the synthesis of $Zr_4O_2(OMc)_9(OPiv)_3$, 0.5 g of $Zr_4O_2(OMc)_{12}$ crystal (0.35 mmol, 1 eq.) was weighed into a Schlenk flask and dissolved in 2 mL of dry dichloromethane (DCM) inside the glovebox before being transferred to Schlenk line. 0.11 g of pivalic acid (1.05 mmol, 3 eq.) was weighed into a sealed glass container inside the glovebox. Until a clear solution was obtained, pivalic acid was added dropwise to $Zr_4O_2(OMc)_{12}$ under argon at room temperature. The mixture was stirred for 1 day to ensure a complete exchange of the ligands.

To purify, the solvent was first evaporated via Schlenk line and cooling trap. 10 mL of dry n-hexane was utilised for washing the colourless solids and removed afterwards with a syringe. The process was repeated 3 times. Eventually, the colourless powder was dried over high vacuum at $10^{-6}$ bar and stored in the glovebox.

| | |
|---|---|
| **Yield:** | 0.39 g (76%), M=1465.2 g·mol$^{-1}$ |
| **$^1$H NMR:** $\delta_H$ (ppm, 400 MHz, $CDCl_3$) | 6.12 (s, 9 H, $CH_2$, cis-H to the carboxylate group), 5.41 (s, 9 H, $CH_2$, trans-H to the carboxylate group), 1.78 (s, 27 H, $CH_3$), 1.03 (s, 27 H, $C(CH_3)_3$) ppm |
| **$^{13}$C NMR:** $\delta_C$ (ppm, 400 MHz, $CDCl_3$) | 168.9 ($COO_{(OPiv)}$), 164.3 ($COO_{(OMc)}$), 141.7 ($CH_2C(CH_3)COO_{(OMc)}$), 134.2 ($(CH_3)_3CCOO_{(OPiv)}$), 126.9 ($CH_{2(OMc)}$), 26.9 ($CH_{3(OPiv)}$), 18.3 ($CH_{3\,(OMc)}$) ppm |
| **FTIR (ATR):** | 2975 (w, CH), 2962 (w, CH), 2928 (w, CH), 1644 (m, C=C), 1575 (s, br, asym. COO), 1544 (m), 1526 (m), 1485 (s, $CH_2$), 1456 (s, sym. COO), 1419 (s), 1372 (m), 1270 (w), 1243 (m), 1230 (m), 1206 (m), 1118 (w), 1032 (w), 1006 (w), 935 (m), 884 (w), 825 (m), 786 (w), 751 (m) cm$^{-1}$ |

### 1.5 Synthesis of $Zr_4O_2(OPiv)_{12}$ (5)

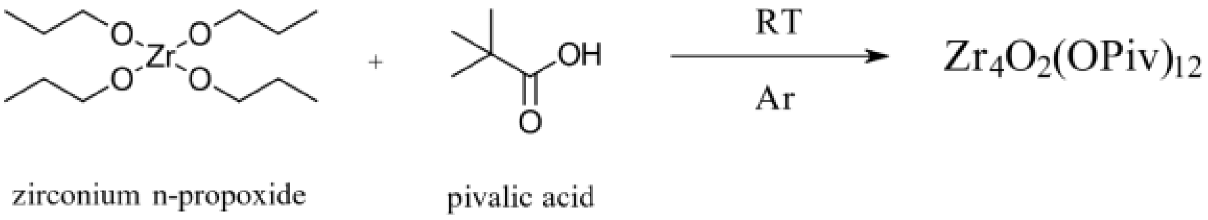

| Compound | Equivalents | n [mmol] | m [g] |
|---|---|---|---|
| Zirconium n-propoxide | 1.00 | 9.15 | 3.00 |
| Pivalic acid | 4.07 | 37.20 | 3.80 |

The reaction and purification procedure were carried out with conventional Schlenk apparatus to exclude influence from oxygen and moisture. For the synthesis of $Zr_4O_2(OPiv)_{12}$, 3.80 g (37.2 mmol, 4.07 eq.) of pre-distilled pivalic acid and 4.28 g of a 70% zirconium propoxide solution (9.15 mmol, 1 eq.) in n-propanol were weighed into a Schlenk flask and a sealed container inside the glovebox, respectively. After the Schlenk flask being transferred to Schlenk line, zirconium propoxide was slowly added to methacrylic acid under argon. The reaction was exothermic. The solution was stirred for 1 hr and allowed to stand at room temperature. Colourless prismatic crystals were generated after 2 days.

To purify, the crystalline products were first separated from the mother liquor. 10 mL of dry n-hexane was added into the Schlenk flask to wash the crystals and then removed by a syringe. The process was repeated 3 times. Eventually, the crystals were dried at $10^{-6}$ bar to evaporate the solvent for 6 hrs before being stored inside the glovebox at room temperature.

| | |
|---|---|
| **Yield:** | 3.47 g (94%), M=1610.4 g·mol$^{-1}$ |
| **$^1$H NMR:** $\delta_H$ (ppm, 400 MHz, $CDCl_3$) | 1.17 (s, 108 H, $C(CH_3)_3$) ppm |
| **$^{13}$C NMR:** $\delta_C$ (ppm, 400 MHz, $CDCl_3$) | 167.8 (COO), 102.5 ($(CH_3)_3CCOO$), 27.6 ($CH_3$) ppm |
| **FTIR (ATR):** | 2964 (m, CH), 2928 (w, CH), 2903 (w, CH), 2870 (w, CH), 1582 (s, br, asym. COO), 1562 (m), 1513 (m), 1483 (s), 1423 (s, sym. COO), 1380 (m), 1360 (m), 1227 (m), 1206 (m), |

1060 (w), 1032 (w), 1010 (w), 960 (w), 940 (m), 909 (m), 860 (w), 816 (w), 788 (w) cm$^{-1}$

## 1.6 Synthesis of $Zr_4O_2(OVinac)_{12}$ (6)

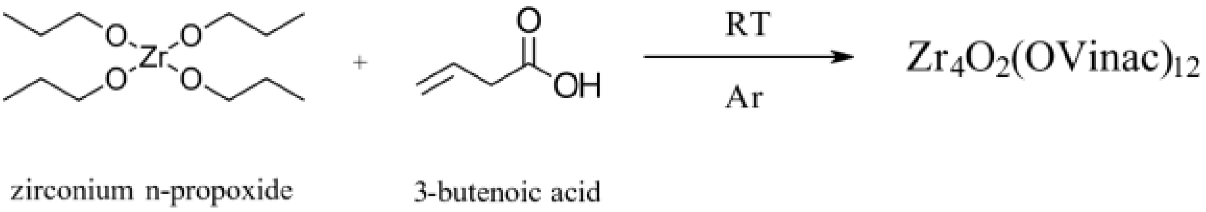

| Compound | Equivalents | n [mmol] | m [g] |
|---|---|---|---|
| Zirconium n-propoxide | 1.00 | 9.15 | 3.00 |
| 3-Butenoic acid | 4.06 | 37.17 | 3.20 |

The reaction and purification procedure were carried out with conventional Schlenk apparatus to exclude influence from oxygen and moisture. For the synthesis of $Zr_4O_2(OVinac)_{12}$, 3.20 g (37.17 mmol, 4.06 eq.) of 3-butenoic acid and 4.28 g of a 70% zirconium propoxide solution (9.15 mmol, 1 eq.) in n-propanol were weighed into a Schlenk flask and a sealed container inside the glovebox, respectively. After the Schlenk flask being transferred to Schlenk line, zirconium propoxide was slowly added to methacrylic acid under argon. The reaction was exothermic. The solution was stirred for 1 hr and allowed to stand at room temperature. Colourless prismatic crystals were generated after 3 days.

To purify, the crystalline products were first separated from the mother liquor. 10 mL of dry n-hexane was added into the Schlenk flask to wash the crystals and then removed by a syringe. The process was repeated 3 times. Eventually, the crystals were dried at 10$^{-6}$ bar to evaporate the solvent for 6 hrs before being stored inside the glovebox at room temperature.

| | |
|---|---|
| **Yield:** | 0.28 g (8.7%), M=1417.8 g·mol$^{-1}$ |
| **$^1$H NMR:** $\delta_H$ (ppm, 400 MHz, $CDCl_3$) | 5.83 (m, 12H, CH), 5.14 (d, 24H, $CH_2=CHCH_2COO$), 3.08 (d, 24H, $CH_2=CH$) ppm |
| **$^{13}$C NMR:** $\delta_C$ (ppm, 400 MHz, $CDCl_3$) | 178.0 (COO), 132.2 ($CH_2CHCH_2COO$), 116.6 ($CH_2$), 31.0 (CH) ppm |

| | |
|---|---|
| **FTIR (ATR):** | 3080 (w, CH), 2982 (w, CH), 2891 (w, CH), 1707 (w, COO), 1639 (m, C=C), 1601 (w), 1534 (s, br, asym. COO), 1432 (s, sym. COO), 1417 (s), 1392 (s), 1317 (w), 1294 (w), 1265 (m), 1200 (w), 1119 (w), 994 (w), 911 (m), 888 (w), 835 (w), 818 (w) cm$^{-1}$ |

## 1.7 Synthesis of $Zr_4O_2(ODiMc)_{12}$ (7)

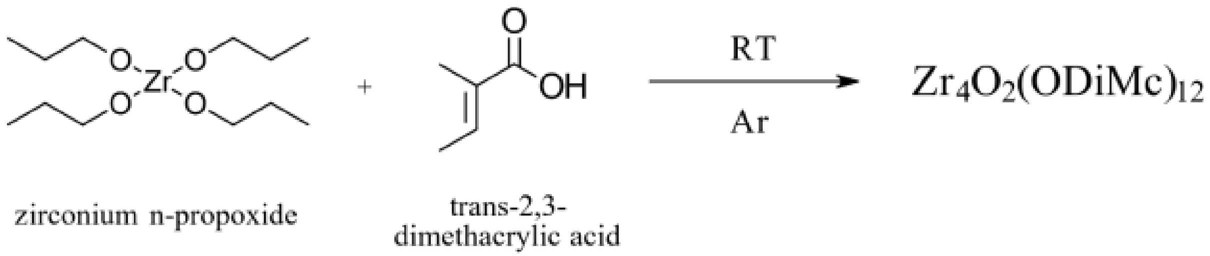

| Compound | Equivalents | n [mmol] | m [g] |
|---|---|---|---|
| Zirconium n-propoxide | 1.00 | 9.15 | 3.00 |
| trans-2,3-Dimethylacrylic acid | 4.06 | 37.16 | 3.72 |

The reaction and purification procedure were carried out with conventional Schlenk apparatus to exclude influence from oxygen and moisture. For the synthesis of $Zr_4O_2(ODiMc)_{12}$, 3.72 g (37.16 mmol, 4.06 eq.) of trans-2,3-dimethacrylic acid and 4.28 g of a 70% zirconium propoxide solution (9.15 mmol, 1 eq.) in n-propanol were weighed into a Schlenk flask and a sealed container inside the glovebox, respectively. After the Schlenk flask being transferred to Schlenk line, zirconium propoxide was slowly added to methacrylic acid under argon. The reaction was exothermic. The solution was stirred for 1 hr and allowed to stand at room temperature. Colourless prismatic crystals were generated after 7 days.

To purify, the crystalline products were first separated from the mother liquor. 10 mL of dry n-hexane was added into the Schlenk flask to wash the crystals and then removed by a syringe. The process was repeated 3 times. Eventually, the crystals were dried at $10^{-6}$ bar to evaporate the solvent for 6 hrs before being stored inside the glovebox at room temperature.

| | |
|---|---|
| **Yield:** | 0.62 g (4.3%), M=1586.3 g·mol$^{-1}$ |

**$^{1}$H NMR:** $\delta_H$ (ppm, 400 MHz, $CDCl_3$) 6.95 (m, 1H, C=CH), 1.75 (d, 6H, $CH_3C=CCH_3$) ppm

**$^{13}$C NMR:** $\delta_C$ (ppm, 400 MHz, $CDCl_3$) 173.7 (COO), 140.0 ($C=CCH_3COO$), 128.1 ($HCH_3C=C$), 14.6 ($C=CCH_3COO$), 11.6 ($HCH_3C=C$) ppm

**FTIR (ATR):** 3066 (w, CH), 2927 (w, CH), 2852 (w, CH), 1686 (w, COO), 1636 (m, C=C), 1556 (s, br, asym. COO), 1424 (s, sym. COO), 1382 (s), 1348 (s), 1287 (s), 1158 (m), 1076 (m), 1018 (m), 926 (s), 870 (m), 787 (s), 734 (s), 652 (s) cm$^{-1}$

## 1.8 Synthesis of $Zr_{12}O_8(OH)_8(OMc)_8(OAc)_{16}\cdot 6HOAc$ (8)

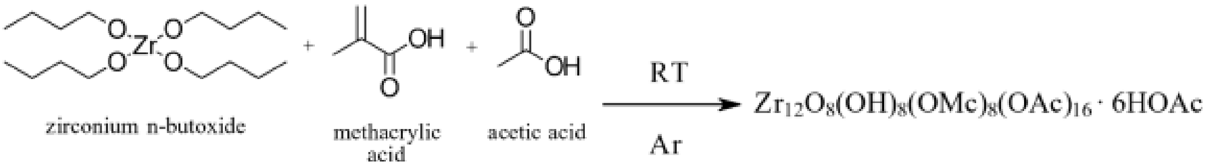

| Compound | Equivalents | n [mmol] | m [g] |
|---|---|---|---|
| Zirconium n-butoxide | 1.00 | 1.98 | 0.76 |
| Methacrylic acid | 1.40 | 2.78 | 0.24 |
| Acetic acid | 3.56 | 7.04 | 0.42 |

The reaction and purification procedure were carried out with conventional Schlenk apparatus to exclude influence from oxygen and moisture. 0.945 g of an 80% zirconium butoxide solution (1.98 mmol, 1 eq.) in n-butanol was weighed into a Schlenk flask inside the glovebox before being transferred to Schlenk line. 0.24 g of pre-distilled methacrylic acid (2.78 mmol, 1.4 eq.) and 0.42 g of dry acetic acid (7.04 mmol, 3.56 eq.) were weighed into two separate and sealed glass containers inside the glovebox. The acids were added dropwise to the zirconium butoxide solution successively under argon. The mixture was stirred for 1 hr and allowed to stand at room temperature. Colourless needles formed after 12 hrs.

To purify, the crystalline products were separated from the mother liquor. 5 mL of dry n-hexane was utilised to wash the solid and removed by a syringe. The process was repeated 3 times.

Eventually, the crystals were dried over high vacuum at $10^{-6}$ bar for 6 hrs before being stored in the glovebox.

| | |
|---|---|
| **Yield:** | 0.47 g (85%), M=3344.3 g·mol$^{-1}$ |
| **$^1$H NMR:** $\delta_H$ (ppm, 400 MHz, $CDCl_3$) | 10.56 (s, br, OH), 6.08 (s, 8 H, $CH_2$, cis-H to the carboxylate group), 5.00 (s, 8 H, $CH_2$, trans-H to the carboxylate group), 1.92 (s, 48 H, $CH_{3(OAC)}$ ), 1.78 (s, 24 H, $CH_{3(OMc)}$) ppm |
| **$^{13}$C NMR:** $\delta_C$ (ppm, 400 MHz, $CDCl_3$) | 183.1 ($COO_{(OMc)}$), 179.3 ($COO_{(OAc)}$), 135.8 ($CH_2C(CH_3)COO$), 127.0 ($CH_2$), 21.7 ($COOCH_3$), 16.6 ($CH_3$) |
| **FTIR (ATR):** | 3223 (w, OH), 2978 (w, CH), 2958 (w, CH), 2925(w, CH), 2874 (w, CH), 1711 (m, C=O), 1640 (w, C=C), 1598 (w), 1545 (s, COO), 1448 (w), 1423 (s, COO), 1372 (m, COO), 1343 (w), 1299 (w), 1245 (w), 1206 (w), 1178 (w), 1043 (w), 1029 (w), 1006 (w), 940 (w), 903 (w), 882 (w), 851 (w), 827 (w), 799 (w), 676 (w), 641 (w), 633 (w), 610 (w) |

## 2 Preparation of Multi-metallic Oxo Clusters

### 2.1 Synthesis of $Ti_4Zr_4O_6(OBu)_4(OMc)_{16}$ (9)

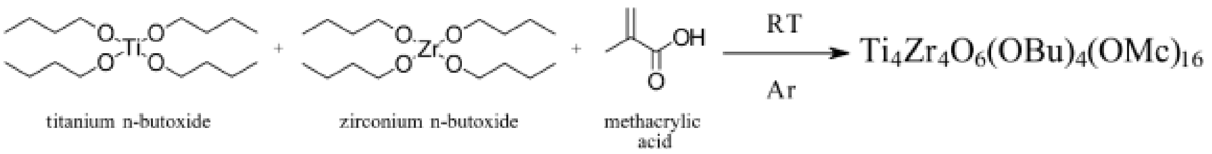

| Compound | Equivalents | n [mmol] | m [g] |
|---|---|---|---|
| Titanium n-butoxide | 1.00 | 5.53 | 1.90 |
| Zirconium n-butoxide | 1.01 | 5.59 | 2.14 |
| Methacrylic acid | 8.52 | 47.10 | 4.10 |

The reaction and purification procedure were carried out with conventional Schlenk apparatus to exclude influence from oxygen and moisture. 1.90 g of a 99% titanium butoxide solution

(5.53 mmol, 1 eq.) and 2.68 g of an 80% zirconium butoxide solution (5.59 mmol, 1.01 eq.) in n-butanol were weighed into a Schlenk flask inside the glovebox before being transferred to Schlenk line. 4.10 g of methacrylic acid (47.10 mmol, 8.52 eq.) was weighed into a sealed container inside the glovebox. After two compounds being stirred for 10 minutes, methacrylic acid was added dropwise to the mixture under argon. The reaction was exothermic. The solution was stirred for 1 hr and allowed to stand at room temperature. Colourless crystals were generated after 7 days.

To purify, the crystalline products were separated from the mother liquor. 10 mL of dry n-hexane was utilised to washed the crystals and removed with a syringe. The process was repeated 3 times. Eventually, the crystals were dried over high vacuum at $10^{-6}$ bar for 6 hrs before being stored in the glovebox.

| | |
|---|---|
| **Yield:** | 3.16 g (64%), M=2306.2 g·mol$^{-1}$ |
| **m.p.** | 123 °C |
| **$^1$H NMR:** $\delta_H$ (ppm, 400 MHz, $CDCl_3$) | 6.10 (m, 16 H, $CH_2$, cis-H to the carboxylate group), 5.53 (m, 16 H, $CH_2$, trans-H to the carboxylate group), 3.42 (t, 16 H, $OCH_2CH_2CH_2CH_3$), 1.83 (m, 48 H, $=C(CH_3)COO$), 1.41 (m, 16 H, $OCH_2CH_2CH_2CH_3$), 1.19 (m, 16 H, $OCH_2CH_2CH_2CH_3$), 0.81 (m, 25 H, $OCH_2CH_2CH_2CH_3$) ppm |
| **$^{13}$C NMR:** $\delta_C$ (ppm, 400 MHz, $CDCl_3$) | 174.6 (COO), 136.9 ($CH_2=C(CH_3)COO$), 125.7 ($CH_2=C(CH_3)COO$), 61.9 ($OCH_2CH_2CH_2CH_3$), 34.8 ($OCH_2CH_2CH_2CH_3$), 29.7 ($OCH_2CH_2CH_2CH_3$), 18.8 ($=C(CH_3)COO$), 13.6 ($OCH_2CH_2CH_2CH_3$) ppm |
| **FTIR (ATR):** | 2957 (w, CH), 2926 (w, CH), 2863 (w, CH), 1727 (w), 1692 (m, COO), 1644 (m, C=C), 1567 (m), 1539 (s, br, asym. COO), 1511 (m) 1500 (w), 1454 (s, sym. COO), 1409 (s), 1369 (m), 1243 (m), 1131 (m), 1095 (m), |

1053 (m), 1039 (m), 1006 (m), 973 (w), 934 (m), 870 (w), 825 (m), 762 (m) cm$^{-1}$

## 2.2 Synthesis of $Ti_2Zr_4O_4(OBu)_2(OMc)_{14}$ (10)

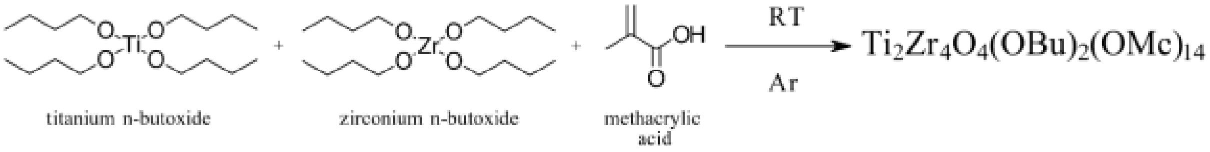

| Compound | Equivalents | n [mmol] | m [g] |
|---|---|---|---|
| Titanium n-butoxide | 1.00 | 3.65 | 1.26 |
| Zirconium n-butoxide | 2.20 | 8.04 | 3.08 |
| Methacrylic acid | 13.48 | 49.20 | 4.28 |

The reaction and purification procedure were carried out with conventional Schlenk apparatus to exclude influence from oxygen and moisture. 1.26 g of a 99% titanium butoxide solution (3.65 mmol, 1 eq.) and 3.86 g of an 80% zirconium butoxide solution (8.04 mmol, 2.20 eq.) in n-butanol were weighed into a Schlenk flask inside the glovebox before being transferred to Schlenk line. 4.28 g of methacrylic acid (49.20 mmol, 13.48 eq.) was weighed into a sealed container inside the glovebox. After two compounds being stirred for 10 minutes, methacrylic acid was added dropwise to the mixture under argon. The reaction was exothermic. The solution was stirred for 1 hr and allowed to stand at room temperature. Colourless crystals were generated after 7 days.

To purify, the crystalline products were separated from the mother liquor. 10 mL of dry n-hexane was utilised to washed the crystals and removed with a syringe. The process was repeated 3 times. Eventually, the crystals were dried over high vacuum at 10$^{-6}$ bar for 6 hrs before being stored in the glovebox.

| | |
|---|---|
| **Yield:** | 6.49 g (62%), M=1862.0 g·mol$^{-1}$ |
| **m.p.** | 129 °C |
| **$^1$H NMR:** $\delta_H$ (ppm, 400 MHz, $CDCl_3$) | 6.10 (m, 14 H, $CH_2$, cis-H to the carboxylate group), 5.42 (m, 14 H, $CH_2$, trans-H to the carboxylate group), 3.43 (t, 24 H, $OCH_2CH_2CH_2CH_3$), 1.91 (m, 42 H, |

$=C(CH_3)COO)$, 1.46 (m, 24 H, $OCH_2CH_2CH_2CH_3)$, 1.19 (m, 24 H, $OCH_2CH_2CH_2CH_3)$, 0.81 (m, 35 H, $OCH_2CH_2CH_2CH_3)$ ppm

**$^{13}$C NMR:** $\delta_C$ (ppm, 400 MHz, $CDCl_3$) 174.2 (COO), 136.9 ($CH_2=C(CH_3)COO$), 125.8 ($CH_2=C(CH_3)COO$), 62.0 ($OCH_2CH_2CH_2CH_3$), 34.5 ($OCH_2CH_2CH_2CH_3$), 30.2 ($OCH_2CH_2CH_2CH_3$), 18.1 ($=C(CH_3)COO$), 13.6 ($OCH_2CH_2CH_2CH_3$) ppm

**Elemental Analysis:** (calc.) (calc.) **Ti**, 5.16; **Zr**, 19.55; **C**, 41.25; **H**, 4.73; **O**, 29.22

(founded) **Ti**, 5.15; **Zr**, 19.59; **C**, 41.28; **H**, 4.76; **O**, 29.21

**FTIR (ATR):** 2970 (w, CH), 2958 (w, CH), 2928 (w, CH), 2874 (w, CH), 1761 (w), 1726 (m, COO), 1644 (m, C=C), 1526 (m), 1456 (s), 1416 (s, sym. COO), 1372 (s), 1243 (m), 1159 (w), 1006 (m), 938 (m), 880 (w), 827 (m) cm$^{-1}$

## 2.3 Synthesis of $Ti_4Zr_2O_4(OBu)_6(OMc)_{10}$ (11)

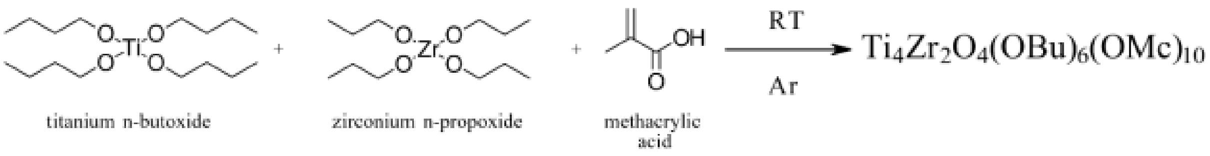

| Compound | Equivalents | n [mmol] | m [g] |
|---|---|---|---|
| Titanium n-butoxide | 1.00 | 4.80 | 1.65 |
| Zirconium n-propoxide | 0.95 | 4.58 | 1.50 |
| Methacrylic acid | 8.06 | 38.70 | 3.36 |

The reaction and purification procedure were carried out with conventional Schlenk apparatus to exclude influence from oxygen and moisture. 1.65 g of a 99% titanium butoxide solution (4.80 mmol, 1 eq.) and 2.14 g of a 70% zirconium propoxide solution (4.58 mmol, 0.95 eq.) in n-butanol were weighed into a Schlenk flask inside the glovebox before being transferred to Schlenk line. 3.36 g of methacrylic acid (38.70 mmol, 8.06 eq.) was weighed into a sealed container inside the glovebox. After two compounds being stirred for 10 minutes, methacrylic acid was added dropwise to the mixture under argon. The reaction was exothermic. The solution was stirred for 1 hr and allowed to stand at room temperature. Colourless crystals were generated after 7 days.

To purify, the crystalline products were separated from the mother liquor. 10 mL of dry n-hexane was utilised to washed the crystals and removed with a syringe. The process was repeated 3 times. Eventually, the crystals were dried over high vacuum at $10^{-6}$ bar for 6 hrs before being stored in the glovebox.

| | |
|---|---|
| **Yield:** | 1.86 g (69%), M=1811.6 g·mol$^{-1}$ |
| **m.p.** | 134 °C |
| **$^{1}$H NMR:** $\delta_H$ (ppm, 400 MHz, $CDCl_3$) | 6.10 (m, 10 H, $CH_2$, cis-H to the carboxylate group), 5.42 (m, 10 H, $CH_2$, trans-H to the carboxylate group), 3.42 (t, 6 H, $OCH_2CH_2CH_2CH_3$), 1.90 (m, 30 H, $=C(CH_3)COO$), 1.45 (m, 12 H, $OCH_2CH_2CH_2CH_3$), 1.19 (m, 12 H, $OCH_2CH_2CH_2CH_3$), 0.81 (m, 35 H, $OCH_2CH_2CH_2CH_3$) ppm |
| **$^{13}$C NMR:** $\delta_C$ (ppm, 400 MHz, $CDCl_3$) | 174.1 (COO), 135.4 ($CH_2=C(CH_3)COO$), 125.3 ($CH_2=C(CH_3)COO$), 61.7 ($OCH_2CH_2CH_2CH_3$), 34.4 ($OCH_2CH_2CH_2CH_3$), 30.6 ($OCH_2CH_2CH_2CH_3$), 18.1 ($=C(CH_3)COO$), 13.6 ($OCH_2CH_2CH_2CH_3$) ppm |
| **FTIR (ATR):** | 2961 (w, CH), 2927 (w, CH), 2874 (w, CH), 2847 (w, CH), 1644 (m, C=C), 1567 (m), 1534 (s), 1512 (m), 1453 (m), 1407 (s, sym. COO), 1370 (s), 1243 (m), 1117 (w), 1097 |

(m),1080 (m), 1047 (w), 1003 (m), 935 (m), 890 (w), 825 (m), 758 (m) cm$^{-1}$

## 2.4 Synthesis of $Ti_4Hf_4O_6(OBu)_4(OMc)_{16}$ (12)

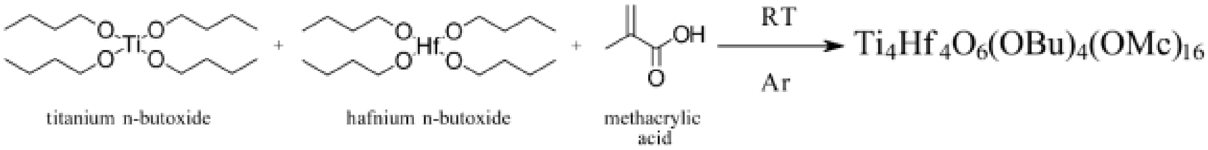

| Compound | Equivalents | n [mmol] | m [g] |
|---|---|---|---|
| Titanium n-butoxide | 1.00 | 1.85 | 0.63 |
| Hafnium n-butoxide | 0.89 | 1.64 | 0.78 |
| Methacrylic acid | 7.95 | 14.70 | 1.26 |

The reaction and purification procedure were carried out with conventional Schlenk apparatus to exclude influence from oxygen and moisture. 0.63 g of a 99% titanium butoxide solution (1.85 mmol, 1 eq.) and 0.82 g of a 95% hafnium butoxide solution (1.64 mmol, 0.89 eq.) in n-butanol were weighed into a Schlenk flask inside the glovebox before being transferred to Schlenk line. 1.26 g of methacrylic acid (14.70 mmol, 7.95 eq.) was weighed into a sealed container inside the glovebox. After two compounds being stirred for 10 minutes, methacrylic acid was added dropwise to the mixture under argon. The reaction was exothermic. The solution was stirred for 1 hr and allowed to stand at 4 ºC. Colourless crystals were generated after 30 days.

To purify, the crystalline products were separated from the mother liquor. 10 mL of dry n-hexane was utilised to washed the crystals and removed with a syringe. The process was repeated 3 times. Eventually, the crystals were dried over high vacuum at 10$^{-6}$ bar for 6 hrs before being stored in the glovebox.

| | |
|---|---|
| **Yield:** | 0.37 g (34%), M=2637.1 g·mol$^{-1}$ |
| **$^1$H NMR:** $\delta_H$ (ppm, 400 MHz, $CDCl_3$) | 6.09 (m, 16 H, $CH_2$, cis-H to the carboxylate group), 5.42 (m, 16 H, $CH_2$, trans-H to the carboxylate group), 3.41 (t, 16 H, $OCH_2CH_2CH_2CH_3$), 1.79 (m, 48 H, $=C(CH_3)COO$), 1.44 (m, 16 H, $OCH_2CH_2CH_2CH_3$), 1.19 (m, 16 H, |

$OCH_2CH_2CH_2CH_3$), 0.82 (m, 25 H, $OCH_2CH_2CH_2CH_3$) ppm

**$^{13}$C NMR:** $\delta_C$ (ppm, 400 MHz, $CDCl_3$) 174.4 (COO), 130.3 ($CH_2$=C($CH_3$)COO), 120.3 ($CH_2$=C($CH_3$)COO), 56.8 ($OCH_2CH_2CH_2CH_3$), 31.0 ($OCH_2CH_2CH_2CH_3$), 25.8 ($OCH_2CH_2CH_2CH_3$), 14.2 (=C($CH_3$)COO), 9.4 ($OCH_2CH_2CH_2CH_3$) ppm

**FTIR (ATR):** 2982 (m, CH), 2890 (m, CH), 1569 (m), 1462 (w), 1428 (s, sym. COO), 1393 (s), 1369 (m), 1250 (m), 1153 (m), 1073 (w), 940 (m), 823 (w) $cm^{-1}$

## 2.5 Synthesis of $Ti_2Zr_5HfO_6(OMc)_{20}$ (13)

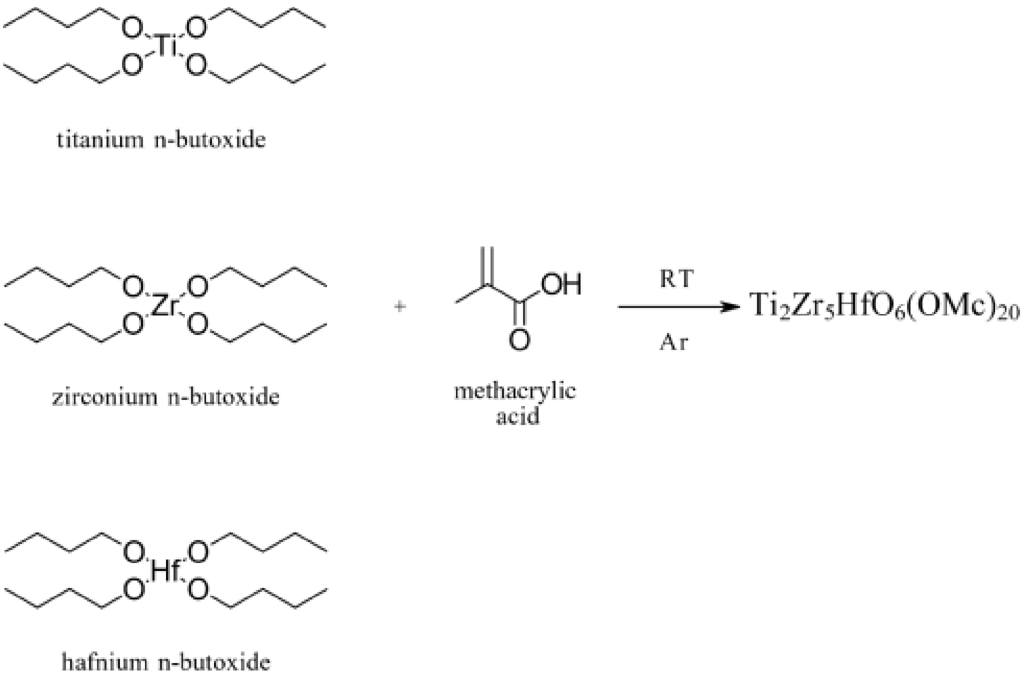

| Compound | Equivalents | n [mmol] | m [g] |
|---|---|---|---|
| Titanium n-butoxide | 1.00 | 1.90 | 0.66 |
| Zirconium n-butoxide | 1.00 | 1.90 | 0.72 |
| Hafnium n-butoxide | 0.95 | 1.80 | 0.86 |
| Methacrylic acid | 11.84 | 22.50 | 1.94 |

The reaction and purification procedure were carried out with conventional Schlenk apparatus to exclude influence from oxygen and moisture. 0.66 g of a 99% titanium butoxide solution (1.90 mmol, 1 eq.), 0.90 g of an 80% zirconium butoxide solution (1.90 mmol, 1 eq.) and 0.90 g of a 95% hafnium butoxide solution (1.80 mmol, 0.95 eq.) in n-butanol were weighed into a Schlenk flask inside the glovebox before being transferred to Schlenk line. 1.94 g of methacrylic acid (22.50 mmol, 11.84 eq.) was weighed into a sealed container inside the glovebox. After three compounds being stirred for 10 minutes, methacrylic acid was added dropwise to the mixture under argon. The reaction was exothermic. The solution was stirred for 1 hr and allowed to stand at 4 °C. Colourless crystals were generated after 30 days.

To purify, the crystalline products were separated from the mother liquor. 10 mL of dry n-hexane was utilised to washed the crystals and removed with a syringe. The process was repeated 3 times. Eventually, the crystals were dried over high vacuum at $10^{-6}$ bar for 6 hrs before being stored in the glovebox.

| | |
|---|---|
| **Yield:** | 1.62 g (32%), M=2528.0 g·mol$^{-1}$ |
| **$^1$H NMR:** $\delta_H$ (ppm, 400 MHz, $CDCl_3$) | 6.07 (s, br, 20 H, $CH_2$, cis-H to the carboxylate group), 5.34 (s, br, 20 H, $CH_2$, cis-H to the carboxylate group), 1.84 (m, 60 H, $=C(CH_3)COO$) ppm |
| **$^{13}$C NMR:** $\delta_C$ (ppm, 400 MHz, $CDCl_3$) | 163.0 (COO), 135.3 ($CH_2C(CH_3)COO$), 128.3 ($CH_2$), 14.2 ($CH_3$) ppm |
| **FTIR (ATR):** | 2982 (m, CH), 2889 (w, CH), 1695 (w, COO), 1581 (m, br, asym. COO), 1534 (m), 1456 (m, sym. COO), 1415 (m), 1393 (m), 1244 (w), 1160 (w), 1073 (w), 940 (w), 830 (w) cm$^{-1}$ |

## 3 Preparation of $Hf_4O_2(OMc)_{12}$ (14)

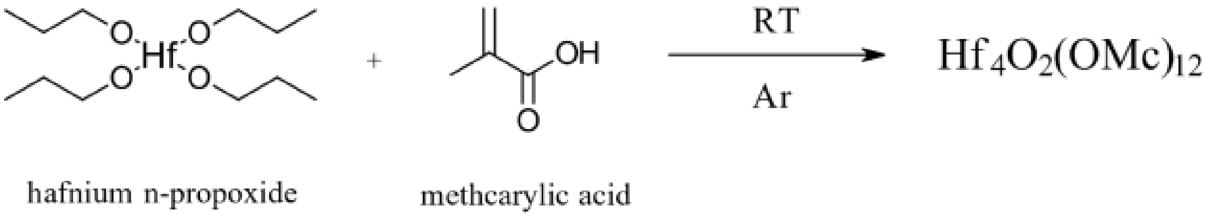

| Compound | Equivalents | n [mmol] | m [g] |
|---|---|---|---|
| Hafnium n-butoxide | 1.00 | 1.68 | 0.79 |
| Methacrylic acid | 4.01 | 6.74 | 0.58 |

The reaction and purification procedure were carried out with conventional Schlenk apparatus to exclude influence from oxygen and moisture. For the synthesis of $Hf_4O_2(OMc)_{12}$, 0.58 g (6.74 mmol, 4.01 eq.) of pre-distilled methacrylic acid and 0.79 g of a 95% hafnium butoxide solution (9.15 mmol, 1 eq.) in n-butanol were weighed into a Schlenk flask and a sealed container inside the glovebox, respectively. After the Schlenk flask being transferred to Schlenk line, hafnium butoxide was slowly added to methacrylic acid under argon. The reaction was exothermic. The solution was stirred for 1 hr and allowed to stand at room temperature. Colourless prismatic crystals were generated after 3 days.

To purify, the crystalline products were first separated from the mother liquor. 10 mL of dry n-hexane was added into the Schlenk flask to wash the crystals and then removed by a syringe. The process was repeated 3 times. Eventually, the crystals were dried at $10^{-6}$ bar to evaporate the solvent for 6 hrs before being stored inside the glovebox at room temperature.

| | |
|---|---|
| **Yield:** | 0.61 g (82%), M=1766.9 g·mol$^{-1}$ |
| **$^1$H NMR:** $\delta_H$ (ppm, 400 MHz, $CDCl_3$) | 6.12 (s, 12 H, $CH_2$, cis-H to the carboxylate group), 5.44 (s, 12 H, $CH_2$, trans-H to the carboxylate group), 1.79 (s, 36 H, $CH_3$) ppm |
| **$^{13}$C NMR:** $\delta_C$ (ppm, 400 MHz, $CDCl_3$) | 168.2 (COO), 136.8 ($CH_2C(CH_3)COO$), 125.6 ($CH_2$), 18.7 ($CH_3$) ppm |
| **Elemental Analysis:** (calc.) | (calc.) **Hf**, 40.41; **C**, 32.60; **H**, 3.40; **O**, 23.54<br>(founded) **Hf**, 40.41; **C**, 32.63; **H**, 3.42; **O**, 23.54 |
| **FTIR (ATR):** | 2976 (w, CH), 2953 (w, CH), 2926 (w, CH), 1648 (m, C=C), 1593 (s, br, asym. COO), 1500 (w), 1459 (s, sym. COO), 1425 (s), 1373 (m), 1248 (m), 1006 (w), 942 (m), 883 (w), 829 (w) cm$^{-1}$ |

# 4 Crystallographic Data

## 4.1 Single Crystal XRD

| | $Zr_4O_2(OMc)_{12}$ | $Hf_4O_2(OMc)_{12}$ | $Ti_2Zr_5Hf(OMc)_{20}$ |
|---|---|---|---|
| **Empirical Formula** | $C_{48}H_{60}O_{26}Zr_4$ | $C_{48}H_{60}O_{26}Hf_4$ | $C_{80}H_{100}O_{46}Ti_2Zr_5Hf$ |
| **Formula Weight (g/mol)** | 1417.9 | 1766.9 | 2528.0 |
| **Space Group** | $P2_1/n$ | $P2_1/n$ | $P\bar{1}$ |
| **Cell Lengths (pm)** | a: 1339.92(7)<br>b:1704.65(8)<br>c: 1370.82 (6) | a:1375.30(4)<br>b:1749.66(5)<br>c:1407.02(6) | a:1362.57(2)<br>b:1733.45(9)<br>c:1393.98(5) |
| **Cell Angles (deg)** | α: 90<br>β: 95.0900(10)<br>γ: 90 | α:90<br>β:103.4127(51)<br>γ:90 | α:95.4019(4)<br>β:93.7931(9)<br>γ:105.2150(8) |
| **Cell Volume ($pm^3$)** | $3118.7(4)\cdot10^6$ | $3173.4(6)\cdot10^6$ | $2905.3(2)\cdot10^6$ |
| **Z** | 4 | 4 | 2 |
| **Calc. Density ($g/cm^3$)** | 1.510 | 1.875 | 1.481 |
| **R-Factor (%)** | 3.74 | 5.12 | 4.86 |

## 4.2 Powder XRD

### 4.2.1 Zirconium Oxo Clusters

a) $Zr_4O_2(ODiMc)_{12}$

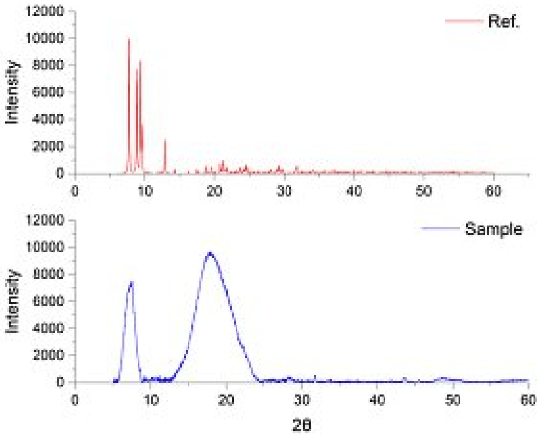

b) $Zr_4O_2(ODiMc)_{12}$

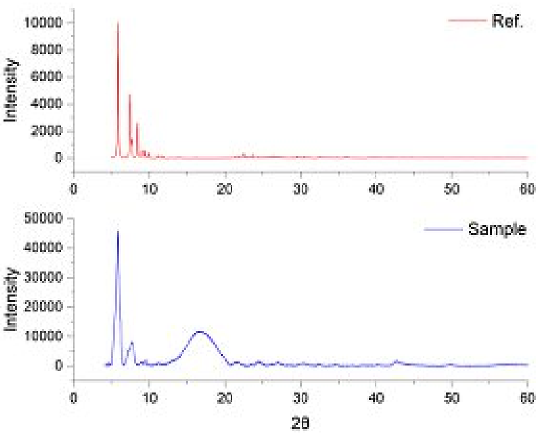

c) $Zr_4O_2(OMc)_3(OPiv)_9$

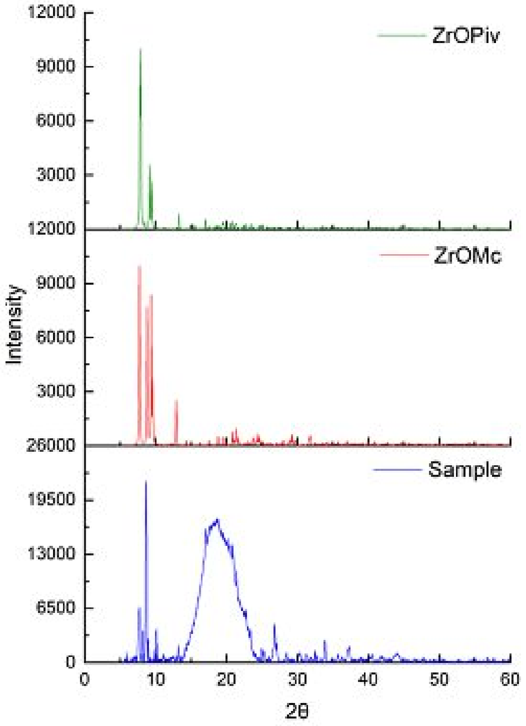

d) $Zr_4O_2(OMc)_6(OPiv)_6$

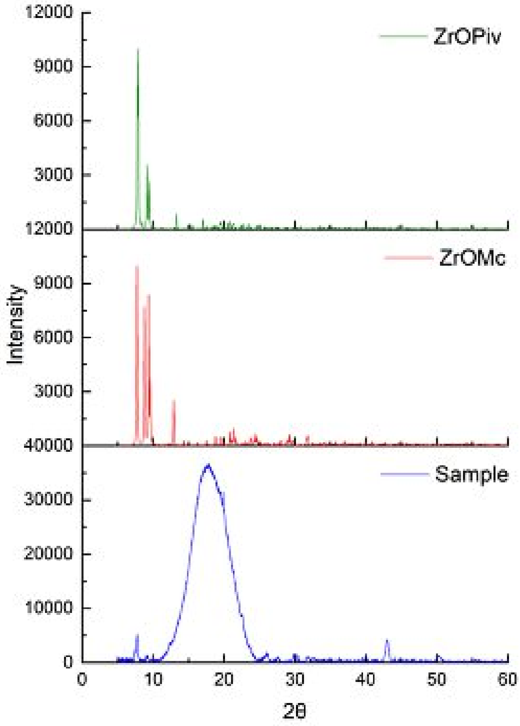

e) $Zr_4O_2(OMc)_9(OPiv)_3$

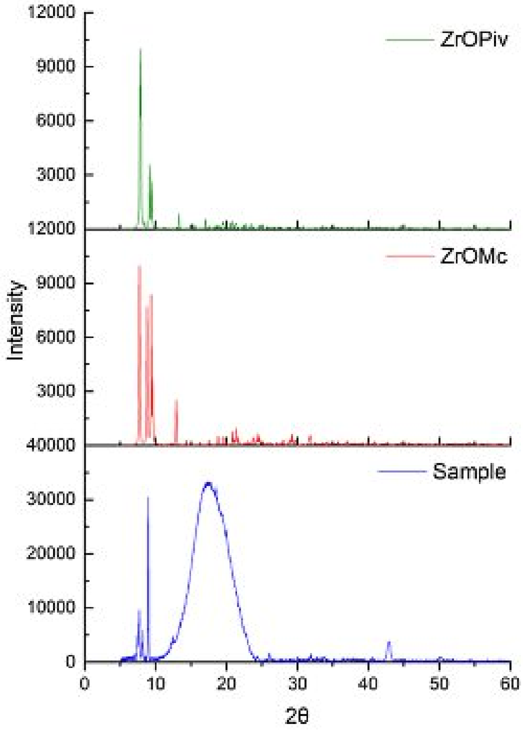

f) $Zr_4O_2(OPiv)_{12}$

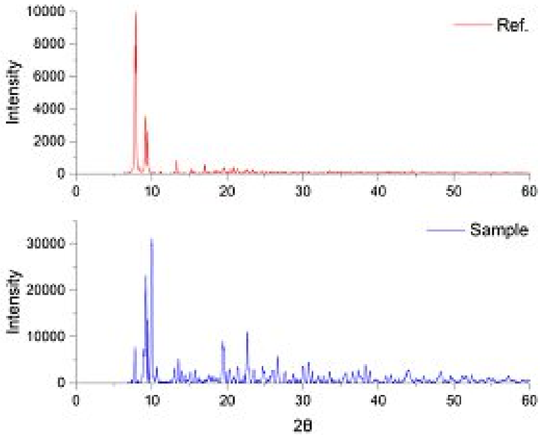

### 4.2.2 Multi-metallic Oxo Clusters

a) $Ti_4Zr_4O_6(OBu)_4(OMc)_{16}$

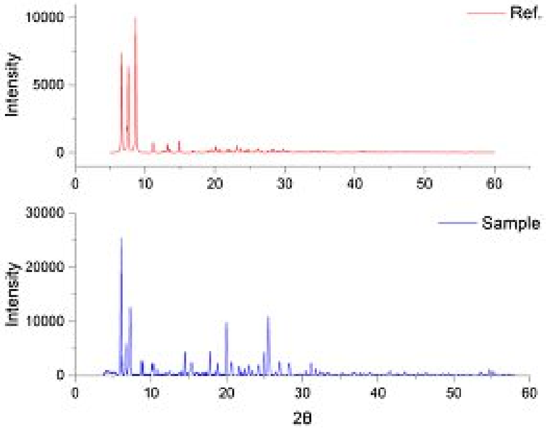

b) $Ti_4Zr_2O_4(OBu)_6(OMc)_{10}$

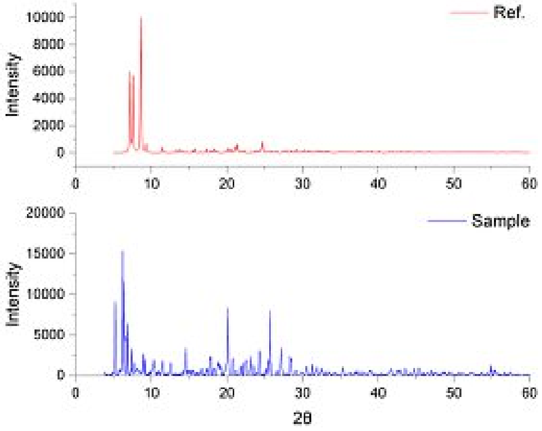

c) $Ti_2Zr_4O_4(OBu)_2(OMc)_{14}$

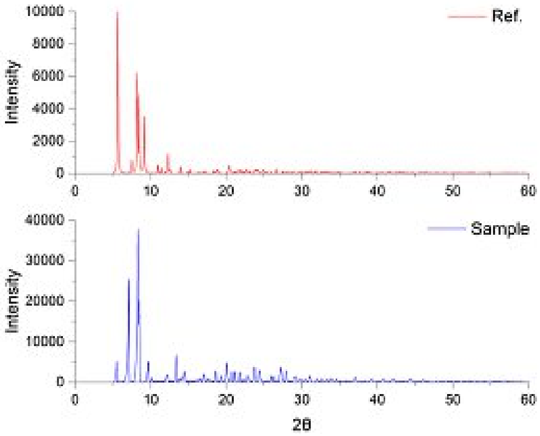

d) $Ti_4Hf_4O_6(OBu)_4(OMc)_{16}$

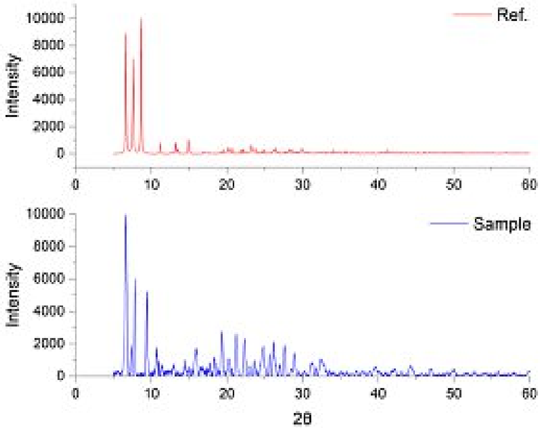

# 5 Characterisations

## 5.1 UV/Vis Spectroscopy

### 5.1.1 Solution

The solution samples for UV/Vis spectroscopy were divided into two categories, saturated and diluted, for different research purposes. The saturated sample was prepared by dissolving 0.01g of the metal-oxo-cluster in 1 mL of anhydrous isopropanol (IPA), leading to a concentration of 1% w/v, while the diluted sample was obtained via mixing 0.1 mL of saturated solution with

10 mL of anhydrous IPA for a concentration of 0.01%. Distance of the quartz cuvette employed (d) was 10 mm.

### 5.1.2 Thin Film

The casting solutions were prepared by dissolving 0.01 g of metal-oxo-clusters in 1 mL of respectively required casting solvents (concentration: 1% w/v) before being spin-coated on clean 1 cm x 1 cm quartz plates. The quartz plates were cleaned with piranha solution and dried with nitrogen prior to use. The sample was spin-coated at 2000 rpm for 45 second to form a thin film with approximately 30 nm in thickness. The coated quartz plates were stored under nitrogen atmosphere to prevent further degradation resulted from oxygen and moisture before measurements.

## 5.2 Fourier-Transform Infrared Spectroscopy (FTIR)

### 5.2.1 Powder (ATR-FTIR)

The metal oxo clusters were packed in sealable small glass containers and taken out from glovebox before measurements to prevent further hydrolysis resulted from moisture in the air.

### 5.2.2 Thin Film (Transmission FTIR)

The casting solutions were prepared by dissolving 0.01 g of metal oxo clusters in 1 mL of respectively required casting solvents (concentration: 1% w/v) before being spin-coated. As substrate, 1 cm x 1 cm silicon wafers with a thickness of 525 +/- 25 µm were soaked in acetone and cleaned via ultrasonic bath, followed by drying at 100 ºC in an oven prior to use. The sample was spin-coated at 2000 rpm for 45 second to form a thin film with approximately 30 nm in thickness. The coated silicon wafers were stored under nitrogen atmosphere to prevent further degradation resulted from oxygen and moisture before measurements.

### 5.2.3 EUV-Exposed Thin-Film Sample (Transmission FTIR)

Sample was spin-coated with respective conditions on a 1 cm x 1 cm silicon wafer for EUV exposure at PSI. Dose of 60 mJ/cm$^2$ was employed and repeated 25 times in the centre of silicon wafer to ensure a complete solubility switch of resist material and an area large enough for transmission FTIR analysis. The exposed area was developed with dry developing solvent required for each cluster, followed by drying of nitrogen gas.

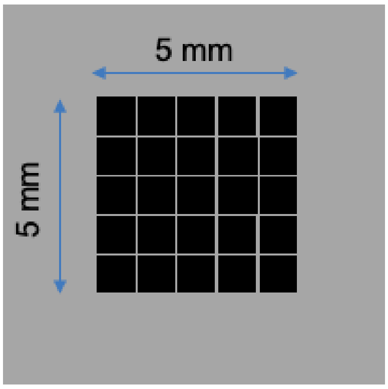

### 5.2.4 EUV-Exposed Thin-Film Sample (GATR-FTIR)

$Ti_2Zr_4O_4(OBu)_2(OMc)_{14}$ was spin-coated on an 8-inch wafer at IMEC cleanroom with the conditions and parameters listed in Chapter 7.2.2. Specific areas on the wafer were exposed to EUV photons with doses from 10 to 50 mJ/cm$^2$. These areas were then separated from the 8-inch wafer via a diamond cutter to make the sample fit into GATR-FTIR spectrometer.

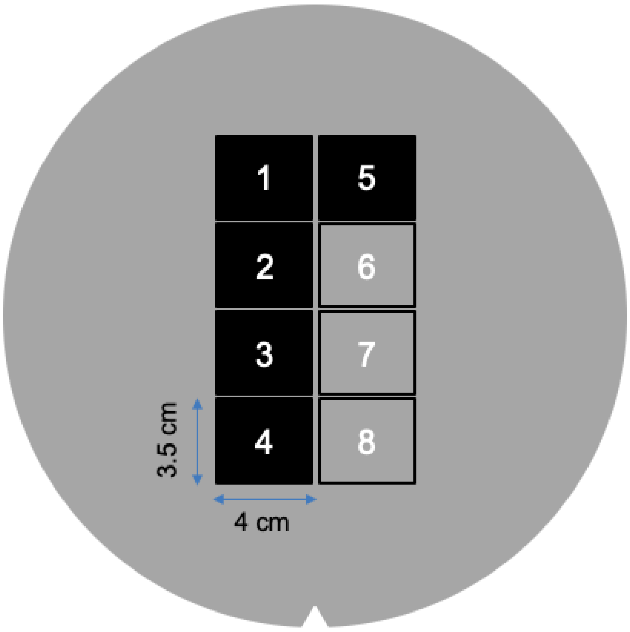

## 5.3 Thermogravimetric Analysis (TGA)

Each metal oxo cluster was packed in an aluminium crucible inside the glovebox with an amount of approximately 10 mg. Shortly prior to measurement, the crucible was taken out for cramping and loaded into the STA chamber in order to avoid further hydrolysis resulted from moisture in the air.

## 5.4 Degradation Test

### 5.4.1 Bulk Material

The degradation test of bulk material was carried out on $Zr_4O_2(OMc)_{12}$. 0.5 g of $Zr_4O_2(OMc)_{12}$ was loaded in a clean glass container covered with a layer of aluminium foil. Holes were made on the cover to expose the metal oxo cluster directly to the air. NMR spectroscopy was performed on the samples collected at 1,2,4,8,24, and 168 hrs of exposing time. And the degree of hydrolysis (%) was determined by the intensity ratio of proton signal on hydroxy group and that on pristine $Zr_4O_2(OMc)_{12}$ cluster.

### 5.4.2 Thin Film

Thin-film degradation test was carried out on $Zr_4O_2(OMc)_{12}$, along with two approaches of anti-hydrolysis in order to extend process window for chip manufacturing. The measures included adding additional 20% wt. of dry methacrylic acid as absorbent for moisture and 20% wt. of bis(2,6-diisopropylphenyl) carbodiimide (BDICDI) as stabilizer. The casting solution was prepared by dissolving 0.01 g of $Zr_4O_2(OMc)_{12}$ clusters and either 20% wt. of dry methacrylic acid or BDICDI in 1 mL of dry toluene (concentration: 1% w/v). 1 cm x 1 cm of silicon wafers with a thickness of 525 +/- 25 µm were used as substrate and cleaned with acetone in ultrasonic bath prior to spin-coating. The sample was spin-coated at 2000 rpm for 45 second to form a thin film with approximately 30 nm in thickness. After the coated silicon wafer being transferred to the sample holder, spectrum was recorded at 0, 1, 5, 10, 30 and 60 minutes with constant exposure under air. The degree of hydrolysis was determined by the intensity of hydroxy signals at different exposing time.

## 5.5 X-ray Diffraction (XRD)

### 5.5.1 Single Crystal XRD

The crystal structures of $Zr_4O_2(OMc)_{12}$, $Hf_4O_2(OMc)_{12}$, $Zr_4O_2(OVinac)_{12}$, and $Ti_2Zr_5HfO_6(OMc)_{20}$ were analysed via single crystal XRD by X-Ray Centre at TU Wien. In order to generate a proper crystal for measurement, 0.1 g of metal oxo cluster powder was dissolved in a small amount of anhydrous dichloromethane, depending on the solubility of each material, inside the glovebox and packed into a sealed glass bottle. A Schlenk flask was connected to Schlenk line and a pumping-venting cycle with argon was carried out on the flask to ensure a clean and inert atmosphere within the glass container. 30 mL of dry n-hexane was transferred into the Schlenk flask with a syringe. The cluster solution was added afterwards to the Schlenk flask dropwise to initiate crystallisation. The solution phase should have turned cloudy and slightly blurry. If nothing happens, it is feasible to use the vacuum to slowly reduce the pressure inside the Schlenk flask to help encourage crystallisation. The crystals formed after 24 to 48 hrs.

### 5.5.2 Powder XRD

Samples were packed in properly sealed glass vials inside the glovebox before being transferred to a special type of sample holder for air-sensitive powder XRD measurement. For sample preparation, the powder of metal oxo cluster was first placed in the centre of a silicon wafer with orientation of (510) to exclude diffraction of silicon. Few drops of heptane were added to the powder in order to evenly distribute sample on the silicon plate. After the holder was sealed tight with a plastic cover, it was transferred into the PANalytical XPert Pro MPD (θ-θ diffractometer) for measurements.

## 5.6 Contrast Curve Analysis

### 5.6.1 EUV Exposure Conducted at PSI

The sample was spin-coated on a 2 cm x 2 cm silicon wafer with respective conditions shortly before loaded into the exposure chamber. Exposure for contrast curve was open-framed, namely no photomask involved, and carried out on 25 different spots of the wafer with increasing doses. Development of sample was performed immediately after EUV exposure. The heights of each exposed block were measured with AFM for depicting contrast curve.

### 5.6.2 EUV Exposure Conducted at IMEC

$Ti_2Zr_4O_4(OBu)_2(OMc)_{14}$ was spin-coated on an 8-inch silicon wafer in IMEC cleanroom with conditions and parameters listed in Chapter 7.2.2 shortly before being loaded into the RGA setup. Film thickness has to reach 30 nm, which was confirmed by ellipsometry. EUV photons were exposed on 44 different spots on the wafer surface with increasing doses. Development was conducted immediately after the exposure with the TEL CLEAN TRACK™ ACT™ 8 programmable spin-coater. Thicknesses of exposed areas were measured with ellipsometry.

## 5.7 Dissociation Electron Attachment (DEA) Experiment

Methacrylic acid, 3-butenoic acid, and trans-2,3-dimethacrylic acid as precursors responsible for the formation of ligands and $Zr_4O_2(OMc)_{12}$ were analysed with DEA spectroscopy in Siedlce University of Natural Sciences and Humanities with the assistance of Prof. Janina

Kopyra as well as her PhD student Mrs. Paulina Wierzbicka. The chamber was pre-heated to 50 to 60 ºC for the carboxylic acids and 120 ºC for $Zr_4O_2(OMc)_{12}$. Prior to measurements, sulphur hexafluoride ($SF_6$) was utilised as a standard gas for calibration of energy scale since $SF_6$ not only has outstanding DEA cross-section, but also is capable of generating the metastable $SF_6^-$ near 0 eV. After calibration, an oil vacuum pump was turned on to evacuate $SF_6$ residue for 15 minutes.

Solution samples (methacrylic acid, 3-butenoic acid) were introduced into the chamber via a capillary, while solid samples (trans-2,3-dimethacrylic acid, $Zr_4O_2(OMc)_{12}$) were heated to melting point before being introduced into the chamber under ultrahigh vacuum (UHV, $10^{-8}$ mbar). Spectra were recorded by either an energy scan or mass scan. The electron energy (energy scan) of the fragments was measured in the range from approximately 0 eV to 12 eV at each channel (mass) of interests. Mass scan approach, on the other hand, was carried out by scanning throw all the channels (mass) at a selected energy, e.g. 0, 1, 2, 12eV, etc.

### 5.8 Outgassing Analysis

$Ti_2Zr_4O_4(OBu)_2(OMc)_{14}$ was spin-coated on an 8-inch silicon wafer in IMEC cleanroom with conditions and parameters listed in Chapter 7.2.2 shortly before being loaded into the RGA setup. EUV photons were exposed on different spots of the wafer surface with a dose at 15 mJ/cm$^2$. RGA was employed to collect the outgassed species and analysed by a quadruple mass spectrometer. The result was depicted in rate of outgassing as a function of mass.

# Appendix 2: Materials and Equipment

**Chemicals:** Titanium n-butoxide (99%, abcr GmbH®), zirconium n-propoxide (70%, Sigma Aldrich®), zirconium n-butoxide (80%, Sigma Aldrich®) and hafnium n-butoxide (95%, abcr GmbH®) were used as received and stored under argon atmosphere. Methacrylic acid (99%, Sigma Aldrich®) was distilled over 300 ppm of phosphorus pentoxide ($P_2O_5$) and 100 ppm of hydroquinone as inhibitor prior to use. It was stored at 4 °C under argon atmosphere to exclude polymerisation and the influence of moisture. Acetic acid (99%, Sigma Aldrich®) was used as received and stored under argon atmosphere.

**Solvents:** Dichloromethane (99%, ACROS®), propylene glycol methyl ether (99%, Fluka®) and ethyl acetate (99%, VWR Chemicals®) were dried over 3Å molecular sieves for 24 hrs before being distilled prior to use. n-Hexane (99%, VWR Chemicals®) and Toluene (99%, ACROS®) were purchased in HPLC grade and dried over Na/benzophenone before use. Chloroform (99%, Merck®) was used as received and stored under inert atmosphere.

**NMR Spectroscopy:** $^1H$ and $^{13}C$ NMR spectroscopy were performed by a Bruker Avance 400 DRX-400 FT-NMR Spectrometer (400MHz). Deuterated chloroform ($CDCl_3$) with a deuteration degree ≥ 99.5 % was used as solvent.

**UV/Vis Spectroscopy:** A Shimadzu UV2700 spectrophotometer with a photomultiplier was utilised for UV/Vis measurements. The range of wavelength measured was from 400 nm to 190 nm since the cut-off of isopropanol is near 190 nm.

**FTIR Spectroscopy:** FTIR measurement of solid samples was carried out on a Perkin Elmer Spectrum 65 FTIR Spectrometer with a Specac MKII Golden Gate ATR system. Thin-film measurements was carried out on a Bruker Vertex 80 FTIR with MCT and DGS detector as well as external reflex optics unit.

**GATR-FTIR Spectroscopy:** A Nicolet 6700 Optical Spectrometer with an MCT-A detector was employed to analyse EUV exposed $Ti_2Zr_4O_4(OBu)_2(OMc)_{14}$ at dose from 10 to 50 mJ/cm$^2$.

Spectral range of MCT-A can be recorded from 11,000 to 650 cm$^{-1}$ with a speed of approximately 10$^{-6}$/s. The detector has to be cooled with liquid nitrogen 30 minutes prior to measurement.

**TGA:** Thermogravimetric measurement was performed on a Netzsch STA 449 F1 under nitrogen atmosphere. The samples were packed in aluminium crucibles with lid covered. Temperature measured was ranged from room temperature to 500 °C with a ramp rate of 10 K/min.

**Melting Point:** Melting points were measured with an Optimelt MPA100 automated melting point device.

**Elemental Analysis:** Elemental analysis was carried out in the microanalysis laboratory at University of Vienna**.**

**Single Crystal XRD:** Single crystal XRD measurement was performed by a Bruker SMART APEX single crystal diffractometer with a Mo X-ray source and a 2D CCD detector.

**Powder XRD:** Powder XRD measurements were conducted via a PANalytical XPert Pro MPD (θ-θ diffractometer) with a Cu X-ray source and a X 'Celerator semiconductor detector (2.1 °) as well as a scintillation detector (0D)

**Spin-coating:** Spin-coating of the metal oxo clusters was primarily performed by a Suss Delta 80 Spin-coater in the cleanroom of AMOLF in Amsterdam**.**

**DUV Exposure:** A YAG-pumped OPA laser (Ekspla NT342B), delivering nanosecond pulses at 225 nm at 10 Hz (2.5 mJ/pulse), was used as the irradiation source at University of Amsterdam. The metal-oxo-cluster was spin-coated on a 1 cm x 1 cm silicon wafer beforehand

and installed in a special sample holder with constant nitrogen flow. The sample was then irradiated under nitrogen atmosphere with a dose of 1.4 J/ $cm^2$.

**E-beam Lithography:** E-beam lithography was performed via Raith e-LiNE lithography system (Voyager) in the cleanroom of AMOLF in Amsterdam. The metal-oxo-clusters were spin-coated on 1 cm x 1 cm silicon wafers and stored under nitrogen atmosphere before being loaded into the Voyager. Each of the sample was irradiated with dose factors from 1 to 9, meaning there were 9 areas in total on a single silicon wafer that was irradiated from (1 x initial dose), (2 x initial dose) to (9 x initial dose) μC/$cm^2$, respectively.

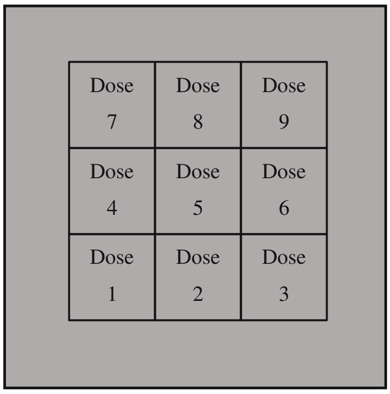

**EUV Lithography:** EUV exposures were performed via EUV light with 13.5 nm from XIL-II beamline of the Swiss Light Source (SLS) at Paul Scherrer Institute (PSI). Two types of exposure were conducted for different purposes. Open frame experiments were carried out using a square aperture to generate 0.5 X 0.5 $mm^2$ squares for contrast curve analysis and thin-film IR measurement. Patterning experiments were done with a transmission mask to create line/space pattern with pitch sizes from 100, 80, 60, 44 nm.

**RGA Setup:** The RGA setup was provided by EUV technology in the United States and installed in FAB 200 cleanroom at IMEC. A Xenon-based source is employed for generating EUV photons. Zr spectral purity filter is embedded to filter the light and a set of ML and beam-split mirrors is used to project the light at desired position. RGA can collect the gas released from condensed resist layer and species are then analysed by a quadruple mass spectrometer. This setup was utilised for both contrast curve and outgassing analysis for $Ti_2Zr_4O_4(OBu)_2(OMc)_{14}$.

**SEM:** SEM imaging for EBL was conducted at ARCNL on a FEI Helios Nanolab 600 Dualbeam FIB / SEM with a Schottky Field Electron Gun (SFEG), equipped with Everhardt Thornley detector (ETD), Through the Lens detector (TLD), and CDEM detector. EUVL patterning was imaged via a FEI Quanta 250 FEGSEM with Schottky emitter as well as ETD, large field secondary electron detector and CBS detector.

**AFM:** A Bruker Dimension Icon atomic force microscopy (AFM) were utilized to measure the thickness of thin film before and after EUV exposure with the PeakForce tapping mode employed.

**DEA Experiment:** DEA experiments were carried out in Siedlce University of Natural Sciences and Humanities with the group of Assoc. Prof. Janina Kopyra. DEA spectroscopy setup primarily consists of an electron source, an oven, and a quadrupole mass spectrometer. The components dwell in an ultrahigh vacuum (UHV) chamber with pressure level of $10^{-8}$ mbar. Introduction of sample is via either a glass capillary with a heating oven and inlet for liquid materials, or a sample holder directly installed into the chamber for solid materials.

# Appendix 3: Abbreviations

| | |
|---|---|
| AD | Autodetachment |
| AFM | Atomic force microscope |
| ArF | Argon fluoride |
| ATR | Attenuated total reflectance |
| BDICDI | Bis (2,6-diisopropylphenyl) carbodiimide |
| CAR | Chemically amplified resist |
| CD | Critical dimension |
| DCM | Dichloromethane |
| DD | Dipolar dissociation |
| DEA | Dissociative electron attachment |
| DI | Dissociative ionisation |
| DNQ | Diazonaphthoquinone |
| DUV | Deep ultraviolet |
| DUVL | Deep ultraviolet lithography |
| EBL | Electron beam lithography |
| EC | Electron capture |
| eq. | Equivalent |
| EtOAc | Ethyl acetate |
| EUV | Extreme ultraviolet |
| EUVL | Extreme ultraviolet lithography |
| FTIR | Fourier-transform infrared spectroscopy |
| GATR | Grazing angle attenuated total reflectance |
| GC-MS | Gas chromatography-mass spectroscopy |

| | |
|---|---|
| Hf4 | $Hf_4O_2(OMc)_{12}$ |
| HMDS | Bis(trimethylsilyl)amine |
| HOAc | Acetic acid |
| HODiMc | Trans-2,3-dimethacrylic acid |
| HOMc | Methacrylic acid |
| HOMO | Highest occupied molecular orbital |
| HOPiv | Pivalic acid |
| HOVinac | Vinylacetic acid |
| HP | Half-pitch |
| HPLC | High performance liquid chromatography |
| HSQ | Hydrogen silsesquioxane |
| HVM | High volume manufacturing |
| IC | Integrated circuit |
| IPA | Isopropanol |
| KrF | Krypton fluoride |
| LEE | Low energy electron |
| LER | Line edge roughness |
| LUMO | Lowest unoccupied molecular orbital |
| LWR | Line width roughness |
| MA | Methacrylic acid |
| MCR | Metal-containing resist |
| MIBK | Methyl isobutyl ketone |
| ML | Multilayer |
| NA | Numerical aperture |

| | |
|---|---|
| ND | Neutral dissociation |
| NMR | Nuclear magnetic resonance |
| OAc | Acetate |
| OBu | Butoxide |
| OMc | Methacrylate |
| OPiv | Pivalate |
| OPr | Propoxide |
| OVinac | Vinylacetate |
| ODiMc | Trans-2,3-dimethacrylate |
| PAB | Post apply bake |
| PAG | Photoacid generator |
| PEB | Post exposure bake |
| PGME | Propylene glycol methyl ether |
| PGMEA | Propylene glycol methyl ether acetate |
| PMMA | Poly(methyl methacrylate) |
| PSI | Paul Scherrer Institute |
| R-Factor | Reliability factor |
| RET | Resolution enhancement technique |
| RGA | Residual gas analyser |
| SEM | Scanning electron microscope |
| SLS | Swiss Light Source |
| TGA | Thermogravimetric analysis |
| Ti2Zr4 | $Ti_2Zr_4O_4(OBu)_2(OMc)_{14}$ |
| Ti4Zr2 | $Ti_4Zr_2O_4(OBu)_6(OMc)_{10}$ |

| | |
|---|---|
| Ti4Zr4 | $Ti_4Zr_4O_6(OBu)_4(OMc)_{16}$ |
| UHV | Ultrahigh vacuum |
| UV/Vis | Ultraviolet/ Visible |
| VASE | J.A. Woollam VB-400 variable angle spectroscopic ellipsometer |
| w/v | Weight/ Volume |
| WS | Witness sample |
| XRD | X-ray diffraction |
| Z (Single Crystal XRD) | Number of formula units in a unit cell |
| Zr12 | $Zr_{12}O_8(OH)_8(OMc)_8(OAc)_{16}\cdot 6HOAc$ |
| Zr4 | $Zr_4O_2(OMc)_{12}$ |
| ZrM3P9 | $Zr_4O_2(OMc)_3(OPiv)_9$ |
| ZrM6P6 | $Zr_4O_2(OMc)_6(OPiv)_6$ |
| ZrM9P3 | $Zr_4O_2(OMc)_9(OPiv)_3$ |
| ZrOPiv | $Zr_4O_2(OPiv)_{12}$ |

# Appendix 4: Literature

1. Moore, G. E., Cramming more components onto integrated circuits (Reprinted from Electronics, pg 114-117, April 19, 1965). *Proceedings of the Ieee* **1998,** *86* (1), 82-85.

2. Williams, R., What's Next? [The End Of Moore's Law]. *Computing in Science & Engineering* **2017,** *19* (2), 7-13.

3. Rotman, D., We're not prepared for the end of Moore's Law. *MIT Technology Review* 2020.

4. Robinson, A.; Lawson, R., *Frontiers of Nanoscience - Materials and Processes for Next Generation Lithography*. Elsevier: 2016; Vol. 11.

5. den Boef, A. J., Optical wafer metrology sensors for process-robust CD and overlay control in semiconductor device manufacturing. *Surface Topography: Metrology and Properties* **2016,** *4* (2), 023001.

6. Veendrick, H., *Nanometer CMOS ICs*. 2 ed.; Springer International Publishing: 2017.

7. Willson, C. G.; Dammel, R.; Reiser, A., *Photoresist materials: a historical perspective*. SPIE: 1997; Vol. 3051.

8. Chao, W.; Kim, J.; Anderson, E. H.; Fischer, P.; Rekawa, S.; Attwood, D. T., *Double patterning HSQ processes of zone plates for 10 nm diffraction limitedperformance*. ; Lawrence Berkeley National Lab. (LBNL), Berkeley, CA (United States): 2009; p Medium: ED; Size: 2.

9. van Setten, E.; Wittebrood, F.; Psara, E.; Oorschot, D.; Philipsen, V., *Patterning options for N7 logic: prospects and challenges for EUV*. SPIE: 2015; Vol. 9661.

10. Abercrombie, D. Will EUV Kill Multi-Patterning? *Semiconductor Engineering* [Online], 2017. https://semiengineering.com/will-euv-kill-multi-patterning/ (accessed 06.07.2020).

11. Wu, B.; Kumar, A., Extreme ultraviolet lithography: A review. *Journal of Vacuum Science & Technology B: Microelectronics and Nanometer Structures Processing, Measurement, and Phenomena* **2007,** *25* (6), 1743-1761.

12. Turkot, B.; Carson, S.; Lio, A.; Liang, T.; Phillips, M.; McCool, B.; Stenehjem, E.; Crimmins, T.; Zhang, G.; Sivakumar, S., *EUV progress toward HVM readiness*. SPIE: 2016; Vol. 9776.

13. Montcalm, C.; Bajt, S.; Mirkarimi, P.; Spiller, E.; Weber, F.; Folta, J., *Multilayer reflective coatings for extreme-ultraviolet lithography*. SPIE: 1998; Vol. 3331.

14. Folta, J.; Bajt, S.; Barbee, T.; Grabner, R. F.; Mirkarimi, P.; Nguyen, T.; Schmidt, M.; Spiller, E.; Walton, C.; Wedowski, M.; Montcalm, C., *Advances in multilayer reflective coatings for extreme ultraviolet lithography*. SPIE: 1999; Vol. 3676.

15. Sugawara, M.; Nishiyama, I.; Takai, M., Mask Pattern Correction by Energy Loss Compensation in Extreme Ultraviolet Lithography. *Japanese Journal of Applied Physics* **2005,** *44* (7B), 5467-5473.

16. Fomenkov, I.; Brandt, D.; Ershov, A.; Schafgans, A.; Tao, Y.; Vaschenko, G.; Rokitski, S.; Kats, M.; Vargas, M.; Purvis, M.; Rafac, R.; La Fontaine, B.; De Dea, S.; LaForge, A.; Stewart, J.; Chang, S.; Graham, M.; Riggs, D.; Taylor, T.; Abraham, M.; Brown, D., Light sources for high-volume manufacturing EUV lithography: technology, performance, and power scaling. *Advanced Optical Technologies* **2017,** *6* (3-4), 173-186.

17. Neisser, M., The 2017 IRDS Lithography Roadmap. *Journal of Microelectronic Manufacturing* **2018,** *1* (2), 1-8.

18. Neisser, M.; Wurm, S., ITRS lithography roadmap: 2015 challenges. *Advanced Optical Technologies* **2015,** *4* (4), 235-240.

19. ASML TWINSCAN NXE:3400C. https://www.asml.com/en/products/euv-lithography-systems/twinscan-nxe3400c (accessed 07.07.2020).

20. Sperling, E. Extending EUV Beyond 3nm 2017. https://semiengineering.com/extending-euv-to-2nm-and-beyond/ (accessed 07.07.2020).

21. Fomenkov, I., EUV Source for Lithography in HVM: performance and prospects. ASML: ASML Source Workshop, 2019.

22. Mack, C., *Fundamental Principles of Optical Lithography: The Science of Microfabrication*. Wiley: 2007.

23. Patsis, G. P.; Gogolides, E., Material and process effects on line-edge-roughness of photoresists probed with a fast stochastic lithography simulator. *Journal of Vacuum Science & Technology B: Microelectronics and Nanometer Structures Processing, Measurement, and Phenomena* **2005,** *23* (4), 1371-1375.

24. Hiraiwa, A.; Nishida, A., Spectral analysis of line edge and line-width roughness with long-range correlation. *Journal of Applied Physics* **2010,** *108* (3), 034908.

25. Jiang, X.; Wang, R.; Yu, T.; Chen, J.; Huang, R., Investigations on Line-Edge Roughness (LER) and Line-Width Roughness (LWR) in Nanoscale CMOS Technology: Part I–Modeling and Simulation Method. *IEEE Transactions on Electron Devices* **2013,** *60* (11), 3669-3675.

26. Kozawa, T., Theoretical study on trade-off relationships between resolution, line edge roughness, and sensitivity in resist processes for semiconductor manufacturing by extreme ultraviolet lithography. *Japanese Journal of Applied Physics* **2019,** *58* (9), 096502.

27. Kozawa, T.; Saeki, A.; Tagawa, S., Modeling and simulation of chemically amplified electron beam, x-ray, and EUV resist processes. *Journal of Vacuum Science & Technology B: Microelectronics and Nanometer Structures Processing, Measurement, and Phenomena* **2004,** *22* (6), 3489-3492.

28. Kozawa, T.; Tamura, T., Theoretical study on protected unit fluctuation of chemically amplified resists used for photomask production by electron beam lithography. *Japanese Journal of Applied Physics* **2020,** *59* (1), 016503.

29. Ito, H.; Willson, C. G.; Frechet, J. H. J. In *New UV Resists with Negative or Positive Tone*, 1982 Symposium on VLSI Technology. Digest of Technical Papers, 1-3 Sept. 1982; 1982; pp 86-87.

30. Kemp, K.; Wurm, S., EUV lithography. *Comptes Rendus Physique* **2006,** *7* (8), 875-886.

31. Lawson, R. Molecular resists for advanced lithography - design, synthesis, characterization, and simulation. Georgia Institute of Technology, 2011.

32. Ito, H., Chemical amplification resists: History and development within IBM. *IBM Journal of Research and Development* **1997,** *41* (1.2), 119-130.

33. Yeh, W.-M.; Noga, D. E.; Lawson, R. A.; Tolbert, L. M.; Henderson, C. L., Comparison of positive tone versus negative tone resist pattern collapse behavior. *Journal of Vacuum Science & Technology B* **2010,** *28* (6), C6S6-C6S11.

34. Mitsuyasu, M.; Yamamoto, H.; Kozawa, T., Dissolution Dynamics of Chemically Amplified Resists for Extreme Ultraviolet Lithography Studied by Quartz Crystal Microbalance. 2015 International Workshop on EUV Lithography, 2015.

35. Jouve, A.; Simon, J.; Foucher, J.; David, T.; Tortai, J.-H.; Solak, H., *Overcoming pattern collapse of ultra high resolution dense lines obtained with EUV resists*. SPIE: 2005; Vol. 5753.

36. Noga, D.; Lawson, R.; Lee, C.-T.; Tolbert, L.; Henderson, C., *Understanding pattern collapse in high-resolution lithography: impact of feature width on critical stress*. SPIE: 2009; Vol. 7273.

37. Lawson, R.; Cheng, J.; Noga, D.; Younkin, T.; Tolbert, L.; Henderson, C., *Aqueous and solvent developed negative-tone molecular resists*. SPIE: 2010; Vol. 7639.

38. Torok, J.; Re, R. D.; Herbol, H.; Das, S.; Bocharova, I.; Paolucci, A.; Ocola, L. E.; Ventrice Jr, C.; Lifshin, E.; Denbeaux, G.; Brainard, R. L., Secondary Electrons in EUV Lithography. *Journal of Photopolymer Science and Technology* **2013,** *26* (5), 625-634.

39. Kozawa, T.; Tagawa, S., Radiation Chemistry in Chemically Amplified Resists. *Japanese Journal of Applied Physics* **2010,** *49* (3), 030001.

40. Danilo De, S.; Yannick, V.; Geert, V., Photoresists in extreme ultraviolet lithography (EUVL). *Advanced Optical Technologies* **2017,** *6* (3-4), 163-172.

41. Nagahara, S.; Yuan, L.; Poppe, W. J.; Neureuther, A.; Kono, Y.; Sekiguchi, A.; Fujiwara, K.; Watanabe, T.; Taira, K.; Kusumoto, S.; Nakano, T.; Shimokawa, T., *Understanding quencher mechanisms by considering photoacid-dissociation equilibrium in chemically amplified resists*. SPIE: 2005; Vol. 5753.

42. Bristol, R., *The tri-lateral challenge of resolution, photospeed, and LER: scaling below 50nm?* SPIE: 2007; Vol. 6519.

43. Wallow, T.; Higgins, C.; Brainard, R.; Petrillo, K.; Montgomery, W.; Koay, C.-S.; Denbeaux, G.; Wood, O.; Wei, Y., *Evaluation of EUV resist materials for use at the 32 nm half-pitch node*. SPIE: 2008; Vol. 6921.

44. De Silva, A.; Felix, N. M.; Ober, C. K., Molecular Glass Resists as High-Resolution Patterning Materials. *Advanced Materials* **2008,** *20* (17), 3355-3361.

45. Frommhold, A.; Yang, D.; McClelland, A.; Xue, X.; Ekinci, Y.; Palmer, R., Performance of negative tone chemically amplified fullerene resists in extreme ultraviolet lithography. *Journal of Micro/Nanolithography, MEMS, and MOEMS* **2013,** *12* (3), 033010.

46. Rathore, A.; Pollentier, I.; Singh, H.; Fallica, R.; De Simone, D.; De Gendt, S., Effect of molecular weight on the EUV-printability of main chain scission type polymers. *Journal of Materials Chemistry C* **2020,** *8* (17), 5958-5966.

47. Lawson, R.; Cheng, J.; Cheshmehkani, A.; Tolbert, L.; Henderson, C., *Postiive tone resists based on network deploymerization of molecular resists*. SPIE: 2013; Vol. 8682.

48. Henke, B. L.; Gullikson, E. M.; Davis, J. C., X-Ray Interactions: Photoabsorption, Scattering, Transmission, and Reflection at E = 50-30,000 eV, Z = 1-92. *Atomic Data and Nuclear Data Tables* **1993,** *54* (2), 181-342.

49. Yasin, E.; Michaela, V.; Mohamad, H.; Li, W.; Nassir, M. In *Evaluation of EUV resist performance with interference lithography towards 11 nm half-pitch and beyond*, Proc.SPIE, 2013.

50. Fallica, R.; Haitjema, J.; Wu, L.; Castellanos, S.; Brouwer, F.; Ekinci, Y. In *Absorption coefficient and exposure kinetics of photoresists at EUV*, Proc.SPIE, 2017.

51. Andrew, G.; Jeremy, T. A.; Benjamin, L. C.; Peter De, S.; Joseph, E.; Michael, G.; Kai, J.; Michael, K.; Stephen, T. M.; Jason, K. S.; Alan, J. T.; Danilo De, S.; Geert, V. In *Integrated fab process for metal oxide EUV photoresist*, Proc.SPIE, 2015.

52. Kryask, M.; Trikeriotis, M.; Ouyang, C.; Chakrabarty, S.; Giannelis, E. P.; Ober, C. K., Nanoparticle Photoresists: Ligand Exchange as a New, Sensitive EUV Patterning Mechanism. *Journal of Photopolymer Science and Technology* **2013,** *26* (5), 659-664.

53. Ober, C. K.; Giannelis, E. P. New oxide nanoparticle extreme-UV photoresists achieve high sensitivity 2014. https://www.spie.org/news/5552-new-oxide-nanoparticle-extreme-uv-photoresists-achieve-high-sensitivity?SSO=1 (accessed 23.07.2020).

54. Sonia, C.; Lianjia, W.; Milos, B.; Giuseppe, P.; Dimitrios, K.; Michaela, V.; Yasin, E.; Thomas, J. In *Ti, Zr, and Hf-based molecular hybrid materials as EUV photoresists*, Proc.SPIE, 2018.

55. Markos, T.; Woo Jin, B.; Evan, S.; Marie, K.; Neal, L.; Peng, X.; Bruce, S.; Paul, A. Z.; Christopher, K. O.; Emmanuel, P. G. In *Development of an inorganic photoresist for DUV, EUV, and electron beam imaging*, Proc.SPIE, 2010.

56. Hinsberg, W. D.; Meyers, S. In *A numeric model for the imaging mechanism of metal oxide EUV resists*, Proc.SPIE, 2017.

57. Moraru, B.; Kickelbick, G.; Schubert, U., Methacrylate-Substituted Mixed-Metal Clusters Derived from Zigzag Chains of [ZrO8]/[ZrO7] and [TiO6] Polyhedra. *European Journal of Inorganic Chemistry* **2001,** *2001* (5), 1295-1301.

58. Moraru, B.; Kickelbick, G.; Schubert, U., Methacrylate-Substituted Mixed-Metal Clusters Derived from Zigzag Chains of [ZrO8]/[ZrO7] and [TiO6] Polyhedra. Centre, C. C. D., Ed. 2001.

59. Cardineau, B.; Passarelli, J.; Sortland, M.; Del Re, R.; Tear, W.; Al-Mashat, H.; Marnell, M.; Heard, K.; Aslam, A.; Pavlich, J.; Kaminski, R.; Nastasi, P.; Sarma, C.; Freedman, D.; Brainard, R., Molecular Organometallic Resists for EUV (MORE). EUV Symposium TWG, 2013.

60. Rispens, G., Status update on outgassing of alternative resists. ASML: Resist TWG, 2016.

61. Passarelli, J.; Sortland, M.; Re, R. D.; Cardineau, B.; Sarma, C.; Freedman, D. A.; Brainard, R. L., Bismuth Resists for EUV Lithography. *Journal of Photopolymer Science and Technology* **2014,** *27* (5), 655-661.

62. Steven, G.; Amrit, N.; Michael, M.; Lee, N.; Daniel, A. F.; Robert, L. B.; Greg, D. In *Reactivity of metal-oxalate EUV resists as a function of the central metal*, Proc.SPIE, 2017.

63. Jarich, H.; Yu, Z.; Michaela, V.; Dimitrios, K.; Yasin, E.; Albert, M. B., Extreme ultraviolet patterning of tin-oxo cages. *Journal of Micro/Nanolithography, MEMS, and MOEMS* **2017,** *16* (3), 1-7.

64. Cardineau, B.; Del Re, R.; Marnell, M.; Al-Mashat, H.; Vockenhuber, M.; Ekinci, Y.; Sarma, C.; Freedman, D. A.; Brainard, R. L., Photolithographic properties of tin-oxo clusters using extreme ultraviolet light (13.5nm). *Microelectronic Engineering* **2014,** *127*, 44-50.

65. Jiang, J.; Chakrabarty, S.; Yu, M.; Ober, C. K., Metal Oxide Nanoparticle Photoresists for EUV Patterning. *Journal of Photopolymer Science and Technology* **2014,** *27* (5), 663-666.

66. Wu, L.; Liu, J.; Vockenhuber, M.; Ekinci, Y.; Castellanos, S., Hybrid EUV Resists with Mixed Organic Shells: A Simple Preparation Method. *European Journal of Inorganic Chemistry* **2019,** *2019* (38), 4136-4141.

67. Gross, S.; Kickelbick, G.; Puchberger, M.; Schubert, U., Mono-, Di-, and Trimetallic Methacrylate-substituted Metal Oxide Clusters Derived from Hafnium Butoxide. *Monatshefte für Chemie / Chemical Monthly* **2003,** *134* (8), 1053-1063.

68. Munro, J. J.; Harrison, S.; Fujimoto, M. M.; Tennyson, J., A dissociative electron attachment cross-section estimator. *Journal of Physics: Conference Series* **2012,** *388* (1), 012013.

69. Vasiliki, K.; Kazuki, K.; Hong, X.; Jérémy, O.; Christopher, K. O.; Emmanuel, P. G., <sup />Elucidating the patterning mechanism of zirconium-based hybrid photoresists. *Journal of Micro/Nanolithography, MEMS, and MOEMS* **2017,** *16* (4), 1-7.

70. Perera, R., Tooling to measure EUV resist outgassing and witness plate contamination. EUV Technology: IEUVI Resist TWG, 2010.

71. Kickelbick, G.; Schubert, U., Oxozirconium Methacrylate Clusters: Zr6(OH)4O4(OMc)12 and Zr4O2(OMc)12 (OMc = Methacrylate). *Chemische Berichte* **1997,** *130* (4), 473-478.

72. Kreutzer, J.; Puchberger, M.; Artner, C.; Schubert, U., Retention of the Cluster Core Structure during Ligand Exchange Reactions of Carboxylato-Substituted Metal Oxo Clusters. *European Journal of Inorganic Chemistry* **2015,** *2015* (12), 2145-2151.

73. Kogler, F. R. Synthesis and Characterization of Transition Metal Oxo Clusters and their Use as Co-Monomers in the Preparation of Hybrid Polymers. TU Wien, 2005.

74. Schubert, U., Organofunctional Metal Oxide Clusters as Building Blocks for Inorganic-Organic Hybrid Materials. *Journal of Sol-Gel Science and Technology* **2004,** *31* (1), 19-24.

75. Kogler, F. R.; Jupa, M.; Puchberger, M.; Schubert, U., Control of the ratio of functional and non-functional ligands in clusters of the type Zr6O4(OH)4(carboxylate)12 for their use as building blocks for inorganic–organic hybrid polymers. *Journal of Materials Chemistry* **2004,** *14* (21), 3133-3138.

76. Schubert, U., Surface chemistry of carboxylato-substituted metal oxo clusters – Model systems for nanoparticles. *Coordination Chemistry Reviews* **2017,** *350*, 61-67.

77. Trimmel, G.; Gross, S.; Kickelbick, G.; Schubert*, U., Swelling behavior and thermal stability of poly(methylmethacrylate) crosslinked by the oxozirconium cluster Zr4O2(methacrylate)12. *Applied Organometallic Chemistry* **2001,** *15* (5), 401-406.

78. Kreutzer, J.; Qin, X.-H.; Gorsche, C.; Peterlik, H.; Liska, R.; Schubert, U., Variation of the crosslinking density in cluster-reinforced polymers. *Materials Today Communications* **2015,** *5*, 10-17.

79. Franssila, S., Thin-Film Materials and Processes. *Introduction to Microfabrication* **2010**, 47-67.

80. Mack, C., *Field Guide to Optical Lithography*. SPIE: 2006.

81. Luo, C.; Xu, C.; Lv, L.; Li, H.; Huang, X.; Liu, W., Review of recent advances in inorganic photoresists. *RSC Advances* **2020,** *10* (14), 8385-8395.

82. Sun, C.; Huang, Z.; Liu, Y.; Li, C.; Tan, H.; Zhang, Y., The Effect of Carbodiimide on the Stability of Wood Fiber/Poly(lactic acid) Composites During Soil Degradation. *Journal of Polymers and the Environment* **2020,** *28* (4), 1315-1325.

83. Stloukal, P.; Jandikova, G.; Koutny, M.; Sedlařík, V., Carbodiimide additive to control hydrolytic stability and biodegradability of PLA. *Polymer Testing* **2016,** *54*, 19-28.

84. May, G. S.; Sze, S. M., *Fundamentals of Semiconductor Fabrication*. illustrated ed.; Wiley: 2003; p 320.

85. Duan, H.; Manfrinato, V. R.; Yang, J. K. W.; Winston, D.; Cord, B. M.; Berggren, K. K., Metrology for electron-beam lithography and resist contrast at the sub-10 nm scale. *Journal of Vacuum Science & Technology B* **2010,** *28* (6), C6H11-C6H17.

86. Yu, M. L.; Coyle, S. T.; DeVore, W.; Shamoun, B., Electron-electron interaction induced beam displacement in a multiple electron beam system. *Journal of Vacuum Science & Technology B: Microelectronics and Nanometer Structures Processing, Measurement, and Phenomena* **2005,** *23* (6), 2589-2595.

87. Chang, T. H. P.; Mankos, M.; Lee, K. Y.; Muray, L. P., Multiple electron-beam lithography. *Microelectronic Engineering* **2001,** *57-58*, 117-135.

88. Miyoshi, H.; Taniguchi, J., Fabrication of a high-resolution mask by using variable-shaped electron beam lithography with a non-chemically amplified resist and a post-exposure bake. *Microelectronic Engineering* **2015,** *143*, 48-54.

89. Paul, P.; Chris, B.; Alan, B.; Allen, C.; Anthony, C.; Luca, G.; Mark, M.; Henry, P.; Keith, S.; Marek, Z. In *REBL nanowriter: Reflective Electron Beam Lithography*, Proc.SPIE, 2009.

90. Lawson, R. A.; Henderson, C. L., Understanding the relationship between true and measured resist feature critical dimension and line edge roughness using a detailed scanning electron microscopy simulator. *Journal of Vacuum Science & Technology B* **2010,** *28* (6), C6H34-C6H39.

91. Richard, A. L.; Clifford, L. H. In *Investigating SEM metrology effects using a detailed SEM simulation and stochastic resist model*, Proc.SPIE, 2015.

92. Ekinci, Y.; Solak, H. H.; Padeste, C.; Gobrecht, J.; Stoykovich, M. P.; Nealey, P. F., 20nm Line/space patterns in HSQ fabricated by EUV interference lithography. *Microelectronic Engineering* **2007,** *84* (5), 700-704.

93. Oyama, T. G.; Oshima, A.; Tagawa, S., Estimation of resist sensitivity for extreme ultraviolet lithography using an electron beam. *AIP Advances* **2016,** *6* (8), 085210.

94. Neha, T.; Li-Ting, T.; Michaela, V.; Yasin, E.; Sonia, C., Stability studies on a sensitive EUV photoresist based on zinc metal oxoclusters. *Journal of Micro/Nanolithography, MEMS, and MOEMS* **2019,** *18* (4), 1-10.

95. Klimeck, G. Nanometer Scale Patterning and Processing. https://nanohub.org/resources/15325/watch?resid=24300 (accessed 16.09.2020).

96. Bernd, T.; Andreas, L.; Birgit, P.; Yasin, E. In *Advanced holographic methods in extreme ultraviolet interference lithography*, Proc.SPIE, 2011.

97. Mojarad, N.; Hojeij, M.; Wang, L.; Gobrecht, J.; Ekinci, Y., Single-digit-resolution nanopatterning with extreme ultraviolet light for the 2.5 nm technology node and beyond. *Nanoscale* **2015,** *7* (9), 4031-4037.

98. Ashby, P. D.; Olynick, D. L.; Ogletree, D. F.; Naulleau, P. P., Resist Materials for Extreme Ultraviolet Lithography: Toward Low-Cost Single-Digit-Nanometer Patterning. *Advanced Materials* **2015,** *27* (38), 5813-5819.

99. Leone, S. R.; Ahmed, M.; Wilson, K. R., Chemical dynamics, molecular energetics, and kinetics at the synchrotron. *Physical Chemistry Chemical Physics* **2010,** *12* (25), 6564-6578.

100. Thorman, R. M.; Kumar T. P., R.; Fairbrother, D. H.; Ingólfsson, O., The role of low-energy electrons in focused electron beam induced deposition: four case studies of representative precursors. *Beilstein Journal of Nanotechnology* **2015,** *6*, 1904-1926.

101. Schaefer, J.; Hoelzl, J., A contribution to the dependence of secondary electron emission from the work function and fermi energy. *Thin Solid Films* **1972,** *13* (1), 81-86.

102. Illenberger, E.; Momigny, J., *Gaseous Molecular Ions*. Steinkopff: Heidelberg, 2014; Vol. 2.

103. Enomoto, S.; Kozawa, T., Study of electron-beam and extreme-ultraviolet resist utilizing polarity change and radical crosslinking. *Journal of Vacuum Science & Technology B* **2018,** *36* (3), 031601.

104. Utke, I.; Moshkalev, S.; Russell, P., *Nanofabrication using focused ion and electron beams*. Oxford University Press: Oxford, 2012.

105. Arumainayagam, C. R.; Lee, H.-L.; Nelson, R. B.; Haines, D. R.; Gunawardane, R. P., Low-energy electron-induced reactions in condensed matter. *Surface Science Reports* **2010,** *65* (1), 1-44.

106. Bald, I.; Kopyra, J.; Illenberger, E., Selective Excision of C5 from D-Ribose in the Gas Phase by Low-Energy Electrons (0–1 eV): Implications for the Mechanism of DNA Damage. *Angewandte Chemie International Edition* **2006,** *45* (29), 4851-4855.

107. Suess, L.; Parthasarathy, R.; Dunning, F. B., Nondissociative low-energy electron attachment to SF6, C6F6, C10F8, and c-C7F14: Negative ion lifetimes. *The Journal of Chemical Physics* **2002,** *117* (24), 11222-11227.

108. Pelc, A.; Sailer, W.; Scheier, P.; Märk, T. D.; Illenberger, E., Fragmentation of propanoic acid by subexcitation electrons. *Chemical Physics Letters* **2004,** *392* (4), 465-469.

109. Pollentier, I.; Neira, I.; Goethals, A. M.; Gronheid, R.; Tarutani, S.; Tamaoki, H.; Tsubaki, H.; Takahashi, T. In *Unraveling the effect of resist composition on EUV optics contamination*, Proc.SPIE, 2011.

110. Kim, R. D.; Iwao, N.; Hiroaki, O.; Anthony, K.; Heidi, C.; Wang, Y.; Takeo, W.; Paolo, L.; Luca, R.; Gregory, D.; Julia, S. In *An analysis of EUV-resist outgassing measurements*, Proc.SPIE, 2007.

111. Shinji, K.; Julius Joseph, S.; Toshiro, I. In *Quantitative analysis of EUV resist outgassing*, Proc.SPIE, 2008.

112. Santillan, J. J.; Kobayashi, S.; Itani, T., Outgassing Quantification Analysis of Extreme Ultraviolet Resists. *Japanese Journal of Applied Physics* **2008,** *47* (6), 4922-4925.

113. Pollentier, I.; Goethals, A. M.; Gronheid, R.; Steinhoff, J.; Dijk, J. V. In *Characterization of EUV optics contamination due to photoresist related outgassing*, Proc.SPIE, 2010.

114. Reusch, W. Mass Spectrometry. https://www2.chemistry.msu.edu/faculty/reusch/VirtTxtJml/Spectrpy/MassSpec/masspec1.htm (accessed 20.08).

115. Schepper, P. D.; Marinov, D.; Otell, Z. e.; Altamirano-Sánchez, E.; Marneffe, J. F. d.; Gendt, S. D.; Braithwaite, N. S. J. In *H2 plasma and neutral beam treatment of EUV photoresist*, Proc.SPIE, 2015.

116. Wu, W.; Nuzhdin, K.; Vyushkova, M.; Janik, I.; Bartels, D., Comparison of Acid Generation in EUV Lithography Films of Poly(4-hydroxystyrene) (PHS) and Noria Adamantyl Ester (Noria-AD50). *The Journal of Physical Chemistry B* **2012,** *116* (21), 6215-6224.

117. Lawrie, K. J.; Blakey, I.; Blinco, J. P.; Cheng, H. H.; Gronheid, R.; Jack, K. S.; Pollentier, I.; Leeson, M. J.; Younkin, T. R.; Whittaker, A. K., Chain scission resists for extreme ultraviolet lithography based on high performance polysulfone-containing polymers. *Journal of Materials Chemistry* **2011,** *21* (15), 5629-5637.

118. IR Spectrum Table & Chart. https://www.sigmaaldrich.com/technical-documents/articles/biology/ir-spectrum-table.html (accessed 21.08).

119. Trimmel, G.; Fratzl, P.; Schubert, U., Cross-Linking of Poly(methyl methacrylate) by the Methacrylate-Substituted Oxozirconium Cluster Zr6(OH)4O4(Methacrylate)12. *Chemistry of Materials* **2000,** *12* (3), 602-604.

120. Gross, S.; Di Noto, V.; Schubert, U., Dielectric investigation of inorganic–organic hybrid film based on zirconium oxocluster-crosslinked PMMA. *Journal of Non-Crystalline Solids* **2003,** *322* (1), 154-159.

121. Schubert, U.; Völkel, T.; Moszner, N., Mechanical Properties of an Inorganic−Organic Hybrid Polymer Cross-linked by the Cluster Zr4O2(methacrylate)12. *Chemistry of Materials* **2001,** *13* (11), 3811-3812.

122. Moraru, B.; Hüsing, N.; Kickelbick, G.; Schubert, U.; Fratzl, P.; Peterlik, H., Inorganic−Organic Hybrid Polymers by Polymerization of Methacrylate- or Acrylate-Substituted Oxotitanium Clusters with Methyl Methacrylate or Methacrylic Acid. *Chemistry of Materials* **2002,** *14* (6), 2732-2740.

# Appendix 5: SEM Images of EBL Patterning

## 1 $Zr_4O_2(OMc)_{12}$

Area Dose: 50 µC/cm$^2$; Line Dose: 50 pC/cm

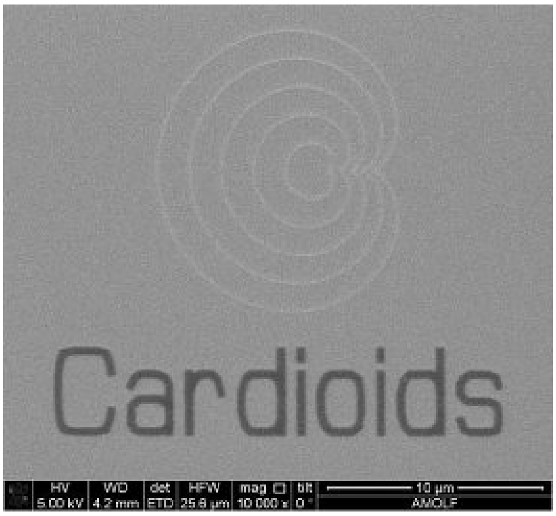

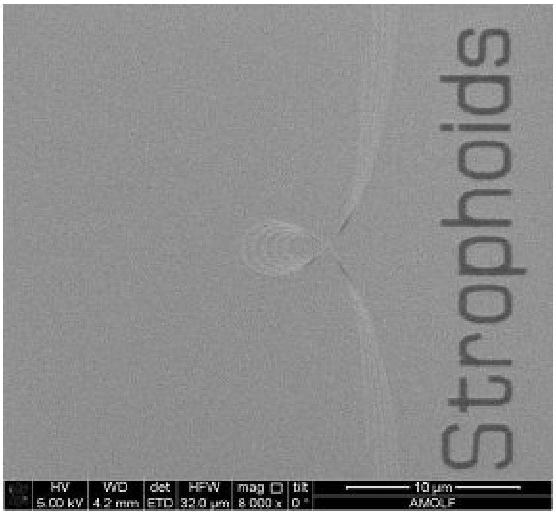

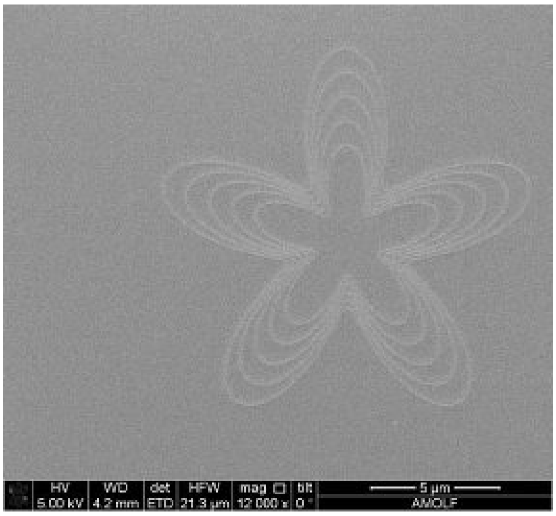

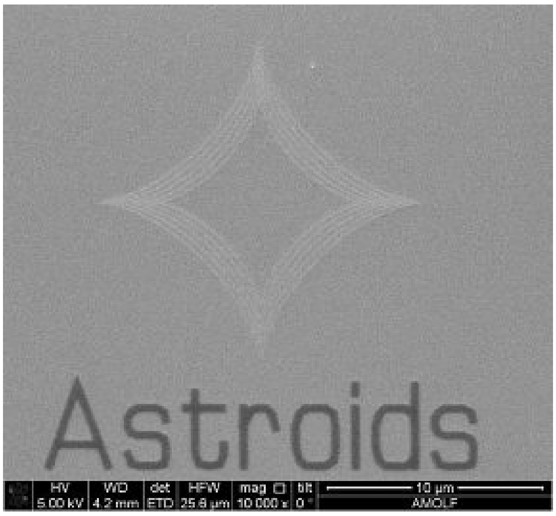

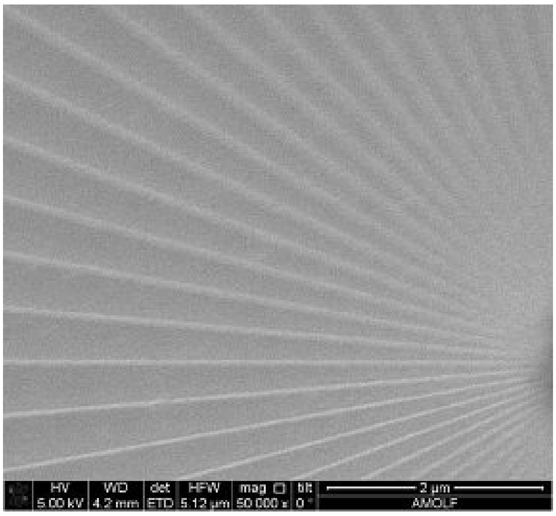

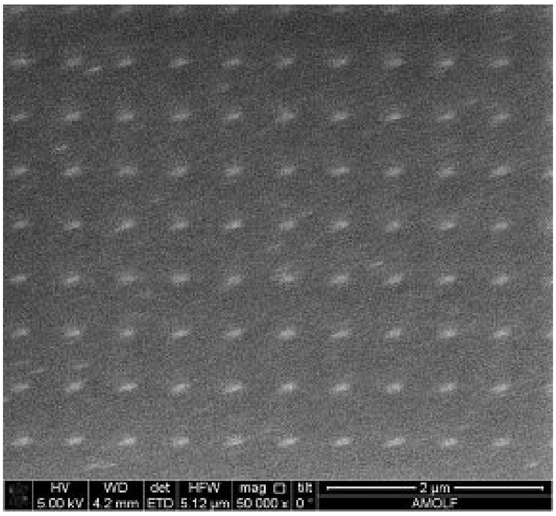

## 2 $Zr_4O_2(OMc)_3(OPiv)_9$

Area Dose: 100 µC/cm$^2$; Line Dose: 100 pC/cm

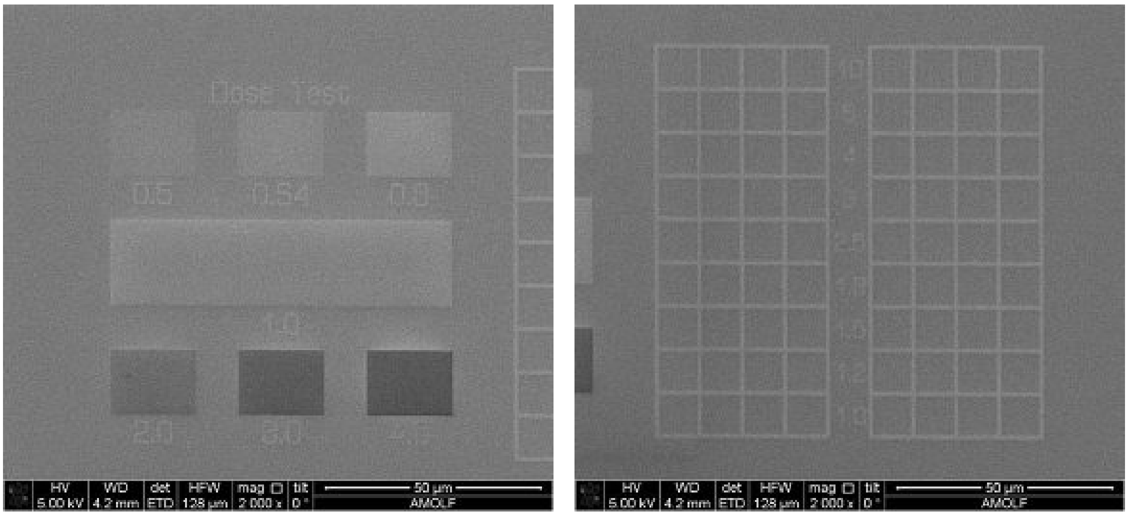

## 3 $Zr_4O_2(OMc)_6(OPiv)_6$

Area Dose: 100 µC/cm$^2$; Line Dose: 100 pC/cm

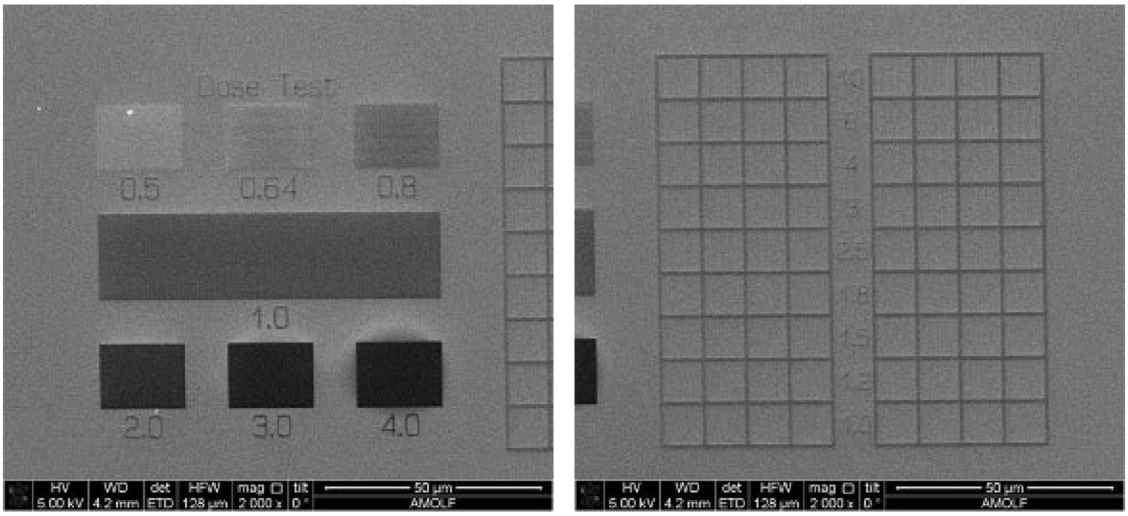

## 4 $Zr_4O_2(OMc)_6(OPiv)_6$

Area Dose: 100 µC/cm$^2$; Line Dose: 100 pC/cm

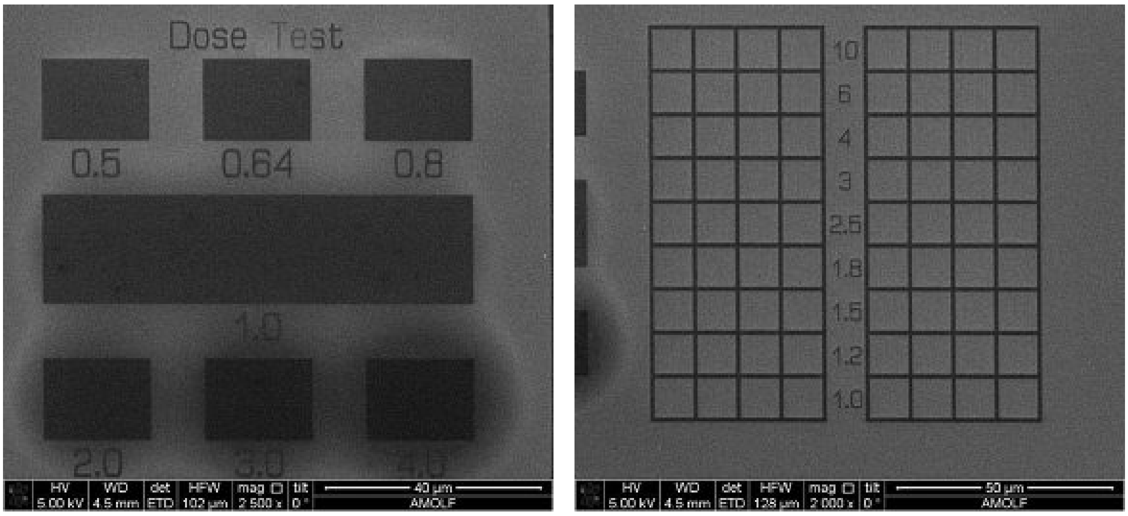

## 5 $Hf_4O_2(OMc)_{12}$

Area Dose: 50 µC/cm$^2$; Line Dose: 50 pC/cm

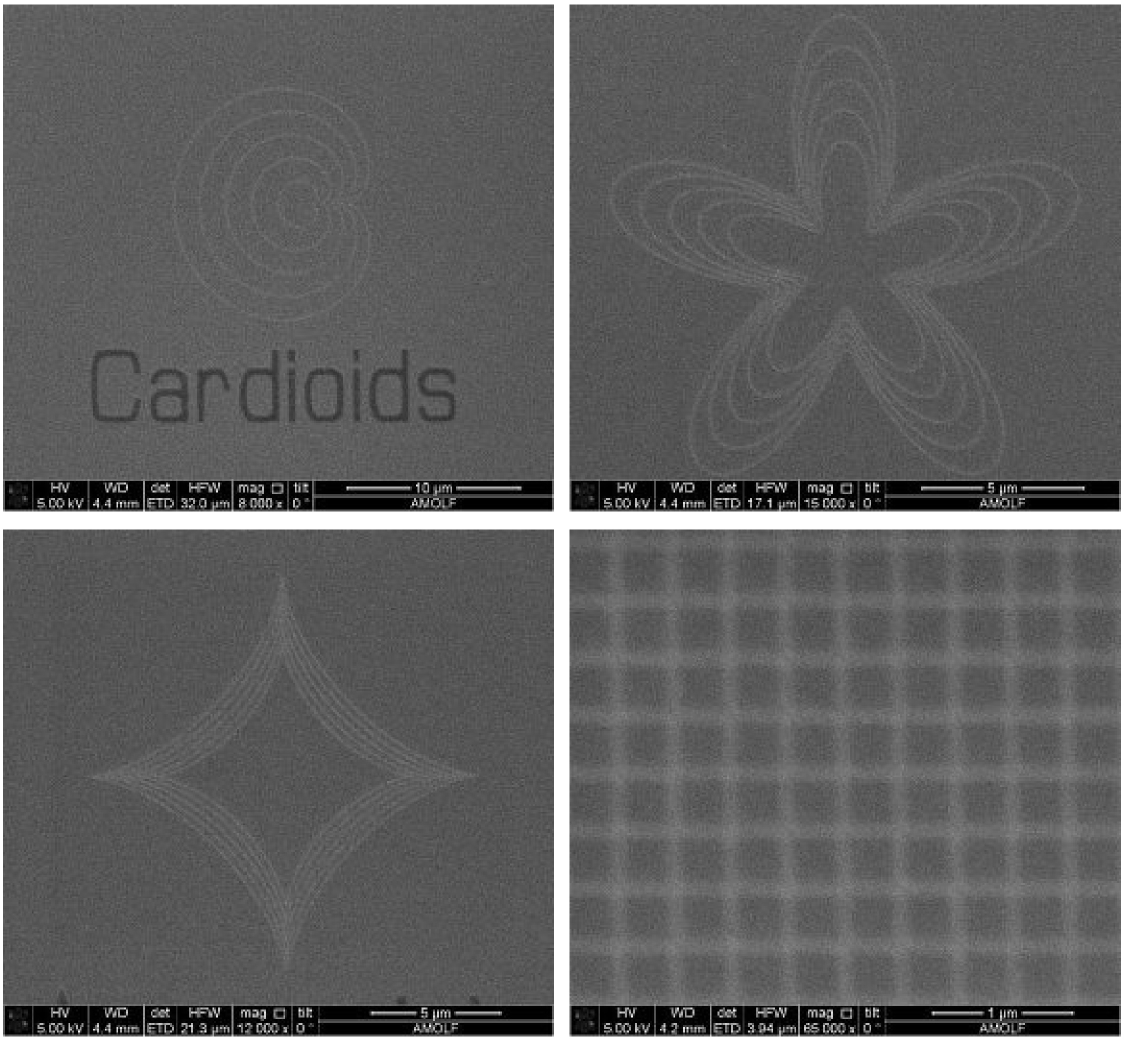

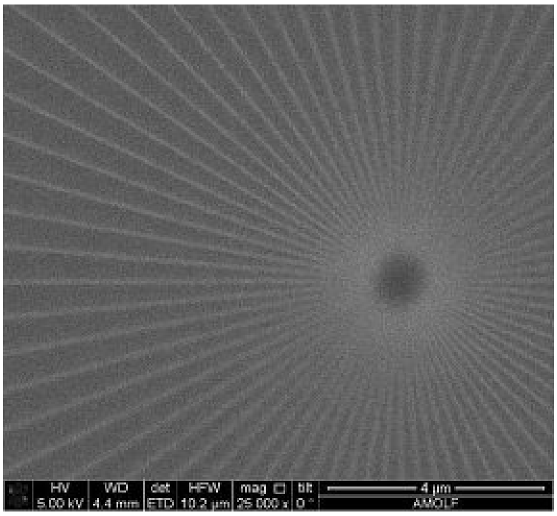
HV
5.00 kV
WD
4.4 mm
det
ETD
HFW
10.2 µm
mag
25 000 x
tilt
0 °
4 µm
AMOLF

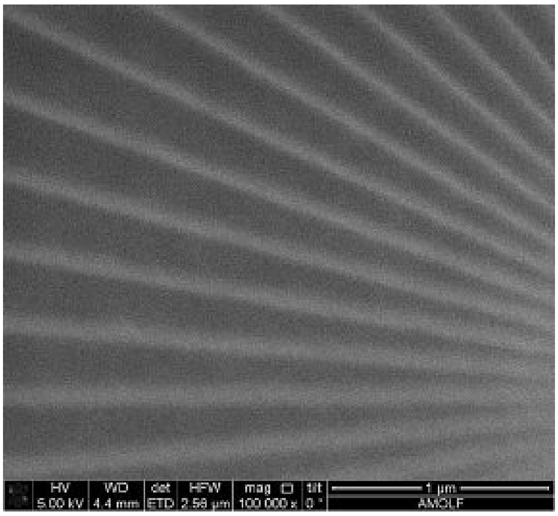
HV
5.00 kV
WD
4.4 mm
det
ETD
HFW
2.56 µm
mag
100 000 x
tilt
0 °
1 µm
AMOLF

## Appendix 6: Experiment Collaboration Partners

| | Experiment | Date | Institute/Location | Collaboration Partner |
|---|---|---|---|---|
| **1** | Thin-Film UV/Vis Spectroscopy | Jul. to Sep. 2020 | ARCNL (Amsterdam, the Netherlands) | Prof. Fred Brouwer<br>Dr. Sonia Castellanos<br>Lianjia Wu<br>Neha Thakur |
| **2** | Electron Beam Lithography | | | |
| **3** | EUV Contrast Curve | Nov. 2019<br>Dec. 2019 | Paul Scherrer Institute (Villigen, Switzerland) | Prof. Fred Brouwer<br>Dr. Sonia Castellanos<br>Lianjia Wu<br>Neha Thakur |
| **4** | EUV Line/Space Patterning | | | |
| **5** | DEA Spectroscopy | Feb. to Mar. 2020 | Siedlce University of Natural Sciences and Humanities (Siedlce, Poland) | Prof. Janina Kopyra<br>Paulina Wierzbicka |
| **6** | EUV Outgassing Analysis | Jul. to Aug. 2020 | IMEC (Leuven, Belgium) | Dr. Danilo De Simone<br>Dr. Ivan Pollentier<br>Ashish Rathore |
| **7** | EUV Contrast Curve (on Ti-Zr Clusters) | | | |

# Curriculum Vitae

## Ching-Chung Huang

Title: M.Sc.

Einsiedlerplatz 6A/ Top 19, A-1050, Wien

Phone: +4367762654709

E-mail: ching-chung.huang@tuwien.ac.at

## Personal Information

Date of Birth: 4th February, 1990

Place of Birth: Tainan City, Taiwan

Citizenship: Taiwan (R.O.C.)

## Professional Experience

| | |
|---|---|
| **Sep. 2017 – Oct. 2020** | **Early Stage Researcher (Project Assistant)**<br>TU Wien (Vienna University of Technology), Austria<br>**Specialization**: EUVL, EBL, Photoresist, Metal Oxo Clusters, DEA Spectroscopy |
| **Jul. 2020 – Aug. 2020** | **Visiting Researcher**<br>imec, Belgium<br>EUV outgassing analysis, Photoresist mechanism study |
| **Jul. 2019 – Sep. 2019** | **Visiting Researcher**<br>ARCNL, the Netherlands<br>Photoresist coatability and developability study, EBL |
| **May. 2016 – Sep. 2016** | **Researcher**<br>Microcosm Technology Co., Ltd, Taiwan |

HT-PEMFC, Transparent conductive film development

## Education

| | |
|---|---|
| **Sep. 2017 – Oct. 2020** | **PhD** in Materials Science and Technology<br>TU Wien (Vienna University of Technology), Austria |
| **Sep. 2014 – Dec. 2015** | **MSc** in Polymer Materials Science and Engineering<br>The University of Manchester, UK<br>Result: Merit (Top 20% of the year) |
| **Sep. 2008 – Jun. 2013** | **BSc** in Chemistry<br>National Cheng Kung University, Taiwan |

## Academic Activities

| | |
|---|---|
| **Sep. 6th, 2019, imec** | Oral presentation at 2nd ELENA Conference, titled’’ Synthesis and Characterizations of Group 4 Metal Oxo Clusters for EUVL Photoresist Applications’’. |
| **Sep. 29th, 2018, Warsaw** | Poster presentation at 1st ELENA Conference, titled’’ Synthesis and Characterizations of Zirconium Oxo Clusters for EUVL Photoresist Applications’’. |
| **Nov. 2017, TU Delft**<br>**Aug. 2018, TESCAN**<br>**Apr. 2019, ZEISS** | Participated in three ELENA Technical Training Schools |
| **Apr. 2018, Minerva**<br>**Mar. 2019, Univ. Iceland** | Participated in two ELENA Personal Skills Training Schools |
| **Oct. 21st , 2016, Beijing** | Invited as professional consultant by **China Centre for International Economic Exchanges (CCIEE)** about “General Properties and Mass Production of Graphene”. |
| **Jul. 13th, 2016, Taipei** | Participated in the **Graphene Training Workshop** held by Industrial Development Bureau, Ministry Economic Affairs, R.O.C. |

## Key Skills

| | | |
|---|---|---|
| Synthesis: | Polymers | Organometallic Compounds |
| | Composites | |
| Instrument: | SEM | AFM |
| | NMR | TEM |
| | TGA | DSC |
| | XRD | FTIR |
| | UV/Vis | E-beam Lithography System-Voyager |
| Software: | MATLAB | UVProbe |
| | OPUS | Microsoft Office |
| | EndNote | Windows |
| | TopSpin | OS (Apple) |
| | Proteus | |
| Software: | Mandarin (Native Language) | |
| | English (Professional Proficiency) | |
| | German (Basic) | |